



HAL
open science

Asymptotic methods for resonant acoustical metamaterials

Carl Zhou Hagström

► **To cite this version:**

Carl Zhou Hagström. Asymptotic methods for resonant acoustical metamaterials. Acoustics [physics.class-ph]. Institut Polytechnique de Paris, 2023. English. NNT : 2023IPPAE004 . tel-04439534

HAL Id: tel-04439534

<https://theses.hal.science/tel-04439534>

Submitted on 5 Feb 2024

HAL is a multi-disciplinary open access archive for the deposit and dissemination of scientific research documents, whether they are published or not. The documents may come from teaching and research institutions in France or abroad, or from public or private research centers.

L'archive ouverte pluridisciplinaire **HAL**, est destinée au dépôt et à la diffusion de documents scientifiques de niveau recherche, publiés ou non, émanant des établissements d'enseignement et de recherche français ou étrangers, des laboratoires publics ou privés.



INSTITUT
POLYTECHNIQUE
DE PARIS

NNT : 2023IPPAAE004

Thèse de doctorat



Asymptotic methods for resonant acoustical metamaterials

Thèse de doctorat de l'Institut Polytechnique de Paris
préparée à l'École nationale supérieure de techniques avancées

École doctorale n°626 de l'Institut Polytechnique de Paris (EDIPParis)
Spécialité de doctorat : Mécanique des fluides et des solides, acoustique

Thèse présentée et soutenue à Palaiseau, le 7 avril 2023, par

JOAR ZHOU HAGSTRÖM

Composition du Jury :

Mathias Fink Professeur, ESPCI Paris (Institut Langevin)	Président
Sébastien Guenneau Directeur de recherche, Imperial College (Department of Mathematics)	Rapporteur
Vincent Pagneux Directeur de recherche, Le Mans Université (LAUM)	Rapporteur
Christophe Josserand Directeur de recherche, École Polytechnique (LadHyx)	Examineur
Agnès Maurel Directrice de recherche, ESPCI Paris (Institut Langevin)	Examinatrice
Kim Pham Professeur associé, ENSTA Paris (IMSIA)	Directeur de thèse

Acknowledgements

My greatest gratitude goes to my supervisors, Kim Pham and Agnès Maurel, for their support and trust during the last years. I thank them for their kindness, and especially their patience during our time working together, as well as their presence in moments of doubt. Their intuition and thoroughness has been of great inspiration for the work presented in this thesis.

I would like to thank Vincent Pagneux and Sébastien Guenneau for their careful reading of the manuscript, as well as Mathias Fink and Christophe Jossierand for being part of the jury. I would also like to acknowledge the funding of the french DGA.

I would also like to thank all my colleagues and friends of the UME, as well as the people I have encountered during the last years.

Finally, I would like to thank all the people that have been present during this thesis, and I am especially grateful to my friends and my family for their love and support.

Résumé

Le domaine des matériaux composites a permis le développement de propriétés exotiques en termes de contrôle de la propagation d'onde. Ces matériaux artificiels, correspondant aux métamatériaux, ont connu un intérêt important durant les deux dernières décennies pour leurs propriétés extraordinaires qu'on ne retrouve pas dans la nature. Ces matériaux composés d'un réseau de cellule microstructurée ont permis des applications dans plusieurs branches de la physique. Initialement développé en électromagnétisme, le domaine des métamatériaux s'est répandu à d'autres disciplines comme l'acoustique, l'élastodynamique, les ondes à la surface de l'eau et en géophysique.

Dans cette thèse, on s'intéresse à la modélisation des métamatériaux acoustiques résonants. En utilisant des techniques d'homogénéisations asymptotiques, on dérive et analyse des modèles effectifs pour deux systèmes acoustiques résonants différents.

La première partie est consacrée à l'étude d'un réseau de période sub-longueur onde composé de fente. Ce type de structure donne lieu à des résonances de Fabry-Pérot, où la résonance fondamentale est associée à une longueur d'onde deux fois plus grande que la longueur de la fente. Cela permet la transmission extraordinaire, observé en acoustique et en électromagnétisme, à des fréquences proches de la résonance.

Dans le cas d'un réseau à double période, composé d'une cellule périodique avec deux fentes, on s'intéresse à la configuration où une certaine symétrie est brisée. Ce faisant, le champ évanescence le long de la structure peut se coupler avec le continuum qui se propage. Les résonances parfaites deviennent des quasi-résonances, ou des modes fuyants, ce qui entraîne un comportement frappant dans le spectre de transmission. Des pics asymétriques de type Fano sont observés et sont caractérisés par une transmission parfaite suivis d'une réflexion parfaite sur une bande de fréquences très étroite.

Des propriétés d'un réseau régulier de période sub-longueur sont d'abord rappelées, ainsi que des résultats d'homogénéisation. On illustre numériquement la présence de modes piégés et le repliement des branches de l'onde guidée, qui conduit à l'apparition de la résonance de Fano. La dérivation du modèle effectif homogénéisé du réseau à période double est obtenue par une combinaison d'homogénéisation en volume et des méthodes de raccordements asymptotiques. Le modèle effectif permet d'obtenir des solutions explicites et analyser les mécanismes résonnants sous-jacents du système.

La deuxième partie porte sur les matériaux enroulés dans l'espace ('space-coiled') dans le contexte acoustique. Dans le but d'avoir un réseau plus compact et de réduire son épaisseur, l'idée d'enrouler les fentes sur elles-mêmes a été introduite. Ces matériaux labyrinthiques ou 'space-coiled' reposent sur l'idée que l'onde acoustique est forcée de suivre la trajectoire de la fente enroulée. Ces structures ont stimulé de nombreuses recherches en matière de manipulation de front d'onde, grâce à leur capacité à obtenir un grand déphasage de l'onde transmise par rapport à l'épaisseur de la structure. On utilise des outils asymptotiques similaires à ceux de la première partie, et étudions deux types d'arrangement labyrinthiques.

On revisite l'enroulement communément rencontré dans la littérature en appliquant des techniques d'homogénéisation classique et on montre que, bien que les études précédentes aient donné de bons résultats par intuition, l'approche par homogénéisation donne un indice effectif équivalent plus précis.

Une deuxième étude est consacrée à ce qu'on appelle un méta-cristal. Il s'agit d'un matériau enroulé dans l'espace avec des fentes droites de l'ordre de la longueur d'onde. Un modèle effectif est dérivé et permet une propagation unidimensionnelle à l'intérieur de chaque

fente et où chaque coude, éloigné de l'ordre de la longueur d'onde, agit comme un diffuseur. Cela peut être interprété comme un cristal phononique unidimensionnel imbriqué dans un réseau sub-longueur d'onde, et bénéficie maintenant de deux échelles de longueurs. La structure peut exhiber des bandes interdites dues à la diffraction de Bragg qui sont couplées aux résonances Fabry-Pérot. La taille totale de l'échantillon reste cependant faible grâce au repliement des fentes. Le modèle effectif permet notamment d'obtenir la relation de dispersion du cristal imbriqué, permettant de mieux comprendre le comportement résonant.

Abstract

The field of composite materials has allowed for the development of exotic properties in terms of manipulation of wave propagation. These artificial materials, corresponding to metamaterials, have seen an increased interest the last two decades for their extraordinary properties not commonly found in nature. These materials are composed of an array of microstructured cells, and has allowed for several applications in various fields of wave physics. Initially developed in electromagnetism, the field of metamaterials has been extended to other branches such as acoustics, elastodynamics, water waves and geophysics. In this thesis, we are interested in the modelling of resonant acoustic metamaterials. Using asymptotic homogenization techniques, we derive and analyse effective models for two different acoustical resonant systems. The first part is devoted to the study of subwavelength gratings composed of slits. Such gratings allow the presence of Fabry-Pérot resonances, where the fundamental resonance corresponds to a wavelength twice as large as the length of the slit. This leads to extraordinary transmission, observed both in acoustics and electromagnetism, at frequencies close to the resonance. We are interested in the case of a dual-period array, sometimes referred to as compound gratings. When dealing with a dual-period grating, composed of a periodic unit cell with two slits, we are interested in the configuration where some symmetry is broken. By doing so, the evanescent field along the structure can couple with the propagating continuum. The perfect resonances become quasi-resonances, or leaky modes, and this leads to some striking behaviour in the transmission spectra. Asymmetric Fano like peaks are observed and are characterised by a perfect transmission followed by a perfect reflection on a very narrow bandwidth of frequencies. We recall some properties of a regular subwavelength grating as well as homogenization results. We illustrate numerically the occurrences of trapped modes and the branch folding of guided wave, which allow the presence of the Fano resonance. The derivation of the homogenized effective model of a dual period metagrating is obtained through a combination of bulk homogenization and matched asymptotic techniques. The obtained model allows for the derivation of closed form solutions and an analytical study of underlying resonant mechanisms. The second part focuses on space-coiled materials in the acoustic setting. In order to obtain a more compact design and reduce the width of the grating, the idea of folding the slits on themselves has been introduced. These space-coiled or labyrinthine materials rely on the idea that the acoustic wave is forced to follow the path of the coiled slot. It has stimulated a lot of research in terms of wave front manipulation, as large phase shift of the transmitted wave compared to the thickness of the structure can be obtained. We use similar asymptotic tools as in the first part, and study two types of coiling arrangement. We revisit the most encountered coiled arrangement through classical homogenization and show that, although previous studies have shown good results through intuition, the homogenization approach gives a more accurate equivalent effective index. A second study is devoted to what we refer to as a meta-crystal. It consists of a space-coiled material, with straight slots of the order of the wavelength. Through some careful scaling, we derive an effective model which allows for one dimensional propagation inside each slot and where each turn distanced at the order of the wavelength acts as a scatterer. This can be interpreted as a one dimensional phononic crystal embedded in a subwavelength grating, which now benefits from two length-scales. The structure benefits from band gaps due to Bragg scattering, that is coupled with the Fabry-Pérot resonances. The total sample size stays however small thanks to the folding of the slots. Thanks to the derived effective model, the dispersion of the embedded crystal can be obtained, giving insight on the resonant behaviour.

Contents

Acknowledgements	iii
Résumé	vi
Abstract	vii
1 Introduction	3
Part I - Dual Period Grating	11
2 Problem setting - Subwavelength grating	11
2.1 Governing equation	11
2.2 Guided modes	14
2.3 Homogenization/effective model	16
2.3.1 Classical homogenization	16
2.3.2 Material properties: Limit cases	18
2.3.3 Application to grating	18
2.4 Conclusion	21
3 Dual Period	23
3.1 Introduction	24
3.2 Problem formulation and results	27
3.2.1 The actual problem	27
3.2.2 Trapped modes	27
3.2.3 Numerical evidence of the perfect trapped-mode through guided-wave excitation	28
3.3 The effective problem	30
3.4 Asymptotic homogenization	33
3.4.1 Analysis in the bulk – Effective wave equations	33
3.4.2 Analysis at an grating interface and effective transmission conditions .	35
3.4.3 Formulation of a unique effective problem	39
3.5 Properties of the effective parameters	40
3.6 Solutions and effective problems	42
3.6.1 Explicit solution of the effective problem	42
3.7 Validation of the effective model for a scattering problem	44
3.7.1 Efficiency of the effective model in a scattering problem	44
3.7.2 Local analysis of the resonances	46
3.8 Guiding Properties	52
3.9 Concluding remarks and perspectives	53
Part II - Space-coiled metamaterials	57

4	Revisiting space-coiled metamaterials	57
4.1	Introduction	57
4.2	Homogenized models	59
4.2.1	Two-scale Homogenization	59
4.2.2	Two-step model	61
4.2.3	The two models in dimensional form	63
4.3	Comparison of the models	64
4.4	Concluding remarks and perspectives	68
5	Modelling of a metacrystal	71
5.1	Introduction	72
5.2	Main results	73
5.2.1	The actual problem	73
5.2.2	The effective problem	73
5.3	Derivation of the effective model	75
5.3.1	Effective propagation in the straight parts of the coiled slot	76
5.3.2	Solutions in the air far from the material	78
5.3.3	Analysis at the junctions at the entry/exit of the slot	78
5.3.4	Analysis at the junctions	82
5.3.5	Effective problem with curvilinear coordinate and unique formulation	86
5.4	Energetic properties	88
5.4.1	Energy balance of the effective model	88
5.4.2	Derivation of the energy balance	89
5.4.3	Positivity of \mathcal{C}	90
5.4.4	Positivity of \mathcal{B}	90
5.4.5	Positivity of \mathcal{D}	91
5.5	Validation of the effective model in the transient regime	92
5.6	Conclusions	93
6	Properties of the meta-crystal	97
6.1	Introduction	97
6.2	Validation of the model in the harmonic regime	97
6.2.1	Explicit solution of the effective model	97
6.2.2	Time domain formulation	99
6.3	Scattering properties of the effective model	100
6.4	Effect of the embedded crystal	102
6.5	Conclusion and perspectives	105
6.A	Multimodal method	107
7	General conclusions and perspectives	109
7.1	General conclusions	109
7.2	Future perspectives	110
	Bibliography	111

Chapter 1

Introduction

The properties of materials encountered in nature are a direct consequence of the interaction of waves and their microscopic structure. For instance, the colours of everyday objects are a result of the interaction of chemical elements composing the material, and their geometrical arrangement. Playing with the arrangement, the field of composite materials has allowed to control wave propagation and obtain materials exhibiting new extraordinary properties. The majority of these discoveries and studies were first done in electromagnetism, where exotic behaviour and ideas such as cloaking, negative refraction, lensing and subwavelength imaging were developed. In the last couple of decades, efforts in extending these ideas into other areas of wave physics have been made, such as the field of acoustics, elasticity, water waves and geophysics [32, 133].

These man-made materials can be divided into two subcategories. The first one is photonic crystals in electromagnetism, and their acoustic analogue phononic crystals [62]. They are composed by a periodic arrangement of unit cells composed of a scatterer. The periodicity of the unit cell is of the same order as the interacting wavelength, and Bragg scattering occurs [19]. Destructive interference takes place at certain frequencies which opens up band gaps, i.e. a range of frequencies where propagation is no longer possible. As their name imply, their behaviour is similar to the one of electrons in solid state physics, governed by energy bands [67]. Nevertheless, a major drawback of these types of structures are their size, as they are of the order of the wavelength. For instance, to obtain some low frequency bandgaps in the audible regime, the sample size will have to be at order of several meters. In the quest of reducing their sizes and improve their performance in the low frequency regime, materials with subwavelength unit cells endowed with a local resonance were envisioned. As the unit cell is of subwavelength size, the structured material can be seen a homogeneous medium with effective parameters, such as the permeability and permittivity in electromagnetism, and mass density and bulk modulus in acoustics. These so-called locally resonant metamaterials allowed for new applications, such as superlensing [121, 64], cloaking [106, 21], where the effective parameters can be interpreted as negative parameters, and opened up a new branch of wave physics. Other applications in terms of guiding properties [74, 66], sound absorption [136, 61, 100] and shielding [30, 29] have also been of large interest within the community.

Obtaining these effective parameters from a given microstructure is not a trivial task. Two main methods can be distinguished, a discrete approach and a homogenization approach, where the latter is favoured in this work. The *discrete* approach consists in studying a discrete system, considered as an analogue of the actual continuous problem, from which the effective parameters are deduced using various retrieval methods [107, 73, 102]. Depending on its complexity, deriving such a system is not straightforward and the approach might be completely flawed as the possibility of inconsistency between the discrete and continuous problem can be present.

The *homogenization* approach on the other hand starts off with the actual continuous

problem. Through some upscaling techniques and rigorous averaging processes, the microstructure is replaced by an equivalent medium described by some effective parameters at the macroscopic level, which faithfully reproduces the behaviour. These methods were initially studied in the static setting, with the asymptotic homogenization as a popular and efficient approach toward periodic microstructures. Specifically, the *two-scale* approach has been of high interest since its introduction in the 1970s. It relies on a scale separation as a variable at the order of the periodic unit cell is introduced to account for the fast oscillation of the microstructure. We refer to the works of [16, 135, 28, 14] for an in-depth presentation of the method. In the case of dynamical problems, the two scale approach has given fruitful results in the low-frequency (equivalently long-wavelength) framework, where the asymptotic are carried out as the period is small compared to the wavelength.

These methods are developed for an infinite periodic domain, and do not take into account any behaviour at presence of a boundary or interface. In the case of metamaterials, these size effects can generally not be neglected as the leading physical property can be governed by the behaviour at the edge. It is especially the case for thin structures. In order to reduce their size, the emergence of metasurfaces, or metafilms has been of great interest as they exhibit striking phenomenon despite their small size. In this case, an asymptotic treatment is needed on the boundary or at the interface. These problems have been of intensive investigation, where we mention for the case of boundary problem the works of [4, 112, 54]. For the case of interface problems between a periodic medium and homogeneous medium, less results exist and are more recent, notably [22, 96, 99, 31]. The derivation of such models is closely linked to the transmission problems through thin films, both homogeneous [15, 128] and periodic [1, 41, 38, 39, 95, 125, 126, 97]. The *boundary layer effects* correspond to the presence of evanescent fields confined to the boundary or interface. From an asymptotic view, two approaches are possible. The first consists of introducing *boundary layer correctors*, depending on the microscopic scale along the surface which exponentially decay away from it, to the homogenized solution depending only on the macroscopic scale. The second approach studies the problem in the vicinity of the layer at the microscopic scale, which is then matched with the homogenized far field at the macroscopic scale. Both approaches yield equivalent results at a given order.

The result is twofold: the homogenized solution is of especial interest for numerical applications. As the metamaterial usually depends on several scales, the numerical results come at an extremely high computational cost. The fine spatial discretization can be avoided by having a homogenized model only dependent of a macroscopic scale, leading to large computational gains. This also allows for an approximated analytical study of the problems, as the solutions are explicit through the effective model description. These methods are however limited by the chosen asymptotic setting, for instance the long wavelength regime. We will use these techniques to derive effective models for different configurations of materials, which benefits of analytical results and a further understanding of the resonant nature of the structures.

We also mention the *Willis approach*, a homogenization method derived from variational formulations. From the early works of [56, 151] initially developed in statics, extensions to dynamical problems have been made [152, 153]. More recently, links between the two approaches have been presented in [114, 104].

Compared to waves of another nature, the possibility of having a local resonance during the propagation of acoustic waves in fluids is limited. Plasmonic-type resonances are not available because there are no fluids with negative-valued compressibility or mass density in

acoustics, as is the case for the permittivity of metals at optical frequencies in electromagnetics [93, 127]. The same is true for Mie-type resonances, which exploit the high contrast value of shear modulus in elasticity [88] and permittivity in electromagnetics [70] to encapsulate a wavelength in an inclusion. Again, the contrast needed to create such a Mie resonance is simply not available in acoustics. The choice is therefore restricted to our knowledge to three types of local resonances in acoustics. The first is the sub-wavelength Minnaert resonance [134, 7, 5], which is a liquid-gas resonance (air bubble in water) that relies on a strong mass density contrast. The second is the Helmholtz resonance associated with the small leakage through an aperture of a perfect cavity mode [61, 8]. Finally, the last one is perhaps the simplest: it is the quarter or half-wavelength resonance which is that of an open straight slit, where the fundamental resonance corresponds to a wavelength four times or two times the slit length. It is this type of resonance that we use in the first part of this work. In order to significantly reduce the size of this type of resonator, the idea of winding the straight slit gave birth to the field of space-coiled metamaterials. This is the main subject of the second part of the thesis.

A result that sparked interests in subwavelength apertures is the one of the pioneering works of the group of Ebbesen [43] in the late 1990s. In the mentioned paper, an experimental study on light transmission through a perforated metallic screen was presented. A hole larger than the wavelength allows virtually all the light to pass, whereas a subwavelength hole allows almost no light to pass. In the latter case, the hole is too small and the incident wave does not 'see' the small aperture. This was widely known, and it was shown theoretically several decades ago [17] that the transmittance of a circular hole decreased quadratically with respect to its radius for a given wavelength. The thickness of the film only weakens the transmittance. However, the group of Ebbesen showed experimentally that a metallic array with periodically spaced subwavelength holes could resonantly enhance the transmittance. Notably, such an array could transmit more energy than a large hole with an equivalent holey surface. This resonance is referred to as extraordinary optical transmission (EOT), and was later on extended to the microwave regime and to its acoustic analogue, extraordinary acoustical transmission (EAT) [90]. The resonant nature was explained by the existence of a surface wave confined along the array and a cavity resonance of the hole. As the EOT is a full three dimensional problem, the acoustic case can be reduced to a two dimensional problem, and is less complicated as it only relies on the cavity resonance of the hole, which is a Fabry-Pérot resonance due to constructive interference. EOT (EAT) was later on extended to gratings of finite size, and have been of high interest in the last two decades. Classical homogenization has shown fruitful results, extending the model to any angle of incidence [53, 105]. By classical homogenization, we refer to the fact that the model is obtained at the dominant order of the asymptotic expansion. These models also capture a more broadbanded EAT, associated with the Brewster angle, corresponding to the impedance matching between the grating and the surrounding medium. Building on these ideas and methods, we extend these studies to more complex geometries, which together with a more involved asymptotical analysis, constitutes the major works of this thesis.

Before going further, we need to disclaim that the bibliography in this section is not exhaustive. As there exists a vast literature in each domain of physics, where the communication between them is not always present, we only present a few which illustrates the extremely vast field of metamaterials. Similarly, the list of references concerning the asymptotical techniques is limited to the most relevant in the sequel.

The manuscript is divided into two parts:

Part I - The first part of the thesis is devoted to the study of dual-period array, sometimes referred to as compound gratings. The geometry is illustrated in figure 1.1. When studying the scattering properties of gratings subject to a certain symmetry, local resonant states exist along the grating and do not interact with the propagating modes. These localized modes are referred to as *trapped modes*, or *guided modes*, in the context of acoustic and mechanical waves, and bound states in the continuum in the electromagnetism and quantum mechanics. They have gained a lot of interest in recent years for applications in filters and for sensing applications. When dealing with a dual-period grating, composed of a periodic unit cell with two slits, we are interested in the configuration where some symmetry is broken. By doing so, the evanescent field along the structure can couple with the propagating continuum. The perfect resonances become quasi-resonance, or *leaky modes*, and this leads to some striking behaviour in the transmission spectra, where asymmetric Fano like peaks are observed.

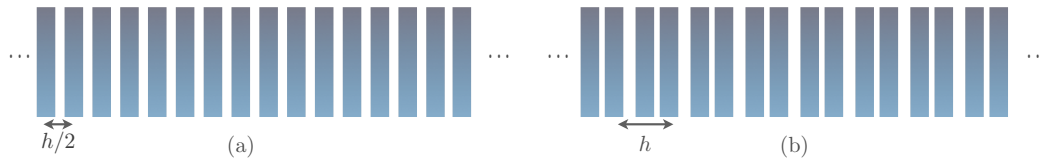


Figure 1.1: Geometry of the considered grating. (a) Regular grating and (b) dual period grating subject to some symmetry breaking.

We treat the acoustic problem for incident pressure waves diffracted by the sound hard rigid parts. This is the analogue problem as for transverse polarized electromagnetic waves impinging on perfect conductors.

From an homogenization perspective, the behaviour of a regular grating is recovered at the dominant order. In order to capture the sharp anomalies, it is not sufficient to derive higher order term in the homogenization process, as the resonance is due to the excitation of an evanescent field along the structure. To proceed, an additional asymptotic treatment needs to be performed at each interface in order to recover the Fano-type behaviour.

In chapter 2, we present the problem setting. We will consider in this work the propagation a scalar wave, corresponding to solving the Helmholtz equation in two dimensions. We recall some properties of a regular subwavelength gratings and the a semi-analytical modelling. We recall some fundamental properties, and establish the homogenization setting for the rest of the manuscript.

In chapter 3, we present the physical properties of the dual period metagrating. We illustrate numerically the occurrences of trapped modes and the branch folding of guided wave, which allow the presence of the Fano resonance. The derivation of the homogenized effective model of a dual period metagrating is then presented, and we show the importance of the analysis at the edges of the array. The results show that the model is accurate up to surprisingly high frequencies. Furthermore, the obtained model allows for the derivation of closed form solutions and an analytical study of resonances. The results have been published in the paper [159].

[159] Zhou Hagström, Joar and Maurel, Agnès and Pham, Kim. (2021). The interplay between Fano and Fabry-Pérot resonances in dual-period metagratings, *Proceedings of the Royal Society A*, 477(2255):20210632.

Part II - The second part focuses on space-coiled materials in the acoustic setting. As mentioned above, these space-coiled or labyrinthine materials rely on the idea that the acoustic waves are forced to follow the path of the coiled slot. Spiral geometries and folding of the slot has allowed for compact design when dealing with surface waves.

It has also stimulated a lot of research in terms of wave front manipulation. This can result in possibly large phase shift of the transmitted wave compared to the thickness of the structure. By varying the coiling from a cell to another, one can tune the phase shift and thus obtain beam steering.

From a theoretical point of view, few attempts of deriving effective coefficient have been made. The question of effective length, i.e. the equivalent length of its uncoiled analogue, has been of great interest, and the few results rely on some heuristic definition of the uncoiled analogue. We tackle this problem through a more rigorous homogenization approach, and show that through some rearrangement of the coiling, one can obtain a richer response.

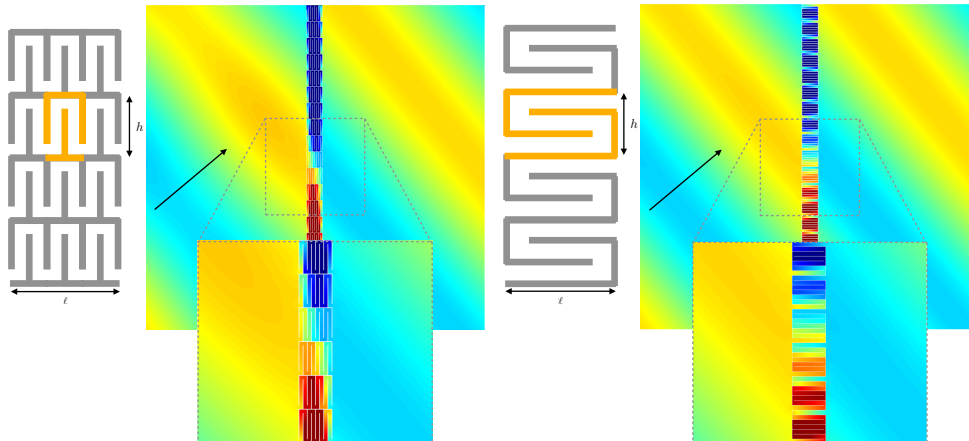


Figure 1.2: (a) Classical space-coiled metasurface (b) Space-coiled metacrystal. The orange parts show the unit cell. Both structures can exhibit large phase shifts, here of the order π , much larger than the thickness of the structure.

In chapter 4, we revisit the classical space-coiled materials through classical homogenization and show that, although previous results have shown good results through intuition, the homogenization approach gives a more accurate equivalent effective index. The results are illustrated with numerical examples, and results from the existing literature are compared. The result reported in this chapter mainly reproduces the results obtained in [161] currently under revision at *wave motion*.

[161] Zhou Hagström, Joar and Maurel, Agnès and Pham, Kim. (2022) Revisiting effective acoustic propagation in labyrinthine metasurfaces, *under revision*

Chapter 5 concerns the study of what we refer to as a meta-crystal. It consists of a space-coiled material, with straight slots of the order of the wavelength. The considered

configurations is depicted in figure 1.2. Through some careful scaling, we derive an effective model which allows for one dimensional propagation inside each slot and where each turn distanced at the order of the wavelength acts as a scatterer. This can be interpreted as a one dimensional phononic crystal embedded in a subwavelength grating, which now benefits from two length-scales. The structure benefits from band gaps due to Bragg scattering, that is coupled with the Fabry-Pérot resonances. The total sample size stays however small thanks to the folding of the slots. Thanks to the derived effective model, the dispersion of the embedded crystal can be obtained, giving insight on the underlying mechanism. The derivation of the effective model is the main contribution of the following paper submitted in October 2022.

[160] Zhou Hagström, Joar and Maurel, Agnès and Pham, Kim. (2022) Modeling acoustic space-coiled metacrystals, *submitted to SIAM*

Finally, the results are summarised in a last chapter. We make final conclusions and discuss possible perspectives.

Part I - Dual Period Grating

Chapter 2

Problem setting - Subwavelength grating

Chapter summary: This chapter gives an introductory outline of the studied problem and the general setting is defined. We recall properties of a periodic grating and present the homogenization scheme of a layered material applied to the study of a regular sound hard grating.

Contents

2.1	Governing equation	11
2.2	Guided modes	14
2.3	Homogenization/effective model	16
2.3.1	Classical homogenization	16
2.3.2	Material properties: Limit cases	18
2.3.3	Application to grating	18
2.4	Conclusion	20

2.1 Governing equation

In this section, we lay down the the physical setting and the governing equations. Acoustic wave propagation is a scalar wave propagation in a given dimension, in this case two dimensional. The spacial coordinates are denoted by $\mathbf{x} = (x_1, x_2) \in \mathbb{R}^2$ and the time variable is denoted by t . The linearized Euler equations govern the acoustic wave propagation, namely

$$\rho(\mathbf{x}) \frac{\partial \mathbf{U}}{\partial t}(\mathbf{x}, t) = -\nabla P(\mathbf{x}, t), \quad \frac{1}{B(\mathbf{x})} \frac{\partial P}{\partial t}(\mathbf{x}, t) + \operatorname{div} \mathbf{U}(\mathbf{x}, t) = 0, \quad \forall \mathbf{x} \in \mathbb{R}^2, \quad (2.1)$$

where p is the scalar pressure field, \mathbf{u} is the vectorial velocity field, ρ is the mass density and $B = \rho c^2$ is the bulk modulus, with c is the velocity of the wave in the given fluid. The study is often done in the harmonic regime. This corresponds to a system with a periodic time dependency of $e^{-i\omega t}$. This enables a spectral and modal analysis of the problem, as well as dropping an initial time condition imposed by the time dependence. This allows us to solve the problem by variable separation of the form

$$P(\mathbf{x}, t) = \operatorname{Re} (p(\mathbf{x})e^{-i\omega t}), \quad \mathbf{U}(\mathbf{x}, t) = \operatorname{Re} (\mathbf{u}(\mathbf{x})e^{-i\omega t}), \quad \omega \in \mathbb{R}, \quad (2.2)$$

where ω is the angular frequency. This is justified by a Fourier transform, and a time domain solution can be obtained by an inverse Fourier transform. We have the harmonic problem:

$$\nabla p(\mathbf{x}) = i\omega \rho(\mathbf{x}) \mathbf{u}(\mathbf{x}), \quad \operatorname{div} \mathbf{u}(\mathbf{x}) = i\omega \frac{1}{B(\mathbf{x})} p(\mathbf{x}), \quad (2.3)$$

from which we obtain the wave equation

$$\operatorname{div} \left(\frac{1}{\rho(\mathbf{x})} \nabla p(\mathbf{x}) \right) + \frac{\omega^2}{B(\mathbf{x})} p(\mathbf{x}) = 0, \quad (2.4)$$

where we omitted the time dependency $e^{-i\omega t}$. This is equivalent to the case of transverse magnetic (TM) polarization, where the magnetic field $\mathbf{H} = H(\mathbf{x})\mathbf{e}_z$ is perpendicular to the plane. The waves are in this setting governed by the following equation

$$\operatorname{div} \left(\frac{1}{\epsilon(\mathbf{x})} \nabla H(\mathbf{x}) \right) + \mu(\mathbf{x})\omega^2 H(\mathbf{x}) = 0, \quad (2.5)$$

where ϵ is the permittivity and μ the permeability. Similarly, the same equation describes the out-of-plane elastodynamical wave propagation, where the shear modulus G plays the role of permittivity and the mass density ρ the role of permeability. The elastic scalar displacement field \mathbf{U} is governed by

$$\operatorname{div} (G(\mathbf{x})\nabla \mathbf{U}(\mathbf{x})) + \rho(\mathbf{x})\omega^2 \mathbf{U}(\mathbf{x}) = 0. \quad (2.6)$$

These analogy are of interest as works in different fields have led to the similar results, as will be shown later on. Although we focus on acoustical propagation, the wave equation can be written in its generic form

$$\operatorname{div} (\mathbf{a}(\mathbf{x})\nabla p(\mathbf{x})) + \mathbf{b}(\mathbf{x})\omega^2 p(\mathbf{x}) = 0, \quad (2.7)$$

where \mathbf{a} and \mathbf{b} will be the material parameters. We consider a grating of length 2ℓ centered along $x_1 = 0$ and is of periodicity h . We also consider a layer D_ℓ of material of width 2ℓ with material properties $(\mathbf{a}_i, \mathbf{b}_i)$, surrounded by an ambient medium $(\mathbf{a}_e, \mathbf{b}_e)$. By periodically removing material from the layer, we are left with a grating composed of an array of domains $\cup_i D_i$. The governing equation (2.7) can be rewritten as

$$\begin{cases} \Delta p + k^2 p = 0 & \text{in } \mathbb{R}^2 \setminus \cup_i D_i \\ \Delta p + k_i^2 p = 0 & \text{in } \cup_i D_i, \end{cases} \quad (2.8)$$

where we have the wavenumber $k = \omega\sqrt{\mathbf{b}_e/\mathbf{a}_e}$ and $k_i = \omega\sqrt{\mathbf{b}_i/\mathbf{b}_i}$. As contrasts exists between the material properties, we need the additional natural continuity conditions of both pressure and velocity along the interface of each D_i ,

$$p|_+ = p|_- \quad \text{and} \quad \mathbf{a}_i \frac{\partial p}{\partial \mathbf{n}} \Big|_+ = \mathbf{a}_e \frac{\partial p}{\partial \mathbf{n}} \Big|_- \quad \text{on each } \partial D_i. \quad (2.9)$$

where, \mathbf{n} denotes the outward normal vector of each D_i and $\cdot|_\pm$ denotes the limit of inside and outside of D_i . Let $D_i = \{\mathbf{x} \in (-\ell, \ell) \times (-1, (-1 + \varphi))h/2 \cup ((1 - \varphi), 1)h/2\}$, where φ is the filling fraction, see figure 2.1.

In the following, we illustrate some properties of the gratings when excited by a right going plane wave $p^{\text{inc}}(\mathbf{x}) = e^{i(k_0 x_1 + b_0(x_2 + \ell))}$, where k_0 and b_0 corresponds respectively to the x_1 and x_2 component of the wave number k . The angle of incidence is given by $\theta = \operatorname{atan}(b_0/k_0)$. Knowing that the incident wave only differs by a phase shift of $e^{ib_0 h}$ between (x_1, x_2) and $(x_1, x_2 + h)$, we take advantage of the periodicity of the grating to search for a *pseudo-periodic* solution of the form, referred to as a *Bloch wave* solution,

$$p(\mathbf{x}) = \tilde{p}(\mathbf{x})e^{ib_0 x_2}, \quad (2.10)$$

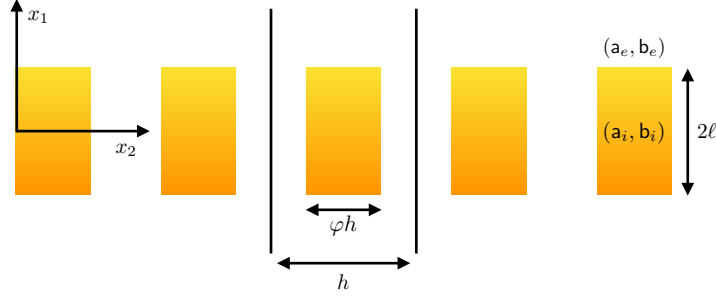


Figure 2.1: Periodic array composed of a finite layered material.

where $\tilde{p}(\mathbf{x})$ is a h -periodic function with respect to x_2 . As $p(\mathbf{x})e^{-ib_0x_2}$ is h -periodic, it admits a fourier series expansion, which gives the following expansion for $p(\mathbf{x})$,

$$p(\mathbf{x}) = \sum_{n \in \mathbb{Z}} p_n(x_1) \varphi_n(x_2), \quad (2.11)$$

where φ_n forms an orthonormal basis and is given by

$$\varphi_n(x_2) = \frac{1}{\sqrt{h}} e^{ib_n x_2}, \quad \text{where } b_n = b_0 + \frac{2\pi}{h} n, \quad n \in \mathbb{Z}. \quad (2.12)$$

Substituting the expansion (2.11) into (2.8) leads to the second order ordinary differential equation

$$p_n''(x_1) + (k^2 - b_n^2) p_n(x_1) = 0, \quad n \in \mathbb{Z}. \quad (2.13)$$

Knowing the general solution to this differential equation, we can obtain the general solution to the Helmholtz equation,

$$p(\mathbf{x}) = \sum_{n \in \mathbb{Z}} \left(A_n e^{ik_n x_1} + B_n e^{-ik_n x_1} \right) \varphi_n(x_2), \quad (2.14)$$

where $A_n, B_n \in \mathbb{C}$, and we have defined

$$k_n = \begin{cases} \sqrt{k^2 - b_n^2} & \text{if } b_n^2 \leq k^2, \\ i\sqrt{b_n^2 - k^2} & \text{otherwise.} \end{cases} \quad (2.15)$$

We identify two types of modes. When k_n is a real number, the terms $e^{\pm ik_n x_1}$ represents left/right-going propagation modes. When k_n is imaginary, the modes are evanescent as the terms are of exponentially decay as $|x_1| \rightarrow \infty$. The propagation modes are of finite number, and the evanescent modes are of infinite number. When we consider the incidence of a plane wave p^{inc} , the solution of the problem is of the form

$$p(\mathbf{x}) = \begin{cases} p^{\text{inc}}(\mathbf{x}) + \sum_{n \in \mathbb{Z}} r_n e^{-ik_n(x_1 + \ell)} e^{ib_n x_2}, & x_1 < -\ell, \\ \sum_{n \in \mathbb{Z}} t_n e^{ik_n(x_1 - \ell)} e^{ib_n x_2}, & x_1 > \ell. \end{cases} \quad (2.16)$$

We have for the moment not specified any conditions when x_1 tend to infinity. Such condition is referred to as a radiation condition. We consider that all scattered fields are bounded

composed of only outgoing plane waves, referred to as outgoing wave condition. It is this condition that leads to the form (2.16), where $A_0 = 1$ and $B_n = r_n$ for $x_1 < -\ell$, and $A_n = t_n$ and $B_n = 0$ for $x_1 > \ell$.

We identify three regions in the (k, b_0) -plane, when supposing $\mathbf{b}_e/\mathbf{a}_e < \mathbf{b}_i/\mathbf{a}_i$:

$$\begin{cases} b_0^2 < \omega^2 \mathbf{b}_e/\mathbf{a}_e, \\ \omega^2 \mathbf{b}_e/\mathbf{a}_e < b_0^2 < \omega^2 \mathbf{b}_i/\mathbf{a}_i, \\ \omega^2 \mathbf{b}_i/\mathbf{a}_i < b_0^2. \end{cases} \quad (2.17)$$

The first one corresponds to the scattering states, a continuous radiation spectrum situated above the light/sound line $b_0 = \omega \mathbf{b}_e/\mathbf{a}_e$ where all outgoing waves satisfy the outgoing radiation condition. In the last region, no scattering nor guided states exists, as the modes are exponential inside and outside the slab.

In the second region, the modes are of exponential decay outside the grating as $|x_1| \rightarrow \infty$, and are confined and propagating along the grating with a phase velocity $v_\phi = \omega/b_0$, slower than the waves of the ambient medium. These correspond to guided modes, which are modes localized along the grating and are the nontrivial solution to the Helmholtz equation without source term. The decay on either side of the grating are given by a relation between k and b_0 , corresponding to the branches of the dispersion relation. These branches start off from the light/sound lines for a given k depending on the thickness of the grating. In contrast to the scattering states which are excited by incoming sources infinitely far away from the structures, guided modes can only be excited through a source in the near field or inside the grating, corresponding to an evanescent field confined to the grating.

Due to the pseudo-periodicity of the problem, the Bloch wave form allow one to reduce the problem. In fact, as the solution $p(\mathbf{x}) = \tilde{p}(\mathbf{x})e^{ib_0x_2}$ is periodic, by a change of periodicity one has $p(\mathbf{x}) = \tilde{p}(\mathbf{x})e^{i(b_0+n)x_2}$ with n an integer. The wavenumber b_0 can therefore be restricted to the first Brillouin zone $b_0 \in (-\pi/h, \pi/h)$. We will study reciprocal problem, which means that the Brillouin zone is symmetric. Our results will therefore be illustrated for $b_0 \in (0, \pi/h)$.

2.2 Guided modes

Surface waves, also referred to as Rayleigh-Bloch waves or guided waves, are of great importance when studying the response of gratings. They are the origin of several intriguing phenomenon, where the Wood anomaly might the first observed case. In 1902, Wood published some astonishing experimental results [154] when he studied the diffraction of a continuous light source upon a grating. He explains, in an almost romanticised way, how he instead of exhibiting a smooth spectrum, he observed sharp drops from maximum illumination to minimums. Fascinated, without any explanation, he termed them anomalies. Later on, Rayleigh [131] suggested that these anomalies were due the passing to higher order term of diffraction, and that the energy was redistributed. Although the order passing accounts to some extend the original observation, it does not fully explain the underlying mechanism, see [89]. In fact, this conditions can easily be observed in the case present in the previous section. As $b_n^2 < k^2$, the modes are propagating, and $b_n^2 > k^2$ are evanescent. The Wood anomaly occurs around the critical case $b_n^2 = k^2$. The wave is now purely guided surface wave, transporting energy only along the grating.

There are several settings where a flat interface supports guided waves. For instance, Rayleigh waves propagating along the interface of an elastic solid, or water waves guided

along the coastline. The very well known surface-plasmon polaritons (SP) at a metal-dielectric interface allows for guided modes in for the optical frequencies, with the typical characteristic of a having only one dispersion branch for a frequency interval lying below the plasma frequency. Hard sound flat boundaries does on the contrary not support surface waves in the acoustic setting. This is also the case of perfectly conducting metal for electromagnetic waves, and out-plane shear waves along a free edge in elasticity. These guided modes can however exist if the interface is subject to some periodic microstructure. Such waves, initially referred to as Rayleigh-Bloch surface waves, has been subjected to intense study for several different wave physics, such as electromagnetism [60, 147], acoustics [65], and water waves [45]. They gained interest and new popularity with the paper by Pendry and coworkers [122] in the middle of the 2000s. They showed that electromagnetic waves localized along a periodically corrugated perfect conductor could produce similar dispersions relation as surface plasmon polaritons. These were dubbed as *Spoof surface plasmons* (SSP), or designer surface plasmons, and subsequently opened up the branch of plasmonics to other areas in wave physics. When the periodic unit cell consists of slots, the wave can propagate along inside the slot, and half-wavelength resonance can be observed. They correspond to standing waves along the slots (this corresponds to quarter-wavelength resonance for grooves). These resonance are inversely proportionate to the length of the slots, and acts as the upper horizontal bounds, similar to the plasma frequency for SP. One can easily tune the dispersion of the SSP by varying the length of the slots. To further bring down the dispersion to low frequencies for thin structures, space-coiled or labyrinthine geometries were envisioned [58], see chapter 4. As we deal with sound hard plates, the third region defined in (2.17) vanishes, and no lower cut-off frequency exist, which allows for even slower surface waves.

We come back to theoretical and numerical modelling of such modes. Taking advantage of the pseudo-periodic decomposition, the problem (2.16) is restricted to the study on an infinite strip of width h . As mentioned before, the guided modes corresponds to the nontrivial solutions to the homogeneous Helmholtz equation (i.e. without source term). The existence of a guided mode at a given frequency is equivalent to the nonuniqueness of the problem. Passing to a weak form of the problem, one obtains an eigenvalue problem where $\lambda = k^2$ act as an eigenvalue of the self-adjoint Laplace operator $-\Delta$ with the appropriate boundary conditions. They are characterised by the min-max principle taken over a specific function space, which we do not specify here. This variational set up is presented in [18], in which they prove the existence of a finite number of guided modes below the continuous spectrum of radiation. For a more general review, see the chapter in [139]. By choosing a suitable test function, it is easy to prove rigorously prove the existence of guided modes below the cut off $b_0 < k$, as is done in [86] for the case of sound hard obstacles. If one insists in solving the scattering problem, which is our case [101], solving the scattering problem with the presences of a guided mode yields an ill posed problem. This leads to a divergence of the scattering coefficients at the frequencies of the guided modes, as shown in figure 2.2. It is worth noting that although the scattering coefficient diverge, the energy conservation is not violated as the incident field is also evanescent. Despite the fact that this is a result of a semi-analytic method, analytic results are hard to come by. We provide in the next section an homogenization approach, corresponding to classical leading order homogenization.

2.3 Homogenization/effective model

2.3.1 Classical homogenization

When studying such problems, an effective medium approach is of interest as one obtains effective parameters. These parameters are useful as they provide information on the physical properties. From a numerical point of view, such approach able one to drastically reduce the computational cost as the microstructure does not have to be meshed. Homogenization is an averaging process where the microstructure is replaced by an effective medium. When dealing with periodic microstructures, asymptotic homogenization [16, 28, 135] has been widely used. It relies on the multiple scale approach, obtained by an asymptotic approach as the periodicity h tends to 0. We provide in this section a brief example of the homogenization scheme of the Helmholtz equation for an infinite stratified media along the x_2 axis. In the context of subwavelength periodicity, the homogenization is done in the small frequency/long wavelength regime, by introducing the small parameter $\varepsilon = kh \ll 1$. To proceed, we start by introducing the dimensionless coordinates $\tilde{\mathbf{x}} = k\mathbf{x}$, where the periodicity of the stratified media now is $\varepsilon = kh \ll 1$. In order to make this dependence explicit in the equations, we introduce the dimensionless coefficients $\mathbf{a}^\varepsilon(\tilde{\mathbf{x}}) = \mathbf{a}(\mathbf{x})$, $\mathbf{b}^\varepsilon(\tilde{\mathbf{x}}) = \mathbf{b}(\mathbf{x})$ and the fields $p^\varepsilon(\tilde{\mathbf{x}}) = p(\mathbf{x})$ and $\mathbf{u}^\varepsilon(\tilde{\mathbf{x}}) = k^{-1}\mathbf{a}(\mathbf{x})\nabla p(\mathbf{x})$. In the dimensionless form, where we drop the $\tilde{\cdot}$ for simplicity, the governing equations reads

$$\begin{cases} \operatorname{div} \mathbf{u}^\varepsilon(\mathbf{x}) + \mathbf{b}^\varepsilon(\mathbf{x})p^\varepsilon(\mathbf{x}) = 0, \\ \mathbf{u}^\varepsilon(\mathbf{x}) = \mathbf{a}^\varepsilon(\mathbf{x})\nabla p^\varepsilon(\mathbf{x}), \end{cases} \quad (2.18)$$

where

$$\mathbf{a}^\varepsilon(\mathbf{x}) = \mathbf{a}\left(\frac{x_2}{\varepsilon}\right), \quad \mathbf{b}^\varepsilon(\mathbf{x}) = \mathbf{b}\left(\frac{x_2}{\varepsilon}\right). \quad (2.19)$$

In the above definitions, a and b are 1-periodic function and piecewise constant. We associate the following boundary conditions to (2.18): continuity conditions applies both to the dimensionless pressure p^ε and normal velocity and $\mathbf{u}^\varepsilon \cdot \mathbf{n}$ at each boundary between two stratified layers (\mathbf{n} denotes the normal vector to the boundary). To this end, some radiation condition needs to be applied. As the medium is periodic along x_2 , a conditions needs to be given for some $x_2 = \pm L$. This can be disregarded, or alternatively consider the case $L \rightarrow \infty$. For $|x_1| \rightarrow \infty$, a radiation condition needs to be defined. The homogenization is carried out with bearing in mind the two-scale approach: a macroscopic spatial dependence in \mathbf{x} , taking into account the slow variations of typical scale $O(1/k)$, and a microscopic scale, taking into account the fast variation inside each unit cell at the scale $O(h)$. The two-scale expansion relies on the following postulated *ansatz*, where we expand the fields

$$\begin{aligned} p^\varepsilon(\mathbf{x}) &= p^0\left(\mathbf{x}, \frac{x_2}{\varepsilon}\right) + \varepsilon p^1\left(\mathbf{x}, \frac{x_2}{\varepsilon}\right) + \varepsilon^2 p^2\left(\mathbf{x}, \frac{x_2}{\varepsilon}\right) + \dots, \\ \mathbf{u}^\varepsilon(\mathbf{x}) &= \mathbf{u}^0\left(\mathbf{x}, \frac{x_2}{\varepsilon}\right) + \varepsilon \mathbf{u}^1\left(\mathbf{x}, \frac{x_2}{\varepsilon}\right) + \varepsilon^2 \mathbf{u}^2\left(\mathbf{x}, \frac{x_2}{\varepsilon}\right) + \dots, \end{aligned} \quad (2.20)$$

where we have made evident the explicit dependency of the microstructure ε . We define the microscopic coordinate $y_2 = x_2/\varepsilon$. Each terms (p^n, \mathbf{u}^n) are functions of both variables \mathbf{x} and y_2 , and are Y -periodic in y_2 with $Y = (-1/2, 1/2)$. By injecting the *ansatz* into (2.18), we obtain the field (p^i, \mathbf{u}^i) for any $i \in \mathbb{N}$. For any vectorial function $\mathbf{f}(\mathbf{x}, y_2)$ and scalar function $f(\mathbf{x}, y_2)$, the divergence and gradient operator now reads

$$\nabla f \rightarrow \nabla_{\mathbf{x}} f + \frac{1}{\varepsilon} \frac{\partial f}{\partial y_2} \mathbf{e}_2, \quad \operatorname{div} \mathbf{f} \rightarrow \operatorname{div}_{\mathbf{x}} \mathbf{f} + \frac{1}{\varepsilon} \frac{\partial \mathbf{f}}{\partial y_2} \cdot \mathbf{e}_2 \quad (2.21)$$

where $\nabla_{\mathbf{x}}$ denotes the gradient *w.r.t.* \mathbf{x} . This leads to the cascade of equation in each order of ε , namely

$$\begin{aligned} \frac{1}{\varepsilon} \frac{\partial u_2^0}{\partial y_2} + \operatorname{div}_{\mathbf{x}} \mathbf{u}^0 + \frac{\partial u_2^1}{\partial y_2} + \mathbf{b}(y_2) p^0 + \sum_{i \geq 1} \varepsilon^i \left(\operatorname{div}_{\mathbf{x}} \mathbf{u}^i + \frac{\partial u_2^{i+1}}{\partial y_2} + \mathbf{b}(y_2) p^i \right) &= 0 \\ \frac{1}{\varepsilon} \mathbf{a}(y_2) \frac{\partial p^0}{\partial y_2} \mathbf{e}_2 + \mathbf{a}(y_2) \left(\nabla_{\mathbf{x}} p^0 + \frac{\partial p^1}{\partial y_2} \mathbf{e}_2 \right) - \mathbf{u}^0 + \sum_{i \geq 1} \varepsilon^i \left(\mathbf{a}(y_2) \left(\nabla_{\mathbf{x}} p^i + \frac{\partial p^{i+1}}{\partial y_2} \mathbf{e}_2 \right) - \mathbf{u}^i \right) &= 0. \end{aligned} \quad (2.22)$$

We conduct the derivation of the homogenized solutions, we introduce the average for any function f

$$\langle f \rangle(\mathbf{x}) = \int_Y f(\mathbf{x}, y_2) dy_2. \quad (2.23)$$

Note that if the unit cell is not of unity, one should divide the average over the periodic cell by its measure $|Y|$.

At leading order $O(1/\varepsilon)$, the equations reads $\partial_{y_2} p^0 = \partial_{y_2} u_2^0 = 0$ for $y_2 \in Y$ and where \mathbf{x} act as a parameter in the unit cell. This implies that (p^0, u_2^0) are independent of the fast variable y_2 ,

$$p^0(\mathbf{x}, y_2) = p^0(\mathbf{x}), \quad u_2^0(\mathbf{x}, y_2) = u_2^0(\mathbf{x}), \quad (2.24)$$

and that p^0 and u_2^0 are equal to their averages over the unit cell. Moving on to the next order, we establish the relation between the average $\langle \mathbf{u}^0 \rangle$ and p^0 . At order $O(1)$, the equations reads

$$\begin{aligned} \mathbf{u}^0(\mathbf{x}, y_2) &= \mathbf{a}(y_2) \left(\nabla_{\mathbf{x}} u^0(\mathbf{x}) + \frac{\partial u_2^1}{\partial y_2}(\mathbf{x}, y_2) \mathbf{e}_2 \right), \\ \operatorname{div}_{\mathbf{x}} \mathbf{u}^0(\mathbf{x}, y_2) + \frac{\partial u_2^1}{\partial y_2}(\mathbf{x}, y_2) + \mathbf{b}(y_2) p^0(\mathbf{x}) &= 0. \end{aligned} \quad (2.25)$$

As p^1 and u_2^1 are periodic *w.r.t.* y_2 , we have $\langle \partial_{y_2} p^1 = \partial_{y_2} u_2^1 = 0 \rangle$. Averaging the above equations gives us the wave equation at the dominant order

$$\begin{cases} \operatorname{div}_{\mathbf{x}} \langle \mathbf{u}^0 \rangle(\mathbf{x}) + \langle \mathbf{b} \rangle p^0(\mathbf{x}) = 0, \\ \langle \mathbf{u}^0 \rangle(\mathbf{x}) = \begin{pmatrix} \langle \mathbf{a} \rangle & 0 \\ 0 & \langle 1/\mathbf{a} \rangle^{-1} \end{pmatrix} \nabla_{\mathbf{x}} p^0(\mathbf{x}), \end{cases} \quad (2.26)$$

Coming back to the dimensional form, we obtain the highly anisotropic effective tensor \mathbf{a} , with the principal axis (x_1, x_2) , of the wave propagation at dominant order

$$\begin{cases} \operatorname{div} \mathbf{u}(\mathbf{x}) + \langle \mathbf{b} \rangle k^2 p(\mathbf{x}) = 0, \\ \mathbf{u}(\mathbf{x}) = \mathbf{a} \nabla p(\mathbf{x}), \quad \mathbf{a} = \begin{pmatrix} \langle \mathbf{a} \rangle & 0 \\ 0 & \langle 1/\mathbf{a} \rangle^{-1} \end{pmatrix}. \end{cases} \quad (2.27)$$

Note that the geometry is simple, a rather incremental method has been used in order to derive the form at the dominant order, as the solution is explicit. As the unit cell might be more complex, the derivation usually requires the definition of a so-called *elementary problem*, posed on the unit cell [16, 28, 135]. This is the case in chapter 4. If we consider that the layer is of width φh , where φ is the filling fraction, we obtain the following averages

$$\begin{cases} \langle \mathbf{a} \rangle = (1 - \varphi)/\mathbf{a}_i + \varphi/\mathbf{a}_e, \\ \langle 1/\mathbf{a} \rangle^{-1} = ((1 - \varphi)\mathbf{a}_i + \varphi\mathbf{a}_e)^{-1}, \\ \langle \mathbf{b} \rangle = (1 - \varphi)\mathbf{b}_i + \varphi\mathbf{b}_e, \end{cases} \quad (2.28)$$

For the moment, we have only formally derived the solution by injecting the *ansatz* into the governing equation. It is however necessary to assure some convergence of $(\mathbf{u}^\varepsilon, p^\varepsilon)$ to some solution as ε tends to 0, which can justify the formal derivation *a posteriori*. Several methods exist for such justification, and without being exhaustive we only mention the two-scale convergence [3, 116], and a variational method, relying on Γ -convergence [35].

2.3.2 Material properties: Limit cases

We take a moment to discuss the different cases and limitations of the homogenized solutions in terms of material properties for different kinds of physical wave propagation. Up to this point, we have only considered the case where the material properties of the grating are of the same order. In this case, the obtained effective solutions is valid in the low frequency regime for the three types of waves considered, TM-polarized electromagnetic waves, elastodynamical shear waves and acoustic pressure waves. When allowing for a large contrast, a new scaling needs to be done in order to take into account the local resonance within the inclusions. The material parameters are scaled $\mathbf{a}_i/\mathbf{a}_e = O(\varepsilon^2)$ and $\mathbf{b}_i/\mathbf{b}_e = O(1)$. This has been studied for bulk homogenization in [13, 12, 158, 49], and for the transmission problem across an interface of highly contrasted inclusions [125]. As mentioned before, this is possible only in electromagnetism and elasticity, but not in acoustics as there is no high contrast material in this range.

Considering the limit case of Neumann boundary conditions, corresponding to vanishing normal derivative along the layers, consists in a large impedance of the material, $|Z| = 1/|\sqrt{\mathbf{a}_i\mathbf{b}_i}| \rightarrow \infty$. In acoustics, such conditions are associated to a large density $\rho = 1/\mathbf{a}_i$ and a large bulk modulus $B = \rho c^2 = 1/\mathbf{b}_i$. As the velocity c does not vary much from one material to another, it means that the large wavelength approximation still holds in such a media, and one can safely consider the limit $Z \rightarrow \infty$. However, this is not the case in electromagnetism as the double limit does not commute. This has been studied in [113, 117, 48]. The Neumann limit applies to several material for different types of waves. In acoustics, it is associated to sound hard walls, and in elastodynamics to cracks or void. In electromagnetism, it is the case of perfectly conducting material for TM-polarised waves. This limit also coincides with the surface elevation of water waves in the shallow water regime. Taking the above limit corresponds to $\mathbf{a}_i, \mathbf{b}_i \rightarrow 0$ and setting the fraction $\mathbf{a}_i/\mathbf{b}_i$ equal to a constant. This results in the equivalent effective parameters $\langle \mathbf{a} \rangle = \langle \mathbf{b} \rangle = \varphi$ and $\langle 1/\mathbf{a} \rangle^{-1} = 0$, and the homogenized wave equation

$$\operatorname{div} \mathbf{u}(\mathbf{x}) + \langle \mathbf{b} \rangle k^2 p(\mathbf{x}) = 0, \quad \mathbf{u}(\mathbf{x}) = \begin{pmatrix} 1 - \varphi & 0 \\ 0 & 0 \end{pmatrix} \nabla p(\mathbf{x}). \quad (2.29)$$

2.3.3 Application to grating

In the preceding section, we considered the case of an infinite medium. In the case of a grating, the layered media is of finite size, and in order to apply the effective medium theory, we simply truncate the domain at $x_1 = \pm\ell$. Outside of the layered media, $|x_1| > \ell$, we consider an homogeneous medium. The question of the transmission conditions at the edge of the layered medium $x_1 = \pm\ell$ needs to be addressed. The natural and intuitive choice is the one of continuity of the both the pressure and normal velocity across each interface at $x_1 = \pm\ell$

$$[[p]] = 0, \quad [[u_1]] = 0, \quad (2.30)$$

where the jump is defined for any scalar function f for a given interface for instance in $x_1 = e$, $\llbracket f \rrbracket = f(e^+) - f(e^-)$. As it will be shown in the following chapters, by doing an additional asymptotic treatment around the interface one does indeed obtain the transmission conditions (2.30) at the leading order, although their derivation are far from being trivial. At higher order, correction appears from the asymptotic in general both for the pressure and flux. However, as the physical properties of the problem are mainly governed by the anisotropy of the effective slab, the leading order solution does accurately reproduces the original problem.

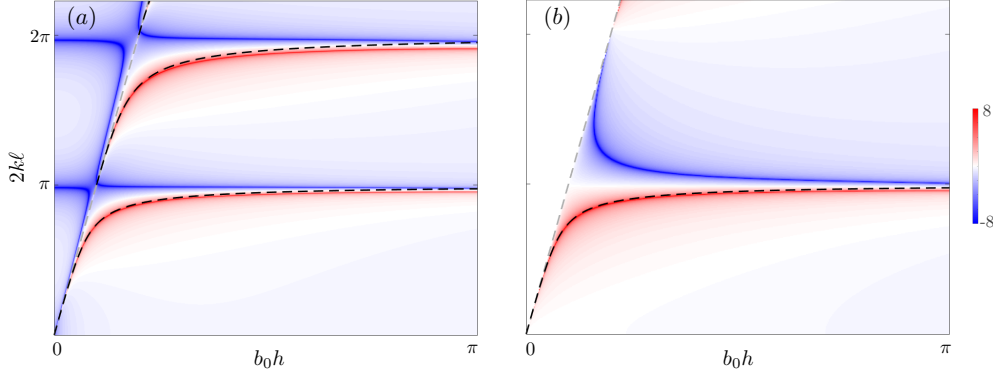


Figure 2.2: Dispersion relation for the SPP. The colormap corresponds to direct numerics $\log|r|$, and the relation is visible by diverging $\log|r|$ in red. The dashed grey line corresponds to the light/sound line. The dashed black lines corresponds to the dispersion relation obtained from homogenization. (a) corresponds to the transmission grating, and (b) to the reflection grating, which does not support antisymmetric modes, opening up a bandgap.

We shift our attention to the case of slits in a sound hard slab. The scattering properties are detailed in the next chapter 3, and we shift our focus to the guiding properties. In the following, we present some approximated closed forms of the dispersion branches. As specified, we look for solution of the wave equation without source term, namely, the homogenized problem for guided waves reads

$$\begin{cases} \frac{\partial^2 p}{\partial x_1^2} + k^2 p = 0, & \text{for } |x_1| < \ell, \\ \Delta p + k^2 p = 0, & \text{for } |x_1| > \ell, \\ \llbracket p \rrbracket = 0, \llbracket \frac{\partial p}{\partial x_1} \rrbracket = 0, & \text{for } x_1 = \pm \ell, \end{cases} \quad (2.31)$$

where some Bloch-Floquet condition needs to be taken into account at $x_2 = \pm L$. The layered material has been replaced by an equivalent effective medium. The solution of (2.31) is of the form

$$p(\mathbf{x}) = e^{ib_0 x_2} \times \begin{cases} e^{\gamma x_1}, & \text{for } x_1 < -\ell, \\ Ae^{kx_1} + Be^{-kx_1}, & \text{for } |x_1| < \ell, \\ Ce^{-\gamma x_1}, & \text{for } x_1 > \ell, \end{cases} \quad (2.32)$$

where γ is real valued and positive. The coefficients A, B and C can easily be obtained, from which we can determine for all $b_0 > k$ the explicit dispersion relation $b_0 = b_0(k)$,

$$\begin{cases} b_0 = k\sqrt{1 + \varphi^2 \tan^2 k\ell}, & \text{for } \tan k\ell > 0, \\ b_0 = k\sqrt{1 + \varphi^2 \cotan^2 k\ell}, & \text{for } \tan k\ell < 0. \end{cases} \quad (2.33)$$

This is in fact the same dispersion relation as recovered in [53, 105, 83] for subwavelength periodicity. We report in figure 2.2 the logarithm of the reflection coefficient $\log|r|$ in the $(2k\ell, b_0h)$ -plane from a scattering problem. The numerical method is presented in the following chapter, and is based on a multimodal method similar to [85]. The guided surface waves lie below the light/sound line, and can be observed by diverging parts of $\log|r|$ (in red).

We note that the term of spoof plasmons was introduced due to its ability to mimic the dispersion of plasmon polaritons at the interface between metal and air. The usual context is that of a grating composed of an array of length $\ell/2$ above a sound hard material. This problem is equivalent to the array with a Dirichlet conditions along the axis $x_1 = 0$, preventing the excitation of anti-symmetric modes, see the figure 2.3. This leads to the dispersion relation

$$b_0 = k\sqrt{1 + \varphi^2 \tan^2 2k\ell}, \quad \text{for } \tan 2k\ell > 0, \quad (2.34)$$

resulting in bandgaps for $\tan 2k\ell < 0$. In the analogy, the air above the grating corresponds to the air above the metal, and the grating corresponds to the metal. In the air above, surface waves propagates along the interface and are evanescent away from the interface, whereas as the behaviour differs in the metal and grating, see figure 2.3. As the wave can not propagate in the metal, it is also evanescent, while standing waves are present in the slots.

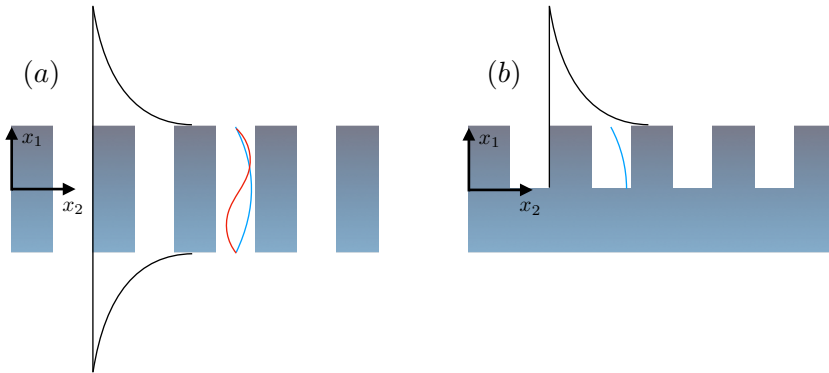


Figure 2.3: Sketch of SPP along a transmission and reflection grating. (a) Sketch of the exponential decay in black on the upper and lower side of the grating. Inside a slit, the first symmetric and antisymmetric half wavelength resonance are illustrated in blue and red respectively. (b) The same representation as (a) is done for a reflection grating. In this case, only symmetric resonances are allowed, and the first quarter wavelength resonance is illustrated in blue.

2.4 Conclusion

We have presented classical homogenization techniques for layered materials and a sound hard grating. We have illustrated how the model can recover the dispersion relation of the SPPs thanks to a closed form solution. The effective model is obtained at leading order in the bulk, where continuity conditions applies both for the pressure and velocity at the interfaces of the grating. Carrying out the asymptotical derivation to the next order will yield non trivial jump conditions at the edges. In the case of regular gratings, such correction will indeed improve the accuracy of the model, although the model at dominant order faithfully reproduces the behaviour of the grating. We present in the following chapter a case where a first order model is necessary, as the dominant order model fails.

Chapter 3

Dual Period

Chapter summary: This chapter is devoted to the study of the properties of a dual period grating of subwavelength periodicity. We consider the propagation of a scalar wave in the two dimensional plane, with a grating composed of slits in a non penetrable slab. At low frequency, a grating composed of a long enough slit supports Fabry-Pérot resonances, upon which Fano superimposes when the grating acquires dual period. The resulting transmission spectrum consists a flat-banded peaks of transmission scared by a sharp asymmetric dips of perfect and zero transmission over a small bandwidth. The modelling is done using a homogenization scheme combined with matched asymptotics at each interface. The obtained model consists in two non identical effective media which are coupled at each interface through effective jump conditions. These jump conditions efficiently 'encapsulate' the effect of the evanescent field which allows for the guided/trapped modes to be excited by a propagating wave. The model is validated by comparing to direct full wave numerics, and the approximated model allows for a physical analysis where closed forms solution can be derived.

The main results of this chapter have been published in the following article [159] Zhou Hagström, Joar and Maurel, Agnès and Pham, Kim. (2021). The interplay between Fano and Fabry-Pérot resonances in dual-period metagratings, *Proceedings of the Royal Society A*, 477(2255):20210632.

Contents

3.1	Introduction	24
3.2	Problem formulation and results	27
3.2.1	The actual problem	27
3.2.2	Trapped modes	27
3.2.3	Numerical evidence of the perfect trapped-mode through guided-wave excitation	28
3.3	The effective problem	30
3.4	Asymptotic homogenization	33
3.4.1	Analysis in the bulk – Effective wave equations	33
3.4.2	Analysis at an grating interface and effective transmission conditions	35
3.4.3	Formulation of a unique effective problem	39
3.5	Properties of the effective parameters	40
3.6	Solutions and effective problems	42
3.6.1	Explicit solution of the effective problem	42
3.7	Validation of the effective model for a scattering problem	44
3.7.1	Efficiency of the effective model in a scattering problem	44
3.7.2	Local analysis of the resonances	46

3.8	Guiding Properties	52
3.9	Concluding remarks and perspectives	52

3.1 Introduction

Striking asymmetric peaks of transmission or absorption can be observed in several physical settings. These peaks are attributed to Fano resonances, presented in the seminal works by Ugo Fano [47] dealing with autoionization of helium. Such resonance peaks were explained as the result of an interference between a 'discrete state' and a background 'continuum'. This discrete state is typically due to a defect or perturbation, allowing the scattering states to interact with the localized modes of the original configuration, see the review [108]. In the original work, Fano derived a formula describing the asymmetric line shape of the transmitted energy,

$$f(e) = \frac{|q + e|^2}{1 + e^2}, \quad (3.1)$$

where $e = (E - E_{\text{res}})/(\Gamma/2)$ is the dimensionless energy in the units of the resonance width Γ for a resonant energy E_{res} . q is the parameter, fano factor, that controls the asymmetry of the line shape. As q ranges from 0 to infinity, the line shape transforms from a *inverted Lorentzian* $e^2/(1 + e^2)$ to a *Lorentzian* $1/(1 + e^2)$. The asymmetric lineshapes are recovered for values in between, and their orientation depends on the sign of q , see figure 3.1.

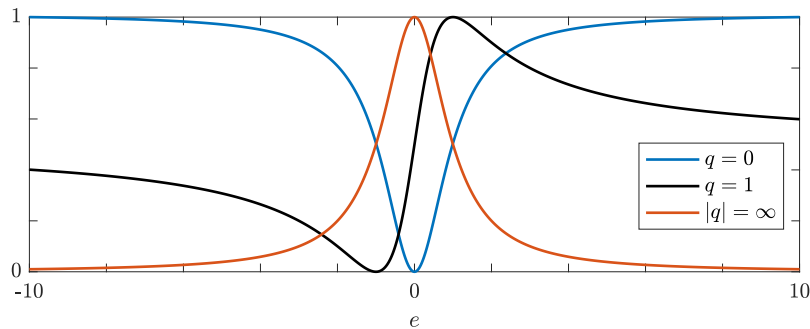


Figure 3.1: The transmitted energy given by the formula (3.1) for different values of q .

In this chapter, we study asymmetric peaks of transmission of a subwavelength grating composed of sound hard material. When these gratings are subjected to some symmetry breaking, the spectrum is scared by asymmetric peaks of perfect transmission and perfect reflection over an extremely small bandwidth, as shown in figure 3.2. This Fano resonance is due to the interaction of the scattering state and the resonant nature of the grating. As regular gratings are highly symmetric, they prevent any excitation of non-symmetric modes. These modes are trapped modes, corresponding to guided waves lying below the light line and are uncoupled to the continuum of propagating modes. For grating of thickness larger than the half-sepaing, constructive interferences occurs of the Fabry-Pérot (FP) type, leading to flat-banded peaks of perfect transmission 3.2(a). When considering a dual period structure, for instance the case of two identical slits brought closer together, and still preserving the symmetry of the unit cell, a local periodicity is introduced and the threshold is divided by two 3.2(b). By breaking some symmetry of the unit cell, for instance by considering two slits

of different width, it allows for the coupling of antisymmetric modes with the propagating waves. The perfect resonance becomes a quasi-resonance with radiative damping, as it gains a small imaginary part. The perfect trapped mode becomes a quasi-trapped mode. This coupling occurs instantaneously for any perturbation of the initial symmetry, resulting in scars in the spectra with characteristic asymmetric Fano shapes, see figure 3.2(c). In the classical explanation, the 'continuum' corresponds to the smooth Fabry-Pérot resonances, and the 'discrete state' is due to the quasi-trapped mode.

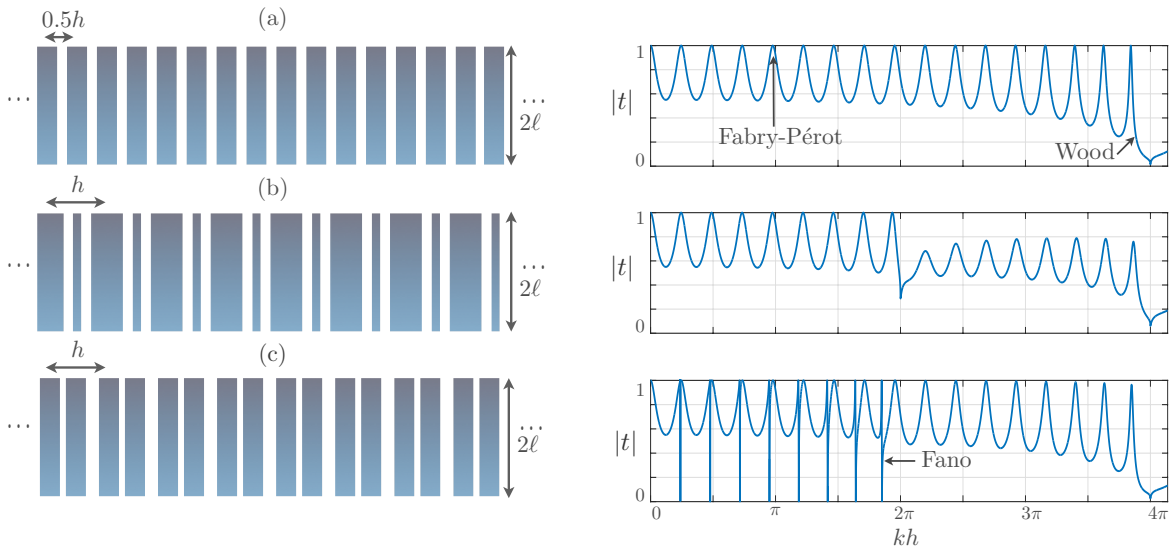


Figure 3.2: (a) A periodic grating with slits of width $0.15h$ and length 2ℓ . (b) The same grating with two identical slits brought closer together, introducing a local periodicity resulting in a lower threshold. (c) The same grating after symmetry breaking with two slits in the unit cell of widths $0.1h$ and $0.2h$. The symmetry breaking produces the appearance of Fano resonances with sharp variations of the scattering coefficients. Right-panels show the transmission coefficient for $2\ell = 4h$ at normal incidence.

The scattering by dual-period or compound gratings has been analyzed in a series of papers in two-dimensions for p -polarized electromagnetic waves [141, 57, 92, 140, 115, 82] and for their acoustic counterparts [157, 150]. In electromagnetism, the case of s -polarized wave for which the Neumann condition is replaced by a Dirichlet condition has been considered in [34]. Also, breaking the symmetry by using different dielectric materials in neighbouring slits has been sought [142, 103, 155, 94, 52]. From a theoretical point of view, models have been proposed using approximate modal method [140, 94] and using equivalent circuit models for normal wave incidences [103]. Recently, a rigorous mathematical theory has been conducted for narrow slit gratings [82, 84]. We also mention theoretical works on Fano-resonances occurring in high-contrasted regular gratings [145] and for dual-period gratings of resonant bubbly inclusions [6]. In the context of applications and metascreens, we refer to [69, 75] for a high contrast dual-period setting. Recently, efforts to extend the study to the full three dimensional Maxwell's equation has been done in [9].

As shown in chapter 2, the homogenization theory is a good approach to handle subwavelength gratings. Indeed, the Fabry-Pérot resonances are recovered within classical asymptotic homogenization for regular gratings [118, 105, 83, 129], and a better estimate is obtained at higher order when size effects have been taken into account [96].

To the opposite the occurrence of Fano resonances in dual-period gratings is surprising as the gratings (a), (b) and (c) in the figure 3.2 have the same filling fraction of air hence they should behave the same. In this study we show that conducting the homogenization beyond the classical dominant order allows us to capture the coupling between the Fabry-Perot and the quasi-trapped mode resonances, leading to the emergence of a Fano resonance. Indeed, while waves in the slits propagate independently, they are coupled at the grating interfaces through the evanescent field; the coupling is in general weak except when the evanescent field resonates, which is rendered possible by the branch folding of guided modes being the acoustic counterpart of Spoof Plasmon Polaritons. This coupling is recovered by the asymptotic analysis, which provides non trivial effective transmission conditions encapsulating the effect of the evanescent field.

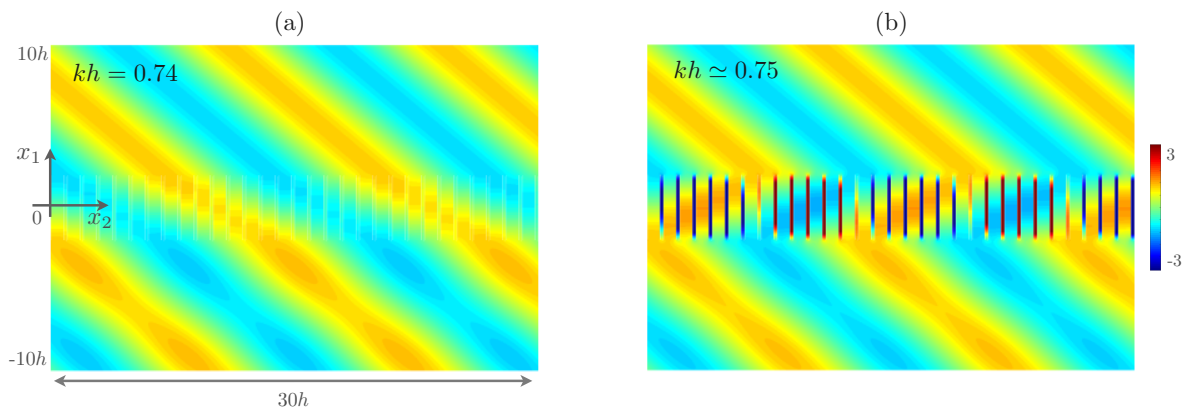


Figure 3.3: Scattering by an ultra-sparse grating – In general the scattering is weak, panel (a). Near the Fano resonance, the pattern mimics a negative refraction system (panel (b) similar to that reported in [129] for a regular grating of inclined plates). The rigid slab is patterned with large slits of length $2\ell = 4h$ (widths $0.20h$ and $0.76h$) living rigid parts $0.02h$ thick (the incidence is 40°).

The rest of the chapter is organized as follows. In section 3.2, we present the problem setting of the actual problem, give some theoretical background of trapped modes and illustrate their existence through numerical simulation. Next, in section 3.3 we summarize the main results of the analysis specifically the effective problem involving a homogenized version of the pressure fields (\hat{p}, \check{p}) within each slit in the unit cell (3.7) complemented by effective transmission conditions (3.8)-(3.9) applying at the slab interfaces. We do not make assumption on the slit widths and our result holds for slits separated by ultra-thin rigid parts, which give rise to unexpected scattering as illustrated in figure 3.3. The technical derivation of the model is detailed in section 3.4; it is done for two slits of arbitrary widths and inter-distance but with the same length 2ℓ . Properties of the obtained effective parameters is given in section 3.5. We provide an extension of this to the case of rigid part of different length in an additional part. We solve the effective problem for a scattering problem in section 3.6, which is then validated in section 3.7. In particular, we conduct a local analysis, which highlights the links between the Fano complex poles, the zero-transmission and the trapped mode for the case of slits of different width.

3.2 Problem formulation and results

3.2.1 The actual problem

The dual-periodic grating has spacing h and thickness 2ℓ . It contains two rigid parts and two slits with the sequence of thicknesses $(\hat{\eta}, \hat{\varphi}, \tilde{\eta}, \tilde{\varphi})h$ ($0 \leq \hat{\varphi}, \tilde{\varphi} \leq 1$, $0 \leq \hat{\eta}, \tilde{\eta} \leq 1$ and $\hat{\eta} + \tilde{\eta} + \hat{\varphi} + \tilde{\varphi} = 1$), see figure 3.4. In the harmonic regime with $e^{-i\omega t}$ time dependence, the wavenumber is $k = \omega/c$ with c the speed of sound in the fluid. The acoustic pressure p^r satisfies the Helmholtz equation with Neumann boundary conditions on the rigid part boundaries, namely

$$\begin{cases} \Delta p^r + k^2 p^r = 0, \\ \nabla p^r \cdot \mathbf{n} = 0 \quad \text{on the boundaries with rigid parts.} \end{cases} \quad (3.2)$$

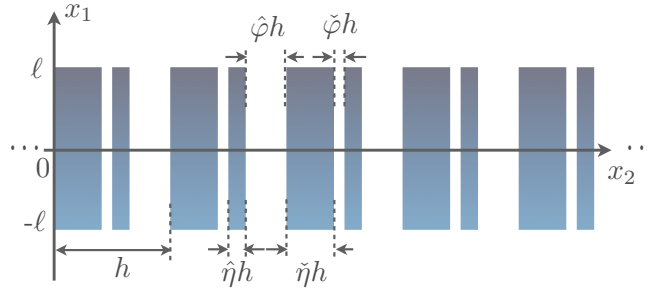


Figure 3.4: The actual problem set on the pressure p^r satisfying (3.2). The dual-period grating is of period h and extend 2ℓ and contains two rigid parts and two slits with the sequence of thicknesses $(\hat{\eta}, \hat{\varphi}, \tilde{\eta}, \tilde{\varphi})h$.

3.2.2 Trapped modes

As mentioned in chapter 2, trapped modes, or guided modes, are modes that are solution to the homogeneous Helmholtz problem (3.2). In case of a regular grating with rigid parts, guided modes exist below the light/sound line. Trapped modes can nonetheless exist in the continuum of propagating states above the light line under certain symmetry conditions. From an operator point of view, such modes are associated with real eigenvalues embedded in the continuous spectrum. Such modes are referred to as *Bound States in the Continuum* in the context of quantum mechanics, see [59] for a recent review. It was first studied in the works [149], where the authors theoretically constructed a potential well that extends to infinity with a tailored in a specific way to support the bound states in the continuum. It has since then been several studies of other setting where such modes are observed. In the case of acoustics and waterwaves, trapped modes have been of large interest in the study of closed waveguides, where we mention the works of [148, 23, 44, 36, 87, 26, 46, 120]. To construct such modes, the following configuration is often studied, see [46]: consider a two dimensional closed waveguide propagating along the x_1 -axis of unity width, along with Neumann boundary conditions on its lateral boundary $x_2 = \pm 1/2$. A sound hard obstacle, symmetric with respect to x_2 , is placed along the centre line of the guide. The continuum of propagating states consist of all real frequencies, as no lower cut on frequency exist. By

separating the problem into symmetric and antisymmetric parts, we obtain two decoupled problems. The even transverse modes are associated to the symmetric problem, and the odd transverse modes to the antisymmetric problem. The symmetry preserves the lower cut-on frequency for the even modes, whereas the cut on only appears at π for the odd modes. This implies that evanescent waves can exist below this threshold, leaving room for a trapped mode to exist. Through a variational formulation, simple test functions can prove the existence of such modes in the continuum of propagating modes. Extending these ideas to gratings, the existence of trapped modes above the light/sound line were proven in [18] under the symmetry condition, see also [139] and references there in. These modes are known to be non robust, meaning that any perturbation that breaks the symmetry results a trapped modes becoming a quasi-trapped modes with a small imaginary part. These antisymmetric quasi-trapped modes can interact with the propagating states. In the case of non penetrable obstacles, a dual period is needed to observe any trapped mode.

Before proceeding to the homogenization scheme, it is useful to have some insight into the physical properties of such a grating. To do so, we start by showing some numerical results.

3.2.3 Numerical evidence of the perfect trapped-mode through guided-wave excitation

The numerical solution is obtained following a multimodal method similar to the Rigorous Coupled-Wave Analysis developed in electromagnetism [109] or the Eigenfunction Matching Method developed for water waves [85]. To start off, we consider the configuration consisting of rigid parts with same width $\hat{\eta} = \check{\eta}$ while the two slits may have different widths $\check{\varphi} \neq \hat{\varphi}$. We consider an incident wave of the form

$$p^{\text{inc}}(\mathbf{x}) = e^{ik_m(x_1+\ell)+ib_mx_2}, \quad m \in \mathbb{Z}, \quad (3.3)$$

with $k_n : n \mapsto \sqrt{k^2 - b_n^2}$ (with $b_n = b_0 + 2n\pi/h$ for a given b_0) and the solution of the resulting scattering problem is expanded as follows

$$p(\mathbf{x}) = \begin{cases} p^{\text{inc}}(\mathbf{x}) + \sum_{n=-\infty}^{\infty} r_{mn} e^{-ik_n(x_1+\ell)} \psi_n(x_2), & x_1 \in (-\infty, -\ell), \\ \sum_{n=-\infty}^{\infty} t_{mn} e^{ik_n(x_1-\ell)} \psi_n(x_2), & x_1 \in (\ell, +\infty), \end{cases} \quad (3.4)$$

with $\psi_n(x_2) = e^{ib_n x_2}$ forming a basis of the pseudo-periodic functions for $x_2 \in X = (0, h)$. Next, for $x_1 \in (-\ell, \ell)$ and $x_2 \in \hat{X} = (\hat{x}, \hat{x} + \hat{\varphi}h)$ or $x_2 \in \check{X} = (\check{x}, \check{x} + \check{\varphi}h)$, we write the fields in each slit as

$$\begin{aligned} \hat{p}(x_1, x_2 \in \hat{X}) &= \sum_{n=0}^{\infty} \left(\hat{\mathcal{S}}_{mn} \cos \hat{k}_n x_1 + \hat{\mathcal{A}}_{mn} \sin \hat{k}_n x_1 \right) \hat{\psi}_n(x_2), \\ \check{p}(x_1, x_2 \in \check{X}) &= \sum_{n=0}^{\infty} \left(\check{\mathcal{S}}_{mn} \cos \check{k}_n x_1 + \check{\mathcal{A}}_{mn} \sin \check{k}_n x_1 \right) \check{\psi}_n(x_2), \end{aligned} \quad (3.5)$$

with $\hat{k}_n = \sqrt{k^2 - \hat{a}_n}$, $\hat{a}_n = n\pi/(\hat{\varphi}h)$, and $\hat{\psi}_n(x_2) = \cos(\hat{a}_n(x_2 - \hat{x}))$ forming a basis of functions with Neumann conditions at $x_2 = \hat{x}$ and at $x_2 = \hat{x} + \hat{\varphi}h$ (the same for $\check{\cdot}$). The

solutions in (3.4) and (3.5) are then matched at $x_1 = \pm\ell$ where we apply the continuity of the pressure and of the velocity by imposing, for $i = 0, \dots$,

$$\begin{aligned} (p|_{\pm\ell}, \hat{\psi}_i)_{\hat{X}} &= (\hat{p}|_{\pm\ell}, \hat{\psi}_i)_{\hat{X}}, & (p|_{\pm\ell}, \check{\psi}_i)_{\check{X}} &= (\check{p}|_{\pm\ell}, \check{\psi}_i)_{\check{X}} \\ (\partial_{x_1} p|_{\pm\ell}, \psi_i^*)_{X} &= (\partial_{x_1} \hat{p}|_{\pm\ell}, \psi_i^*)_{\hat{X}} + (\partial_{x_1} \check{p}|_{\pm\ell}, \psi_i^*)_{\check{X}}, \end{aligned} \quad (3.6)$$

where ψ_i^* denotes the complex conjugate of ψ_i and where, for $Y = X, \hat{X}, \check{X}$, $(a, b)_Y = \int_Y a(x_2)b(x_2)dx_2$. In the last relation, we have accounted for the Neumann boundary condition $\partial_{x_1} p|_{\pm\ell} = 0$ for $x_2 \in X \setminus (\hat{X} \cup \check{X})$. In practice the series are truncated to M terms \hat{p} and \check{p} and to N terms for p . Thus, the problem (3.6) is reduced to the determination of $(4M + 2N)$ unknowns $(\hat{S}_{mn}, \hat{A}_{mn}, \check{S}_{mn}, \check{A}_{mn}, r_{mn}, t_{mn})$, which are obtained from the $2 \times (2M + N)$ equations in (3.6) by simple matrix inversion, the source being composed of the projections of $p|_{\pm\ell}^{\text{inc}}$ on $(\hat{\psi}_i, \check{\psi}_i)$ and of $\partial_{x_1} p|_{\pm\ell}^{\text{inc}}$ on ψ_i^* .

The numerics allows the two resonances of regular gratings to be evidenced although one is a perfect resonance prevented by symmetry. The Fabry-Pérot resonance is excitable through scattering that is for an incident propagating mode. By sending the mode 0, it is observed at perfect-transmissions $|t_{00}| = 1$ when $2k\ell \simeq n\pi$ with n integer. The second resonance is that of a trapped mode associated with the excitation of guided waves whose dispersion branches lie below the light-line (these guided waves are the acoustic analogs of spoof plasmon polaritons). By sending the evanescent mode 1 which breaks the symmetry of

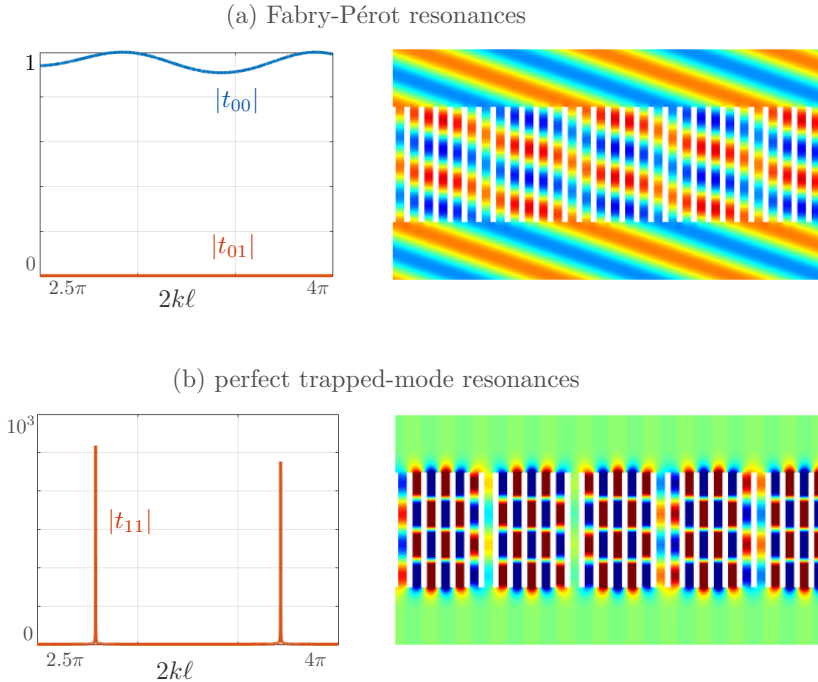


Figure 3.5: FP resonance and perfect trapped-mode resonance in regular gratings – (a) FP resonances with perfect transmissions $|t_{00}| = 1$, the right panel shows the pressure field near $2k\ell = 4\pi$. (b) Perfect trapped-mode resonances due to guided wave excitation producing arbitrarily large $|t_{11}|$ in the numerics, the left panel shows pressure field near $2k\ell = 4\pi$ ($\hat{\varphi} = \check{\varphi} = 0.3, 2\ell = 4h$).

the array, the guided waves can be excited which is visible by means of arbitrarily large values of $|t_{11}|$. This allows the formation of the perfect trapped-mode with nearby slits oscillating out-of-phase. The variations of $|t_{00}|$ and $|t_{11}|$ for $2k\ell \in (2.5, 4)\pi$ are reported in figure 3.5 along with the fields at resonances.

To further illustrate the double periodicity of the grating, we report the full $(b_0h, 2k\ell)$ -plane in figure 3.7. For both a regular and a dual period array, we $\log_{10}|r_{00}|$ and $\log_{10}|r_{01}|$. In the radiative region $2k\ell > b_0h$, we observe Fabry-Pérot resonances for the regular array with $r_{00} = 0$ visible for $2k\ell \simeq n\pi$, with n an integer. For $2k\ell < b_0h$, the branches of the guided modes being the SPPs are visible by means of diverging $|r_{00}|$, and are clearly characterised by their horizontal asymptotes at the edge of the Brillouin zone. The range $b_0h \in (0, \pi)$ corresponds to half the Brillouin zone of the actual periodicity $h/2$ of a regular grating. As the Brillouin zone is reduced by half, the branch of the SSPs is folded upon itself and brought into the radiative region, hence becoming excitable through scattering. This corresponds to the interaction of the quasi-trapped mode and the propagating states.

Indeed, this branch folding can be seen by examining the variations of $|r_{01}|$. For the dual-period array, this evanescent mode can be excited. Below the light/sound line, the SPP branch is still visible as it corresponds to the divergence of the evanescent field. Note that it corresponds to the whole evanescent field and not only the first evanescent mode. Above the light/sound line, the folded branch that corresponds to the quasi-trapped modes can be seen by the large, although finite amplitudes of the evanescent field. For the regular array, the pseudo-periodicity conditions applies at the actual periodicity $h/2$, hence $r_{0n} = t_{0n} = 0$ for all odd n . These somewhat artificial perfect trapped modes can be visualized by the emergence of noise in the numerical computation. A related study exploiting the noised spectrum to reveal trapped modes has been presented in [119]. This allows us to observe the perfect branch folding occurring at the edge of the first Brillouin zone $b_0h = \pi$. As the symmetry is broken, a band gap opens up.

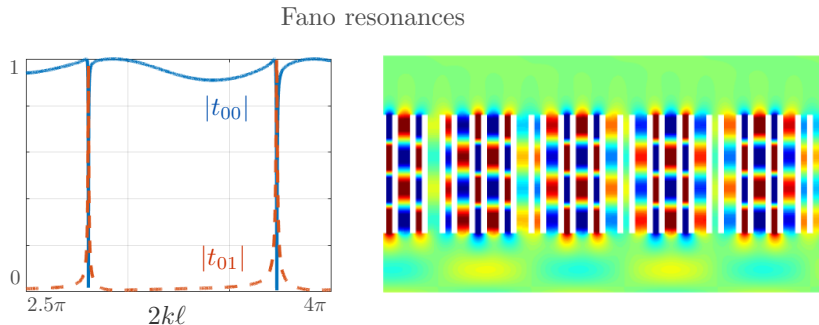


Figure 3.6: Fano resonances in dual-period gratings – Variations of $|t_{00}| \in (0, 1)$ (plain blue line) and $|t_{01}|$ normalized to its maximum value (dashed red line) and field patterns at the zero-transmissions near $2k\ell = 4\pi$ ($\hat{\varphi} = 0.4, \check{\varphi} = 0.2, 2\ell = 4h$).

3.3 The effective problem

In the subwavelength regime, $\varepsilon = kh \ll 1$ is a small parameter that can be used to conduct asymptotic analysis within each slit far from the grating interfaces at $x_1 = \pm\ell$ (analysis in the bulk) and in their close vicinity (analysis at a grating interface). In the resulting homogenized

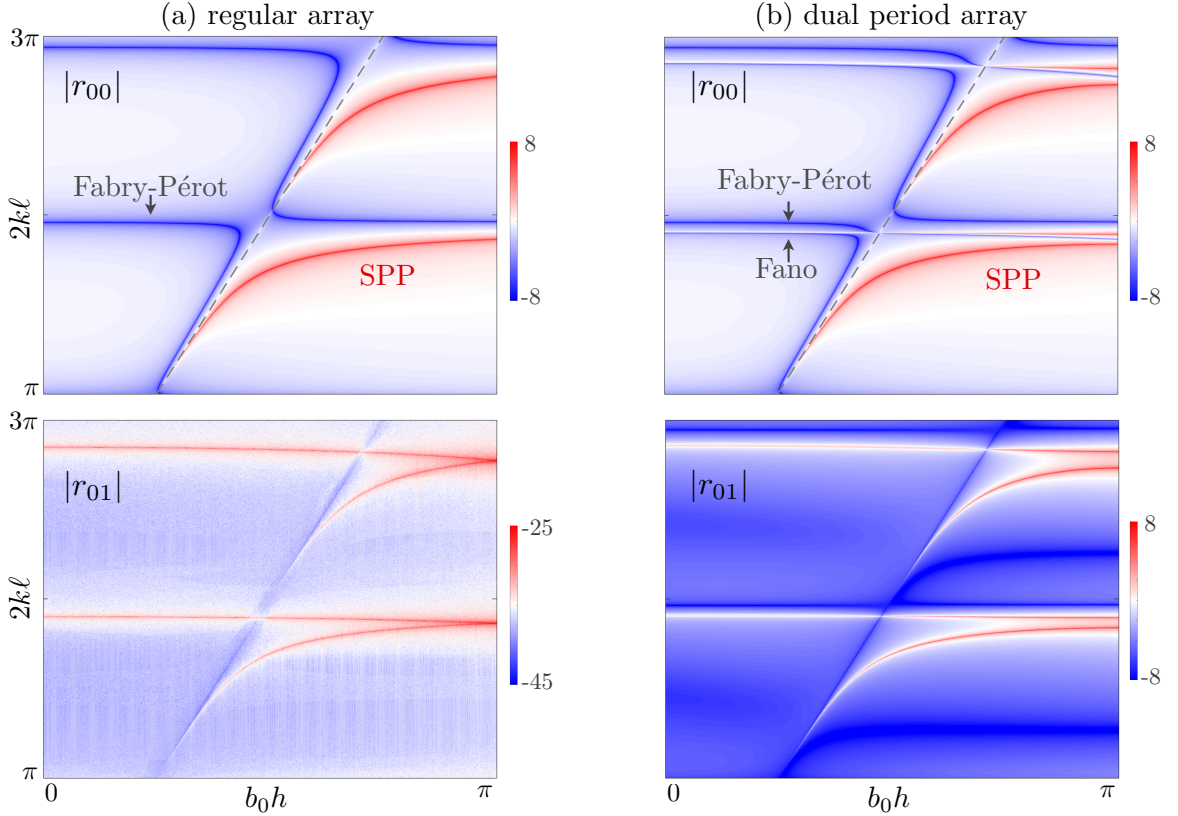


Figure 3.7: Overall behaviors of the regular and dual-period gratings by means of the reflection coefficients $|r_0|$ and $|r_1|$ (in \log_{10} scale) against b_0h and $2k\ell$, (a) for the regular grating, and (b) for the dual-period grating.

model, we obtain two distinct pressure fields, \hat{p} being associated to the actual pressure field in the slit of thickness $\hat{\eta}h$ and \check{p} being associated to the slit of thickness $\check{\eta}h$. It is worth noticing that these two solutions coexist in the whole domain $x_1 \in (-\ell, \ell)$ as sketched in figure 3.8. Specifically we have

$$\begin{aligned}
 &\text{for } x_1 \notin (-\ell, \ell), & \Delta p + k^2 p &= 0, \\
 &\text{for } x_1 \in (-\ell, \ell), & \frac{\partial^2 \hat{p}}{\partial x_1^2} + k^2 \hat{p} &= 0, & \text{and} & \frac{\partial^2 \check{p}}{\partial x_1^2} + k^2 \check{p} &= 0,
 \end{aligned} \tag{3.7}$$

and as it should be, each wave equation is one-dimensional within the slits as the propagation is allowed along x_1 only.

In the effective problem, the region of the grating is defined by $x_1 \in (-\ell, \ell)$ where the propagation involves the two fields \hat{p} and \check{p} . Outside this region, $x_1 \notin (-\ell, \ell)$, the propagation involves a single field p . At the boundaries $x_1 = \pm\ell$, the analysis provides effective jump, or

transmission conditions, which complement (3.7). They read, at $x_1 = -\ell$,

$$\left\{ \begin{array}{l} \hat{p}|_{-\ell^+} - p|_{-\ell^-} = h\hat{\varphi}\hat{B}_1 \frac{\partial \hat{p}}{\partial x_1} \Big|_{-\ell^+} + h\check{\varphi}b \frac{\partial \check{p}}{\partial x_1} \Big|_{-\ell^+} + h\hat{B}_2 \frac{\partial p}{\partial x_2} \Big|_{-\ell^-}, \\ \check{p}|_{-\ell^+} - p|_{-\ell^-} = h\hat{\varphi}b \frac{\partial \hat{p}}{\partial x_1} \Big|_{-\ell^+} + h\check{\varphi}\check{B}_1 \frac{\partial \check{p}}{\partial x_1} \Big|_{-\ell^+} + h\check{B}_2 \frac{\partial p}{\partial x_2} \Big|_{-\ell^-}, \\ \hat{\varphi} \frac{\partial \hat{p}}{\partial x_1} \Big|_{-\ell^+} + \check{\varphi} \frac{\partial \check{p}}{\partial x_1} \Big|_{-\ell^+} - \frac{\partial p}{\partial x_1} \Big|_{-\ell^-} = h\hat{\varphi}\hat{B}_2 \frac{\partial^2 \hat{p}}{\partial x_1 \partial x_2} \Big|_{-\ell^+} + h\check{\varphi}\check{B}_2 \frac{\partial^2 \check{p}}{\partial x_1 \partial x_2} \Big|_{-\ell^+} - hC \frac{\partial^2 p}{\partial x_2^2} \Big|_{-\ell^-}, \end{array} \right. \quad (3.8)$$

and similarly at $x_1 = \ell$,

$$\left\{ \begin{array}{l} p|_{\ell^+} - \hat{p}|_{\ell^-} = h\hat{\varphi}\hat{B}_1 \frac{\partial \hat{p}}{\partial x_1} \Big|_{\ell^-} + h\check{\varphi}b \frac{\partial \check{p}}{\partial x_1} \Big|_{\ell^-} + h\hat{B}_2 \frac{\partial p}{\partial x_2} \Big|_{\ell^+}, \\ p|_{\ell^+} - \check{p}|_{\ell^-} = h\hat{\varphi}b \frac{\partial \hat{p}}{\partial x_1} \Big|_{\ell^-} + h\check{\varphi}\check{B}_1 \frac{\partial \check{p}}{\partial x_1} \Big|_{\ell^-} + h\check{B}_2 \frac{\partial p}{\partial x_2} \Big|_{\ell^+}, \\ \frac{\partial p}{\partial x_1} \Big|_{\ell^+} - \hat{\varphi} \frac{\partial \hat{p}}{\partial x_1} \Big|_{\ell^-} - \check{\varphi} \frac{\partial \check{p}}{\partial x_1} \Big|_{\ell^-} = h\hat{\varphi}\hat{B}_2 \frac{\partial^2 \hat{p}}{\partial x_1 \partial x_2} \Big|_{\ell^-} + h\check{\varphi}\check{B}_2 \frac{\partial^2 \check{p}}{\partial x_1 \partial x_2} \Big|_{\ell^-} - hC \frac{\partial^2 p}{\partial x_2^2} \Big|_{\ell^+}, \end{array} \right. \quad (3.9)$$

In (3.8)-(3.9), the six parameters $(\hat{B}_1, \check{B}_1, \hat{B}_2, \check{B}_2, b, C)$ are *effective* parameters obtained from the solving of elementary static problems, which only depend on $(\check{\eta}, \hat{\eta}, \check{\varphi}, \hat{\varphi})$. It is worth noticing that even for a grating of slits with same width ($\hat{\varphi} = \check{\varphi}$), the two solutions \hat{p} and \check{p} in $x_1 \in (-\ell, \ell)$ differ as their role is not symmetric in the jump conditions. The above transmission conditions further simplify in the case where the slits or the rigid parts of the grating have the same width, specifically we have

$$\begin{array}{ll} \text{for slits with the same widths,} & \hat{\varphi} = \check{\varphi}, \quad \hat{B}_2 = -\check{B}_2, \\ \text{for rigid parts with the same widths,} & \hat{\eta} = \check{\eta}, \quad \hat{B}_2 = \check{B}_2 = 0. \end{array} \quad (3.10)$$

Finally for a regular grating (the slits and the rigid parts have the same width), we have

$$\hat{\varphi} = \check{\varphi}, \quad \hat{\eta} = \check{\eta}, \quad \hat{B}_1 + b = \check{B}_1 + b = -\frac{1}{\pi} \log \sin \pi \hat{\varphi}, \quad \hat{B}_2 = \check{B}_2 = 0, \quad (3.11)$$

which enforce the limiting case $\hat{p} = \check{p}$. These properties are shown in the section 3.5.

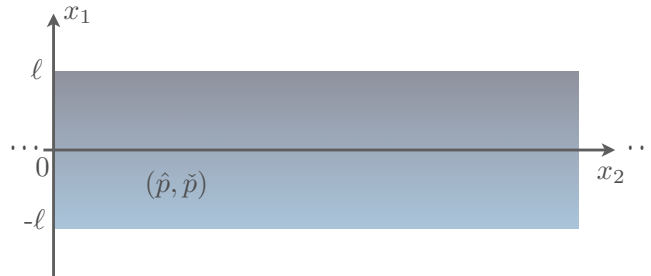


Figure 3.8: The effective problem is set on p for $x_1 \notin (-\ell, \ell)$ and on (\check{p}, \hat{p}) which coexist for $x_1 \in (-\ell, \ell)$, with (p, \check{p}, \hat{p}) satisfying (3.7) with jump conditions (3.8)-(3.8) at $x_1 = \pm\ell$.

3.4 Asymptotic homogenization

In this section we present the two-scale asymptotic analysis to derive the set of equations (3.7) and (3.8)-(3.9). This is done thanks to a field p^ε approximating p^r in the limit $\varepsilon = kh \rightarrow 0$. For the ease of the calculations, we introduce the field $\mathbf{u}^\varepsilon = \nabla p^\varepsilon$ which is proportional to the acoustic velocity and, without loss of generality, we keep dimensional space variable \mathbf{x} and set $k = 1$. Doing so, we get that $(p^\varepsilon, \mathbf{u}^\varepsilon)$ satisfy

$$\begin{aligned} \operatorname{div} \mathbf{u}^\varepsilon + p^\varepsilon &= 0, & \mathbf{u}^\varepsilon &= \nabla p^\varepsilon, \\ \mathbf{u}^\varepsilon \cdot \mathbf{n} &= 0 & \text{on the boundaries with rigid parts.} \end{aligned} \quad (3.12)$$

Note that the grating has now a period $\varepsilon = kh \ll 1$ and an extension $kl = O(1)$. In the homogenization process two different regions have to be considered. The first one corresponds to the region within a single slit far from the grating interfaces at $x_1 = \pm\ell$. Here classical homogenization techniques are used. The second one corresponds to a region near a grating interface at $x_1 = -\ell$ or $x_1 = \ell$. Here matched asymptotic expansions together with homogenization techniques will be used to derive effective jump conditions.

3.4.1 Analysis in the bulk – Effective wave equations

The analysis in the bulk is identical to that conducted in [96] for a regular grating. The calculations are recalled below for the sake of completeness and because we shall need them when the analysis near the grating interfaces will be considered.

Preliminaries

The effective model is obtained for averaged fields defined in the elementary unit cell depicted in figure 3.9 and the averaging process is achieved over the fast variable $y_2 = x_2/\varepsilon$, which accounts for the subscale laminar structuration. As the two slits are disconnected, the solution follows two different expansions, which at this stage are independent. The two expansions hold in the domains \hat{Y} of width $\hat{\varphi}$ and \check{Y} of width $\check{\varphi}$

$$\hat{Y} = \{y_2 \in (\hat{\eta}, \hat{\eta} + \hat{\varphi})\}, \quad \check{Y} = \{y_2 \in (1 - \check{\varphi}, 1)\}.$$

Accordingly, the expansions read

$$\begin{aligned} p^\varepsilon &= \hat{p}^0(\mathbf{x}, y_2) + \varepsilon \hat{p}^1(\mathbf{x}, y_2) + \dots, & \mathbf{u}^\varepsilon &= \hat{\mathbf{u}}^0(\mathbf{x}, y_2) + \varepsilon \hat{\mathbf{u}}^1(\mathbf{x}, y_2) + \dots, & \text{in } \hat{Y}, \\ p^\varepsilon &= \check{p}^0(\mathbf{x}, y_2) + \varepsilon \check{p}^1(\mathbf{x}, y_2) + \dots, & \mathbf{u}^\varepsilon &= \check{\mathbf{u}}^0(\mathbf{x}, y_2) + \varepsilon \check{\mathbf{u}}^1(\mathbf{x}, y_2) + \dots, & \text{in } \check{Y}. \end{aligned} \quad (3.13)$$

Following [96] we define the macroscopic pressure and velocity fields in the two slits as

$$\langle \hat{p}^n \rangle(\mathbf{x}) = \frac{1}{\hat{\varphi}} \int_{\hat{Y}} \hat{p}^n(\mathbf{x}, y_2) \, dy_2, \quad \langle \hat{\mathbf{u}}^n \rangle(\mathbf{x}) = \int_{\hat{Y}} \hat{\mathbf{u}}^n(\mathbf{x}, y_2) \, dy_2, \quad (3.14)$$

(the same for $\langle \check{p}^n \rangle$ and $\langle \check{\mathbf{u}}^n \rangle$). It is worth noticing that we anticipate the conservation of the flowrates at the dominant order by defining $\langle \check{u}_1, \hat{u}_1 \rangle$ as the flowrates rather than as the mean velocities. Eventually, due to the multiple scale variables in the field expansions (3.13), the divergence operator applied to any vectorial function $\mathbf{f}(\mathbf{x}, y_2)$ and the gradient operator applied to any scalar function $f(\mathbf{x}, y_2)$ become

$$\operatorname{div} \mathbf{f} = \operatorname{div}_{\mathbf{x}} \mathbf{f} + \frac{1}{\varepsilon} \frac{\partial \mathbf{f}}{\partial y_2} \cdot \mathbf{e}_2, \quad \nabla f = \nabla_{\mathbf{x}} f + \frac{1}{\varepsilon} \frac{\partial f}{\partial y_2} \mathbf{e}_2. \quad (3.15)$$

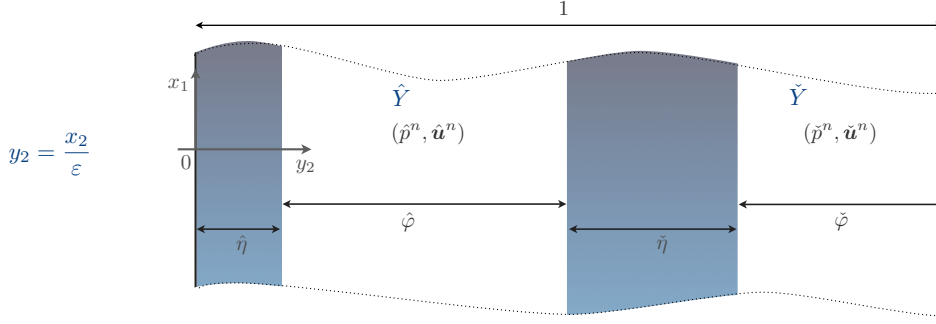


Figure 3.9: Elementary unit strip in which the analysis in the bulk is conducted. The analysis involves the terms (\hat{p}^n, \hat{u}^n) in \hat{Y} and $(\check{p}^n, \check{u}^n)$ in \check{Y} in the expansions (3.13).

In the following, we conduct the analysis in \hat{Y} for the terms (\hat{p}^n, \hat{u}^n) . The results hold in \check{Y} using $\hat{\varphi} \rightarrow \check{\varphi}$ and $(\hat{p}^n, \hat{u}^n) \rightarrow (\check{p}^n, \check{u}^n)$.

The zero order solution in \hat{Y}

Injecting the expansions (3.13) in the dimensionless Euler equations (3.12) and using (3.15), we get at the dominant order (in $O(\varepsilon^{-1})$) that $\partial_{y_2} \hat{p}^0 = 0$. Hence \hat{p}^0 do not depend on y_2 . We also have $\partial_{y_2} \hat{u}_2^0 = 0$ and accounting for the boundary condition $\hat{u}_2^0|_{y_2=\hat{\eta}} = 0$ we deduce that \hat{u}_2 is zero everywhere. Hence we have

$$\hat{p}^0(\mathbf{x}) = \langle \hat{p}^0 \rangle(\mathbf{x}), \quad \hat{u}_2^0 = 0. \quad (3.16)$$

At the order $O(1)$, we retain the two following equations

$$\hat{u}_1^0(\mathbf{x}) = \frac{\partial \hat{p}^0}{\partial x_1}(\mathbf{x}), \quad \hat{p}^0(\mathbf{x}) + \operatorname{div}_{\mathbf{x}} \hat{u}^0(\mathbf{x}) + \frac{\partial \hat{u}_2^1}{\partial y_2}(\mathbf{x}, y_2) = 0, \quad (3.17)$$

that we integrate over \hat{Y} according to the definitions (3.14). It results

$$\langle \hat{u}^0 \rangle(\mathbf{x}) = \hat{\varphi} \frac{\partial \langle \hat{p}^0 \rangle}{\partial x_1}(\mathbf{x}) \mathbf{e}_1, \quad \operatorname{div}_{\mathbf{x}} \langle \hat{u}^0 \rangle(\mathbf{x}) + \hat{\varphi} \langle \hat{p}^0 \rangle(\mathbf{x}) = 0, \quad (3.18)$$

which describes expected one-dimensional propagation.

The first order solution in \hat{Y}

From (3.17), we obtain that $\partial_{y_2} \hat{u}_2^1$ is independent of y_2 , hence \hat{u}_2^1 is linear with respect to y_2 . However, as the boundary conditions on the rigid parts impose $\hat{u}_2^1 = 0$ at $y_2 = \hat{\eta}, \hat{\eta} + \hat{\varphi}$, we must have $\hat{u}_2^1 = 0$ everywhere. At the order $O(1)$, we have written the form of \hat{u}_1^0 in (3.17) and we now consider the second component $\hat{u}_2^0 = 0$ (from (3.16)), which reads $\hat{u}_2^0 = \partial_{y_2} \hat{p}^1(\mathbf{x}, y_2) + \partial_{x_2} \hat{p}^0(\mathbf{x}) = 0$. By integration, we obtain the form of \hat{p}^1 , and we have

$$\hat{u}_2^1 = 0, \quad \hat{p}^1(\mathbf{x}, y_2) = (\hat{y}_c - y_2) \frac{\partial \langle \hat{p}^0 \rangle}{\partial x_2}(\mathbf{x}) + \langle \hat{p}^1 \rangle(\mathbf{x}), \quad (3.19)$$

where $\hat{y}_c = \hat{\eta} + \hat{\varphi}/2$ is the center the channel (hence $\langle \hat{y}_c - y_2 \rangle = 0$). We now write the equivalent of (3.17) at the order $O(\varepsilon)$, which reads

$$\hat{u}_1^1(\mathbf{x}, y_2) = \frac{\partial \hat{p}^1}{\partial x_1}(\mathbf{x}, y_2), \quad \hat{p}^1(\mathbf{x}, y_2) + \operatorname{div}_{\mathbf{x}} \hat{\mathbf{u}}^1(\mathbf{x}, y_2) + \frac{\partial \hat{u}_2^2}{\partial y_2} = 0. \quad (3.20)$$

By integrating both equations over \hat{Y} and accounting for (3.19), we obtain the first order wave equation

$$\langle \hat{\mathbf{u}}^1 \rangle(\mathbf{x}) = \hat{\varphi} \frac{\partial \langle \hat{p}^1 \rangle}{\partial x_1}(\mathbf{x}) \mathbf{e}_1, \quad \operatorname{div}_{\mathbf{x}} \langle \hat{\mathbf{u}}^1 \rangle(\mathbf{x}) + \hat{\varphi} \langle \hat{p}^1 \rangle(\mathbf{x}) = 0, \quad (3.21)$$

which reads the same as at the dominant order. As previously said, the analysis holds in \tilde{Y} and we shall now see how the two solutions are linked through the analysis at the grating interfaces.

Solutions in the fluid far from the grating

We have established the effective wave equations satisfied by the first two terms of the expansions in the region of the plates (far from the interfaces). As the surrounding fluid is already a homogeneous medium, such expansions are strictly not required. However, when effective transmission conditions will be sought, we shall need the equivalent of the expansions (3.13). Hence, in the fluid for $|x_1| > \ell$, expansions are written in the form

$$p^\varepsilon = p^0(\mathbf{x}) + \varepsilon p^1(\mathbf{x}) + \dots, \quad \mathbf{u}^\varepsilon = \mathbf{u}^0(\mathbf{x}) + \varepsilon \mathbf{u}^1(\mathbf{x}) + \dots, \quad (3.22)$$

and at each order we simply have

$$\operatorname{div}_{\mathbf{x}} \mathbf{u}^i + p^i = 0, \quad \mathbf{u}^i = \nabla_{\mathbf{x}} p^i, \quad i = 0, 1, \dots. \quad (3.23)$$

3.4.2 Analysis at an grating interface and effective transmission conditions

Preliminaries

We now investigate the effective transmission conditions that apply at the interfaces between the fluid and the slab. This is done by zooming in the vicinity of one boundary at $x_1 = \pm\ell$. We consider the boundary $x_1 = -\ell$ and for simplicity we use a translation of the origin $x_1 = -\ell \rightarrow x_1 = 0$ (the result will hold for the other boundary at $x_1 = \ell$).

In the slab far from the boundary, the two-scale expansions (3.13) holds and the dependence on y_2 of the two first terms of the expansions have been determined (3.16), (3.17), (3.19) and (3.20). In the region of the fluid far from the boundary, the expansions (3.22) hold and the two first terms of the expansions satisfied (3.23). The objective is to match the two expansions by performing a dedicated analysis of the boundary layer at $x_1 = 0$. We thus analyze the solution of the linearized Euler equations in an intermediate region corresponding to a rescaled zoom around $x_1 = 0$. The rescaling is done by means of the change of variable $\mathbf{y} = \mathbf{x}/\varepsilon$ to which we associate an elementary unit strip $\mathcal{Y} = \mathcal{Y}^- \cup \hat{\mathcal{Y}} \cup \check{\mathcal{Y}}$ where \mathcal{Y}^- , $\hat{\mathcal{Y}}$ and $\check{\mathcal{Y}}$ correspond to the regions of the fluid and the two slits, see figure 3.10. Specifically, they are defined by

$$\begin{aligned} \mathcal{Y}^- &= \{\mathbf{y} \in \mathbb{R}^2 \mid y_1 < 0, y_2 \in (0, 1)\}, & \hat{\mathcal{Y}} &= \{\mathbf{y} \in \mathbb{R}^2 \mid y_1 > 0, y_2 \in \hat{Y}\}, \\ & & \check{\mathcal{Y}} &= \{\mathbf{y} \in \mathbb{R}^2 \mid y_1 > 0, y_2 \in \check{Y}\}. \end{aligned}$$

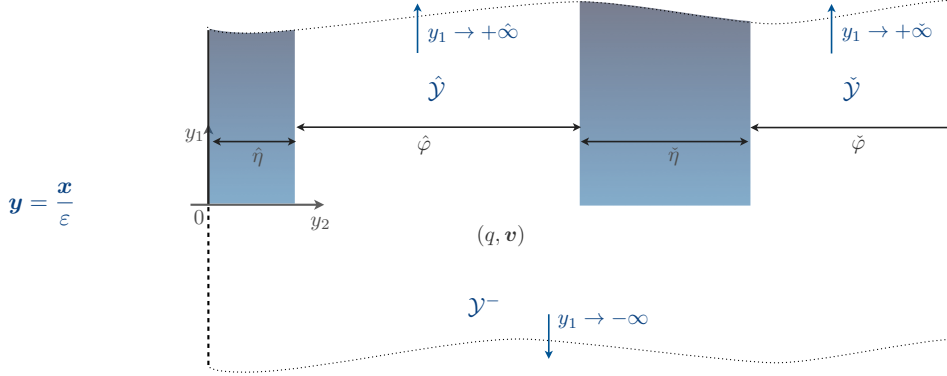


Figure 3.10: Elementary unit strip in which the analysis at a single grating interface is conducted. The analysis involves the terms (q^n, \mathbf{v}^n) in \mathcal{Y} and their matchings (3.27)-(3.28).

In \mathcal{Y} , the fields are expanded as follows

$$p^\varepsilon = q^0(\mathbf{y}, x_2) + \varepsilon q^1(\mathbf{y}, x_2) + \dots, \quad \mathbf{u}^\varepsilon = \mathbf{v}^0(\mathbf{y}, x_2) + \varepsilon \mathbf{v}^1(\mathbf{y}, x_2) + \dots. \quad (3.24)$$

and for $y_1 < 0$, the (q^i, \mathbf{v}^i) are assumed to be y_2 -periodic. As in the region of the grating, due to the multiple scale variables in the field expansions, the divergence operator applied to any vectorial function $\mathbf{g}(\mathbf{y}, x_2)$ and the gradient operator applied any scalar function $g(\mathbf{y}, x_2)$ become

$$\operatorname{div} \mathbf{g} = \frac{1}{\varepsilon} \operatorname{div}_{\mathbf{y}} \mathbf{g} + \frac{\partial \mathbf{g}}{\partial x_2} \cdot \mathbf{e}_2, \quad \nabla g = \frac{1}{\varepsilon} \nabla_{\mathbf{y}} g + \frac{\partial g}{\partial x_2} \mathbf{e}_2. \quad (3.25)$$

We now explicit the matching conditions as we ask the solution (3.24) valid in the vicinity of the interface to match the solutions (3.13) and (3.22) valid far from the interface when $y_1 \rightarrow \pm\infty$. Note that for $y_1 \rightarrow +\infty$, we have to specify in which slit the limit is considered and we denote these two limits $y_1 \rightarrow +\hat{\infty}$ in $\hat{\mathcal{Y}}$ and $y_1 \rightarrow +\tilde{\infty}$ in $\tilde{\mathcal{Y}}$. Looking, *e.g.* at the pressure, the matching for $y_1 \rightarrow -\infty$ and $x_1 \rightarrow 0^-$ reads

$$q^0(\mathbf{y}, x_2) + \varepsilon q^1(\mathbf{y}, x_2) + \dots \sim p^0(\mathbf{x}) + \varepsilon p^1(\mathbf{x}) + \dots,$$

with $x_1 = \varepsilon y_1$. Note that the above relation tells us that the q^n , $n = 0, 1, \dots$ become independent of y_2 as $y_1 \rightarrow -\infty$. This is because the rapid variations (with y_2) of the fields are due to evanescent field, which vanishes when moving away from the interface. Using Taylor expansions of the $p^n(\varepsilon y_1, x_2)$ and identifying the terms with same power in ε provides the matching conditions at each order. At the dominant order and at the first order, we get

$$p^0(0^-, x_2) = \lim_{y_1 \rightarrow -\infty} q^0(\mathbf{y}, x_2), \quad p^1(0^-, x_2) = \lim_{y_1 \rightarrow -\infty} \left(q^1(\mathbf{y}, x_2) - y_1 \frac{\partial p^0}{\partial x_1}(0^-, x_2) \right). \quad (3.26)$$

The same holds when $y_1 \rightarrow +\hat{\infty}$ or when $y_1 \rightarrow +\tilde{\infty}$. Looking, *e.g.* at the pressure, the matching for $y_1 \rightarrow +\hat{\infty}$ and $x_1 \rightarrow 0^+$ reads

$$q^0(\mathbf{y}, x_2) + \varepsilon q^1(\mathbf{y}, x_2) + \dots \sim \hat{p}^0(\mathbf{x}, y_2) + \varepsilon \hat{p}^1(\mathbf{x}, y_2) + \dots,$$

We hence obtain at the zero-order

$$\hat{p}^0(0^+, x_2, y_2) = \lim_{y_1 \rightarrow +\hat{\infty}} q^0(\mathbf{y}, x_2), \quad (3.27)$$

and at the first-order

$$\hat{p}^1(0^+, x_2, y_2) = \lim_{y_1 \rightarrow +\infty} \left(q^1(\mathbf{y}, x_2) - y_1 \frac{\partial \hat{p}^0}{\partial x_1}(0^+, x_2, y_2) \right). \quad (3.28)$$

By replacing formally the $\hat{\cdot}$ by $\check{\cdot}$ in (3.27)-(3.28), we obtain the matching conditions when $y_1 \rightarrow +\infty$.

Similar matching conditions on the velocity are obtained by replacing formally $(p^i, \hat{p}^i, \check{p}^i, q^i)$ in (3.27)-(3.28) by their counterparts $(\mathbf{u}^i, \hat{\mathbf{u}}^i, \check{\mathbf{u}}^i, \mathbf{v}^i)$.

The transmission conditions at zero-order

By injecting the expansions (3.24) in the dimensionless Euler equations (3.12) together with (3.25), we get

$$\nabla_{\mathbf{y}} q^0 = 0, \quad \operatorname{div}_{\mathbf{y}} \mathbf{v}^0 = 0.$$

Hence q^0 is independent of \mathbf{y} and in virtue of the matching conditions (3.26)-(3.27), we obtain $q^0(\mathbf{y}, x_2) = p^0(0^-, x_2) = \hat{p}^0(0^+, x_2) = \check{p}^0(0^+, x_2)$. We express this continuity of the pressure fields as

$$[[\hat{p}^0]] = \hat{p}^0(0^+, x_2) - p^0(0^-, x_2) = 0, \quad [[\check{p}^0]] = \check{p}^0(0^+, x_2) - p^0(0^-, x_2) = 0. \quad (3.29)$$

Next, by integrating $\operatorname{div}_{\mathbf{y}} \mathbf{v}^0 = 0$ over \mathcal{Y} and using the periodic conditions for $y_1 < 0$ and the condition of vanishing normal velocity on the rigid boundaries for $y_1 > 0$, we obtain

$$\lim_{y_1^* \rightarrow +\infty} \left(\int_{\hat{\mathcal{Y}}} v_1^0(y_1^*, y_2, x_2) dy_2 + \int_{\check{\mathcal{Y}}} v_1^0(y_1^*, y_2, x_2) dy_2 - \int_0^1 v_1^0(-y_1^*, y_2, x_2) dy_2 \right) = 0.$$

The matching conditions (3.26) and (3.27) expressed in terms of the velocities provides

$$\int_{\hat{\mathcal{Y}}} \hat{u}_1^0(0^+, x_2) dy_2 + \int_{\check{\mathcal{Y}}} \check{u}_1^0(0^+, x_2) dy_2 - u_1^0(0^-, x_2) dy_2 = 0, \quad (3.30)$$

where we have used from (3.17) that $\hat{u}_1^0(\mathbf{x})$ and $\check{u}_1^0(\mathbf{x})$ do not depend on y_2 . At this dominant order, we obtain the continuity of the flow-rate written as

$$[[\langle u_1^0 \rangle]] = \langle \hat{u}_1^0 \rangle(0^+, x_2) + \langle \check{u}_1^0 \rangle(0^+, x_2) - u_1^0(0^-, x_2) = 0. \quad (3.31)$$

At the leading order, the continuity conditions (3.29) and (3.31) together with the bulk equations (3.18) imply that the two channels would behave identically, *i.e.* $(\hat{p}^0, \hat{\mathbf{u}}^0) = (\check{p}^0, \check{\mathbf{u}}^0)$. To retrieve the possible different solutions, we must go further in the analysis and derive first order corrections.

The transmission conditions at first-order

We first determine the field q^1 associated to \mathbf{v}^0 through the following boundary layer problem

$$\begin{cases} \operatorname{div}_{\mathbf{y}} \mathbf{v}^0 = \mathbf{0}, & \mathbf{v}^0 = \nabla_{\mathbf{y}} q^1 + \frac{\partial p^0}{\partial x_2}(0^-, x_2) \mathbf{e}_2, \\ \lim_{y_1 \rightarrow +\infty} \mathbf{v}^0 = \langle \hat{u}_1^0 \rangle(0^+, x_2) \frac{\mathbf{e}_1}{\hat{\varphi}}, & \lim_{y_1 \rightarrow +\infty} \mathbf{v}^0 = \langle \check{u}_1^0 \rangle(0^+, x_2) \frac{\mathbf{e}_1}{\check{\varphi}}, \\ \lim_{y_1 \rightarrow -\infty} \mathbf{v}^0 = (\langle \hat{u}_1^0 \rangle(0^+, x_2) + \langle \check{u}_1^0 \rangle(0^+, x_2)) \mathbf{e}_1 + \frac{\partial p^0}{\partial x_2}(0^-, x_2) \mathbf{e}_2. \end{cases} \quad (3.32)$$

with $\mathbf{v}^0 \cdot \mathbf{n} = 0$ on the rigid boundaries and (q^1, \mathbf{v}^0) y_2 -periodic for $y_1 < 0$.

In (3.32), we have used that (i) $q^0 = p^0(0^-, x_2)$ from (3.29), (ii) $\hat{u}_2^0 = \check{u}_2^0 = 0$, $\langle \hat{u}_1^0 \rangle(\mathbf{x}) = \hat{\varphi} \hat{u}_1^0(\mathbf{x})$ and $\langle \check{u}_1^0 \rangle(\mathbf{x}) = \check{\varphi} \check{u}_1^0(\mathbf{x})$ from (3.16) and (3.17) (for the limit $y_1 \rightarrow +\infty, +\infty$) and (iii) $\mathbf{u}^0 = u_1^0 \mathbf{e}_1 + u_2^0 \mathbf{e}_2$ with $u_1^0(0^-, x_2) = \langle \hat{u}_1^0 \rangle(0^+, x_2) + \langle \check{u}_1^0 \rangle(0^+, x_2)$ from (3.30) and $u_2^0 = \partial_{x_2} p^0$ from (3.23), which holds at $x_1 = 0^-$ (for the limit $y_1 \rightarrow -\infty$). Doing so, the macroscopic contributions $\partial_{x_2} p^0(0^-, x_2)$, $\langle \hat{u}_1^0 \rangle(0^+, x_2)$ and $\langle \check{u}_1^0 \rangle(0^+, x_2)$ appearing in (3.32) are independent. This implies that the solution $q^1(\mathbf{y}, x_2)$ of the boundary layer problem (3.32) can be linearly decomposed as (up to a function $\tilde{Q}_1(x_2)$ independent of \mathbf{y})

$$q^1(\mathbf{y}, x_2) = \langle \hat{u}_1^0 \rangle(0^+, x_2) \hat{Q}_1(\mathbf{y}) + \langle \check{u}_1^0 \rangle(0^+, x_2) \check{Q}_1(\mathbf{y}) + \frac{\partial p^0}{\partial x_2}(0^-, x_2) Q_2(\mathbf{y}) + \tilde{Q}_1(x_2), \quad (3.33)$$

where $(\hat{Q}_1(\mathbf{y}), \check{Q}_1(\mathbf{y}))$ are the solutions of the elementary problems

$$\begin{cases} \Delta_{\mathbf{y}} \hat{Q}_1 = 0, & \Delta_{\mathbf{y}} \check{Q}_1 = 0, \\ \lim_{y_1 \rightarrow -\infty} \nabla_{\mathbf{y}} \hat{Q}_1 = \mathbf{e}_1, & \lim_{y_1 \rightarrow +\infty} \nabla_{\mathbf{y}} \hat{Q}_1 = \frac{\mathbf{e}_1}{\hat{\varphi}}, & \lim_{y_1 \rightarrow +\infty} \nabla_{\mathbf{y}} \hat{Q}_1 = \mathbf{0}, \\ \lim_{y_1 \rightarrow -\infty} \nabla_{\mathbf{y}} \check{Q}_1 = \mathbf{e}_1, & \lim_{y_1 \rightarrow +\infty} \nabla_{\mathbf{y}} \check{Q}_1 = \mathbf{0}, & \lim_{y_1 \rightarrow +\infty} \nabla_{\mathbf{y}} \check{Q}_1 = \frac{\mathbf{e}_1}{\check{\varphi}}, \end{cases} \quad (3.34)$$

and $Q_2(\mathbf{y})$ is the solution of the elementary problem

$$\begin{cases} \Delta_{\mathbf{y}} Q_2 = 0, \\ \lim_{y_1 \rightarrow -\infty} \nabla_{\mathbf{y}} Q_2 = \mathbf{0}, & \lim_{y_1 \rightarrow +\infty} \nabla_{\mathbf{y}} Q_2 = -\mathbf{e}_2, & \lim_{y_1 \rightarrow +\infty} \nabla_{\mathbf{y}} Q_2 = -\mathbf{e}_2. \end{cases} \quad (3.35)$$

with $Q = \hat{Q}_1, \check{Q}_1$ (respectively Q_2) satisfying the conditions of vanishing normal velocity $\nabla_{\mathbf{y}} Q \cdot \mathbf{n} = 0$ on the rigid boundaries (respectively $\nabla_{\mathbf{y}} Q_2 \cdot \mathbf{n} = -\mathbf{e}_2 \cdot \mathbf{n}$) and $(Q, \nabla_{\mathbf{y}} Q)$ (respectively $(Q_2, \nabla_{\mathbf{y}} Q_2)$) y_2 -periodic for $y_1 < 0$. It follows that the solutions of the elementary problems have the following behaviors at infinity

	\hat{Q}_1	\check{Q}_1	Q_2
$y_1 \rightarrow -\infty$	y_1	y_1	0
$y_1 \rightarrow +\infty$	$\frac{y_1}{\hat{\varphi}} + \hat{B}_1$	\check{b}	$(\hat{y}_c - y_2) + \hat{B}_2$
$y_1 \rightarrow +\infty$	\hat{b}	$\frac{y_1}{\check{\varphi}} + \check{B}_1$	$(\check{y}_c - y_2) + \check{B}_2$

(3.36)

(it is shown in section 3.5 that $\hat{b} = \check{b}$). The average jump of the pressure p^1 derives directly from the matching conditions (3.28) along with (3.33) and (3.36). We get

$$\begin{cases} \hat{p}^1(0^+, x_2, y_2) = \hat{B}_1 \langle \hat{u}_1^0 \rangle(0^+, x_2) + \hat{b} \langle \check{u}_1^0 \rangle(0^+, x_2) + \frac{\partial p^0}{\partial x_2}(0^-, x_2) \left((\hat{y}_c - y_2) + \hat{B}_2 \right) + \tilde{Q}_1(x_2), \\ \check{p}^1(0^+, x_2, y_2) = \check{b} \langle \hat{u}_1^0 \rangle(0^+, x_2) + \check{B}_1 \langle \check{u}_1^0 \rangle(0^+, x_2) + \frac{\partial p^0}{\partial x_2}(0^-, x_2) \left((\check{y}_c - y_2) + \check{B}_2 \right) + \tilde{Q}_1(x_2), \\ p^1(0^-, x_2) = \tilde{Q}_1(x_2), \end{cases} \quad (3.37)$$

and using (3.19) and (3.29), we finally obtain the jump conditions on the pressure at the first order

$$\begin{cases} \llbracket \langle \hat{p}^1 \rangle \rrbracket = \hat{B}_1 \langle \hat{u}_1^0 \rangle(0^+, x_2) + b \langle \check{u}_1^0 \rangle(0^+, x_2) + \hat{B}_2 \frac{\partial p^0}{\partial x_2}(0^-, x_2), \\ \llbracket \langle \check{p}^1 \rangle \rrbracket = b \langle \hat{u}_1^0 \rangle(0^+, x_2) + \check{B}_1 \langle \check{u}_1^0 \rangle(0^+, x_2) + \check{B}_2 \frac{\partial p^0}{\partial x_2}(0^-, x_2). \end{cases} \quad (3.38)$$

It remains to derive the jump condition on the velocity field at first order. At the zero order, we have integrated the equation of mass conservation $\operatorname{div}_{\mathbf{y}} \mathbf{v}^0 = 0$ to get (3.31); at the order 1, the equation of mass conservation now reads

$$\operatorname{div}_{\mathbf{y}} \mathbf{v}^1 + \frac{\partial v_2^0}{\partial x_2} + p^0(0^-, x_2) = 0,$$

that we integrate over the finite domain \mathcal{Y} . We have on the one hand that

$$\begin{aligned} \int_{\mathcal{Y}} \operatorname{div}_{\mathbf{y}} \mathbf{v}^1 \, d\mathbf{y} &= \langle \hat{u}_1^1 \rangle(0^+, x_2) + \langle \check{u}_1^1 \rangle(0^+, x_2) - u_1^1(0^+, x_2) \\ &+ \lim_{y_1^* \rightarrow \infty} y_1^* \frac{\partial}{\partial x_1} (\langle \hat{u}_1^0 \rangle(0^+, x_2) + \langle \check{u}_1^0 \rangle(0^+, x_2) - u_1^0(0^+, x_2)), \end{aligned} \quad (3.39)$$

and on the other hand

$$\begin{aligned} \int_{\mathcal{Y}} \left(\frac{\partial v_2^0}{\partial x_2} + p^0(0^-, x_2) \right) \, d\mathbf{y} &= -\hat{B}_2 \frac{\partial \langle \hat{u}_1^0 \rangle}{\partial x_2} - \check{B}_2 \frac{\partial \langle \check{u}_1^0 \rangle}{\partial x_2} + C \frac{\partial^2 p^0}{\partial x_2^2}(0^-, x_2) \\ &+ \lim_{y_1^* \rightarrow \infty} y_1^* \left(\frac{\partial^2 p^0}{\partial x_2^2}(0^-, x_2) + (1 + \hat{\varphi} + \check{\varphi})p^0(0^-, x_2) \right). \end{aligned} \quad (3.40)$$

We have used the periodicity of \hat{Q}_1, \check{Q}_1 and Q_2 in \mathcal{Y}^- and we have defined the new parameter

$$C = \int_{\hat{\mathcal{Y}} \cup \check{\mathcal{Y}}} \left(\frac{\partial Q_2}{\partial y_2} + 1 \right) \, d\mathbf{y}.$$

Eventually we used that (\hat{B}_2, \check{B}_2) defined in (3.36) satisfy the relations

$$\hat{B}_2 = - \int_{\hat{\mathcal{Y}} \cup \check{\mathcal{Y}}} \frac{\partial \hat{Q}_1}{\partial y_2} \, d\mathbf{y}, \quad \check{B}_2 = - \int_{\hat{\mathcal{Y}} \cup \check{\mathcal{Y}}} \frac{\partial \check{Q}_1}{\partial y_2} \, d\mathbf{y},$$

(this relation is shown in section 3.5). We now use that $\partial_{x_1} \hat{u}_1^0(0^+, x_2) + \hat{\varphi} p^0(0^-, x_2) = \partial_{x_1} \check{u}_1^0(0^+, x_2) + \check{\varphi} p^0(0^-, x_2) = 0$ from (3.18) along with (3.29), and that $\partial_{x_1} u_1^0(0^-, x_2) + \partial_{x_2}^2 p^0(0^-, x_2) + p^0(0^-, x_2) = 0$ from (3.23). Doing so, summing the two integrals (3.39) and (3.40) makes the terms linear in y_1^* to cancel. It results that the jump in the flow rate at the first-order reads

$$\llbracket \langle u_1^1 \rangle \rrbracket = \langle \hat{u}_1^1 \rangle(0^+, x_2) + \langle \check{u}_1^1 \rangle(0^+, x_2) - u_1^1(0^-, x_2) = \hat{B}_2 \frac{\partial \langle \hat{u}_1^0 \rangle}{\partial x_2} + \check{B}_2 \frac{\partial \langle \check{u}_1^0 \rangle}{\partial x_2} - C \frac{\partial u_2^0}{\partial x_2}. \quad (3.41)$$

3.4.3 Formulation of a unique effective problem

The unique effective problem is expressed gathering the zero and first-order contributions that is for the field (p, \hat{p}, \check{p}) and $(\mathbf{u}, \hat{\mathbf{u}}, \check{\mathbf{u}})$ defined by

$$\begin{aligned} p &= p^0 + \varepsilon p^1, & \hat{p} &= \langle \hat{p}^0 \rangle + \varepsilon \langle \hat{p}^1 \rangle, & \check{p} &= \langle \check{p}^0 \rangle + \varepsilon \langle \check{p}^1 \rangle, \\ \mathbf{u} &= \mathbf{u}^0 + \varepsilon \mathbf{u}^1, & \hat{\mathbf{u}} &= \langle \hat{\mathbf{u}}^0 \rangle + \varepsilon \langle \hat{\mathbf{u}}^1 \rangle, & \check{\mathbf{u}} &= \langle \check{\mathbf{u}}^0 \rangle + \varepsilon \langle \check{\mathbf{u}}^1 \rangle. \end{aligned}$$

From the wave equations in the two slits (3.18) and (3.21) and those in the surrounding fluid (3.23) along with the transmission conditions on the pressure (3.29) and (3.38) and on the flow-rate (3.31) and (3.41), the unique problem reads

$$\begin{cases} \operatorname{div} \mathbf{u} + p = 0, & \mathbf{u} = \nabla p, & \text{in the fluid,} \\ \operatorname{div} \hat{\mathbf{u}} + \hat{\varphi} \hat{p} = 0, & \hat{\mathbf{u}} = \hat{\varphi} \frac{\partial \hat{p}}{\partial x_1} \mathbf{e}_1, & \text{in the equivalent slab,} \\ \operatorname{div} \check{\mathbf{u}} + \check{\varphi} \check{p} = 0, & \check{\mathbf{u}} = \check{\varphi} \frac{\partial \check{p}}{\partial x_1} \mathbf{e}_1, & \end{cases} \quad (3.42)$$

complemented by transmission conditions applying at an interface $x_1 = 0$

$$\begin{aligned} \llbracket \hat{p} \rrbracket &= \varepsilon \hat{B}_1 \hat{u}_1(0^+, x_2) + \varepsilon b \check{u}_1(0^+, x_2) + \varepsilon \hat{B}_2 \frac{\partial p}{\partial x_2}(0^-, x_2), \\ \llbracket \check{p} \rrbracket &= \varepsilon b \hat{u}_1(0^+, x_2) + \varepsilon \check{B}_1 \check{u}_1(0^+, x_2) + \varepsilon \check{B}_2 \frac{\partial p}{\partial x_2}(0^-, x_2), \\ \llbracket u_1 \rrbracket &= \varepsilon \hat{B}_2 \frac{\partial \hat{u}_1}{\partial x_2}(0^+, x_2) + \varepsilon \check{B}_2 \frac{\partial \check{u}_1}{\partial x_2}(0^+, x_2) - \varepsilon C \frac{\partial u_2}{\partial x_2}(0^-, x_2). \end{aligned} \quad (3.43)$$

Once coming back in dimensional form, we obtain (3.7) and (3.8)-(3.9).

3.5 Properties of the effective parameters

We deduce some properties of the effective parameters obtained in the previous section. Depending on the chosen configuration, we can show the following properties directly from the formulation of the elementary problems.

Proof of $\hat{b} = \check{b}$

We introduce the restriction $\mathcal{Y}^* \subset \mathcal{Y}$, with $\mathcal{Y}^* = \{(y_1, y_2) \in (-y_1^*, 0) \times (0, 1) \cup (0, y_1^*) \times \hat{Y} \cup (0, y_1^*) \times \check{Y}\}$ for $y_1^* > 0$ sufficiently large. Multiplying by \check{Q}_1 the equilibrium equation on \hat{Q}_1 in the elementary problem (3.34) and integrate it over \mathcal{Y}^* , which gives after an integration by parts

$$0 = \int_{\mathcal{Y}^*} \check{Q}_1 \operatorname{div}_{\mathbf{y}} (\nabla_{\mathbf{y}} \hat{Q}_1) \, d\mathbf{y} = - \int_{\mathcal{Y}^*} \nabla_{\mathbf{y}} \check{Q}_1 \cdot \nabla_{\mathbf{y}} \hat{Q}_1 \, d\mathbf{y} + \int_{\partial \mathcal{Y}^*} \check{Q}_1 (\nabla_{\mathbf{y}} \hat{Q}_1 \cdot \mathbf{n}) \, d\mathbf{y}. \quad (3.44)$$

Now, knowing that \check{Q}_1 and $\nabla_{\mathbf{y}} \hat{Q}_1$ are periodic with respect to y_2 for $y_1 < 0$ (with \mathbf{n} anti-periodic), then the boundary terms on the lateral sides for $y_1 < 0$ compensate and vanish. Same holds for the contribution on the rigid walls which are zero in virtue of the Neumann conditions. We are left with the terms on the boundaries at $y_1 = \pm y_1^*$ which can be made explicit up to vanishing contributions from the asymptotic behavior of \check{Q}_1 and \hat{Q}_1 given by (3.36)

$$0 = \int_{\mathcal{Y}^*} \check{Q}_1 \operatorname{div}_{\mathbf{y}} (\nabla_{\mathbf{y}} \hat{Q}_1) \, d\mathbf{y} = - \int_{\mathcal{Y}^*} \nabla_{\mathbf{y}} \check{Q}_1 \cdot \nabla_{\mathbf{y}} \hat{Q}_1 \, d\mathbf{y} + \check{b} - y_1^* + o(1), \quad (3.45)$$

where $o(1)$ is a vanishing contribution as y_1^* tends to infinity. Using the same arguments, but switching the roles \hat{Q}_1 and \check{Q}_1 , we have

$$0 = \int_{\mathcal{Y}^*} \hat{Q}_1 \operatorname{div}_{\mathbf{y}} (\nabla_{\mathbf{y}} \check{Q}_1) \, d\mathbf{y} = - \int_{\mathcal{Y}^*} \nabla_{\mathbf{y}} \hat{Q}_1 \cdot \nabla_{\mathbf{y}} \check{Q}_1 \, d\mathbf{y} + \hat{b} - y_1^* + o(1). \quad (3.46)$$

Combining (3.45) and (3.46), and passing to the limit as y_1^* tends to infinity, we deduce that $\hat{b} = \check{b}$.

Properties on the parameters \hat{B}_2 and \check{B}_2

Integral form of \hat{B}_2 and \check{B}_2

Multiplying the equilibrium equation on \hat{Q}_1 in the elementary problem (3.34) by Q_2 and integrating by parts over \mathcal{Y} leads to

$$0 = \int_{\mathcal{Y}} Q_2 \operatorname{div}_{\mathbf{y}} (\nabla_{\mathbf{y}} \hat{Q}_1) \, d\mathbf{y} = - \int_{\mathcal{Y}} \nabla_{\mathbf{y}} Q_2 \cdot \nabla_{\mathbf{y}} \hat{Q}_1 \, d\mathbf{y} + \hat{B}_2. \quad (3.47)$$

Similarly to the previous paragraph, we have simplified the expression of the boundary terms in (3.47) by using the periodicity conditions, the Neumann boundary conditions on the rigid walls as well as the asymptotic behavior of \hat{Q}_1 and Q_2 at infinity given by (3.36). Next, multiplying the equilibrium equation on Q_2 in the elementary problem (3.35) by \hat{Q}_1 and integrating by parts over \mathcal{Y} leads to

$$0 = \int_{\mathcal{Y}} \hat{Q}_1 \operatorname{div}_{\mathbf{y}} (\nabla_{\mathbf{y}} (Q_2 + y_2)) \, d\mathbf{y} = - \int_{\mathcal{Y}} \nabla_{\mathbf{y}} Q_2 \cdot \nabla_{\mathbf{y}} \hat{Q}_1 \, d\mathbf{y} - \int_{\mathcal{Y}} \frac{\partial \hat{Q}_1}{\partial y_2} \, d\mathbf{y}, \quad (3.48)$$

with the same arguments on \hat{Q}_1 and Q_2 to eliminate the vanishing contributions on the boundaries involving the periodicity and the rigid walls. Combining (3.47) and (3.48), and noticing that the periodicity of \hat{Q}_1 on \mathcal{Y}^- implies that $\int_{\mathcal{Y}^-} \frac{\partial \hat{Q}_1}{\partial y_2} \, d\mathbf{y} = 0$, we conclude that

$$\hat{B}_2 = - \int_{\tilde{\mathcal{Y}} \cup \hat{\mathcal{Y}}} \frac{\partial \hat{Q}_1}{\partial y_2} \, d\mathbf{y}. \quad (3.49)$$

Conversely, replacing \hat{Q}_1 by \check{Q}_1 in (3.47) and (3.48), we obtain

$$\check{B}_2 = - \int_{\tilde{\mathcal{Y}} \cup \hat{\mathcal{Y}}} \frac{\partial \check{Q}_1}{\partial y_2} \, d\mathbf{y}. \quad (3.50)$$

Explicit relations for symmetric obstacles

We can now establish the properties given in (3.10) when $\hat{\eta} = \check{\eta}$ or when $\hat{\varphi} = \check{\varphi}$. First let us extend to \mathbb{R}^2 , in virtue of the periodicity with respect to y_2 , the solutions $\hat{Q}_1(\mathbf{y})$ and $\check{Q}_1(\mathbf{y})$ defined on the unit cell \mathcal{Y} , see figure 3.10.

Case $\hat{\eta} = \check{\eta}$. By making the change of variable $\tilde{y}_2 = y_2 - \hat{\eta} - \hat{\varphi}/2$, it suffices to notice that $(y_1, \tilde{y}_2) \mapsto \hat{Q}_1(y_1, \tilde{y}_2 + \hat{\eta} + \hat{\varphi}/2)$ and $(y_1, \tilde{y}_2) \mapsto \check{Q}_1(y_1, \tilde{y}_2 + \hat{\eta} + \hat{\varphi}/2)$ are even functions of $\tilde{y}_2 \in (-1/2, 1/2)$ when $\hat{\eta} = \check{\eta}$. Thus, their derivative with respect to \tilde{y}_2 are odd functions of \tilde{y}_2 . Using the integral forms (3.49) and (3.50) of the effective parameters established previously and which remain invariant by translation along direction \mathbf{e}_2 of the unit cell in virtue of the periodicity, we deduce that $\hat{B}_2 = \check{B}_2 = 0$.

Case $\hat{\varphi} = \check{\varphi}$. By making the change of variable $\tilde{y}_2 = y_2 - \hat{\eta}/2$, it suffices to notice that $(y_1, \tilde{y}_2) \mapsto Q(y_1, \tilde{y}_2) = \hat{Q}_1(y_1, \tilde{y}_2 + \hat{\eta}/2) + \check{Q}_1(y_1, \tilde{y}_2 + \hat{\eta}/2)$ is an even function of $\tilde{y}_2 \in (-1/2, 1/2)$ when $\hat{\varphi} = \check{\varphi}$. Thus its derivative with respect to \tilde{y}_2 is an odd function of \tilde{y}_2 . Using again (3.49) and (3.50) by summing the two integrals, we deduce that $\hat{B}_2 + \check{B}_2 = 0$.

Finally, we mention that for approximate solutions exists for the regular grating, which are given by 3.11. For simple geometries, closed form approximations can be obtained, see for instance [98, 146].

3.6 Solutions and effective problems

We consider rigid parts with same width $\hat{\eta} = \check{\eta}$ while the two slits may have different widths $\check{\varphi} \neq \hat{\varphi}$. This leads to some simplification in the transmission conditions (3.8)-(3.9) thanks to (3.10) while keeping the whole complexity of the spectra. In the following we use the notations $\hat{B} = \hat{B}_1$ and $\check{B} = \check{B}_1$.

3.6.1 Explicit solution of the effective problem

From now on, we consider a propagating incident wave at incidence θ , with

$$k_0 = k \cos \theta, \quad b_0 = k \sin \theta.$$

The homogenized scattering problem is set on (p, \hat{p}, \check{p}) satisfying (3.7) and (3.8)(3.9). As the effective transmission conditions are translational invariant, the solution is explicit and it reads in the surrounding fluid

$$p(\mathbf{x}) = e^{ik \sin \theta x_2} \times \begin{cases} e^{ik \cos \theta(x_1 + \ell)} + r e^{-ik \cos \theta(x_1 + \ell)}, & x_1 \in (-\infty, -\ell), \\ t e^{ik \cos \theta(x_1 - \ell)}, & x_1 \in (\ell, +\infty), \end{cases} \quad (3.51)$$

while within the effective slab $x_1 \in (-\ell, \ell)$ we have the coexistence of the two solutions

$$\hat{p}(\mathbf{x}) = \left(\hat{S} \cos kx_1 + \hat{A} \sin kx_1 \right) e^{ik \sin \theta x_2}, \quad \check{p}(\mathbf{x}) = \left(\check{S} \cos kx_1 + \check{A} \sin kx_1 \right) e^{ik \sin \theta x_2}. \quad (3.52)$$

The scattering coefficients (r, t) and the amplitudes $(\hat{S}, \check{S}, \hat{A}, \check{A})$ within the effective slab are given by (3.8)-(3.9), which provides 6 equations. We obtain the scattering coefficients (r, t)

$$r = \frac{zz^* - 1}{1 - z^2}, \quad t = \frac{z - z^*}{1 - z^2}, \quad (3.53)$$

where z is given by

$$z = \frac{1}{\varphi z_3} \left((i \cos \theta - khC \sin^2 \theta) z_1 \sin 2k\ell - \varphi z_2 \cos 2k\ell \right), \quad (3.54)$$

along with

$$\begin{aligned} z_1 &= (1 + \gamma)^2 - \beta^2 + 2\beta(1 - \gamma) \cotan 2k\ell + 4\gamma \cotan^2 2k\ell, \\ z_2 &= 1 - \gamma - \alpha\beta + 2\alpha \cotan 2k\ell + (\alpha(\gamma + 1) - \beta) \tan 2k\ell, \\ z_3 &= 1 + \gamma - \alpha\beta + 2\alpha \cotan 2k\ell, \end{aligned} \quad (3.55)$$

and

$$\varphi = \hat{\varphi} + \check{\varphi}, \quad \alpha = \frac{\hat{\varphi}\check{\varphi}}{\varphi} \left(\hat{B} + \check{B} - 2b \right) kh, \quad \beta = (\hat{\varphi}\hat{B} + \check{\varphi}\check{B})kh, \quad \gamma = \hat{\varphi}\check{\varphi} \left(\hat{B}\check{B} - b^2 \right) (kh)^2. \quad (3.56)$$

The coefficients (r, t) are expected to approximate (r_0, t_0) in the actual problem and the solutions (3.52) with $(\hat{\mathcal{S}}, \check{\mathcal{S}}, \hat{\mathcal{A}}, \check{\mathcal{A}})$ are expected to approximate the actual solutions in the slits. The amplitudes are of the form

$$\left\{ \begin{array}{l} \hat{\mathcal{S}} = \frac{1}{2} \frac{\cos kl - \check{\varphi}(\check{B} - b) \sin kl}{\cos^2 kl - \beta \sin kl \cos kl + \gamma \sin^2 kl} \frac{z - z^*}{1 + z}, \\ \check{\mathcal{S}} = \frac{1}{2} \frac{\cos kl - \hat{\varphi}(\hat{B} - b) \sin kl}{\cos^2 kl - \beta \sin kl \cos kl + \gamma \sin^2 kl} \frac{z - z^*}{1 + z}, \\ \hat{\mathcal{A}} = \frac{1}{2} \frac{\sin kl + \check{\varphi}(\check{B} - b) \cos kl}{\sin^2 kl + \beta \sin kl \cos kl + \gamma \cos^2 kl} \frac{z - z^*}{1 - z}, \\ \check{\mathcal{A}} = \frac{1}{2} \frac{\sin kl + \hat{\varphi}(\hat{B} - b) \cos kl}{\sin^2 kl + \beta \sin kl \cos kl + \gamma \cos^2 kl} \frac{z - z^*}{1 - z}. \end{array} \right. \quad (3.57)$$

In the following section, we show that the parameters (α, β, γ) are positive.

Positivity of the quadratic form $(\chi, \zeta) \mapsto \hat{B}\chi^2 + \check{B}\zeta^2 + 2b\chi\zeta$

We aim to prove the semi positivity of the quadratic form $(\chi, \zeta) \mapsto \hat{B}\chi^2 + \check{B}\zeta^2 + 2b\chi\zeta$ for any $(\chi, \zeta) \in \mathbb{R}^2$. We start from the elementary problems on \hat{Q}_1 and \check{Q}_1 defined in (3.34). Setting $Q_1 = \hat{Q}_1\chi + \check{Q}_1\zeta$ with χ, ζ two reals, the function Q_1 satisfies by linearity

$$\Delta_{\mathbf{y}} Q_1 = 0 \text{ in } \mathcal{Y}, \quad \lim_{y_1 \rightarrow -\infty} \nabla_{\mathbf{y}} Q_1 = (\chi + \zeta)\mathbf{e}_1, \quad \lim_{y_1 \rightarrow +\infty} \nabla_{\mathbf{y}} Q_1 = \chi \frac{\mathbf{e}_1}{\hat{\varphi}}, \quad \lim_{y_1 \rightarrow +\infty} \nabla_{\mathbf{y}} Q_1 = \zeta \frac{\mathbf{e}_1}{\check{\varphi}}. \quad (3.58)$$

We define $F(\mathbf{y})$ as a piecewise linear function with $F(y_1 < 0, y_2) = (\chi + \zeta)y_1$, $F(y_1 > 0, y_2 \in \hat{Y}) = y_1\chi/\hat{\varphi}$ and $F(y_1 > 0, y_2 \in \check{Y}) = y_1\zeta/\check{\varphi}$. Introducing the function $Q = Q_1 - F$ which is continuous in 0, we have

$$Q \underset{y_1 \rightarrow -\infty}{\sim} 0, \quad Q \underset{y_1 \rightarrow +\infty}{\sim} \hat{B}\chi + b\zeta, \quad \text{and} \quad Q \underset{y_1 \rightarrow +\infty}{\sim} b\chi + \check{B}\zeta. \quad (3.59)$$

We introduce again the restriction $\mathcal{Y}^* \subset \mathcal{Y}$, with $\mathcal{Y}^* = \{(y_1, y_2) \in (-y_1^*, 0) \times (0, 1) \cup (0, y_1^*) \times \hat{Y} \cup (0, y_1^*) \times \check{Y}\}$ and $y_1^* > 0$. Using the values as $y_1 \rightarrow \infty$, we obtain by integration

$$0 = \int_{\mathcal{Y}^*} Q \Delta_{\mathbf{y}} Q_1 \, d\mathbf{y} = - \int_{\mathcal{Y}^*} \nabla_{\mathbf{y}} Q \cdot \nabla_{\mathbf{y}} (Q + F) \, d\mathbf{y} + \hat{B}\chi^2 + \check{B}\zeta^2 + 2b\chi\zeta + o(1), \quad (3.60)$$

where $o(1)$ is a vanishing contribution as y_1^* tends to infinity. By a similar integration, we obtain

$$0 = \int_{\mathcal{Y}^*} F \Delta_{\mathbf{y}} Q_1 \, d\mathbf{y} = - \int_{\mathcal{Y}^*} \nabla_{\mathbf{y}} F \cdot \nabla_{\mathbf{y}} (Q + F) \, d\mathbf{y} + \left(\frac{\chi^2}{\hat{\varphi}} + \frac{\zeta^2}{\check{\varphi}} + (\chi + \zeta)^2 \right) y_1^* + o(1). \quad (3.61)$$

Since $\int_{\mathcal{Y}^*} \nabla_{\mathbf{y}} F \cdot \nabla_{\mathbf{y}} F \, d\mathbf{y} = \left(\frac{\chi^2}{\hat{\varphi}} + \frac{\zeta^2}{\check{\varphi}} + (\chi + \zeta)^2 \right) y_1^* + o(1)$, by passing to the limit $y_1^* \rightarrow \infty$, we finally obtain the positivity of the quadratic form :

$$0 \leq \int_{\mathcal{Y}} \nabla_{\mathbf{y}} Q \cdot \nabla_{\mathbf{y}} Q \, d\mathbf{y} = \hat{B}\chi^2 + \check{B}\zeta^2 + 2b\chi\zeta, \quad \forall (\chi, \zeta) \in \mathbb{R}^2. \quad (3.62)$$

We can now establish some properties on the effective coefficients (\hat{B}, \check{B}, b) and the parameters (α, β, γ) given in (3.56). In particular, we have

$$\alpha \geq 0, \quad \beta \geq 0, \quad \gamma \geq 0, \quad \beta \geq \alpha. \quad (3.63)$$

First, choosing $(\chi, \zeta) = (1, 0)$ or $(0, 1)$ in (3.62), we have obviously that $\hat{B} \geq 0$ and $\check{B} \geq 0$, hence $\beta \geq 0$. Next, choosing $(\chi, \zeta) = (b, -\hat{B})$ gives $\hat{B}\check{B} \geq b^2$, hence $\gamma \geq 0$. Likewise, choosing $(\chi, \zeta) = (1, -1)$ leads to $\hat{B} + \check{B} - 2b \geq 0$, hence $\alpha \geq 0$. Finally, by taking $(\chi, \zeta) = (\sqrt{\hat{\varphi}/\check{\varphi}}, \sqrt{\check{\varphi}/\hat{\varphi}})$, we get $(\hat{\varphi}/\check{\varphi})\hat{B} + (\check{\varphi}/\hat{\varphi})\check{B} + 2b \geq 0$, which is equivalent to $\beta \geq \alpha$.

3.7 Validation of the effective model for a scattering problem

3.7.1 Efficiency of the effective model in a scattering problem

To begin with, and as a rough illustration of the efficiency of the model, we report in figure 3.11 the pressure fields (3.51)-(3.52) along with (3.53) and (3.57), which are the effective counterparts of the fields shown in figure 3.3 (calculated using the modal method presented in §3.6.3.2.3). Note that in principle, $\hat{p}(\mathbf{x})$ and $\check{p}(\mathbf{x})$ in (3.52) both live in the whole region $x_1 \in (-\ell, \ell)$; to allow for a comparison with the actual solution, we represent them in the region of the actual slits. For $kh = 0.74$ reasonably far from the Fano resonance, the scattering is very weak, which is expected for this ultra-sparse grating. Next $kh \simeq 0.75$ corresponds to the close end of the Fano resonance, that we have chosen for the amusing capacity to mimic negative refraction. The effective fields nicely reproduce those of the figure 3.3; to go further in the validation of the effective model, we provide below quantitative comparisons of the effective and numerical solutions.

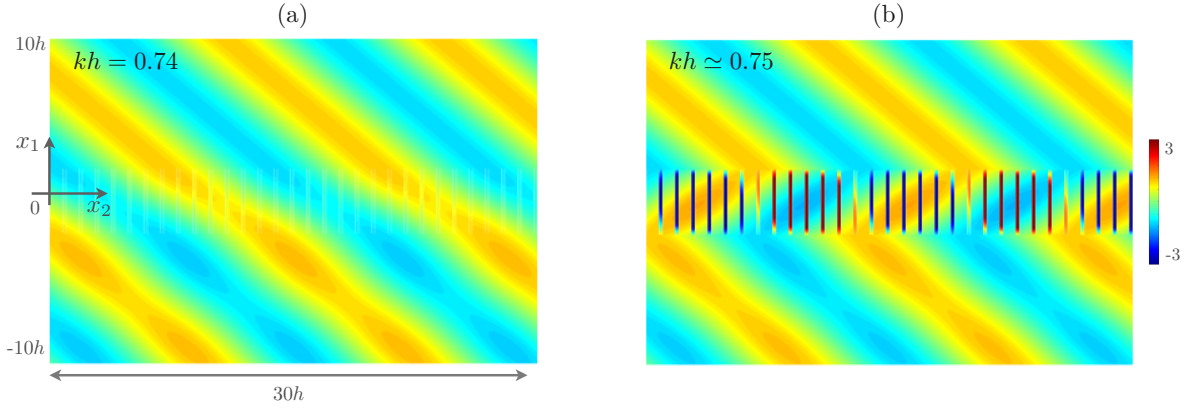


Figure 3.11: Pressure fields p and (\hat{p}, \check{p}) of the homogenized problem, (3.51)-(3.52) for the ultra-sparse grating of figure 3.3 ($\hat{\varphi} = 0.20$, $\check{\varphi} = 0.76$, $2\ell = 4h$ and $\theta = 40^\circ$).

Regular gratings

A classical result for the regular grating corresponds to our effective model at the dominant order see, *e.g.* [105, 118, 83, 129]. In this case, the conditions (3.8)-(3.9) simplify to continuity relations. As a result, we have $\alpha = \beta = \gamma = 0$ in (3.56), hence $z_1 = z_2 = z_3 = 1$ in (3.55) and

eventually $z = \frac{i \cos \theta}{\varphi} \sin 2k\ell - \cos 2k\ell + O(\varepsilon)$ in (3.54). Thus, the scattering coefficients up to $O(\varepsilon)$ read

$$r = \frac{(\cos^2 \theta - \varphi^2) \sin 2k\ell}{(\cos^2 \theta + \varphi^2) \sin 2k\ell - 2i\varphi \cos \theta \cos 2k\ell}, \quad t = \frac{2i\varphi \cos \theta}{(\cos^2 \theta + \varphi^2) \sin 2k\ell - 2i\varphi \cos \theta \cos 2k\ell}, \quad (3.64)$$

These estimates correctly predict the scattering properties of a regular grating. Namely, a perfect transmission is reached (i) for $\cos \theta_B = \varphi$ for any frequency, which corresponds to the so-called extraordinary acoustic transmission at the Brewster angle and (ii) at the Fabry-Pérot resonances at $2k_{\text{FP}}\ell = n\pi$ for any incidence. The effective model at the order 1 (3.53) is expectedly more accurate than (3.64), this has been discussed [96] and it is illustrated in figure 3.12 for a grating of plates of length $2\ell = 4h$ and $\hat{\varphi} = \check{\varphi} = 0.15$.

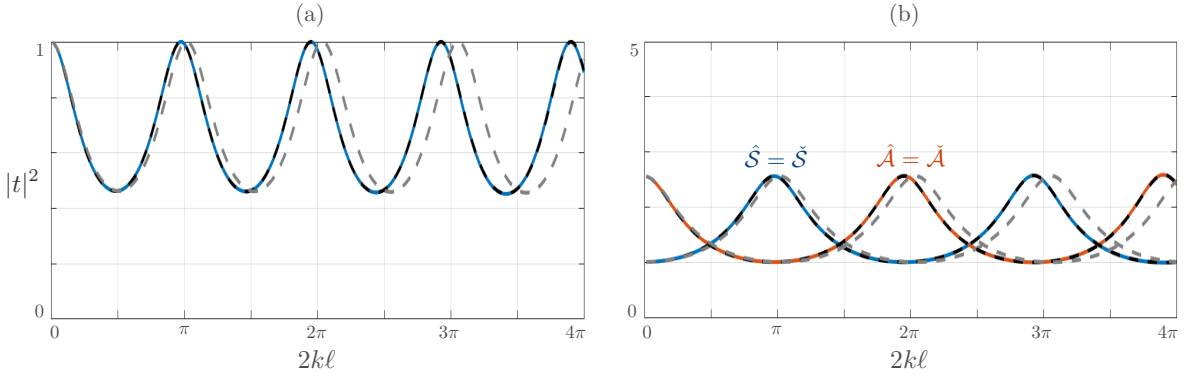


Figure 3.12: Fabry-Pérot resonances in a regular grating ($\hat{\varphi} = \check{\varphi} = 0.15$, $2\ell = 4h$, $\theta = 30^\circ$). Variations against the dimensionless frequency $2k\ell$ of (a) the transmittance $|t|^2$ and (b) the amplitudes in the slits. Coloured plain lines show the direct numerics, grey and black dashed lines show the effective model at the order 0 with $h = 0$ in (3.52)-(3.53), and at the order 1 from (3.52)-(3.53).

Dual-period gratings

With the same range of frequencies as in figure 3.12, we now consider two dual-period gratings ($\hat{\varphi} = 0.20$, $\check{\varphi} = 0.10$) and ($\hat{\varphi} = 0.29$, $\check{\varphi} = 0.01$). Depending on the asymmetry between the two slits, the wide Fabry-Pérot peaks located at $2k_{\text{FP}}\ell = n\pi$ are scared by sharp dips on their low or high frequency sides. Next, odd resonances (odd n) are characterized by large amplitudes of the symmetric component \hat{S} of $\hat{p}(\boldsymbol{x})$ in (3.52), even resonances by large amplitudes of the antisymmetric component \hat{A} . All these features are accurately reproduced by the effective model as shown in figure 3.13. Fano resonances are characterized by the succession of a perfect-transmission and, what is more demanding, a zero-transmission. In the present case, this is attributable to the appearance of a quasi-trapped mode sometimes called π -mode because the fields in two nearby slits oscillate out-of-phase. This is illustrated in the figures 3.14 where we report the fields for $|t| = 1$ and $t = 0$ at the third Fano resonance (for $\hat{\varphi} = 0.20$, $\check{\varphi} = 0.10$). It is worth noting that the out-of-phase oscillations of the fields in the slits are made possible as they are coupled at the grating interfaces $x_1 = \pm\ell$ through a strong evanescent fields. In the effective model, this coupling is encapsulated in the jump conditions (3.8)-(3.9). Eventually, as the effective model is translational invariant, the solution involves

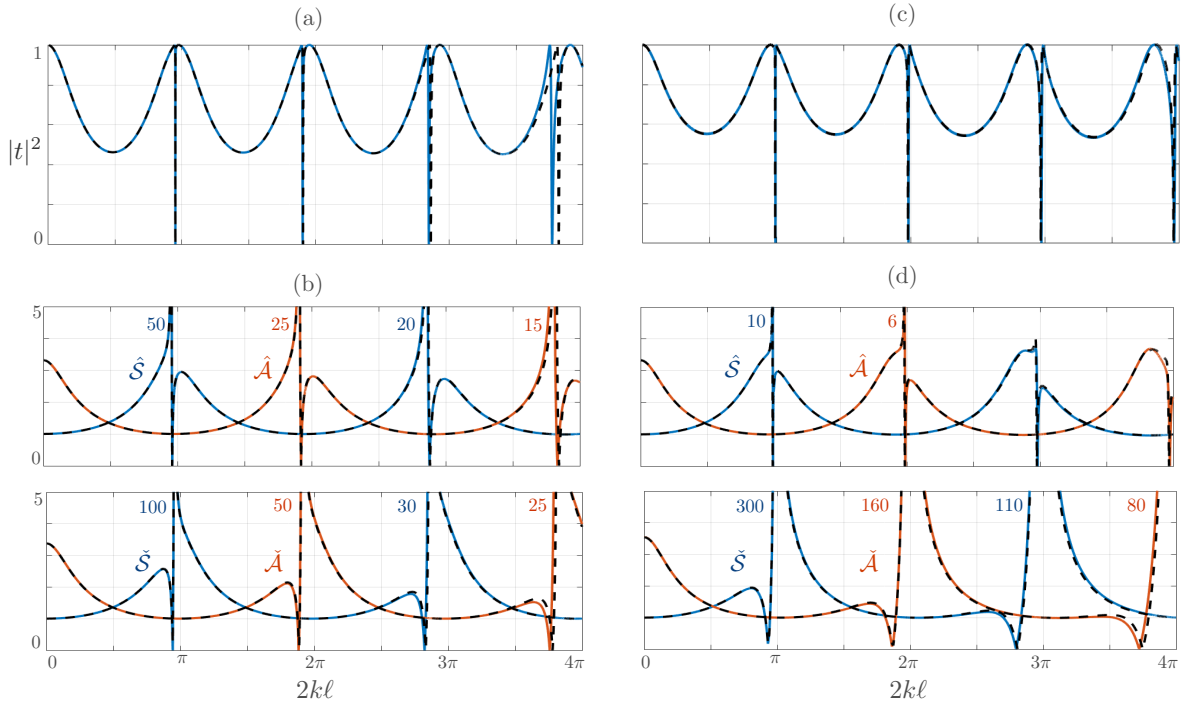


Figure 3.13: Occurrence of Fano resonances in dual-period gratings for (a-b) $\hat{\varphi} = 0.20$, $\check{\varphi} = 0.10$ and (c-d) $\hat{\varphi} = 0.29$, $\check{\varphi} = 0.01$ (in both cases $2\ell = 4h$, $\theta = 0$). Same representation as in figure 3.12 with in (b) and (d) the numbers near each peak indicating the maximum amplitude of the peaks.

only the propagating wave and, as it should be, does not reproduce the strong evanescent field close to the interfaces.

3.7.2 Local analysis of the resonances

The effective solution used in the previous section is explicit but it remains difficult to analyze the mechanism responsible for the occurrence of Fano resonances and their proximity with the Fabry-Pérot resonances observed in the figure 3.2 and 3.13. To get physical insights of this mechanism, we conduct a local analysis in a vicinity, of the order of $kh \ll 1$, of the Fabry-Pérot resonances $2k\ell = n\pi$ with n an integer. Hence in this section we consider (α, β, γ) in (3.56) at the dominant order with

$$\alpha = \frac{\hat{\varphi}\check{\varphi}}{\varphi} \left(\hat{B} + \check{B} - 2b \right) \frac{n\pi h}{2\ell}, \quad \beta = (\hat{\varphi}\hat{B} + \check{\varphi}\check{B}) \frac{n\pi h}{2\ell}, \quad \gamma = \hat{\varphi}\check{\varphi} \left(\hat{B}\check{B} - b^2 \right) \left(\frac{n\pi h}{2\ell} \right)^2, \quad (3.65)$$

being now real positive constants in the vicinity of the n -th Fabry-Pérot/Fano resonance (the positiveness is proven in (3.63)). With $k\ell = O(1)$, α and β are of order kh and γ of order $(kh)^2$.

Complex poles of the Fano resonance

To obtain simplified expressions of (r, t) from (3.53), we consider that the wavenumber k is close to a resonance at $\frac{n\pi}{2\ell}$ in a vicinity measured by $2k\ell - n\pi = O(kh) \ll 1$. At the dominant

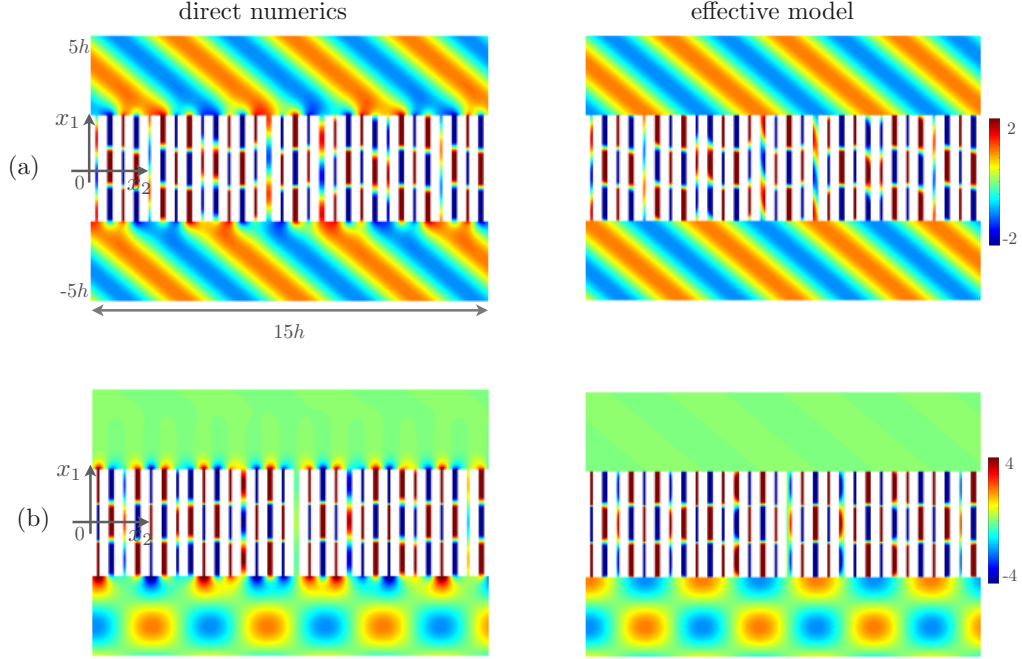


Figure 3.14: Pressure fields at the third Fano resonance, (a) perfect transmission and (b) zero-transmission ($\theta = 40^\circ$). Left panels show the results from direct numerics ($2k\ell \simeq 2.84$ and 2.85), right panels the results given by the effective model (3.51)-(3.52) ($2k\ell \simeq 2.85$ and 2.86).

order, we obtain

$$t = \frac{i(-1)^n \varphi}{\ell \cos \theta} \frac{(k - k_{t=0})}{(k - k_{\text{Fano}}^+)(k - k_{\text{Fano}}^-)}, \quad r = 1 - (-1)^n t, \quad (3.66)$$

where $k_{t=0} = \frac{n\pi - 2\alpha}{2\ell}$, k_{Fano}^\pm are the two complex-roots of $P(2k\ell - n\pi)$, with $P(\xi) = \xi^2 + 2(\beta + i\frac{\varphi}{\cos \theta})\xi + 4(\gamma + i\frac{\varphi}{\cos \theta}\alpha)$ and (α, β, γ) are given by (3.65). The two complex poles ($k_{\text{Fano}}^-, k_{\text{Fano}}^+$) are characteristic of the Fano resonance and we discriminate them by their imaginary parts denoting k_{Fano}^+ the pole of the strongest resonance being closer to the real axis.

It is worth noticing that for regular gratings, $\hat{B} = \check{B}$ hence, from (3.56), $\beta = \alpha + \gamma/\alpha$. It results that $k_{\text{Fano}}^+ = k_{t=0}$ and $k_{\text{Fano}}^- = k_{\text{FP}} = \frac{n\pi - 2\gamma/\alpha}{2\ell} - i\frac{\varphi}{\ell \cos \theta}$ and the transmission (3.66) simplifies to

$$t_{\text{FP}} = \frac{i(-1)^n \varphi}{\ell \cos \theta} \frac{1}{k - k_{\text{FP}}}. \quad (3.67)$$

As expected zero-transmissions are not possible anymore and $t_{\text{FP}} = (-1)^n$ when k equals the real part of k_{FP} .

We report in figure 3.15 the trajectories of the complex pole k_{Fano}^\pm in the complex plane when varying the detuning parameter for $\theta = 40^\circ$ (note that the trajectories remain almost identical for all θ -values). Here, the detuning parameter is defined as $\check{\varphi}$ for given $\hat{\varphi} = 0.10$, which measures the strength in the symmetry breaking and the arrows indicate the path

with increasing $\check{\varphi}$. As it was already visible on figure 3.13, the two resonances have very different thinnesses as their imaginary parts differ by a factor 10^3 . Expectedly, the pole k_{Fano}^- of weaker resonance is close to the pole of the Fabry-Pérot resonance k_{FP} of regular arrays which is reported for comparison (the trajectory of k_{FP} is obtained by varying $\check{\varphi} = \hat{\varphi}$). They coincide for $\check{\varphi} = \hat{\varphi}$ and asymptotically for vanishing rigid part thickness $\check{\varphi} + \hat{\varphi} \rightarrow 1$. The pole k_{Fano}^+ is associated to the strong resonance of the quasi trapped-mode. It becomes real when the grating becomes regular; there, the quasi-trapped becomes a perfect trapped mode and the Fano resonance disappears.

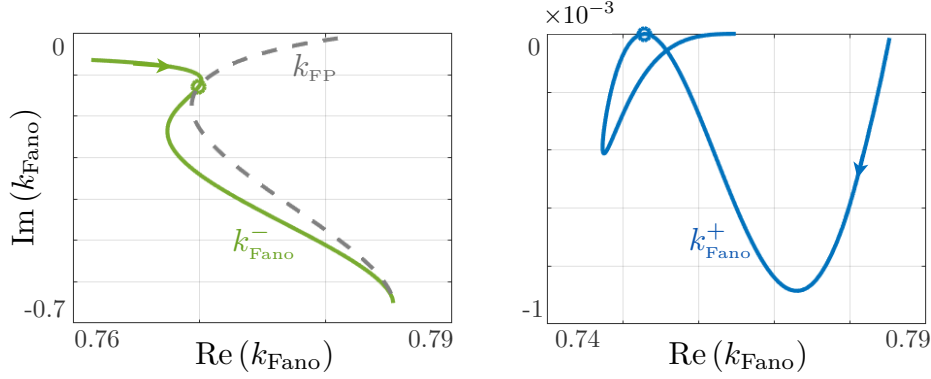


Figure 3.15: Trajectories of the complex poles k_{Fano}^- (left panel) and k_{Fano}^+ (right panel) varying the detuning parameter $\check{\varphi} \in (0, 0.90)$ for $\hat{\varphi} = 0.10$ ($2\ell = 4h$, $\theta = 40^\circ$). Fano resonance disappears in the regular grating $\check{\varphi} = \hat{\varphi}$ (open symbols), resulting in $k_{\text{Fano}}^- = k_{\text{FP}}$ and real k_{Fano}^+ .

Perfect-transmissions and zero-transmissions

From (3.66), perfect and zero-transmissions are obtained for real wavenumbers

$$\begin{aligned} \text{perfect transmissions,} \quad k_{|t|=1}^\pm &= \frac{1}{2\ell}(n\pi - \beta \pm \sqrt{\beta^2 - 4\gamma}), \\ \text{zero-transmissions,} \quad k_{t=0} &= \frac{1}{2\ell}(n\pi - 2\alpha), \end{aligned} \quad (3.68)$$

with $k_{|t|=1}^- \leq k_{t=0} \leq k_{|t|=1}^+$. This relation is valid for any values for $\hat{\varphi}$ and $\check{\varphi}$, and a proof is given.

Proof of $k_{|t|=1}^- \leq k_{t=0} \leq k_{|t|=1}^+$

Given the definition (3.68) of $k_{t=0}$ and $k_{|t|=1}^\pm$, a straightforward manipulation shows that proving the inequality $k_{|t|=1}^- \leq k_{t=0} \leq k_{|t|=1}^+$ is equivalent to proving $\gamma \leq \alpha(\beta - \alpha)$. Thus, from the definitions of (α, β, γ) in (3.65), we must prove that

$$\hat{\varphi}\check{\varphi}(\hat{B}\check{B} - b^2) \leq \frac{\hat{\varphi}\check{\varphi}}{\hat{\varphi} + \check{\varphi}}(\hat{B} + \check{B} - 2b) \left(\hat{\varphi}\hat{B} + \check{\varphi}\check{B} - \frac{\hat{\varphi}\check{\varphi}}{\hat{\varphi} + \check{\varphi}}(\hat{B} + \check{B} - 2b) \right), \quad (3.69)$$

which is equivalent after simplification to

$$(\hat{\varphi} + \check{\varphi})^2(\hat{B}\check{B} - b^2) \leq (\hat{B} + \check{B} - 2b)(\hat{\varphi}^2\hat{B} + \check{\varphi}^2\check{B} + 2\hat{\varphi}\check{\varphi}b). \quad (3.70)$$

Now, it is sufficient to remark the following identity

$$(\hat{B} + \check{B} - 2b)(\hat{\varphi}^2 \hat{B} + \check{\varphi}^2 \check{B} + 2\hat{\varphi}\check{\varphi}b) - (\hat{\varphi} + \check{\varphi})^2(\hat{B}\check{B} - b^2) = (\hat{\varphi}\hat{B} - \check{\varphi}\check{B} + (\hat{\varphi} - \check{\varphi})b)^2 \geq 0, \quad (3.71)$$

from which we deduce that (3.70) is fulfilled and thus that $k_{|t|=1}^- \leq k_{t=0} \leq k_{|t|=1}^+$.

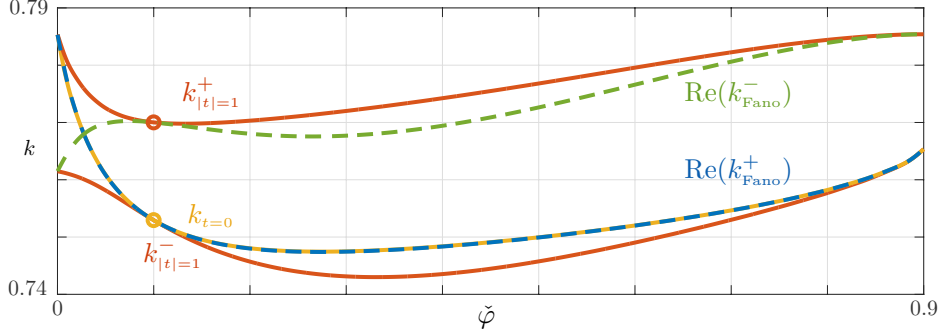
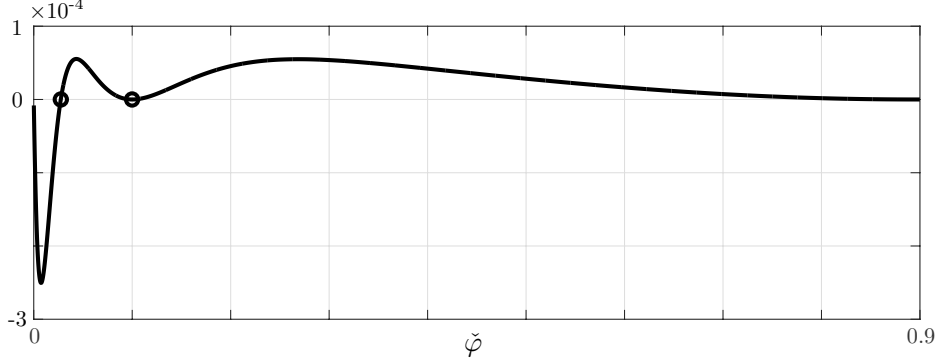


Figure 3.16: Real wavenumbers $k_{|t|=1}^\pm$ realizing perfect-transmissions (red plain lines) and $k_{t=0}$ realizing zero-transmission (plain yellow line). Dashed lines show the real parts of the Fano complex poles, $\text{Re}(k_{\text{Fano}}^-)$ associated to the FP resonance (green) and $\text{Re}(k_{\text{Fano}}^+)$ associated to the trapped-mode (blue, almost superimposed to $k_{t=0}$).

The figure 3.16 shows the variations of $k_{t=0}$ and of $k_{|t|=1}^\pm$ against $\check{\varphi}$; to draw the link with the resonances we also report the real parts of the complex poles k_{Fano}^\pm . As said above, for any value of $\check{\varphi}$, we observe the occurrence of a zero-transmission (yellow curve) between two perfect transmissions (red curves) except for $\check{\varphi} = \hat{\varphi} = 0.10$ where the Fano resonance disappears ($k_{t=0} = k_{|t|=1}^-$). Eventually, the proximity of $k_{|t|=1}^\pm$ with the real part of k_{Fano}^- associated with FP resonances is enlightening on the shapes observed in figures 3.13 when increasing the frequency. For small $\check{\varphi}$, the first perfect transmission is associated to the FP resonance while the following zero- and perfect-transmission are associated to the trapped-mode resonance, as in figure 3.13(b). The opposite situation occurs as $k_{|t|=1}^+$ is closer to $\text{real}(k_{\text{Fano}}^-)$ as in figure 3.13(a). Next, the real part of k_{Fano}^+ (dashed blue line) almost coincides with $k_{t=0}$ which strongly suggests that the trapped-mode resonance is responsible for the zero-transmission. They coincide perfectly for two distinct values, as shown in figure 3.17. The first one being the case of regular grating $\check{\varphi} = \hat{\varphi} = 0.10$. The second occurs when the two perfect transmissions change associated resonances as the real parts of the resonances k_{Fano}^\pm are equal. As $\check{\varphi} + \hat{\varphi} \rightarrow 1$, the regular array is recovered, and the difference asymptotically tends to 0.

Eventually, we have also seen from figure 3.13(c) that the pole of the Fano resonance has a real part that nearly coincides with $k_{t=0}$ realizing zero-transmission. The link between geometries realizing zero-transmissions and those supporting trapped modes has been investigated recently [27, 25] and we report here evidences of this link for the π -mode. To do so, we consider the wave amplitudes in the slits and we conduct the same local analysis as we


 Figure 3.17: Difference between $k_{t=0}$ and $\text{Re}(k_{\text{Fano}}^+)$.

have done to get (3.66). For $n = 2i + 1$ an odd integer, we obtain

$$\begin{aligned}\hat{\mathcal{S}} &= -\frac{(-1)^i}{\ell} \frac{k - \hat{k}}{(k - k_{\text{Fano}}^+)(k - k_{\text{Fano}}^-)}, & \hat{\mathcal{A}} &= (-1)^i, \\ \check{\mathcal{S}} &= -\frac{(-1)^i}{\ell} \frac{k - \check{k}}{(k - k_{\text{Fano}}^+)(k - k_{\text{Fano}}^-)}, & \check{\mathcal{A}} &= (-1)^i,\end{aligned}\quad (3.72)$$

where $\hat{k} = \frac{n\pi}{2\ell} - \frac{\hat{\varphi}}{\ell}(\hat{B} - b)\frac{n\pi h}{2\ell}$ and $\check{k} = \frac{n\pi}{2\ell} - \frac{\check{\varphi}}{\ell}(\hat{B} - b)\frac{n\pi h}{2\ell}$. For $n = 2i$ an even integer, the roles of $(\hat{\mathcal{S}}, \check{\mathcal{S}})$ and $(\hat{\mathcal{A}}, \check{\mathcal{A}})$ are reversed. It is worth noticing that for regular gratings, with $\hat{\varphi} = \check{\varphi} = \frac{\varphi}{2}$ and $\hat{B} = \check{B}$, we obtain $\hat{k} = \check{k} = k_{t=0}$ and as in (3.67) we have $k_{\text{Fano}}^+ = k_{t=0}$ and $k_{\text{Fano}}^- = k_{\text{FP}}$. It follows that near the FP resonances, the amplitudes in the identical slits have smooth variations, as we have

$$\hat{\mathcal{S}}_{\text{FP}} = \check{\mathcal{S}}_{\text{FP}} = -\frac{(-1)^i}{(k - k_{\text{FP}})\ell}. \quad (3.73)$$

Coming back to dual-period gratings, we notice from (3.72), with $k_{t=0} = \frac{n\pi - 2\alpha}{2\ell}$ and α in (3.65), that $\hat{\varphi}\hat{k} + \check{\varphi}\check{k} = \varphi k_{t=0}$ hence

$$\hat{\varphi}\hat{\mathcal{S}} + \check{\varphi}\check{\mathcal{S}} = -\frac{(-1)^i\varphi}{\ell} \frac{k - k_{t=0}}{(k - k_{\text{Fano}}^+)(k - k_{\text{Fano}}^-)}. \quad (3.74)$$

It follows that for $k = k_{t=0}$ the π -mode takes place with zero-flux over two nearby slits, $\hat{\varphi}\hat{\mathcal{S}} + \check{\varphi}\check{\mathcal{S}} = 0$. The trajectories of the complex values t and $(\hat{\varphi}\hat{\mathcal{S}}, \check{\varphi}\check{\mathcal{S}}, \hat{\varphi}\hat{\mathcal{A}}, \check{\varphi}\check{\mathcal{A}})$ shown in figure 3.18 are obtained numerically (plain lines) and from the effective model (3.53) and (3.57) (dashed line). The observed features are very similar to that reported in [145] for high-contrast gratings. In particular for the regular grating, the Q -factor of the Fabry-Pérot resonance being small, the effect of the poles merges, hence forming a peanut shape (a detailed analysis on the positions of the poles and the trajectory of t in the complex plane can be found in [145]).

In the vicinity of Fano resonances the trajectories describe circles whose equations are given by (3.66) and (3.72), specifically for n even integers

$$\left|(-1)^n t - \frac{1}{2}\right|^2 = \frac{1}{4}, \quad \left|\hat{\mathcal{S}} - \hat{R}\right|^2 = \hat{R}^2, \quad \hat{R} = \frac{k_{t=0} - \hat{k}}{2\ell \text{Im}(k_{\text{Fano}}^-)\text{Im}(k_{\text{Fano}}^+)}, \quad (3.75)$$

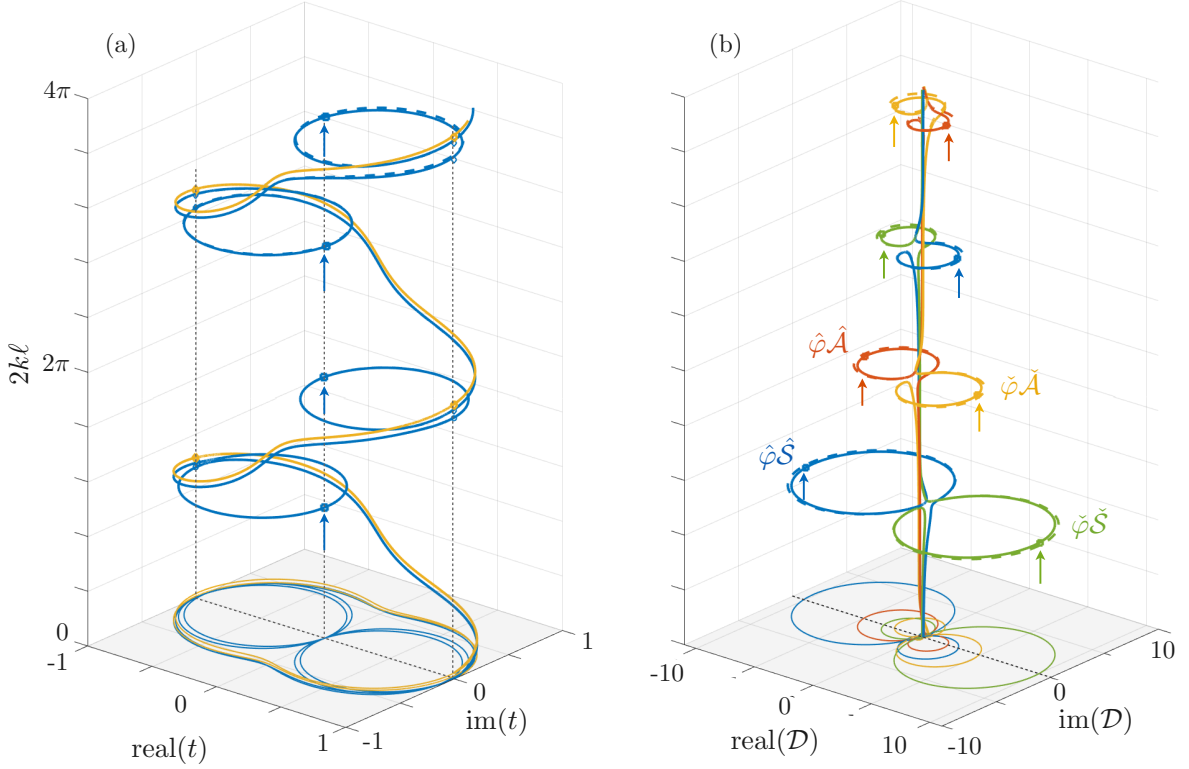


Figure 3.18: Trajectories of $t(k)$ (a) and of $\mathcal{D}(k)$, with $\mathcal{D} = \hat{\varphi}\hat{\mathcal{A}}, \check{\varphi}\check{\mathcal{A}}, \hat{\varphi}\hat{\mathcal{S}}, \check{\varphi}\check{\mathcal{S}}$ (b) through the complex-plane obtained numerically (plain line) and from the effective model (dashed lines). In (a) the yellow curve shows the result for the regular grating, the blue curve for the dual-period grating. In (a) and (b), the vertical arrows show the place, marked with a square symbol, where $t = 0$.

the same for $\check{\mathcal{S}}$ with $\check{\varphi}\check{\mathcal{R}} = \hat{\varphi}\hat{\mathcal{R}}$ (and for n even integers, the roles of $(\hat{\mathcal{A}}, \check{\mathcal{A}})$ and $(\hat{\mathcal{S}}, \check{\mathcal{S}})$ are reversed). Expectedly, as $\text{Im}(k_{\text{Fano}}^-) \simeq \text{Im}(k_{\text{FP}})$ does not depend much on the symmetry breaking, the amplitudes (\hat{R}, \check{R}) within the slits are inversely proportional to the distance $\text{Im}(k_{\text{Fano}}^+)$ of k_{Fano}^+ from the real axis.

In the vicinity of the FP resonances, with $2k\ell - n\pi = O(kh)$, the above expressions simplify to (3.72). Denoting $\xi = 2k\ell - n\pi$, (3.72) can be written

$$\begin{aligned} \hat{\mathcal{S}} &= (-1)^i \frac{\frac{i \cos \theta}{\varphi} (\xi + 2\check{\varphi}(\hat{B} - b) \frac{n\pi h}{2\ell})}{(\xi + 2\alpha) - \frac{i \cos \theta}{2\varphi} (\xi^2 + 2\beta\xi + 4\gamma)}, \\ \check{\mathcal{S}} &= (-1)^i \frac{\frac{i \cos \theta}{\varphi} (\xi + 2\hat{\varphi}(\check{B} - b) \frac{n\pi h}{2\ell})}{(\xi + 2\alpha) - \frac{i \cos \theta}{2\varphi} (\xi^2 + 2\beta\xi + 4\gamma)}, \end{aligned} \quad (3.76)$$

where $\xi = O(kh) \ll 1$ and from (3.65), (α, β, γ) are $O(kh)$ (as $k\ell = O(1)$). It follows that $(\hat{\mathcal{S}}, \check{\mathcal{S}})$ are in general $O(1)$ except if $\xi = -2\alpha$, that is $k = k_{t=0}$ where $(\hat{\mathcal{S}}, \check{\mathcal{S}})$ become $O(\frac{1}{kh}) \gg 1$. At zero-transmissions, we have

$$\hat{\mathcal{S}} = (-1)^i \frac{\alpha - \check{\varphi}(\hat{B} - b) \frac{n\pi h}{2\ell}}{\alpha^2 - \beta\alpha + \gamma}, \quad \check{\mathcal{S}} = (-1)^i \frac{\alpha - \hat{\varphi}(\check{B} - b) \frac{n\pi h}{2\ell}}{\alpha^2 - \beta\alpha + \gamma}, \quad (3.77)$$

hence, from (3.65), we have

$$\hat{\varphi}\hat{\mathcal{S}} + \check{\varphi}\check{\mathcal{S}} = \frac{(-1)^i}{\alpha^2 - \beta\alpha + \gamma} \left(\varphi\alpha - \hat{\varphi}\check{\varphi}(\hat{B} + \check{B} - 2b)\frac{n\pi h}{2\ell} \right) = 0. \quad (3.78)$$

3.8 Guiding Properties

We move our focus to the guided modes lying below the light/sound line. We start with the regular grating. As the dispersion branch approaches the edge of the first Brillouin zone, it admits a horizontal asymptote before decreasing as it enters the second Brillouin zone. As the effective medium does not possess any periodicity, the notion of Brillouin zones becomes irrelevant. The slab act as an homogeneous slab as the dispersion branch appears along the light/sound line at the cut-on frequencies $2k\ell \simeq n\pi$ with n an integer. The n -th dispersion branch of the effective medium tend asymptotically to $2k\ell \simeq n\pi$ as b tends to infinity as no Brillouin zone exists. This means that the effective model becomes more accurate as ℓ increases, which is expected. It has already been shown that a better estimate of the first branch is obtained when taking into account the size effects of the structure [96].

The story for the dual period is different. As mentioned, the symmetry breaking reduces the Brillouin zone by two which the homogeneous slab cannot do. As seen in section 3.2.3, the symmetry breaking opens up a band gap as the branch of dispersion relation is folded in the new irreducible Brillouin zone $(0, \pi/h)$ compared to the regular grating with an irreducible Brillouin zone $(0, 2\pi/h)$. A distinct property of the folded branch is its negative slope, which has been of large interest when designing material exhibiting negative refraction, *e.g.* [64], as it exhibits negative phase velocity. Its cut-on frequency k_c is lies below $2k\ell = n\pi$. As for regular gratings, we expect to recover the first branch of the dispersion relation before the opening of the band gap, and the accuracy depends on ℓ as the branch approaches the Brillouin zone $(0, \pi/h)$. The nature of the equivalent folded branch is on the other hand completely different. The quasi-trapped mode will act as a local resonance and a hybridized dispersion relation appears. This leads a second branch with positive slope, and thus the band gap is also erroneous. The divergence of the model is shown in figure 3.19. To overcome this, one may apply some high frequency homogenization scheme, see for instance [33].

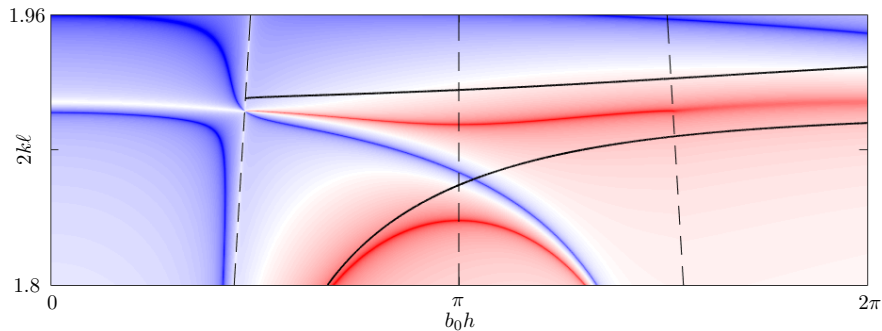


Figure 3.19: Behaviour of the dispersion branch over the first two Brillouin zones $(0, 2\pi)$ by means of the reflection coefficient $\log_{10}|r_{00}|$ against $2k\ell$ ($\hat{\varphi} = 0.4$, $\check{\varphi} = 0.2$, $2\ell = 4h$). Direct numerics (colorscale) are compared to the dispersion of the homogenized model. The first Brillouin zone is delimited by the dashed vertical line at $b_0h = \pi$.

3.9 Concluding remarks and perspectives

The focus of this chapter has been on the coupling of Fano resonances to Fabry-Pérot resonances in gratings with symmetry breaking. We have proposed an effective model relying on asymptotical homogenization. As the propagation is independent in a slit to another, two distinct effective media are obtained in the effective model. An additional treatment is done at each boundary to capture the evanescent field, yielding effective transmission conditions. We have shown that the model accurately reproduces the scattering properties of such a dual-period gratings. In the limiting case of identical slits and rigid parts, we recover the behaviour of a regular grating, for which Fano resonances are prevented by symmetry.

Furthermore, a local analysis of the model around the Fabry-Pérot resonances has allowed for approximate closed form expressions of the two complex resonances poles, shedding further light on their link with the perfect- and zero-transmissions. Besides, we showed that the occurrence of a π - or trapped-mode produces zero-transmissions, which confirms the “negative role of resonant plasmons in the transmission of grating” stressed in [24] (in the present case, resonant SPPs).

We discuss the possible extensions and perspectives:

Extending the model to the case of multiple slits in the unit-cell is straightforward although the resulting model might be cumbersome. The underlying mechanism remains however the same, though associating the resonances becomes more complicated.

Another technical extension is the one to three dimensional wave propagation. The three-dimensional problems offers new symmetries to exploit. Dual-periods of square lattices is a straightforward extension of the two-dimensional problem. Extensions toward other lattices, such as the honeycomb structures seems more interesting and should be rather incremental process. Extending the model to other types of physics is also possible. The three dimensional elastodynamical problem is unambiguous, although more technical. The case of three-dimensional electromagnetism differs, as the boundary conditions changes depending on the polarization. The problem is much more involved, as the case of a single slit is not evident.

We have presented some limitations of the model. The model is accurate for surprisingly high frequencies, and is somewhat expected as no local resonances are involved. However, the model does not capture the folded branch of the guided mode, nor the band gap at the edge of the Brillouin zone. A high frequency approach, as presented in [33], could be a compelling technique to tackle the surface homogenization. Another possibility to overcome this could be by choosing a different scaling. In this chapter, we have considered a subwavelength periodicity, with the asymptotics performed for $kh = \varepsilon \ll 1$, which leads to the horizontal asymptote as b_0h tends to infinity. By considering another asymptotic parameter, for instance the width of the slit compared to the periodicity, *i.e.* $\varphi \ll h$, one could investigate the behaviour beyond the first region of propagating modes. Note that the distance between two slits must also be of the order of the slit width.

Lastly, we discuss the possibility of observing similar behaviour in other types of settings. As mentioned in the introduction, the case of anti symmetric inclusion with local resonances of the Mie type is of great interest [69]. Using similar techniques and adapting the homogenization process present in [125], an effective model of such an array can be obtained. Similarly for the case of minnaert resonance, a dual period setting has been considered in [6] in the linear regime. In the work [126], the focus was on the nonlinear bubble to bubble

interaction in a metascreen in the dilute regime. Inspired by this approach, we can consider the nonlinear bubble to bubble interaction in a dual-periodic setting.

Part II - Space-coiled metamaterials

Chapter 4

Revisiting space-coiled metamaterials

Chapter summary: This chapter is the first in this part dealing with space-coiled or labyrinthine metamaterial. These structures gained a lot of interest ever since their introduction as they allowed for structures of compact design. By elongating the wave path, large phase shifts can be obtained for the transmitted field. Few attempts has been done in deriving effective models, and we revisit the problem by applying a homogenization scheme at the dominant order. We compare the obtained model with some existing results, and show that the homogenized model is more accurate. We discuss the differences and their advantages.

The main results of this chapter are under revision at *Wave Motion* in the following paper [161] Zhou Hagström, Joar and Maurel, Agnès and Pham, Kim. (2022) Revisiting effective acoustic propagation in labyrinthine metasurfaces, *under revision*

Contents

4.1	Introduction	57
4.2	Homogenized models	59
4.2.1	Two-scale Homogenization	59
4.2.2	Two-step model	61
4.2.3	The two models in dimensional form	63
4.3	Comparison of the models	64
4.4	Concluding remarks and perspectives	67

4.1 Introduction

As mentioned in the introductory chapter 1, the acoustic setting in fluid is considerably limited in terms of resonance compared to other types of waves. As seen in part I, this limitation has been overcome by exploiting the low frequency waveguiding in rigid slabs perforated by subwavelength apertures. The use of straight slot has been a successful approach, resulting in perfect transmissions due to resonances of the Fabry-Pérot (FP) type [90, 20]. As this mechanism relies on the halfwavelength resonance of the slits, the thickness is of the order of the wavelegnth. To reduce their size, the idea that the slits can be coiled up without modifying the underlying resonant mechanism was persued.

In 2012, Liang and Li [81] proposed such a metamaterial whose unit cell is an elongated curled waveguide dug in a rectangular rigid material. The acoustical waves are forced to follow the coiling path of the guide resulting in a phase accumulation possibly much larger than the unit cell width. It quickly gained a lot of attention as the main idea is fairly simple. Note that similar structures can be found in other applications, such a bass woofers [68] and meandering structures in the antenna community [144].

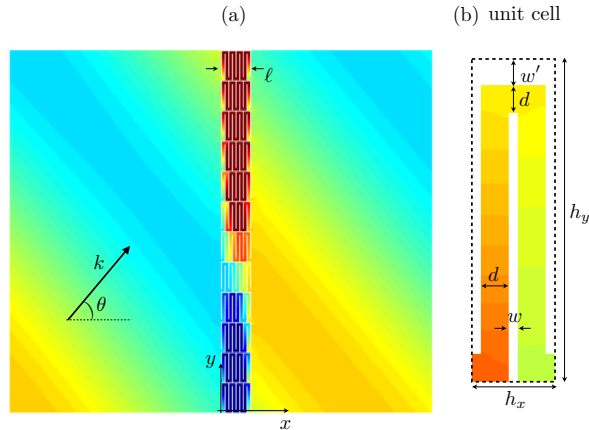


Figure 4.1: Labyrinthine metasurface and its unit cell. The metasurface is infinite along y and of thickness ℓ ($w = w' = 0.03h_y$, $d = 0.012h_y$, $h_x = 0.242h_y$, $\ell = h_y$ with $kh_x = 0.096$ and $\theta = 40^\circ$).

As it enables possibly large phase shift compared to its size, lot of efforts were made in terms of transmittive or reflective metasurfaces [76]. This is illustrated in figure 4.1, where the wave travels in a curled waveguide whose total length in the unit cell is about $2h_y$ much larger than its thickness h_x . As a result, a metasurface made of a periodic arrangement of this unit cell enables unexpected large phase shifts in view of its thickness. This allows to tailor phase shifts within the full $0-2\pi$ range resulting in practical applications including acoustic focusing [78, 110, 130], negative refraction devices [156, 80], one-way transmission and lenses [77, 110, 79] or high absorption [111]. Reviews can be found in [91, 11].

Although the relative simplicity of the structure, few attempts have been done in terms of the effective modelling of space-coiled metasurfaces. The effective parameters are in most cases obtained through retrieval methods which presents several ambiguities [51]. They are typically retrieved from the scattering coefficient obtained from numerical results of the direct scattering problem, simulated for instance at a given angle of incidence. In such a case, the effective parameters are in fact dependent on the angle of incidence. To overcome this, we simply revisit the problem by applying classical homogenization results [16] as done in the previous chapters. From this, we unambiguously obtain the effective parameters for a given geometry.

We take the time to reflect on the classical model encountered in the existing literature. A model, which we refer to as the two-step model, was introduced in [79, 2] and we show that this model corresponds to the homogenization of an array of straight slots, as seen in the chapter 2. The length ℓ_t of the slot is supposed to correspond to the uncoiled labyrinthine path, and is estimated heuristically.

We compare the ability of both the models to reproduce the scattering properties of the actual metasurface with full wave numerical results. We notice that, when the labyrinth can be uncoiled, the two-step model offers a nice physical interpretation of the resonant mechanism which lacks in the homogenized model. However, it is in general less accurate and it relies on the notion of the uncoiled labyrinth length which is already fuzzy for simple geometries and may become very ambiguous for non trivial ones.

4.2 Homogenized models

4.2.1 Two-scale Homogenization

We present below the derivations of the direct homogenized model of the labyrinth and the two-step model involving the homogenization of a straight slot. In the actual problem, the pressure p satisfies the Helmholtz equation in the air along with vanishing normal velocity on the boundaries of the labyrinth walls. Specifically, we consider p solution to

$$\begin{cases} \Delta p + k^2 p = 0, & \text{in the air,} \\ \nabla p \cdot \mathbf{n} = 0, & \text{on the sound hard walls.} \end{cases} \quad (4.1)$$

We start with the model based on a direct, single step, homogenization, as sketched in figure 4.2. We proceed in the same way as in 2, and reproduces them in the following for completeness. Following the two-scale homogenization procedure [16], two systems of coordinates are used, $\mathbf{x} = k\mathbf{x}$ (at the macroscopic scale of the wavelength) and $\boldsymbol{\xi} = \frac{\mathbf{x}}{h_x}$ (at the microscopic scale of the unit cell, figure 4.3(a)). We also introduce the small parameter $\varepsilon = kh_x \ll 1$ which is a measure of the subwavelength regime (hence $\boldsymbol{\xi} = \mathbf{x}/\varepsilon$). For simplicity, we write the governing equation in non-dimensional coordinate in the following way

$$\operatorname{div} \mathbf{u} + p = 0, \quad \mathbf{u} = \nabla p, \quad (4.2)$$

where \mathbf{u} is proportional to the acoustic velocity. Next, we use the expansions

$$\begin{aligned} p &= p^0(\mathbf{x}, \boldsymbol{\xi}) + \varepsilon p^1(\mathbf{x}, \boldsymbol{\xi}) + \dots, \\ \mathbf{u} &= \mathbf{u}^0(\mathbf{x}, \boldsymbol{\xi}) + \varepsilon \mathbf{u}^1(\mathbf{x}, \boldsymbol{\xi}) + \dots, \end{aligned} \quad (4.3)$$

with (p^n, \mathbf{u}^n) , $n = 0, 1, \dots$ are periodic *w.r.t* ξ_x in the unit cell. The above expansions are used in (4.2), with the differential operator of the form $\nabla \rightarrow \nabla_{\mathbf{x}} + \frac{1}{\varepsilon} \nabla_{\boldsymbol{\xi}}$. It follows that (4.2) provides a hierarchy of equations at each order in ε . At the leading order, we have

$$\nabla_{\boldsymbol{\xi}} p^0 = \mathbf{0}, \quad p^0 = P^0(\mathbf{x}), \quad (4.4)$$

which tells us that the pressure is uniform at the microscopic scale, that is within the unit cell \mathcal{Y} (figure 4.3(a)). We then gather the following system set on (\mathbf{u}^0, p^1)

$$\begin{cases} \operatorname{div}_{\boldsymbol{\xi}} \mathbf{u}^0 = 0, & \mathbf{u}^0 = \nabla_{\boldsymbol{\xi}} p^1 + \nabla_{\mathbf{x}} P^0(\mathbf{x}), \\ \mathbf{u}^0 \cdot \mathbf{n} = 0, & \text{on the rigid parts,} \\ p^1, \mathbf{u}^0 & 1\text{-periodic along } \xi_x. \end{cases} \quad (4.5)$$

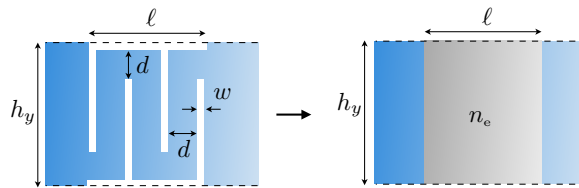


Figure 4.2: Direct homogenization of the labyrinthine structure resulting in an effective slab.

This problem is linear with respect to the components of $\nabla_{\mathbf{x}}P^0$, hence we can set

$$\begin{aligned} p^1(\mathbf{x}, \boldsymbol{\xi}) &= Q(\boldsymbol{\xi}) \frac{\partial P^0}{\partial \mathbf{x}}(\mathbf{x}) - \xi_y \frac{\partial P^0}{\partial \mathbf{y}}(\mathbf{x}) + P^1(\mathbf{x}), \\ \mathbf{u}^0(\mathbf{x}, \boldsymbol{\xi}) &= (\nabla_{\boldsymbol{\xi}} Q(\boldsymbol{\xi}) + \mathbf{e}_x) \frac{\partial P^0}{\partial \mathbf{x}}(\mathbf{x}), \end{aligned} \quad (4.6)$$

with $Q(\boldsymbol{\xi})$ solution to

$$\begin{cases} \Delta Q = 0, & \int_{\mathcal{Y}} Q d\boldsymbol{\xi} = 0 \\ \nabla(Q + \xi_x) \cdot \mathbf{n} = 0, & \text{on the rigid parts,} \\ Q, \nabla(Q + \xi_x) & 1\text{-periodic along } \xi_x, \end{cases} \quad (4.7)$$

(the condition $\int_{\mathcal{Y}} Q d\boldsymbol{\xi} = 0$ defined $P^1(\mathbf{x})$ in (4.6), namely $\int_{\mathcal{Y}} p^1(\mathbf{x}, \boldsymbol{\xi}) d\boldsymbol{\xi} = P^1(\mathbf{x})$). The above problem corresponds to the so called *elementary problem* posed on the periodic unit cell.

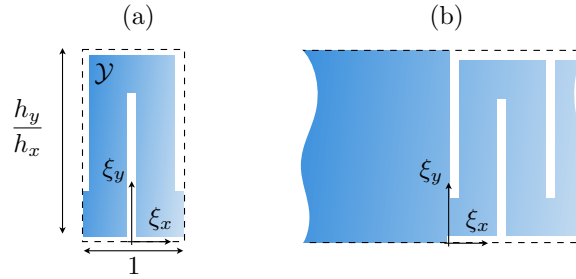


Figure 4.3: (a) Unit cell \mathcal{Y} in which the homogenization far from the boundary is performed. (b) Domain (a strip unbounded along ξ_x) in which the asymptotic analysis at a boundary is performed.

The flow associated to (p^1, \mathbf{u}^0) is incompressible, from which the flux $U_x^0(\mathbf{x})$ through a section of \mathcal{Y} at constant $\xi_x \in (0, 1)$ is conserved, namely

$$U_x^0(\mathbf{x}) = \int_{\xi_x=0} u_x^0(\mathbf{x}, \boldsymbol{\xi}) d\xi_y \left(= \int_{\mathcal{Y}} u_x^0(\mathbf{x}, \boldsymbol{\xi}) d\boldsymbol{\xi} \right). \quad (4.8)$$

We notice that Q is odd with respect to ξ_x hence $\int_{\mathcal{Y}} \frac{\partial Q}{\partial \xi_y} = 0$ (this result is general and would hold in the absence of symmetry of the unit cell). Evaluating the integral over \mathcal{Y} of \mathbf{u}^0 in (4.6), we obtain

$$U_x^0(\mathbf{x}) = c \frac{\partial P^0}{\partial \mathbf{x}}(\mathbf{x}), \quad c = \int \left(\frac{\partial Q}{\partial \xi_x} + 1 \right) d\xi_y. \quad (4.9)$$

Eventually, we use the incompressibility condition at the order 0, $\text{div}_{\boldsymbol{\xi}} \mathbf{u}^1 + \text{div}_{\mathbf{x}} \mathbf{u}^0 + P^0 = 0$ that we integrate over \mathcal{Y} to get

$$\frac{\partial U_x^0}{\partial \mathbf{x}}(\mathbf{x}) + \mathcal{S} P^0(\mathbf{x}) = 0, \quad (4.10)$$

with \mathcal{S} is the normalized surface of air in the unit cell (normalized to h_x^2). Eqs. (4.9) and (4.10) constitute the main result of the present analysis and they will be put in dimensional form in the following.

As we are interested in the transmission problem, we need to derive the transmission conditions at the boundary between the labyrinth and the surrounding fluid. We use the same matched asymptotic technique as in 3. This is done at $x = 0$ (the same applies at $x = \ell$). To do so we have to introduce the pressure and acoustic fields in an intermediate region containing the boundary (figure 4.3(b)). They are written

$$\begin{aligned} p &= q^0(\mathbf{y}, \boldsymbol{\xi}) + \varepsilon q^1(\mathbf{y}, \boldsymbol{\xi}) + \dots, \\ \mathbf{v} &= \mathbf{v}^0(\mathbf{y}, \boldsymbol{\xi}) + \varepsilon \mathbf{v}^1(\mathbf{y}, \boldsymbol{\xi}) + \dots, \end{aligned} \quad (4.11)$$

which do not depend on \mathbf{x} since these fields are defined close to the boundary at the microscopic scale. Accordingly, the differential operator now reads $\nabla \rightarrow \frac{\partial}{\partial \mathbf{y}} \mathbf{e}_y + \frac{1}{\varepsilon} \nabla_{\boldsymbol{\xi}}$. We shall consider the dominant order only for which the matching conditions read

$$\begin{cases} \lim_{\xi_x \rightarrow \pm\infty} q^0(\mathbf{y}, \boldsymbol{\xi}) = p^0(0^\pm, \mathbf{y}), \\ \lim_{\xi_x \rightarrow -\infty} \mathbf{v}^0(\mathbf{y}, \boldsymbol{\xi}) = \mathbf{u}^0(0^-, \mathbf{y}), \\ \lim_{\xi_x \rightarrow +\infty} \mathbf{v}^0(\mathbf{y}, \boldsymbol{\xi}) = \mathbf{u}^0(0^+, \mathbf{y}, \boldsymbol{\xi}). \end{cases} \quad (4.12)$$

Note that \mathbf{v}^0 does not depend on $\boldsymbol{\xi}$ when $\xi_x \rightarrow -\infty$ while it tends to the periodic function $\mathbf{u}^0(0^+, \mathbf{y}, \boldsymbol{\xi})$ (with respect to ξ_x) when $\xi_x \rightarrow +\infty$. At the dominant order, we have $\nabla_{\boldsymbol{\xi}} q^0 = 0$ from which q^0 does not depend on $\boldsymbol{\xi}$. According to (4.12), we thus have

$$p^0(0^+, \mathbf{y}) = p^0(0^-, \mathbf{y}). \quad (4.13)$$

We also have $\operatorname{div}_{\boldsymbol{\xi}} \mathbf{v}^0 = 0$ that we integrate over $\xi_x \in (-\xi_x^*, \xi_x^*)$. Passing to the limit $\xi_x^* \rightarrow \infty$, this provides

$$\frac{h_y}{h_x} u_x^0(0^-, \mathbf{y}) = \int_{\xi_x=0} u_x^0(0^+, \mathbf{y}, \boldsymbol{\xi}) d\xi_y = U_x^0(0^+, \mathbf{y}), \quad (4.14)$$

which constitutes the continuity of the flux.

4.2.2 Two-step model

We now move on on the analysis of the two-step model. Basically, it uses the main ideas developed in [79] and allows us to obtain the expressions of scattering coefficients given in this reference. The procedure follows different steps, sketched in figure 4.4, the main ingredient being to invoke the uncoiled version of the labyrinth (Step 1).

The homogenization of a periodic set of straight slots has been presented in 2, and for the sake of readability, we briefly recal the homogenization result.

We start with (4.2) and (4.3) in a unit cell which is now reduced to a straight duct of length unity and of width d/h_x (figure 4.5(a); note that the periodicity h_x is arbitrary as long as it is chosen $O(h_y)$). As previously, we obtain at the dominant order that $p^0 = P^0(\mathbf{x})$ is constant within a unit cell. Then we have to solve (4.5) but due to the simplicity of the geometry, the boundary condition reads $\mathbf{u}^0 \cdot \mathbf{n} = u_2^0 = 0$ on the rigid part of the duct. As a result, the solution is explicit and reads

$$\begin{aligned} p^1(\mathbf{x}, \boldsymbol{\xi}) &= -\xi_y \frac{\partial P^0}{\partial \mathbf{y}}(\mathbf{x}) + P^1(\mathbf{x}), \\ \mathbf{u}^0(\mathbf{x}) &= \frac{\partial P^0}{\partial \mathbf{x}}(\mathbf{x}) \mathbf{e}_x, \end{aligned} \quad (4.15)$$

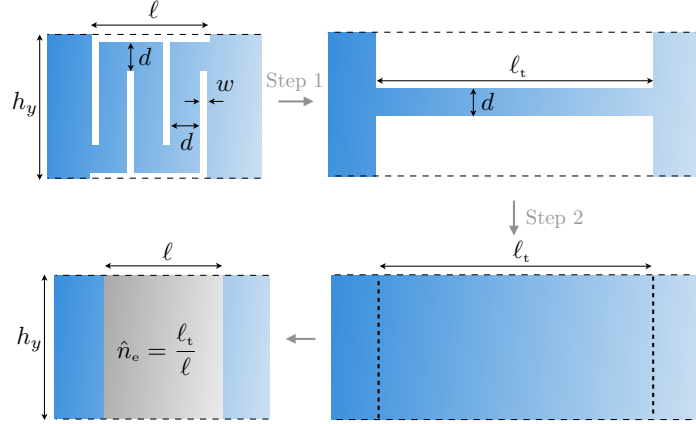


Figure 4.4: Homogenization of a straight slot with effective length ℓ_t corresponding to the model in [79].

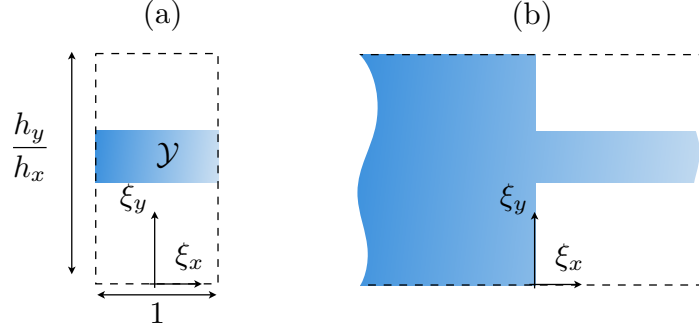


Figure 4.5: Homogenization of a straight slot (two-step model) - same representation as in figure 4.3.

and $\mathbf{u}^0(\mathbf{x})$ is constant within a unit cell (and the function $Q = 0$). Then we still have a constant flux given by

$$U_x^0(\mathbf{x}) = \frac{d}{h_x} u_x^0(\mathbf{x}). \quad (4.16)$$

Eventually, we use the incompressibility condition at the order 0, $\text{div}_\xi \mathbf{u}^1 + \text{div}_x \mathbf{u}^0 + P^0 = 0$, that we integrate over \mathcal{Y} , and we obtain

$$\frac{\partial U_x^0}{\partial x}(\mathbf{x}) + \frac{d}{h_x} P^0(\mathbf{x}) = 0, \quad (4.17)$$

with d/h_x is the normalized surface of air in the unit cell (normalized to h_x^2). Eqs. (4.16) and (4.17) are the equivalent of (4.9) and (4.10).

Repeating the same exercise as for the direct homogenization, the matching conditions (4.12) remain unchanged, but \mathbf{v}^0 now tends to $\mathbf{u}^0(0^+, y)$ which does not depend on ξ when $\xi_x \rightarrow +\infty$ (figure 4.5(b)). As q^0 does not depend on ξ , we still have continuity of the pressure $p^0(0^+, y) = p^0(0^-, y)$. Next, we integrate the incompressibility condition $\text{div}_\xi \mathbf{v}^0 = 0$ over $\xi_x \in (-\xi_x^*, \xi_x^*)$ which provides the continuity of the flux

$$\frac{h_y}{h_x} u_x^0(0^-, y) = U_x^0(0^+, y). \quad (4.18)$$

4.2.3 The two models in dimensional form

For simplicity, we shall use the cell-problem (4.7) in dimensional form that is in the unit cell of dimensions (h_x, h_y) . It reads

$$\begin{cases} \Delta Q = 0, \\ \nabla(Q + x) \cdot \mathbf{n} = 0, & \text{on the rigid parts,} \\ Q, \nabla(Q + x) & h_x - \text{periodic along } x, \end{cases} \quad (4.19)$$

(hence Q in (4.7) $\rightarrow h_x Q$) and we define the length d_e

$$d_e = \int_{x=0} \left(\frac{\partial Q}{\partial x}(\mathbf{x}) + 1 \right) dy. \quad (4.20)$$

Gathering (4.9) and (4.10) in dimensional form, we obtain the equation of propagation in the effective slab and the boundary conditions applying at the interfaces with the surrounding air, specifically the pressure satisfies

$$\begin{cases} \frac{\partial^2 p}{\partial x^2}(\mathbf{x}) + n_e^2 k^2 p(\mathbf{x}) = 0, & x \in (0, \ell), \\ p(0^-, y) = p(0^+, y), & h_y \frac{\partial p}{\partial x}(0^-, y) = d_e \frac{\partial p}{\partial x}(0^+, y), \\ p(\ell^-, y) = p(\ell^+, y), & d_e \frac{\partial p}{\partial x}(\ell^-, y) = h_y \frac{\partial p}{\partial x}(\ell^+, y). \end{cases} \quad (4.21)$$

with n_e the effective refractive index

$$n_e = \sqrt{\frac{\varphi h_y}{d_e}}, \quad (4.22)$$

where φ is the surface of the labyrinthine normalized to the surface of the unit cell (with S the surface of the labyrinth within the unit cell, $S = \varphi h_x h_y$). As a first insight of the accuracy of the homogenized model, we report in figure 4.6 the pressure field from (4.21) (see also the forthcoming explicit solution (4.25)-(4.27)). With the dimensions of the unit cell (see the caption of figure 4.1), we have $\varphi = 0.7526$ and after $Q(\mathbf{x})$ has been solved, $d_e = 0.0121 h_y$ (hence $n_e = 7.89$). As it should be, the scattered pressure field outside the metasurface is accurately reproduced; we also notice that the homogenized solution provides a continuous version of the pressure field within the labyrinth structure.

We do the same for the two-step model, using (4.16) and (4.17) in dimensional form. We obtain an equation of propagation and the boundary conditions applying at the interfaces with the surrounding air

$$\begin{cases} \frac{\partial^2 p}{\partial x^2}(\mathbf{x}) + k^2 p(\mathbf{x}) = 0, & x \in (0, \ell_t), \\ p(0^-, y) = p(0^+, y), & h_y \frac{\partial p}{\partial x}(0^-, y) = d \frac{\partial p}{\partial x}(0^+, y), \\ p(\ell_t^-, y) = p(\ell_t^+, y), & d \frac{\partial p}{\partial x}(\ell_t^-, y) = h_y \frac{\partial p}{\partial x}(\ell_t^+, y). \end{cases} \quad (4.23)$$

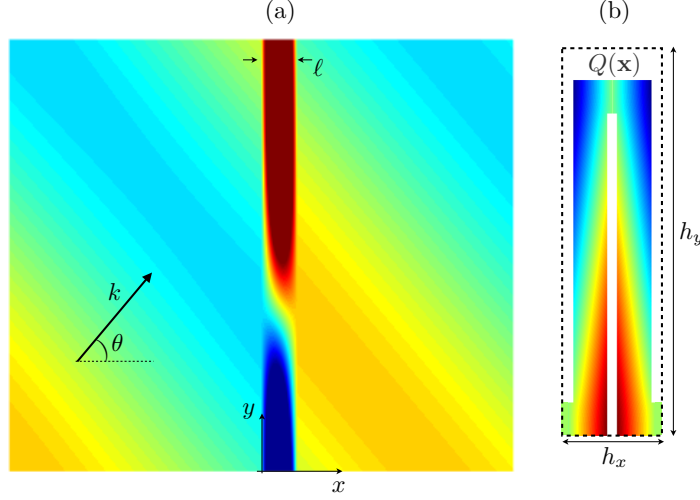


Figure 4.6: (a) Pressure field solution of the direct homogenized problem in the configuration of figure 4.1, from (4.21) (see also (4.25)). (b) Solution $Q(\mathbf{x})$ of the unit cell problem (4.19) entering in d_e (4.20).

The phase accumulation of a plane wave at normal incidence is $k\ell_t$ which can be identified to the phase accumulation in an effective slab of width ℓ by introducing the refractive index

$$\hat{n}_e = \frac{\ell_t}{\ell}, \quad (4.24)$$

which is the last step (not labelled) sketched in figure 4.4. Hence, if a good estimate of ℓ_t can be found, we expect that \hat{n}_e coincides with n_e in (4.22). In particular, if the labyrinth consists of a straight slot, no uncoiling is necessary and $\ell_t = \ell$. Then $Q = 0$ is an exact solution of (4.19), hence $d_e = d$ in (4.20); this implies further that, with $\varphi = d/h_y$, the refractive index is $n_e = 1$ in (4.22). As it should be in this limiting case, the two models coincide.

4.3 Comparison of the models

From now on, we consider the scattering of an incident plane wave at oblique incidence θ on the labyrinthine structure as reported in figures 4.1 and 4.6. As the two effective problems restore translational invariance along y , explicit forms of the solutions can be obtained. In the homogenized model, owing to (4.21), the solution reads

$$p(\mathbf{x}) = e^{i\beta y} \times \begin{cases} (e^{i\alpha x} + r e^{-i\alpha x}), & x \in (-\infty, 0), \\ (a^+ e^{i\alpha_e x} + a^- e^{-i\alpha_e x}), & x \in (0, \ell), \\ t e^{i\alpha(x-\ell)}, & x \in (\ell, +\infty), \end{cases} \quad (4.25)$$

with $\alpha = k \cos \theta$, $\beta = k \sin \theta$ and $\alpha_e = n_e k$. Using further the transmission conditions in (4.21), the impedance mismatch at oblique incidence of the form

$$\xi = \frac{\xi_0}{\cos \theta}, \quad \xi_0 = \sqrt{\frac{\varphi d_e}{h_y}}, \quad (4.26)$$

we get

$$\begin{aligned} t &= \frac{4\xi}{(\xi+1)^2 e^{-i\alpha\ell} - (\xi-1)^2 e^{i\alpha\ell}}, \\ r &= \frac{(\xi^2-1)(e^{i\alpha\ell} - e^{-i\alpha\ell})}{(\xi+1)^2 e^{-i\alpha\ell} - (\xi-1)^2 e^{i\alpha\ell}}, \end{aligned} \quad (4.27)$$

and $a^\pm = \frac{1}{2} \left(1 \pm \frac{1}{\xi}\right) t e^{\mp i\alpha\ell}$. Similarly, using (4.23) the solution of the two-step problem reads

$$p(\mathbf{x}) = e^{i\beta y} \times \begin{cases} (e^{i\alpha x} + \hat{r}e^{-i\alpha x}), & x \in (-\infty, 0), \\ (\hat{a}^+ e^{ikx} + \hat{a}^- e^{-ikx}), & x \in (0, \ell_t), \\ \hat{t}e^{i\alpha(x-\ell)}, & x \in (\ell_t, +\infty), \end{cases} \quad (4.28)$$

along with the transmission conditions in (4.23). The solution is similar to the previous one, with

$$\begin{aligned} \hat{t} &= \frac{4\hat{\xi}}{(\hat{\xi}+1)^2 e^{-ik\ell_t} - (\hat{\xi}-1)^2 e^{ik\ell_t}}, \\ \hat{r} &= \frac{(\hat{\xi}^2-1)(e^{ik\ell_t} - e^{-ik\ell_t})}{(\hat{\xi}+1)^2 e^{-ik\ell_t} - (\hat{\xi}-1)^2 e^{ik\ell_t}}, \end{aligned} \quad (4.29)$$

with

$$\hat{\xi} = \frac{\hat{\xi}_0}{\cos\theta}, \quad \hat{\xi}_0 = \frac{d}{h_y}. \quad (4.30)$$

It is then sufficient to restore the actual thickness of the slab, namely

$$k\ell_t = k\hat{n}_e\ell, \quad (4.31)$$

thanks to (4.24) in order to recover the forms proposed in [79], see eq. (1), and by [2], see eq. (4) given at normal incidence (and $\rho_s = \rho_0$). Note that the homogenization that we have inferred for this two-step model comes from the fact that \hat{n}_e does not enter in $\hat{\xi}$ in this model contrarily to (4.26) which means that the effective medium has a unitary refractive index. To

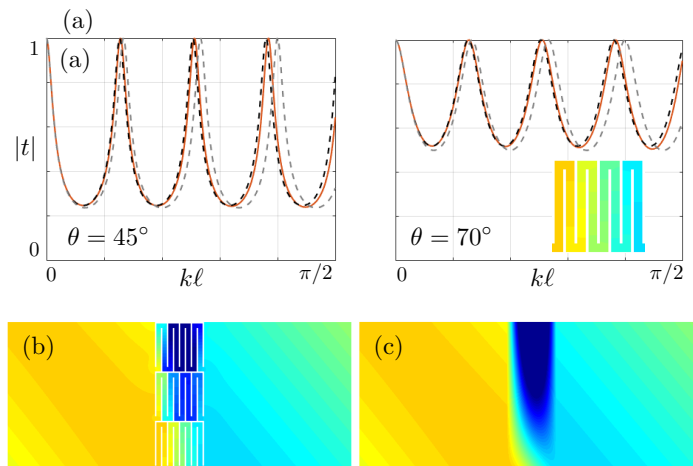


Figure 4.7: Case C1- [79] - (a) $|t|$ against $k\ell$ from numerics (plain line), homogenized model (4.27) (black dashed line) and two-step model (4.29) (grey dashed lines). (b-c) Pressure fields at the first perfect transmission.

begin with, we consider the configurations presented in [79] and [2] since these authors provide valuable informations on the geometry of the unit cell and on the total length of the uncoiled labyrinths, see C1 and C2 in table 4.1 respectively. In [79], the authors use a retrieval method to determine the refractive index $\hat{n}_e = 7.5$. One notices that this value is close though not identical to the prediction of their model. It is in fact determined heuristically $\ell_t = 7.03\ell$, hence \hat{n}_e should be 7.03 from (4.31). Next, $\hat{\xi}_0 = 0.0913$ is simply obtained from (4.30). The prediction of the direct homogenization are as follows: $\varphi = 0.7526$ and $d_e = 0.0121$ (from the resolution of the cell problem), from which $n_e = 7.89$ and $\xi_0 = 0.0954$. We notice the agreement between both (however, we stress that $\hat{n}_e = 7.03$ would produce significant discrepancies). We report in figure 4.7 the transmission against $k\ell \in (0, \pi/2)$. Expectedly, the labyrinthine structure allows for the occurrence of Fabry-Pérot resonances at low frequency that is for $k\ell \ll 1$. Specifically, FPs take place when $\alpha_e \ell / \pi$ in (4.25) is integer, hence for

$$k_{\text{FP}} = N \frac{\pi}{n_e \ell}, \quad N \text{ integer}, \quad (4.32)$$

independently of the incidence θ . The agreement with the two models is good, although the overall accuracy of the direct homogenized prediction is better.

We now move to the labyrinthine structure proposed in [2]. In this reference, the authors consider that the labyrinth can be filled with a fluid of different refractive index than that of the air surrounding the metasurface. Here, we disregard this fact, specifically we use $\xi_0 = \xi_s$ in the expressions of the scattering coefficients, (4) and (5) in [2], and $f = d/h_y$ is our $\hat{\xi}_0$. Doing this, the scattering coefficients have the same form as (4.29) at normal incidence. The authors estimate the total length $\ell_t = 9.9$, hence $\hat{n}_e = 1.65$; next the impedance mismatch $\hat{\xi}_0$ is defined as in (4.30), hence $\hat{\xi}_0 = 0.190$. With $\varphi = 0.346$ and $d_e = 0.1185$ (from the resolution of the cell problem), we obtain $n_e = 1.69$ and $\xi_0 = 0.267$; the agreement is reasonable for the refractive index, significantly different for the impedance mismatch. We show in figure 4.8 the same sequence of results as in figure 4.7; again the two models are comparable in accuracy with a slight improvement in using the direct homogenized result.

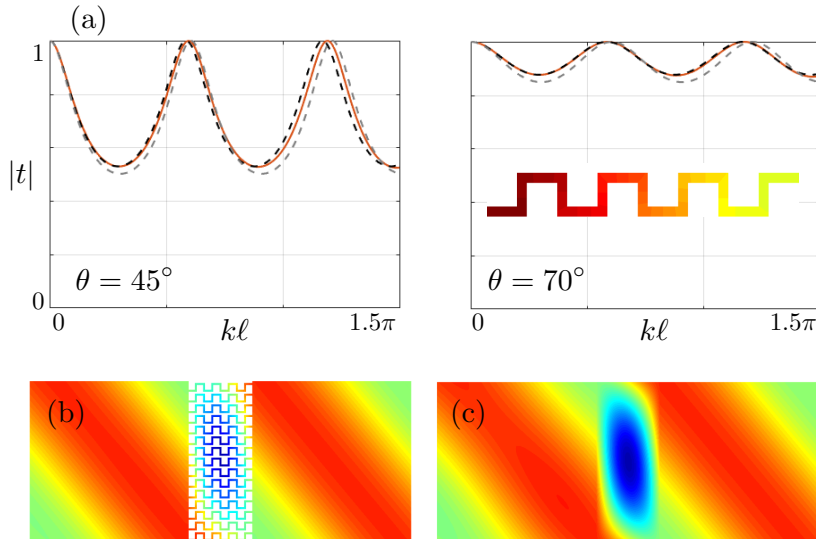


Figure 4.8: Case C2 - [2] - (a) Same representation as in figure 4.7. (b-c) show the fields at the first perfect transmission for $k\ell = 0.6\pi$ ($kh_y = 0.31$).

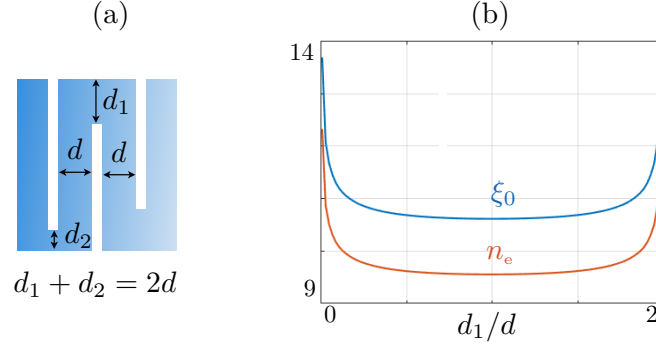


Figure 4.9: (a) labyrinth with dissymmetric turning regions. (b) Resulting effective parameters (n_e, ξ_0) deduced from (4.22) against d_1/d .

The geometry of the two structures discussed above clearly differ, hence their effective properties are intuitively also very different. Very different scattering properties can be obtained from structures whose uncoiled versions would be difficult more delicate to define. This is expected to happen when strong evanescent fields are triggered in the turning regions of the labyrinth.

To inspect this case, we consider the case C3 in table 4.1; we keep the thickness of the vertical channels equal to d and we introduce a dissymmetry in the width of the openings on the top (d_2) and on the bottom (d_1) while keeping $d_1 + d_2 = 2d$ (figure 4.9(a)). Doing so, $\varphi = 0.9$ is kept constant and it should be possible to find a trick to evaluate ℓ_t but not an obvious one. For $d_1/d \in (0.01, 1.99)$ we have solved the cell problems to get d_e which is found to increase with $d_1/d \in (0.01, 1)$. We report in figure 4.9(b) the resulting variations of the effective parameters (n_e, ξ). Expectedly, the strongest variations of the effective parameters take place when d_1/d tends to zeros which fosters strong evanescent fields. The consequence of such evanescent field in the turning regions is illustrated in figure 4.10 where we report the transmission against $k\ell \in (0, 0.2)\pi$ for two structures with $d_1 = d_2 = d$ and with $d_1 = 0.01d$, $d_2 = d - d_1$.

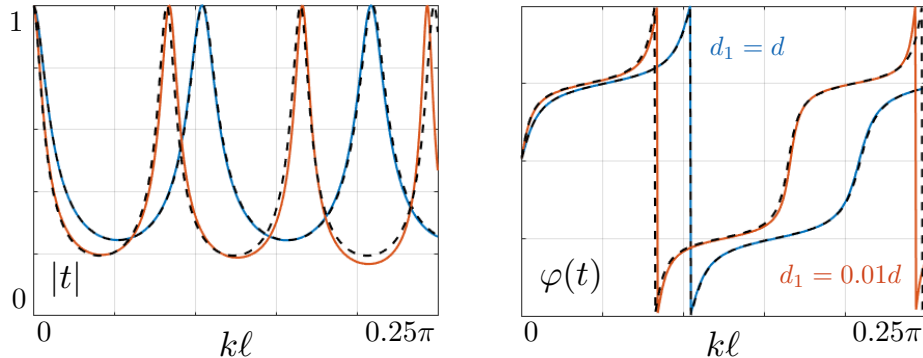


Figure 4.10: Transmission (amplitude and phase) against $k\ell$ for $d_1 = d_2 = d$ and for $d_1 = 0.01d$ (see figure 4.9), numerics (plain lines) and direct homogenized model, (4.27) (dashed black lines).

	C1 [79]	C2 [2]	C3
w	0.03	0.5837	0.01
w'	0.03	0.1750	0.01
h_x	0.2425	1.5475	0.2
ℓ	$4h_x$	6	1.01
d	0.0913	0.19	0.09

Table 4.1: Characteristics of considered labyrinths.

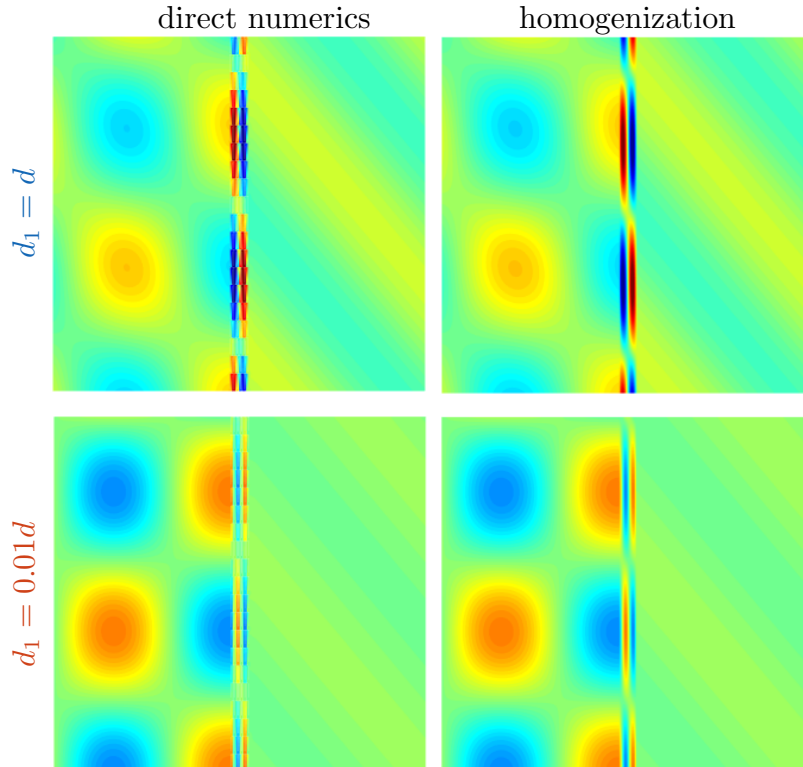


Figure 4.11: Pressure fields of the two labyrinthine structures with symmetrical turning regions ($d_1 = d_2 = d$) and non-symmetrical turning regions ($d_1 = 0.01d$ and $d_2 = 2d - d_1$), direct numerics (left panels) and homogenized solutions (4.25)-(4.27).

It is visible that the scattering properties differ significantly notably by the positions of the FP resonances. This is further illustrated in figure 4.11 where we report a comparison of the pressure fields in the actual problems for $k\ell = 0.2\pi$ close to the second perfect transmission of the symmetric labyrinthine structure, along with their homogenized counterparts.

4.4 Concluding remarks and perspectives

This chapter has been dedicated to the study of so called space-coiled metasurfaces. We have revisited the problem, and obtained through asymptotic homogenization the effective refractive index and impedance mismatch without any ambiguity. The obtained model faithfully reproduces the properties of the actual problem, and is in general more accurate than the so

called two-step model. As shown, the two-step model's major flaw is the heuristical determination of the uncoiled labyrinthine path. We note that the underlying physics is not new, as it relies on Fabry-Pérot resonance of an array of equivalent slots. The two-step model relies on good intuition, and the asymptotic homogenization simply provides a more rigorous result.

We discuss the possible extensions and perspectives:

The use of acoustical space-coiled metasurfaces gained a lot of interest for its application towards wave front manipulation. This can be done by varying the size of the coiling from one unit cell to another, either along the surface of the metasurfaces, or along its thickness, or both. Implementing gradients of dissymmetries from one unit cell to another along the thickness has been considered in [55] to produce horn-like behaviour. Results in the context of focusing and wave steering are presented in [42, 138], with quasi-periodicity along the metasurface. With this in mind, one could apply quasi-periodic homogenization, which has been applied in the case of static solid mechanics in [10, 72], and recent efforts in the dynamical case have been presented in [42, 138]. When variations are only present along the thickness, quasi-periodic homogenization in bulk would result in a smoothly varying effective refractive index. In the case of variations along the interface, the derivation of non-trivial transmission conditions obtained at higher order might be necessary. This has recently been done for the case of thin film in the work [123].

Chapter 5

Modelling of a metacrystal

Chapter summary: This chapter is devoted to the modelling of space-coiled material where the winding arrangement differs from the one presented in the previous chapter, and has got little to no attention in the literature. It consists of slots in the direction as the propagation of the incident wave. The identification of a periodic unit cell is thus not evident, and the classical homogenization approach is not applicable. Indeed, one has to take into account the one dimensional propagation in the straight slots, and the effect at each bend. This results in a crystal like behaviour where the bend act as scatterer. Combined with the subwavelength nature of the periodicity of the slab, we refer to such structures as metacrystals. We derive a model that takes into account the dispersive behaviour of the embedded crystal through a combination of asymptotic homogenization and matched asymptotic techniques. The validation is done in the time domain which allows to illustrate the delay of the transmitted field.

The main results of this chapter has been submitted in the following paper

[160] Zhou Hagström, Joar and Maurel, Agnès and Pham, Kim. (2022) Modeling acoustic space-coiled metacrystals, *submitted to SIAM*

Contents

5.1	Introduction	72
5.2	Main results	73
5.2.1	The actual problem	73
5.2.2	The effective problem	73
5.3	Derivation of the effective model	75
5.3.1	Effective propagation in the straight parts of the coiled slot	76
5.3.2	Solutions in the air far from the material	78
5.3.3	Analysis at the junctions at the entry/exit of the slot	78
5.3.4	Analysis at the junctions	83
5.3.5	Effective problem with curvilinear coordinate and unique formulation	86
5.4	Energetic properties	88
5.4.1	Energy balance of the effective model	88
5.4.2	Derivation of the energy balance	89
5.4.3	Positivity of \mathcal{C}	90
5.4.4	Positivity of \mathcal{B}	90
5.4.5	Positivity of \mathcal{D}	91
5.5	Validation of the effective model in the transient regime	92
5.6	Conclusions	94

5.1 Introduction

In the present chapter, we are interested in a space-coiled structure that differs from the one studied in the previous chapter. Although both configurations can exhibit large phase shift, as shown in figure 5.1, the scattering properties are significantly different. As the long straight parts of the slots are not constrained by the subwavelength periodicity h of the array, identifying a repeating unit cell is not evident. The classical homogenization is therefore directly applicable in this case. One does have to take into account the one dimensional propagation in each straight part of the coiled slot, and the the evanescent field triggered in the turning regions. To model the structure, we apply two-scale homogenization to deal with periodicity combined with asymptotic techniques to take into account the effects of the turning regions. The modelling allows us to shed some insight in the physical phenomenon. As the propagation present in the straight parts, which is anisotropic but homogeneous, can be of the order of the wavelength, it will be scattered by a bend that is periodically spaced. It is in fact the case a one dimensional phononic crystal embedded in a subwavelength array.

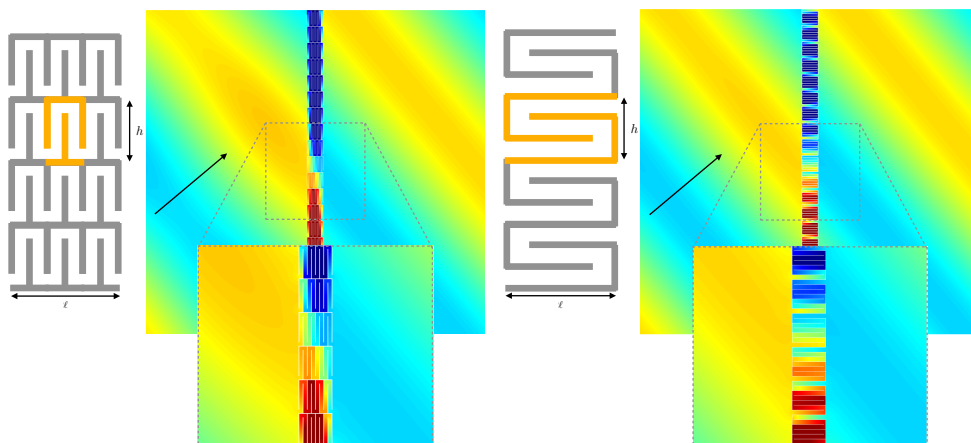


Figure 5.1: (a) Classical space-coiled metasurface presented in chapter 4 (b) Space-coiled metacrystal which is the object of the present study. The orange parts show the unit cell. Both structures can exhibit large phase shifts, here of the order π .

The treatment of the turning region which will be presented later on in the chapter corresponds to the wave propagation at a junction of two semi infinite closed wave guides. Such problems shares a lot of similarity with the studies devoted to wave propagation in graph and lattice like structures, for a review see [71]. It is generally done in the asymptotical setting as the width of the waveguide tends to 0, leading to a graph structures with adequate conditions at the nodes, referred to as Kirchhoff conditions. In quantum mechanics, such systems are associated to the case of Dirichlet boundary conditions, and is complicated as trapped modes often exist at bends and nodes. For the Neumann boundary conditions, which is our case, the existence of trapped modes typically requires some symmetry conditions (see chapter 3). This simplifies the problem as we will derive non-trivial transmission conditions for both the pressure field and the flux. The analysis performed in this chapter shares a lot of similarities with the works performed in [63] and [137]. Their study was on fractal tree systems, with the aim to model wave propagation in the human lung. They derived the transmission conditions for the junction of two, or several thin slots, at a given angle in the

acoustical setting. Our case deals with the case of the junction of two parallel slots with the presence of a turning region, which will need some additional treatment.

We start by presenting the main result of the model. We will perform the derivation in the time domain, which we have favoured to illustrate the time delay of the transmitted field. We can however recover the harmonic formulation, and this will be presented in the next chapter. The derivation in the time domain also allows us to perform an energy analysis, which we discuss in section 5.4. The model is then validated by comparison with direct numerics done in section 5.5.

5.2 Main results

5.2.1 The actual problem

We consider the scattering of acoustic waves by a metacrystal as shown in figure 5.1(b). It is made of a periodic arrangement of identical cells along the vertical, x_2 , direction with subwavelength periodicity h and horizontal thickness ℓ (along x_1). Each cell contains a coiled slot resulting in N horizontal slots connected between them through turning regions. Note that for a transmissive structure, N is odd ($N = 1$ corresponds to a straight, uncoiled, slot and we show the case $N = 3$ in figure 5.1(b)). In the air, the acoustic pressure p and velocity \mathbf{u} satisfy the linearized Euler equations

$$\frac{\partial \mathbf{u}}{\partial t} = -\frac{1}{\rho} \nabla p, \quad \chi \frac{\partial p}{\partial t} + \operatorname{div} \mathbf{u} = 0, \quad \mathbf{u} \cdot \mathbf{n}_{|\Gamma} = 0, \quad (5.1)$$

where (ρ, χ) are the mass density and the compressibility of the air (and t is the time). The above problem is complemented by Neumann boundary conditions on the pressure (vanishing normal velocity) applying on the boundaries of the sound-rigid walls. To simplify the notations, we do not add any specific notation to distinguish the time dependent variables and the harmonic formulation carried out in the previous chapter. All the pressure and velocity fields (p, \mathbf{u}) are time dependent in this chapter.

5.2.2 The effective problem

In the effective model, whose derivation is detailed in the forthcoming §5.3, we distinguish two regions, as sketched in figure 5.2. In the outside region $x_1 \notin (0, \ell)$, the linearized Euler equations still apply, namely

$$\frac{\partial \mathbf{u}}{\partial t} = -\frac{1}{\rho} \nabla p, \quad \chi \frac{\partial p}{\partial t} + \operatorname{div} \mathbf{u} = 0, \quad \text{for } x_1 \notin (0, \ell), \quad (5.2)$$

with p and \mathbf{u} depending of \mathbf{x} and t as in the actual problem.

Next, in the metacrystalline region $x_1 \in (0, \ell)$, we denote (P, U) the acoustic pressure and velocity, respectively. This region is described in terms of a strongly anisotropic effective medium, the spatial variable x_1 being replaced by the curvilinear abscissa s , $s \in (0, L_t)$ with $L_t = N\ell$ the total length of the coiled slot. In each straight part of the slot for $s \in (s_n^+, s_{n+1}^-)$, $n \in \{0, \dots, N-1\}$, (blue segments associated with specific s -orientation in figure 5.2), (P, U) are solutions to the one-dimensional propagation equations

$$\frac{\partial U}{\partial t} = -\frac{\delta}{\rho} \frac{\partial P}{\partial s}, \quad \chi \delta \frac{\partial P}{\partial t} + \frac{\partial U}{\partial s} = 0, \quad \text{for } s \in (s_n^+, s_{n+1}^-), \quad (5.3)$$

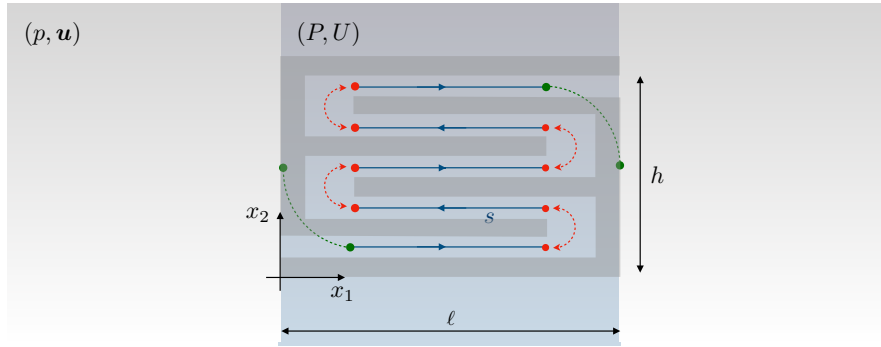


Figure 5.2: The effective problem where the unit cell of the metacrystal has been replaced by a homogenized anisotropic region with one-dimensional propagation. It is set on a curvilinear coordinate s that follows the coiled path (blue lines). Jump conditions account for boundary layer effects in the turning regions (red dotted lines) and at the extremities of the coiled slot connected to the surrounding air (green dotted lines). The actual rigid, pierced, block is shown in light grey to assist in the understanding.

where

$$s_0^+ = 0, \quad s_N^- = N\ell, \quad s_n^\pm = n\ell \pm e, \quad \text{otherwise,} \quad (5.4)$$

with $e = (\eta + \gamma)h$ the width of the turning region (δ , η and γ are geometrical parameters defined in figure 5.3). Note that the fields (P, U) depend on s which allows us to describe the propagation within a single cell but they also depend on x_2 which allows us to describe the field variations from one cell to the others (and they depend on time t). Next, the effect of the turning region connecting two consecutive slots (sketched in red in figure 5.2) is encapsulated in jump conditions of the form

$$\begin{cases} \llbracket P \rrbracket_n = -\rho h \mathcal{D} \frac{\partial \langle U \rangle_n}{\partial t} - h(\delta + \xi) \frac{\partial \langle P \rangle_n}{\partial x_2}, \\ \llbracket U \rrbracket_n = -\chi h(2\delta + \xi) \eta \frac{\partial \langle P \rangle_n}{\partial t} - h(\delta + \xi) \frac{\partial \langle U \rangle_n}{\partial x_2}, \end{cases} \quad (5.5)$$

for $n \in \{1, \dots, N-1\}$ (ξ is a geometrical parameter defined in figure 5.3), and where the jump and the average of the field $F = (P, U)$ are defined by

$$\llbracket F \rrbracket_n = F(s_n^+, x_2, t) - F(s_n^-, x_2, t), \quad \langle F \rangle_n = \frac{1}{2} (F(s_n^+, x_2, t) + F(s_n^-, x_2, t)). \quad (5.6)$$

Eventually at the extremities $s = s_0^+$ and $s = s_N^-$ of the coiled slot, which communicate with the surrounding air at $x_1 = 0$ and $x_1 = \ell$ (these regions are sketched in green in figure 5.2), jump conditions of a different type apply, of the form

$$n \in \{0, N\}, \quad \begin{cases} \llbracket P \rrbracket_n = -\rho h \mathcal{B} \frac{\partial \langle U \rangle_n}{\partial t}, \\ \llbracket U \rrbracket_n = -h \mathcal{C} \frac{\partial W_n}{\partial x_2}, \quad \text{where} \quad \frac{\partial W_n}{\partial t} = -\frac{1}{\rho} \frac{\partial \langle P \rangle_n}{\partial x_2}, \end{cases} \quad (5.7)$$

where we have defined, for $f = (p, u_1)$ and $F = (P, U)$, the jumps

$$\begin{cases} \llbracket F \rrbracket_0 = F(s_0^+, x_2, t) - f(0^-, x_2, t), & \langle F \rangle_0 = \frac{1}{2} (F(s_0^+, x_2, t) + f(0^-, x_2, t)), \\ \llbracket F \rrbracket_N = f(\ell^+, x_2, t) - F(s_N^-, x_2, t), & \langle F \rangle_N = \frac{1}{2} (f(\ell^+, x_2, t) + F(s_N^-, x_2, t)). \end{cases} \quad (5.8)$$

The effective model involves, in addition to geometrical parameters, three effective parameters ($\mathcal{B}, \mathcal{C}, \mathcal{D}$) which are boundary layer coefficients given by elementary static problems that will appear in the asymptotic analysis.

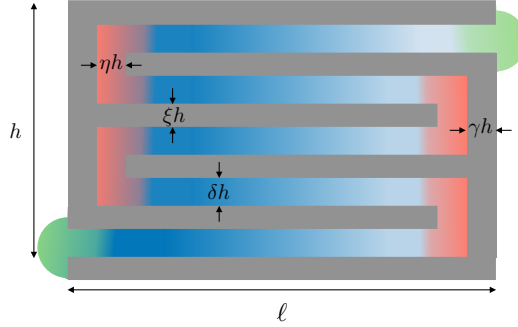


Figure 5.3: Decomposition of the unit cell into sub-regions requiring appropriate asymptotic analysis. In the straight parts of the coiled slot (blue area) the propagation is accounted for; in the turning regions connecting two of these straight slots (red area) and in the regions connecting the extremities of the coiled slot to the surrounding air (green area), matched asymptotic methods are used to capture the effect of the boundary layers.

5.3 Derivation of the effective model

We derive in this section the effective model based on asymptotic analysis valid in the sub-wavelength regime. As we are working in the time domain, the subwavelength regime implicitly assumes that the spectral content of the sources, once they will be defined, is limited by a maximum angular frequency ω satisfying $\varepsilon = \omega h/c \ll 1$, with $c = 1/\sqrt{\rho\chi}$ the speed of sound. We shall use non-dimensional forms of the linearized Euler equations (5.1), with

$$p \rightarrow \chi p, \quad \mathbf{u} \rightarrow \mathbf{u}/c, \quad t \rightarrow \omega t, \quad \mathbf{x} \rightarrow \omega \mathbf{x}/c, \quad (5.9)$$

resulting in

$$\frac{\partial \mathbf{u}}{\partial t} = -\nabla p, \quad \frac{\partial p}{\partial t} + \operatorname{div} \mathbf{u} = 0, \quad \mathbf{u} \cdot \mathbf{n}|_{\Gamma} = 0. \quad (5.10)$$

In the asymptotic procedure, we shall consider sub-regions where appropriate analysis will be achieved. Specifically, as sketched in figure 5.3 (the figure uses the same color code as in figure 5.2), we shall distinguish the straight parts of the coiled slot (blue area) where one-dimensional wave propagation takes place resulting in (5.3), the turning regions connecting two straight slots (red area) and eventually the regions connecting the coiled slot to the surrounding air (green area). These two families of intermediate regions involve evanescent fields whose signatures in the effective model are the jump conditions announced in (5.5) and (5.7).

5.3.1 Effective propagation in the straight parts of the coiled slot

Setting of the asymptotic procedure

In the straight slots far from the turning regions, the medium is structured along x_2 only. It follows the same analysis as the one presented in chapter 3, but for N straight slots. Hence, we assume the following expansions

$$p^\varepsilon = \sum_{i \geq 0} \varepsilon^i p^i(\mathbf{x}, x_2, t), \quad \mathbf{u}^\varepsilon = \sum_{i \geq 0} \varepsilon^i \mathbf{u}^i(\mathbf{x}, x_2, t) \quad \text{with} \quad \mathbf{u}^i = (u^i, v^i), \quad (5.11)$$

where $x_2 = x_2/\varepsilon \in (0, 1)$ is a fast variable describing the vertical position towards the N slots. We denote $Y_{(n)}$ the region of the n -th slot within the unit cell $x_2 \in (0, 1)$, specifically

$$Y_{(n)} = (y_{(n)} - \delta/2, y_{(n)} + \delta/2), \quad y_{(n)} = (n-1)(\delta + \xi) + \delta/2, \quad (5.12)$$

see figure 5.4. For the n -th slot and at any order i , we define the average pressure field $p_{(n)}^i$ and the flow rate $u_{(n)}^i$ as

$$p_{(n)}^i(\mathbf{x}, t) = \frac{1}{\delta} \int_{Y_{(n)}} p^i(\mathbf{x}, x_2, t) dx_2, \quad u_{(n)}^i(\mathbf{x}, t) = \int_{Y_{(n)}} u^i(\mathbf{x}, x_2, t) dx_2, \quad (5.13)$$

which are the effective, macroscopic, fields we are interested in.

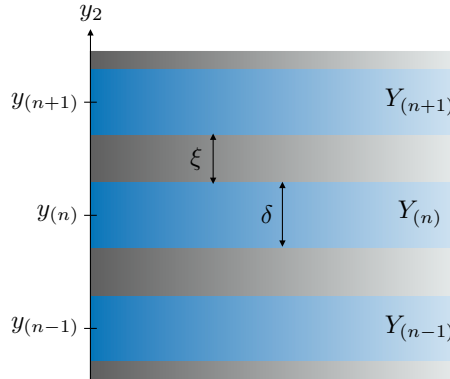


Figure 5.4: The one-dimensional representative cell defined by $x_2 \in (0, 1)$ inside the coiled region far from the extremities. It is made of N fluid segments of thickness δ (blue region) separated by walls of thickness ξ (grey region).

The Neumann condition on the horizontal rigid walls, separating each slot from the other, holds at each order of the expansion and reads

$$v^i(\mathbf{x}, y_{(n)} \pm \delta/2, t) = 0. \quad (5.14)$$

Due to the two-scale expansions in (5.11), the divergence operator and the gradient operator now read

$$\operatorname{div} \mathbf{f} = \operatorname{div}_{\mathbf{x}} \mathbf{f} + \frac{1}{\varepsilon} \frac{\partial \mathbf{f}}{\partial x_2} \cdot \mathbf{e}_2, \quad \nabla f = \nabla_{\mathbf{x}} f + \frac{1}{\varepsilon} \frac{\partial f}{\partial x_2} \mathbf{e}_2, \quad (5.15)$$

for any vectorial function $\mathbf{f}(\mathbf{x}, x_2, t)$ and for any scalar function $f(\mathbf{x}, x_2, t)$. Accordingly, applying the differential operators (5.15) to (5.10) along with (5.11) and identifying the terms with same powers in ε , we obtain

$$\begin{cases} \frac{\partial v^0}{\partial x_2} = 0, & \frac{\partial p^i}{\partial t} + \operatorname{div}_{\mathbf{x}} \mathbf{u}^i + \frac{\partial v^{i+1}}{\partial x_2} = 0 \quad \text{for } i \geq 0, \\ 0 = \frac{\partial p^0}{\partial x_2}, & \frac{\partial \mathbf{u}^i}{\partial t} = -\nabla_{\mathbf{x}} p^i - \frac{\partial p^{i+1}}{\partial x_2} \mathbf{e}_2 \quad \text{for } i \geq 0. \end{cases} \quad (5.16)$$

The zero-th order in the slots

We deduce from the leading order in (5.16) that p^0 and v^0 take constant values in each slot (yet possible different values due to the rigid walls between the slots). Using the definition (5.13) of the average, we get

$$p^0(\mathbf{x}, x_2 \in Y_{(n)}, t) = p_{(n)}^0(\mathbf{x}, t). \quad (5.17)$$

and from the Neumann boundary conditions (5.14), we have

$$v^0(\mathbf{x}, x_2 \in Y_{(n)}, t) = 0. \quad (5.18)$$

At the next order in (5.16), we obtain that $\frac{\partial u^0}{\partial t} = -\frac{\partial p^0}{\partial x_1}$ with p^0 piecewise constant. We deduce using (5.13) that

$$\mathbf{u}^0(\mathbf{x}, x_2 \in Y_{(n)}, t) = \frac{1}{\delta} u_{(n)}^0(\mathbf{x}, t) \mathbf{e}_1. \quad (5.19)$$

Next, integrating the mass balance in (5.16) at order $i = 0$ over $Y_{(n)}$ and using (5.13) as well as Neumann boundary conditions (5.14) to get rid of the contribution of v^1 at the walls, we also obtain

$$\frac{\partial u_{(n)}^0}{\partial t} + \delta \frac{\partial p_{(n)}^0}{\partial x_1} = 0, \quad \frac{\partial u_{(n)}^0}{\partial x_1} + \delta \frac{\partial p_{(n)}^0}{\partial t} = 0, \quad (5.20)$$

which describes the expected one-dimensional propagation in the n -th slot.

The first order in the slots

From the balance of mass given by (5.16) (with $i = 0$) and equations (5.17) and (5.20) derived at the dominant order, we get that $\frac{\partial p^0}{\partial t} + \operatorname{div}_{\mathbf{x}} \mathbf{u}^0 = 0$, hence we have $\partial_{x_2} v^1 = 0$ and v^1 is piecewise constant. By taking into account the Neumann boundary conditions (5.14) at order 1, we deduce that $v^1 = 0$ in all the slots. From the balance of momentum in (5.16) along \mathbf{e}_2 at order 0 and (5.18), we have

$$0 = -\frac{\partial p^1}{\partial x_2} - \frac{\partial p^0}{\partial x_2}, \quad (5.21)$$

which after integration gives

$$p^1 = (y_{(n)} - x_2) \frac{\partial p_{(n)}^0}{\partial x_2} + p_{(n)}^1, \quad (5.22)$$

with $\int_{Y_{(n)}} (y_{(n)} - x_2) dx_2 = 0$. Integrating the mass balance (5.16) for $i = 1$ and using the Neumann boundary conditions (5.14), we get the one-dimensional wave equation at the first order in the n -th slot

$$\frac{\partial u_{(n)}^1}{\partial t} + \delta \frac{\partial p_{(n)}^1}{\partial x_1} = 0, \quad \frac{\partial u_{(n)}^1}{\partial x_1} + \delta \frac{\partial p_{(n)}^1}{\partial t} = 0, \quad (5.23)$$

which is the same as the one obtained at order 0.

5.3.2 Solutions in the air far from the material

Since the surrounding air for $x_1 \notin (0, \ell)$ is a homogeneous medium, the asymptotic expansion is straightforward and does not involve two scales expansion. Specifically, we have

$$p^\varepsilon = \sum_{i \geq 0} \varepsilon^i p^i(\mathbf{x}, t), \quad \mathbf{u}^\varepsilon = \sum_{i \geq 0} \varepsilon^i \mathbf{u}^i(\mathbf{x}, t), \quad (5.24)$$

which after injection in (5.10) results at each order in

$$\forall i \geq 0, \quad \frac{\partial p^i}{\partial t} + \operatorname{div}_{\mathbf{x}} \mathbf{u}^i = 0, \quad \frac{\partial \mathbf{u}^i}{\partial t} = -\nabla_{\mathbf{x}} p^i. \quad (5.25)$$

5.3.3 Analysis at the junctions at the entry/exit of the slot

We shall now derive the effective jump conditions applying between the extremities of the coiled slot and the surrounding air. The analysis is presented at the extremity $x_1 = 0$ as the jump conditions at $x_1 = \ell$ can be deduced by mirroring the analysis.

Setting of the asymptotic procedure

It consists in matching the *outer* expansions (5.11) and (5.24) through an intermediate inner region governed by boundary layer effect. To do that, we introduce the representative unit cell \mathcal{Y} , obtained by rescaling spatially the extremity of the slot near $x_1 = 0$ owing to the variable $\mathbf{y} = \mathbf{x}/\varepsilon$, see figure 5.5. This cell is the union $\mathcal{Y} = \mathcal{Y}^+ \cup \mathcal{Y}^-$ of the semi-infinite

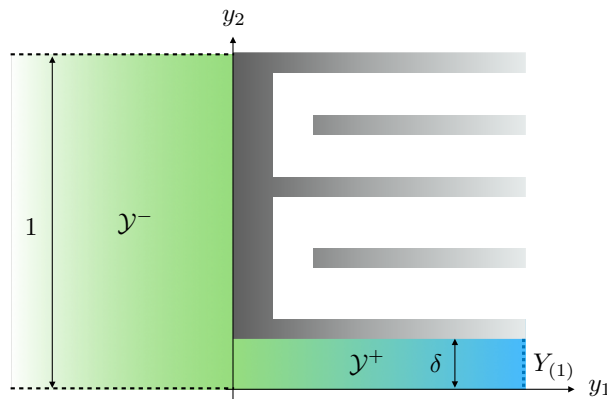


Figure 5.5: The representative unit cell $\mathcal{Y} = \mathcal{Y}^+ \cup \mathcal{Y}^-$ near one extremity of the slot at $x_1 = 0$ connects the surrounding air (green region) to the interior of the slot (blue region).

region \mathcal{Y}^- in the surrounding fluid and of the semi-infinite region \mathcal{Y}^+ in the first straight slot, specifically

$$\mathcal{Y}^- = (-\infty, 0) \times (0, 1), \quad \mathcal{Y}^+ = (0, \infty) \times Y_{(1)}. \quad (5.26)$$

In this inner region, we use the following expansion of the fields

$$p^\varepsilon = \sum_{i \geq 0} \varepsilon^i p^i(x_2, \mathbf{y}, t), \quad \mathbf{u}^\varepsilon = \sum_{i \geq 0} \varepsilon^i \mathbf{u}^i(x_2, \mathbf{y}, t), \quad \mathbf{u} = (u, v), \quad (5.27)$$

where $(\mathbf{p}^i, \mathbf{u}^i)$ are assumed to be periodic with respect to y_2 in \mathcal{Y}^- and $\mathbf{u}^i \cdot \mathbf{n} = 0$ on the boundaries of the rigid walls, denoted Γ . As in the previous section, the divergence operator and the gradient operator are affected by the two-scale expansion, which in this case read

$$\operatorname{div} \mathbf{f} = \frac{\partial \mathbf{f}}{\partial x_2} \cdot \mathbf{e}_2 + \frac{1}{\varepsilon} \operatorname{div}_y \mathbf{f}, \quad \nabla f = \frac{\partial f}{\partial x_2} \cdot \mathbf{e}_2 + \frac{1}{\varepsilon} \nabla_y f, \quad (5.28)$$

for any vectorial function $\mathbf{f}(x_2, \mathbf{y})$ and for any scalar function $f(x_2, \mathbf{y})$. Injecting the expansions (5.27) in (5.10), we get at the leading orders

$$\begin{cases} \operatorname{div}_y \mathbf{u}^0 = 0, & \operatorname{div}_y \mathbf{u}^1 + \partial_{x_2} v^0 + \frac{\partial p^0}{\partial t} = 0, \\ 0 = \nabla_y p^0, & \frac{\partial \mathbf{u}^0}{\partial t} = -\frac{\partial p^0}{\partial x_2} \mathbf{e}_2 - \nabla_y p^1, \\ \mathbf{u}^0 \cdot \mathbf{n}_{|\Gamma} = \mathbf{u}^1 \cdot \mathbf{n}_{|\Gamma} = 0. \end{cases} \quad (5.29)$$

The matching conditions are obtained by pairing the outer expansions (5.11) and (5.24) valid far from the entry at $y_1 = 0$ with the inner expansions (5.27) valid in the vicinity of the entry. For the pressure expansions in (5.24) and (5.27), the matching reads

$$p^0(x_2, \mathbf{y}, t) + \varepsilon p^1(x_2, \mathbf{y}, t) + \dots \sim p^0(\mathbf{x}, t) + \varepsilon p^1(\mathbf{x}, t) + \dots, \quad (5.30)$$

as $x_1 \rightarrow -\infty$ and $x_1 \rightarrow 0^-$. By recalling that $x_1 = \varepsilon x_1$ and by using a Taylor expansion of the outer expansion with respect to ε , we get at the dominant order and at the first order in the fluid

$$p^0(0^-, x_2, t) = \lim_{x_1 \rightarrow -\infty} p^0(x_2, \mathbf{y}, t), \quad (5.31)$$

$$p^1(0^-, x_2, t) = \lim_{x_1 \rightarrow -\infty} \left(p^1(x_2, \mathbf{y}, t) - x_1 \frac{\partial p^0}{\partial x_1}(0^-, x_2, t) \right). \quad (5.32)$$

Doing the same for the expansions in (5.11) and (5.27) results in

$$p^0(x_2, \mathbf{y}, t) + \varepsilon p^1(x_2, \mathbf{y}, t) + \dots \sim p^0(\mathbf{x}, x_2, t) + \varepsilon p^1(\mathbf{x}, x_2, t) + \dots, \quad (5.33)$$

as $x_1 \rightarrow +\infty$ (with $x_2 \in Y_{(1)}$) and $x_1 \rightarrow 0^+$, hence for $x_2 \in Y_{(1)}$, we get

$$p^0(0^+, x_2, x_2, t) = \lim_{x_1 \rightarrow +\infty} p^0(x_2, \mathbf{y}, t), \quad (5.34)$$

$$p^1(0^+, x_2, x_2, t) = \lim_{x_1 \rightarrow +\infty} \left(p^1(x_2, \mathbf{y}, t) - x_1 \frac{\partial p^0}{\partial x_1}(0^+, x_2, x_2, t) \right). \quad (5.35)$$

The exact same matching conditions as (5.31) and (5.34) are obtained for the velocity field by replacing formally \mathbf{p} by \mathbf{u} and p by \mathbf{u} .

The continuity conditions at dominant order

From (5.29), we deduce that p^0 is independent of \mathbf{y} and we obtain from the matching conditions (5.31) and (5.34) that

$$p_{(1)}^0(0^+, x_2, t) = p^0(x_2, \mathbf{y}, t) = p^0(0^-, x_2, t), \quad (5.36)$$

since $p^0 = p_{(1)}^0$ for $x_2 \in Y_{(1)}$ from (5.17). Next, by integrating the free divergence equation in (5.29) set on \mathbf{u}^0 over the subset domain $\mathcal{Y}^* \subset \mathcal{Y}$, truncated at $x_1 = \pm y_1^*$ with $y_1^* \gg 1$, and using the Neumann boundary conditions on the rigid walls and the periodic boundary condition in $\mathcal{Y}^* \cap \mathcal{Y}^-$, we obtain

$$\int_{Y_{(1)}} \mathbf{u}^0(x_2, y_1^*, x_2, t) dx_2 - \int_Y \mathbf{u}^0(x_2, -y_1^*, x_2, t) dx_2 = 0. \quad (5.37)$$

Passing to the limit as $y_1^* \rightarrow +\infty$ and using the matching conditions (5.31) and (5.34) written on the velocity, we obtain

$$u_{(1)}^0(0^+, x_2, t) = u^0(0^-, x_2, t). \quad (5.38)$$

Therefore, there is no boundary layer correction at the dominant order, meaning that the usual continuity conditions on pressure and flow rate apply. Conducting the same analysis at the extremity $x_1 = \ell$ of the slot, we get the same continuity conditions, namely

$$p_{(N)}^0(\ell^-, x_2, t) = p^0(\ell^+, x_2, t), \quad u_{(N)}^0(\ell^-, x_2, t) = u^0(\ell^+, x_2, t). \quad (5.39)$$

The jump conditions at first order

Jump condition on the pressure From (5.29), the problem set on \mathcal{Y} for the couple $(\mathbf{p}^1, \mathbf{u}^0)$ is given by

$$\begin{cases} \frac{\partial \mathbf{u}^0}{\partial t} = -\frac{\partial p^0}{\partial x_2} \Big|_{0^-} \mathbf{e}_2 - \nabla_y \mathbf{p}^1, & \operatorname{div}_y \mathbf{u}^0 = 0, \quad \mathbf{u}^0 \cdot \mathbf{n}_{|\Gamma} = 0, \\ \lim_{x_1 \rightarrow -\infty} \frac{\partial \mathbf{u}^0}{\partial t} = \frac{\partial u^0}{\partial t} \Big|_{0^-} \mathbf{e}_1 - \frac{\partial p^0}{\partial x_2} \Big|_{0^-} \mathbf{e}_2, \\ \lim_{x_1 \rightarrow +\infty} \frac{\partial \mathbf{u}^0}{\partial t} = \frac{1}{\delta} \frac{\partial u^0}{\partial t} \Big|_{0^-} \mathbf{e}_1, \end{cases} \quad (5.40)$$

with $\frac{\partial p^0}{\partial x_2} \Big|_{0^-} = \frac{\partial p^0}{\partial x_2}(0^-, x_2, t)$ and $\frac{\partial u^0}{\partial t} \Big|_{0^-} = \frac{\partial u^0}{\partial t}(0^-, x_2, t)$. In (5.40), we have used the continuities of the pressure and of the flow rate given by (5.36) and (5.38), along with (5.17) (for $n = 1$). By linearity, the solution of (5.40) can be decomposed as a linear combination of the macroscopic fields $\frac{\partial p^0}{\partial x_2} \Big|_{0^-}$ and $\frac{\partial u^0}{\partial t} \Big|_{0^-}$ which do not depend on \mathbf{y} . Specifically, we have

$$\mathbf{p}^1(x_2, \mathbf{y}, t) = \frac{\partial p^0}{\partial x_2} \Big|_{0^-} Q_2(\mathbf{y}) - \frac{\partial u^0}{\partial t} \Big|_{0^-} Q_1(\mathbf{y}) + Q_*(x_2, t), \quad (5.41)$$

where the functions (Q_1, Q_2) satisfy the so-called elementary problems given by ($i = 1, 2$)

$$i \in \{1, 2\}, \quad \begin{cases} \operatorname{div}_y(\nabla_y Q_i + \delta_{i2} \mathbf{e}_2) = 0 \text{ in } \mathcal{Y}, & (\nabla_y Q_i + \delta_{i2} \mathbf{e}_2) \cdot \mathbf{n}_{|\Gamma} = 0, \\ (Q_i, \nabla Q_i) \text{ } x_2 \text{-periodic for } x_1 < 0, \\ \lim_{x_1 \rightarrow -\infty} \nabla_y Q_i = \delta_{i1} \mathbf{e}_1, \\ \lim_{x_1 \rightarrow +\infty} \nabla_y Q_i = \delta_{i1} \mathbf{e}_1 / \delta - \delta_{i2} \mathbf{e}_2, \end{cases} \quad (5.42)$$

with $\delta_{ij} = 0$ if $i \neq j$ and $\delta_{ij} = 1$ otherwise. The behavior of (Q_1, Q_2) at infinity reads

	$\lim_{x_1 \rightarrow -\infty}$	$\lim_{x_1 \rightarrow +\infty}$
Q_1	x_1	$\frac{x_1}{\delta} + \mathcal{B}$
Q_2	0	$y_{(1)} - x_2$

(5.43)

with $y_{(1)} = \delta/2$ from (5.12) and where \mathcal{B} is a boundary layer corrector. We have used that Q_2 is odd with respect to $x_2 = \delta/2$ in the slot, hence its behavior at infinity when $x_1 \rightarrow +\infty$. From the matching condition (5.31) with the exterior together with (5.25), we get

$$p^1(0^-, x_2, t) = \lim_{x_1 \rightarrow -\infty} \left(p^1(\mathbf{y}, x_2, t) + x_1 \frac{\partial u^0}{\partial t} \Big|_{0^-} \right) = Q_*(x_2, t). \quad (5.44)$$

From the matching condition (5.34) with the first slot together with (5.20) and (5.38) which gives $\frac{\partial u^0}{\partial t} \Big|_{0^-} = \frac{\partial u_{(1)}^0}{\partial t} \Big|_{0^+} = -\delta \frac{\partial p^0}{\partial x_1} \Big|_{0^+}$, we get

$$\begin{aligned} p^1(0^+, x_2, x_2 \in Y_{(1)}, t) &= \lim_{x_1 \rightarrow +\infty} \left(p^1(\mathbf{y}, x_2, t) + \frac{x_1}{\delta} \frac{\partial u^0}{\partial t} \Big|_{0^-} \right) \\ &= -\mathcal{B} \frac{\partial u^0}{\partial t} \Big|_{0^-} + \frac{\partial p^0}{\partial x_2} \Big|_{0^-} (y_{(1)} - x_2) + Q_*(x_2, t). \end{aligned} \quad (5.45)$$

Using (5.22) (since $p^0|_{0^-} = p_{(1)}^0|_{0^+}$), we deduce

$$p_{(1)}^1(0^+, x_2, t) = -\mathcal{B} \frac{\partial u^0}{\partial t} \Big|_{0^-} + Q_*. \quad (5.46)$$

Finally, subtracting (5.44) to (5.46) we get the jump conditions on the pressure field

$$p_{(1)}^1(0^+, x_2, t) - p^1(0^-, x_2, t) = -\mathcal{B} \frac{\partial u^0}{\partial t} \Big|_{0^-}. \quad (5.47)$$

By conducting the same analysis at the other extremity $x_1 = \ell$ of the slot, we obtain

$$p^1(\ell^+, x_2, t) - p_{(N)}^1(\ell^-, x_2, t) = -\mathcal{B} \frac{\partial u^0}{\partial t} \Big|_{\ell^+}. \quad (5.48)$$

Jump condition on the flow rate We start from the divergence relation on \mathbf{u}^1 in (5.29) that we integrate over the truncated domain \mathcal{Y}^* after taking the time derivative, specifically we get

$$\int_{\mathcal{Y}^*} \left(\operatorname{div}_y \frac{\partial \mathbf{u}^1}{\partial t} + \frac{\partial^2 v^0}{\partial t \partial x_2} + \frac{\partial^2 \mathbf{p}^0}{\partial t^2} \right) d\mathbf{y} = 0. \quad (5.49)$$

We evaluate separately the three contributions in the integral in (5.49). First, since \mathbf{p}^0 is constant in \mathcal{Y} , see (5.36), we have

$$\int_{\mathcal{Y}^*} \frac{\partial^2 \mathbf{p}^0}{\partial t^2} d\mathbf{y} = (1 + \delta) y_1^* \frac{\partial^2 p^0}{\partial t^2} \Big|_{0^-}. \quad (5.50)$$

Next, using the divergence theorem and the matching conditions (5.31)-(5.34) written for the velocity as well as the definitions (5.13) of the flow rate, we have the asymptotic estimate

$$\int_{\mathcal{Y}^*} \operatorname{div}_y \frac{\partial \mathbf{u}^1}{\partial t} d\mathbf{y} = \frac{\partial u_{(1)}^1}{\partial t} \Big|_{0^+} - \frac{\partial u^1}{\partial t} \Big|_{0^-} + y_1^* \frac{\partial^2 u_{(1)}^0}{\partial t \partial x_1} \Big|_{0^+} + y_1^* \frac{\partial^2 u^0}{\partial t \partial x_1} \Big|_{0^-} + o(1) \quad (5.51)$$

where $o(1)$ are vanishing terms as $y_1^* \rightarrow +\infty$. Adding the two contributions (5.50) and (5.51) and using mass balance equations (5.20) and (5.25), we get

$$\int_{\mathcal{Y}^*} \left(\operatorname{div}_y \frac{\partial \mathbf{u}^1}{\partial t} + \frac{\partial^2 \mathbf{p}^0}{\partial t^2} \right) d\mathbf{y} = \frac{\partial u_{(1)}^1}{\partial t} \Big|_{0^+} - \frac{\partial u^1}{\partial t} \Big|_{0^-} - y_1^* \frac{\partial^2 v^0}{\partial t \partial x_2} \Big|_{0^-} + o(1). \quad (5.52)$$

The remaining term of the integral (5.49) can be expressed using (5.40) as

$$\int_{\mathcal{Y}^*} \frac{\partial^2 v^0}{\partial t \partial x_2} d\mathbf{y} = -(1 + \delta) y_1^* \frac{\partial^2 p^0}{\partial x_2^2} \Big|_{0^-} - \int_{\mathcal{Y}^*} \frac{\partial^2 \mathbf{p}^1}{\partial x_2 \partial x_2} d\mathbf{y}. \quad (5.53)$$

The last integral can be made explicit using (5.41) to get

$$\begin{aligned} \int_{\mathcal{Y}^*} \frac{\partial^2 \mathbf{p}^1}{\partial x_2 \partial x_2} d\mathbf{y} &= \frac{\partial^2 p^0}{\partial x_2^2} \Big|_{0^-} \left(\int_{\mathcal{Y}^* \cap \mathcal{Y}^-} \frac{\partial Q_2}{\partial x_2} d\mathbf{y} + \int_{\mathcal{Y}^* \cap \mathcal{Y}^+} \left(\frac{\partial Q_2}{\partial x_2} + 1 \right) d\mathbf{y} - \delta y_1^* \right) \\ &\quad - \frac{\partial^2 u^0}{\partial t \partial x_2} \Big|_{0^-} \int_{\mathcal{Y}^*} \frac{\partial Q_1}{\partial x_2} d\mathbf{y} + o(1). \end{aligned} \quad (5.54)$$

Note that due to periodicity conditions in \mathcal{Y}^- , we have $\int_{\mathcal{Y}^* \cap \mathcal{Y}^-} \frac{\partial Q_i}{\partial x_2} d\mathbf{y} = 0$ for $i = 1, 2$. One can also remark that the loading being in the direction \mathbf{e}_1 for Q_1 , the solution is symmetric with respect to $x_2 = \delta/2$ in the slot and hence we have $\int_{\mathcal{Y}^* \cap \mathcal{Y}^+} \frac{\partial Q_1}{\partial x_2} d\mathbf{y} = 0$. Finally, introducing the boundary layer corrector

$$\mathcal{C} = \int_{\mathcal{Y}^+} \left(\frac{\partial Q_2}{\partial x_2} + 1 \right) d\mathbf{y}, \quad (5.55)$$

and adding (5.52) to (5.53) with the use of (5.54), we get

$$\frac{\partial}{\partial t} (u_{(v)}^1(0^+, x_2, t) - u^1(0^-, x_2, t)) = \mathcal{C} \frac{\partial^2 p^0}{\partial x_2^2}(0^-, x_2, t). \quad (5.56)$$

To get rid of the time derivative, we introduce the auxiliary velocity field $W_0(x_2, t)$ defined as

$$\frac{\partial W_0}{\partial t}(x_2, t) = -\frac{\partial p^0}{\partial x_2}(0^-, x_2, t), \quad (5.57)$$

which allows us to express the jump condition on the normal velocity at first order as

$$u_{(v)}^1(0^+, x_2, t) - u^1(0^-, x_2, t) = -\mathcal{C} \frac{\partial W_0}{\partial x_2}. \quad (5.58)$$

By conducting the same analysis at the exit of the crystalline region, we get

$$u(\ell^+, x_2, t) - u_{(N)}^1(\ell^-, x_2, t) = -\mathcal{C} \frac{\partial W_N}{\partial x_2}, \quad (5.59)$$

with the auxiliary velocity field $W_N(x_2, t)$ defined as

$$\frac{\partial W_N}{\partial t}(x_2, t) = -\frac{\partial p^0}{\partial x_2}(\ell^+, x_2, t) \quad (5.60)$$

5.3.4 Analysis at the junctions

We shall now derive the effective jump conditions applying between two consecutive slots at a turning region. We notice that a similar analysis has been conducted in [63, 37]. For the sake of conciseness, we shall consider a turning region close to $x_1 = 0$, that is to say between the n -th and the $(n + 1)$ -th slot with n even. The conditions for the turning region on the opposite side near $x_1 = \ell$ can be deduced by mirroring the analysis. We also notice that the analysis is very similar but not identical to that developed in the preceding section; to avoid multiple references to this previous analysis, we simply repeat below the exercise.

Setting of the asymptotic procedure

We define the representative cell \mathcal{Y}_c of the turning region (see figure 5.6), using the rescaled space variable $\mathbf{y} = \mathbf{x}/\varepsilon$, as the semi-infinite region

$$\mathcal{Y}_c = (\gamma, \gamma + \eta) \times (y_{(n)} - \delta/2, y_{(n+1)} + \delta/2) \cup (\gamma + \eta, +\infty) \times (Y_{(n)} \cup Y_{(n+1)}), \quad (5.61)$$

with $y_{(n)}$ and $Y_{(n)}$ defined by (5.12).

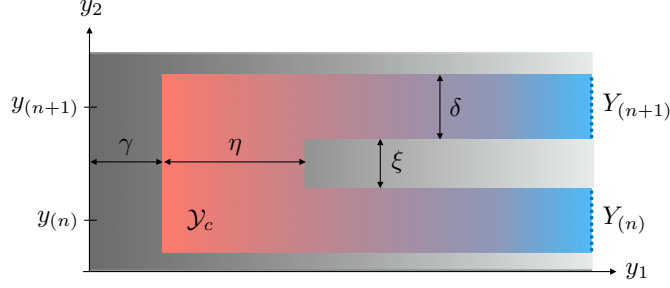


Figure 5.6: The representative cell \mathcal{Y}_c at a turn connecting two consecutive slots (red region).

In this region, we use the following asymptotic expansions

$$p^\varepsilon = \sum_{i \geq 0} \varepsilon^i \mathbf{p}_c^i(x_2, \mathbf{y}, t), \quad \mathbf{u}^\varepsilon = \sum_{i \geq 0} \varepsilon^i \mathbf{u}_c^i(x_2, \mathbf{y}, t). \quad (5.62)$$

Injecting (5.62) in the governing equations (5.10), we get at the leading orders

$$\begin{cases} \operatorname{div}_y \mathbf{u}_c^0 = 0, & \operatorname{div}_y \mathbf{u}_c^1 + \partial_{x_2} v_c^0 + \frac{\partial \mathbf{p}_c^0}{\partial t} = 0, \\ 0 = \nabla_y p_c^0, & \frac{\partial \mathbf{u}_c^0}{\partial t} = -\frac{\partial \mathbf{p}_c^0}{\partial x_2} \mathbf{e}_2 - \nabla_y p_c^1. \\ \mathbf{u}_c^0 \cdot \mathbf{n}_{|\Gamma_c} = \mathbf{u}_c^1 \cdot \mathbf{n}_{|\Gamma_c} = 0, \end{cases} \quad (5.63)$$

where Γ_c denotes the part of the boundary \mathcal{Y}_c associated to the rigid walls. The matching conditions between the inner expansions and the outer expansions (5.11) far in the slots can be derived using the same procedure as in the preceding §5.3.3. For the pressure, they read

$$\begin{aligned} p^0(0^+, \boldsymbol{\alpha}_i) &= \lim_{x_1 \rightarrow +\infty} p_c^0(x_1, \boldsymbol{\alpha}_i), \\ p^1(0^+, \boldsymbol{\alpha}_i) &= \lim_{x_1 \rightarrow +\infty} \left(p_c^1(x_1, \boldsymbol{\alpha}_i) - x_1 \frac{\partial p^0}{\partial x_1}(0^+, \boldsymbol{\alpha}_i) \right), \end{aligned} \quad (5.64)$$

with the notation $\boldsymbol{\alpha}_i = (x_2 \in Y_{(i)}, x_2, t)$ for $i = \{n, n+1\}$. The same matching conditions on the velocity are obtained by replacing formally p by \mathbf{u} and \mathbf{p}_c by \mathbf{u}_c in (5.64).

The continuity conditions at dominant order

At the dominant order, we get from (5.63) that p_c^0 is independent of \mathbf{y} , hence we obtain from the matching condition (5.64) together with the result (5.17) set in the bulk that

$$p_{(n+1)}^0(0^+, x_2, t) = p_c^0(x_2, \mathbf{y}, t) = p_{(n)}^0(0^+, x_2, t), \quad (5.65)$$

which translates in the continuity of the pressure between two consecutive slots. Next, by integrating the divergence free equation in (5.63) over the subset domain $\mathcal{Y}_c^* \subset \mathcal{Y}$, truncated at $x_1 = \pm y_1^*$ with $y_1^* \gg 1$, and eliminating the boundary terms associated to the Neumann boundary conditions on the rigid walls, we obtain

$$\int_{Y_{(n)}} \mathbf{u}_c^0(x_2, x_1^*, x_2, t) x_2 + \int_{Y_{(n+1)}} \mathbf{u}_c^0(x_2, x_1^*, x_2, t) dx_2 = 0. \quad (5.66)$$

Passing to the limit when $y_1^* \rightarrow +\infty$ and using the matching condition (5.64) (written for the velocity) together with the definitions of the flow rate (5.13) in the bulk, we obtain a jump condition on the flow rate

$$u_{(n+1)}^0(0^+, x_2, t) + u_{(n)}^0(0^+, x_2, t) = 0. \quad (5.67)$$

At the dominant order, we recover the continuity conditions on the pressure and on the flowrate.

The jump conditions at the first order

Jump condition on the pressure From (5.63), the problem set for the couple (p_c^1, \mathbf{u}_c^0) is given by

$$\begin{cases} \frac{\partial \mathbf{u}_c^0}{\partial t} = -\frac{\partial p_{(n)}^0}{\partial x_2} \Big|_{0^+} \mathbf{e}_2 - \nabla_y p_c^1, & \operatorname{div}_y \mathbf{u}_c^0 = \mathbf{0}, & \mathbf{u}_c^0 \cdot \mathbf{n}_{|\Gamma_c} = 0, \\ \lim_{x_1 \rightarrow +\infty} \frac{\partial \mathbf{u}_c^0}{\partial t}(x_1, x_2 \in Y_{(n)}, x_2, t) = \frac{1}{\delta} \frac{\partial u_{(n)}^0}{\partial t} \Big|_{0^+} \mathbf{e}_1, \\ \lim_{x_1 \rightarrow +\infty} \frac{\partial \mathbf{u}_c^0}{\partial t}(x_1, x_2 \in Y_{(n+1)}, x_2, t) = -\frac{1}{\delta} \frac{\partial u_{(n)}^0}{\partial t} \Big|_{0^+} \mathbf{e}_1. \end{cases} \quad (5.68)$$

The above formulation has been obtained using i) (5.67) used to express the limit when $x_1 \rightarrow +\infty$ in terms of $\frac{\partial u_{(n)}^0}{\partial t} \Big|_{0^+}$ only, ii) that the vertical velocity v^0 is zero in the slots from (5.18), iii) the continuity of the pressure in (5.65) which shows that $\frac{\partial p_c^0}{\partial x_2} = \frac{\partial p_{(n)}^0}{\partial x_2} \Big|_{0^+}$. The solution of (5.68) can now be expressed as a linear combination of the two macroscopic fields $\frac{\partial p_{(n)}^0}{\partial x_2} \Big|_{0^+}$ and $\frac{\partial u_{(n)}^0}{\partial t} \Big|_{0^+}$ (which are independent of \mathbf{y}), namely we use

$$p_c^1(x_2, \mathbf{y}, t) = \frac{\partial p_{(n)}^0}{\partial x_2} \Big|_{0^+} (y_{(n)} - x_2) - \frac{\partial u_{(n)}^0}{\partial t} \Big|_{0^+} Q^{(n)}(\mathbf{y}) + Q_*^{(n)}(x_2, t), \quad (5.69)$$

with $Q^{(n)}(\mathbf{y})$ being solutions to the elementary problems

$$\begin{cases} \Delta_y Q^{(n)} = 0 & \text{in } \mathcal{Y}_c, & \nabla_y Q^{(n)} \cdot \mathbf{n}_{|\Gamma_c} = 0, \\ \lim_{x_1 \rightarrow +\infty} \nabla_y Q^{(n)}(x_1, x_2 \in Y_{(n)}) = \frac{\mathbf{e}_1}{\delta}, \\ \lim_{x_1 \rightarrow +\infty} \nabla_y Q^{(n)}(x_1, x_2 \in Y_{(n+1)}) = -\frac{\mathbf{e}_1}{\delta}. \end{cases} \quad (5.70)$$

The asymptotic behavior of $Q^{(n)}$ at infinity is given by

	$\lim_{x_2 \in Y_{(n)}, x_1 \rightarrow +\infty}$	$\lim_{x_2 \in Y_{(n+1)}, x_1 \rightarrow +\infty}$	
$Q^{(n)}$	$\frac{x_1}{\delta}$	$-\frac{x_1}{\delta} - \mathcal{D}^*$	(5.71)

Note that the problem (5.70) corresponds to a classical potential flow problem in fluid mechanics, with a fluid flowing in a curved portion of channel; in this context, the parameter \mathcal{D}^* is called the *blockage* coefficient. We can now express jump conditions at the first order. For that, we pass to the limit in (5.69) with the help of the asymptotic behavior (5.71), and then make use of the matching conditions (5.64) together with the form (5.22) of the pressure p^1 in the slots. This leads to

$$\begin{cases} p_{(n+1)}^1(0^+, x_2, t) = (y_{(n)} - y_{(n+1)}) \frac{\partial p_{(n)}^0}{\partial x_2} \Big|_{0^+} - \mathcal{D}^* \frac{\partial u_{(n+1)}^0}{\partial t} \Big|_{0^+} + Q_*^{(n)}(x_2, t), \\ p_{(n)}^1(0^+, x_2, t) = Q_*^{(n)}(x_2, t). \end{cases} \quad (5.72)$$

Noticing that $y_{(n+1)} - y_{(n)} = \delta + \xi$, we deduce the jump condition on the pressure at the junction between each slot

$$p_{(n+1)}^1(0^+, x_2, t) - p_{(n)}^1(0^+, x_2, t) = -\mathcal{D}^* \frac{\partial u_{(n+1)}^0}{\partial t} \Big|_{0^+} - (\delta + \xi) \frac{\partial p_{(n)}^0}{\partial x_2} \Big|_{0^+}. \quad (5.73)$$

Jump condition on the velocity We start from the divergence relation on \mathbf{u}^1 in (5.63) that we integrate over the truncated domain \mathcal{Y}_c^* after taking the time derivative. This reads

$$\int_{\mathcal{Y}_c^*} \left(\operatorname{div}_y \frac{\partial \mathbf{u}_c^1}{\partial t} + \frac{\partial^2 v_c^0}{\partial t \partial x_2} + \frac{\partial^2 p_c^0}{\partial t^2} \right) d\mathbf{y} = 0. \quad (5.74)$$

We evaluate below the three contributions in the integral in (5.74). First, since p_c^0 is constant in \mathcal{Y}_c , see (5.65), we have

$$\int_{\mathcal{Y}_c^*} \frac{\partial^2 p_c^0}{\partial t^2} d\mathbf{y} = (2\delta(y_1^* - \gamma) + \xi\eta) \frac{\partial^2 p_{(n)}^0}{\partial t^2} \Big|_{0^+}. \quad (5.75)$$

Next, using the divergence theorem and the matching conditions (5.64) written for the velocity, we have the asymptotic estimate

$$\int_{\mathcal{Y}_c^*} \operatorname{div}_y \frac{\partial \mathbf{u}_c^1}{\partial t} d\mathbf{y} = \frac{\partial u_{(n+1)}^1}{\partial t} \Big|_{0^+} + \frac{\partial u_{(n)}^1}{\partial t} \Big|_{0^+} + y_1^* \frac{\partial^2 u_{(n+1)}^0}{\partial t \partial x_1} \Big|_{0^+} + y_1^* \frac{\partial^2 u_{(n)}^0}{\partial t \partial x_1} \Big|_{0^+} + o(1), \quad (5.76)$$

where $o(1)$ are vanishing terms as $y_1^* \rightarrow +\infty$. Adding the two contributions (5.75) and (5.76) and using mass balance equations (5.20), we get

$$\int_{\mathcal{Y}_c^*} \left(\operatorname{div}_y \frac{\partial \mathbf{u}_c^1}{\partial t} + \frac{\partial^2 p_c^0}{\partial t^2} \right) d\mathbf{y} = \frac{\partial u_{(n+1)}^1}{\partial t} \Big|_{0^+} + \frac{\partial u_{(n)}^1}{\partial t} \Big|_{0^+} + (\xi\eta - 2\delta\gamma) \frac{\partial^2 p_{(n)}^0}{\partial t^2} \Big|_{0^+} + o(1). \quad (5.77)$$

The remaining term of the integral (5.74) can be further simplified using (5.68), namely

$$\int_{\mathcal{Y}_c^*} \frac{\partial^2 v_c^0}{\partial t \partial x_2} d\mathbf{y} = \frac{\partial^2 u_{(n)}^0}{\partial t \partial x_2} \Big|_{0^+} \int_{\mathcal{Y}_c^*} \frac{\partial Q^{(n)}}{\partial x_2} d\mathbf{y} \quad (5.78)$$

with the integral on the right-hand side being explicit. Indeed, integrating by part of (5.70) after a multiplication by x_2 gives

$$0 = \int_{\mathcal{Y}_c} x_2 \Delta_y Q^{(n)} d\mathbf{y} = \int_{\partial \mathcal{Y}_c} x_2 \nabla_y Q^{(n)} \cdot \mathbf{n} d\mathbf{y} - \int_{\mathcal{Y}_c} \frac{\partial Q^{(n)}}{\partial x_2} d\mathbf{y}. \quad (5.79)$$

Eliminating the zero contribution in the boundary integral, on the rigid walls due to the Neumann boundary condition, it leaves only the contribution when $x_1 \rightarrow +\infty$

$$\int_{\partial\mathcal{Y}_c} x_2 \nabla_y Q^{(n)} \cdot \mathbf{n} \, d\mathbf{y} = \frac{1}{\delta} \int_{Y^{(n)}} x_2 \, dx_2 - \frac{1}{\delta} \int_{Y^{(n+1)}} x_2 \, dx_2 = -(\delta + \xi) \quad (5.80)$$

from which we deduce

$$\int_{\mathcal{Y}_c} \frac{\partial Q^{(n)}}{\partial x_2} \, d\mathbf{y} = -(\delta + \xi). \quad (5.81)$$

Finally, adding (5.77) and (5.78), we find the jump condition at order 1 on the normal velocity

$$u_{(n+1)}^1(0^+, x_2, t) + u_{(n)}^1(0^+, x_2, t) = -(\xi\eta - 2\delta\gamma) \frac{\partial p_{(n)}^0}{\partial t} \Big|_{0^+} + (\delta + \xi) \frac{\partial u_{(n)}^0}{\partial x_2} \Big|_{0^+}. \quad (5.82)$$

5.3.5 Effective problem with curvilinear coordinate and unique formulation

The curvilinear description

The effective problem derived from the asymptotic analysis in the slots can be rewritten *a posteriori* in a more intuitive form. It consists in using the curvilinear coordinate s that runs along the coiled slot. Specifically, s is defined over $(0, N\ell)$ with the mapping from the global frame, made of the N slots, to the curvilinear frame, made of a single path, given by

$$\begin{cases} (n, x_1) \mapsto s = (n - \frac{1}{2})\ell + (-1)^n (\frac{\ell}{2} - x_1), \\ \{1, \dots, N\} \times (0, \ell) \mapsto (0, N\ell). \end{cases} \quad (5.83)$$

Expressing the one-dimensional wave equation (5.20) and (5.23) in terms of s gives

$$i \in \{0, 1\}, \quad s \in (0, N\ell), \quad \frac{\partial U^i}{\partial t} + \delta \frac{\partial P^i}{\partial s} = 0, \quad \frac{\partial U^i}{\partial s} + \delta \frac{\partial P^i}{\partial t} = 0, \quad (5.84)$$

where (P^i, U^i) are the pressure and flow rate variables set in the new frame and defined as

$$(P^i(s, x_2), U^i(s, x_2)) = (p_{(n)}^i(x_1, x_2), (-1)^n u_{(n)}^i(x_1, x_2)). \quad (5.85)$$

The jump conditions (5.65) and (5.67) at order 0, (5.73) and (5.82) at order 1, now apply at $s = n\ell$ with $n \in \{1, \dots, N-1\}$ and read

$$\begin{cases} \llbracket P^0 \rrbracket = \llbracket U^0 \rrbracket = 0, \\ \llbracket P^1 \rrbracket = -\mathcal{D}^* \frac{\partial U^0}{\partial t} \Big|_{n\ell} - (\delta + \xi) \frac{\partial P^0}{\partial x_2} \Big|_{n\ell}, \\ \llbracket U^1 \rrbracket = -(\xi\eta - 2\delta\gamma) \frac{\partial P^0}{\partial t} \Big|_{n\ell} - (\delta + \xi) \frac{\partial U^0}{\partial x_2} \Big|_{n\ell}. \end{cases} \quad (5.86)$$

At the entrance and the exit, at $s = 0$ and $s = N\ell$, the continuity conditions at order 0 with the exterior now read

$$\begin{cases} P^0|_{s=0^+} - p^0|_{x_1=0^-} = p^0|_{x_1=\ell^+} - P^0|_{s=(N\ell)^-} = 0, \\ U^0|_{s=0^+} - u^0|_{x_1=0^-} = U^0|_{x_1=\ell^+} - u^0|_{s=(N\ell)^-} = 0, \end{cases} \quad (5.87)$$

while the jump conditions at order 1 are given by

$$\begin{cases} P^1|_{s=0^+} - p^1|_{x_1=0^-} = -\mathcal{B} \frac{\partial u^0}{\partial t} \Big|_{x_1=0^-}, & U^1|_{s=0^+} - u^1|_{x_1=0^-} = -\mathcal{C} \frac{\partial W_0}{\partial x_2}, \\ P^1|_{x_1=\ell^+} - P^1|_{s=(N\ell)^-} = -\mathcal{B} \frac{\partial u^0}{\partial t} \Big|_{x_1=\ell^+}, & u^1|_{x_1=\ell^+} - U^1|_{s=(N\ell)^-} = -\mathcal{C} \frac{\partial W_N}{\partial x_2}, \end{cases} \quad (5.88)$$

with (W_0, W_N) still given by (5.57) and (5.60).

The unique formulation

The last step in the construction of the effective model is to gather the contributions $(p^0, P^0, \mathbf{u}^0, U^0)$ at order 0 and $(p^1, P^1, \mathbf{u}^1, U^1)$ at order 1 into a unique problem. Inside the equivalent metacrystalline region, we introduce the pressure and flow rate fields (in the curvilinear frame)

$$P = P^0 + \varepsilon P^1 \quad \text{and} \quad U = U^0 + \varepsilon U^1, \quad (5.89)$$

while in the surrounding air we introduce

$$p = p^0 + \varepsilon p^1 \quad \text{and} \quad \mathbf{u} = \mathbf{u}^0 + \varepsilon \mathbf{u}^1. \quad (5.90)$$

Using (5.84) and (5.25), it is straightforward to deduce the final effective wave equations (5.2)-(5.3) after using the dimensionalization procedure (5.9). The derivation of the unique formulation of the jump conditions is more involved as it requires the introduction of mean quantities. At the entry of the metacrystalline region, in virtue of the continuity of the flow rate (5.87) at order 0 combined with (5.89)-(5.90), we have

$$\frac{\partial u^0}{\partial t} \Big|_{x_1=0^-} = \frac{1}{2} \left(\frac{\partial u}{\partial t} \Big|_{x_1=0^-} + \frac{\partial U}{\partial t} \Big|_{s=0^+} \right) + O(\varepsilon). \quad (5.91)$$

Now, summing the contributions (5.87) at order 0 and (5.88) at order 1 on the pressure together with (5.91), we finally get the jump condition on the pressure (5.7) at the entry (up to the second order in ε). Next the continuity equation on the pressure (5.87) implies that (5.57) gives

$$\frac{\partial W_0}{\partial t} = -\frac{1}{2} \left(\frac{\partial p}{\partial x_2} \Big|_{x_1=0^-} + \frac{\partial P}{\partial x_2} \Big|_{s=0^+} \right) + O(\varepsilon), \quad (5.92)$$

which allows to deduce from (5.87) and (5.88) the jump condition on the flow rate (5.7) at the entry (up to the second order in ε). The same exact procedure can be applied to get the final jump conditions at the exit of the metacrystalline region.

Getting the final jump conditions at each junction is more involved because it needs to introduce the enlargement of the interface due to the finite size of the turning region (at order 1). This is done in order to ensure stability of the model which requires that a positive definite energy can be defined; exemples can be found in [38, 95] and the positivity will be proven in the forthcoming section 5.4. To do this, we aim to express the jump conditions, when going from the slot n to the slot $(n+1)$, in terms of s values $s = n\ell - e$ and $s = n\ell + e$ (with $e = (\eta + \gamma)\varepsilon$). By doing a Taylor expansion as $\varepsilon \ll 1$ of the continuity conditions (5.86) on the pressure field and using (5.84), it can be shown that

$$P^0|_{s=n\ell+e} - P^0|_{s=n\ell-e} = -\varepsilon \frac{2}{\delta} (\eta + \gamma) \frac{\partial \langle U \rangle}{\partial t} + O(\varepsilon^2), \quad (5.93)$$

with the mean operation defined as

$$\langle f \rangle = \frac{1}{2} (f|_{s=nl+e} + f|_{s=nl-e}). \quad (5.94)$$

Similarly at the next order, by doing a Taylor expansion on the first order jump condition (5.86) on the pressure, we have

$$P^1|_{s=nl+e} - P^1|_{s=nl-e} = -\mathcal{D}^* \frac{\partial \langle U \rangle}{\partial t} - (\delta + \xi) \frac{\partial \langle P \rangle}{\partial x_2} + O(\varepsilon). \quad (5.95)$$

Now multiplying (5.95) by ε and adding the contribution (5.93), we obtain the desired jump conditions (5.5) at the junction on the pressure field (valid up to the second order in ε) with

$$\mathcal{D} = \mathcal{D}^* + \frac{2(\eta + \gamma)}{\delta}. \quad (5.96)$$

The unique formulation of the jump condition on the flow rate at the junction is obtained similarly. We first enlarged the continuity condition (5.86) with a Taylor expansion to get

$$U^0|_{s=nl+e} - U^0|_{s=nl-e} = -2\delta(\eta + \gamma)\varepsilon \frac{\partial \langle P \rangle}{\partial t} + O(\varepsilon^2), \quad (5.97)$$

with $\langle P \rangle$ defined by (5.94). We proceed similarly with the jump condition at the first order to get

$$U^1|_{s=nl+e} - U^1|_{s=nl-e} = -(\xi\eta - 2\delta\gamma) \frac{\partial \langle P \rangle}{\partial t} - (\delta + \xi) \frac{\partial \langle U \rangle}{\partial x_2} + O(\varepsilon). \quad (5.98)$$

Now multiplying (5.98) by ε and adding the contribution (5.97), we obtain the desired jump conditions (5.5) (valid up to the second order in ε).

5.4 Energetic properties

5.4.1 Energy balance of the effective model

We consider a rectangular domain $\Omega = (-L_1, L_1) \times (-L_2, L_2)$ with $L_1 > \ell$ so that Ω contains the crystalline region. In the direct problem given by (5.1), the classical energy balance equation is given by

$$\frac{d\mathcal{E}_b}{dt} + \int_{\partial\Omega} \boldsymbol{\pi} \cdot \mathbf{n} \, d\mathbf{x} = 0, \quad \text{with} \quad \mathcal{E}_b = \frac{1}{2} \int_{\Omega} (\chi p^2 + \rho |\mathbf{u}|^2) \, d\mathbf{x}, \quad (5.99)$$

where \mathcal{E}_b is the acoustic bulk energy and $\boldsymbol{\pi} = p\mathbf{u}$ the Poynting vector that accounts for the flux energy throughout the boundary $\partial\Omega$. A similar energy balance can be obtained for the effective model (5.2)-(5.8). Specifically, it involves four contributions to the energy and reads

$$\frac{d}{dt} [\mathcal{E}_b^{\text{air}} + \mathcal{E}_b^{\text{slot}} + \mathcal{E}_s^{\text{in/out}} + \mathcal{E}_s^{\text{turn}}] + \int_{\partial\Omega} \boldsymbol{\pi} \cdot \mathbf{n} \, d\mathbf{x} = 0. \quad (5.100)$$

The bulk energy $\mathcal{E}_b^{\text{air}}$ is the standard energy stored in Ω/Ω^* , the region of the surrounding air, with $\Omega^* = (0, \ell) \times (-L_2, L_2) \subset \Omega$, namely

$$\mathcal{E}_b^{\text{air}} = \frac{1}{2} \int_{\Omega/\Omega^*} (\chi p^2 + \rho |\mathbf{u}|^2) \, d\mathbf{x}. \quad (5.101)$$

The bulk energy $\mathcal{E}_b^{\text{slot}}$ is the effective energy stored in the straight slots. Expressed by means of the curvilinear coordinate, it reads:

$$\mathcal{E}_b^{\text{slot}} = \frac{1}{2} \sum_{n=0}^{N-1} \int_{-L_2}^{L_2} \int_{s_n^+}^{s_{n+1}^-} \left(\chi \delta P^2 + \frac{\rho}{\delta} U^2 \right) ds dx_2. \quad (5.102)$$

The surface energy $\mathcal{E}_s^{\text{in/out}}$ is the sum of the effective energies stored in the boundary layers at the entry/exit of the coiled slot and it reads

$$\mathcal{E}_s^{\text{in/out}} = \frac{1}{2} \sum_{n \in \{0, N\}} \int_{-L_2}^{L_2} \rho \left(h \mathcal{C} W_n^2 + h \mathcal{B} \langle U \rangle_n^2 \right) dx_2. \quad (5.103)$$

Finally the surface energy $\mathcal{E}_s^{\text{turn}}$ is the sum of the effective energies stored in the boundary layers at each turning region between two consecutive slots; it reads

$$\mathcal{E}_s^{\text{turn}} = \frac{1}{2} \sum_{n=1}^{N-1} \int_{-L_2}^{L_2} \left(\chi h (2\delta + \xi) \eta \langle P \rangle_n^2 + \rho h \mathcal{D} \langle U \rangle_n^2 \right) dx_2. \quad (5.104)$$

A proof of the positivity of the effective coefficients $(\mathcal{B}, \mathcal{C}, \mathcal{D})$ is given in the supplementary material. This ensures the positivity of the surface energies, hence avoiding numerical instabilities in the time domain, see [40] for a detailed analysis of such issue.

5.4.2 Derivation of the energy balance

Multiplying in (5.3) the momentum balance and the mass balance by $\frac{\rho}{\delta} U$ and P , respectively (for each segment $s \in (s_n^+, s_{n+1}^-)$ with $n \in \{0, \dots, N-1\}$). Adding the contributions, we get

$$s \in (s_n^+, s_{n+1}^-), \quad \chi \delta P \frac{\partial P}{\partial t} + \frac{\rho}{\delta} U \frac{\partial U}{\partial t} + \frac{\partial(PU)}{\partial s} = 0. \quad (5.105)$$

Similarly in the air we have

$$\chi p \frac{\partial p}{\partial t} + \rho \mathbf{u} \cdot \frac{\partial \mathbf{u}}{\partial t} + \text{div}(p\mathbf{u}) = 0. \quad (5.106)$$

To obtain a balance of energy, we start with the energy stored in the surrounding air by integrating (5.106) over Ω/Ω^* , which makes (5.101) appear. Next we integrate (5.105) over $x_2 \in (-L_2, L_2)$ and each segment (s_n^+, s_{n+1}^-) , which makes (5.102) appear. Summing the two contributions, and after application of the divergence theorem, we get

$$\frac{d}{dt} [\mathcal{E}_b^{\text{air}} + \mathcal{E}_b^{\text{slot}}] - \sum_{n=0}^N \int_{-L_2}^{L_2} \llbracket PU \rrbracket_n dx_2 + \int_{\partial\Omega} \boldsymbol{\pi} \cdot \mathbf{n} d\mathbf{x} = 0, \quad (5.107)$$

with $\mathcal{E}_b^{\text{air}}$ and $\mathcal{E}_b^{\text{slot}}$ given by (5.101)-(5.102). The terms associated to the surface energies appear as we have the identity $\llbracket PU \rrbracket_n = \llbracket P \rrbracket_n \langle U \rangle_n + \langle P \rangle_n \llbracket U \rrbracket_n$. Specifically, by using the jump conditions, we get for $n = 0$ or N ,

$$\llbracket PU \rrbracket_n = -\frac{1}{2} \frac{d}{dt} \rho \left(h \mathcal{C} W_n^2 + h \mathcal{B} \langle U \rangle_n^2 \right) - h \mathcal{C} \frac{\partial(\langle P \rangle_n W_n)}{\partial x_2}, \quad (5.108)$$

and, for $1 \leq n \leq (N - 1)$,

$$\llbracket PU \rrbracket_n = -\frac{1}{2} \frac{d}{dt} \left(\chi h(2\delta + \xi) \eta \langle P \rangle_n^2 + \rho h \mathcal{D} \langle U \rangle_n^2 \right) - h(\delta + \xi) \frac{\partial(\langle P \rangle_n \langle U \rangle_n)}{\partial x_2}. \quad (5.109)$$

We obtain the surface energies (5.103)-(5.104) after integration along x_2 of (5.109)-(5.108) (up to some flux terms at the edges of the crystalline region at $x_2 = \pm L_2$ and associated to the integration of the last term in (5.109) and (5.108). These contributions will be left out of the present analysis).

5.4.3 Positivity of \mathcal{C}

The parameter \mathcal{C} is defined by $\mathcal{C} = \int_{\mathcal{Y}^+} \left(\frac{\partial Q_2}{\partial x_2} + 1 \right) d\mathbf{y}$. It is sufficient to remark from (5.42) that

$$0 = \int_{\mathcal{Y}} Q_2 \Delta(Q_2 + x_2) d\mathbf{y} = - \int_{\mathcal{Y}^+} |\nabla_{\mathbf{y}} Q_2 + \mathbf{e}_2|^2 d\mathbf{y} + \mathcal{C} - \int_{\mathcal{Y}^-} |\nabla_{\mathbf{y}} Q_2|^2 d\mathbf{y}, \quad (5.110)$$

to get that

$$\mathcal{C} \geq 0. \quad (5.111)$$

In the above integration by parts, the boundary term $\int_{\partial \mathcal{Y}} (Q_2) \partial_n (Q_2 + x_2) dS$ vanishes since (i) on the rigid parts of \mathcal{Y} , $\partial_n (Q_2 + x_2) = 0$, (ii) in the connected regions, Q_2 and $\nabla_{\mathbf{y}} Q_2$ are periodic, and (iii) at $x_1 \rightarrow \pm\infty$, $\partial_n (Q_2 + x_2) = \nabla_{\mathbf{y}} Q_2 \cdot \mathbf{e}_1 = 0$. Also, we have used that

$$\int_{\mathcal{Y}^-} \nabla_{\mathbf{y}} Q_2 \cdot (\nabla_{\mathbf{y}} Q_2 + \mathbf{e}_2) d\mathbf{y} = \int_{\mathcal{Y}^-} |\nabla_{\mathbf{y}} Q_2|^2 d\mathbf{y} + \int_{\mathcal{Y}^-} \frac{\partial Q_2}{\partial y_2} d\mathbf{y}, \quad (5.112)$$

and the last integral of the right hand-side term vanishes since Q_2 is x_2 -periodic in \mathcal{Y}^- .

5.4.4 Positivity of \mathcal{B}

The proof relies on the variational formulation of the solution Q_1 of the elementary problem (5.42). If we introduce Q_1^* defined on subset domain $\mathcal{Y}^* \subset \mathcal{Y}$, truncated at $x_1 = \pm y_1^*$ and which is solution of

$$\begin{cases} \Delta_{\mathbf{y}} Q_1^* = 0 \text{ in } \mathcal{Y}^*, & \partial_n Q_1^* = 0 \text{ on } \Gamma^*, & Q_1^* \text{ } x_2\text{-periodic in } \mathcal{Y}^- \cap \mathcal{Y}^*, \\ \frac{\partial Q_1^*}{\partial x_1}(y_1^*, x_2 \in Y_{(1)}) = \frac{1}{\delta}, & \frac{\partial Q_1^*}{\partial x_1}(-y_1^*, x_2 \in (0, 1)) = 1, \end{cases} \quad (5.113)$$

then Q_1 solution of (5.42) is the limit of Q_1^* when $y_1^* \rightarrow \infty$ (up to a constant). Next, Q_1^* minimizes the energy functional

$$\begin{cases} E(Q_1^*) \leq E(\tilde{Q}), \\ E(\tilde{Q}) = \int_{\mathcal{Y}^*} \frac{1}{2} |\nabla \tilde{Q}|^2 d\mathbf{y} - D(\tilde{Q}), \end{cases} \quad (5.114)$$

where

$$D(\tilde{Q}) = \frac{1}{\delta} \int_{Y_{(1)}} \tilde{Q}(y_1^*, x_2) dx_2 - \int_0^1 \tilde{Q}(-y_1^*, x_2) dx_2, \quad (5.115)$$

for any test function \tilde{Q} with a gradient being square integrable (in fact \tilde{Q} in $H^1(\mathcal{Y}^*)$) and periodic on $\mathcal{Y}^- \cap \mathcal{Y}^*$. In particular we have

$$E(Q_1^*) = -\frac{D(Q_1^*)}{2}, \quad (5.116)$$

since an integration by part shows that $0 = \int_{\mathcal{Y}}^* Q_1^* \Delta Q_1^* d\mathbf{y} = -2E(Q_1^*) - D(Q_1^*)$. We now choose an admissible test function \tilde{Q} of the form

$$\tilde{Q}(\mathbf{y}) = \begin{cases} x_1, & x_1 < 0, \\ \frac{x_1}{\delta}, & x_1 > 0. \end{cases} \quad (5.117)$$

The energy $E(\tilde{Q})$ of such function using (5.114) is

$$E(\tilde{Q}) = -(1 + 1/\delta)y_1^*/2. \quad (5.118)$$

It is now sufficient to plug (5.116) and (5.118) in the inequality (5.114) to get

$$D(Q_1^*) \geq (1 + 1/\delta)y_1^*. \quad (5.119)$$

Finally, using (5.43), we have for $y_1^* \rightarrow +\infty$ that $D(Q_1^*) \sim \mathcal{B} + (1 + 1/\delta)y_1^*$, whence

$$\mathcal{B} \geq 0. \quad (5.120)$$

5.4.5 Positivity of \mathcal{D}

The proof is identical to the positivity of \mathcal{B} . It relies on the variational formulation of the solution Q of the elementary problem (5.70). If we introduce Q^* defined on subset domain $\mathcal{Y}_c^* \subset \mathcal{Y}_c$, truncated at $x_1 = y_1^*$ and which is solution of

$$\begin{cases} \Delta_y Q^* = 0 \text{ in } \mathcal{Y}_c^*, & \partial_n Q^* = 0 \text{ on } \Gamma_c^*, \\ \frac{\partial Q^*}{\partial x_1}(y_1^*, x_2 \in Y_{(n+1)}) = -\frac{1}{\delta}, & \frac{\partial Q^*}{\partial x_1}(y_1^*, x_2 \in Y_{(n)}) = \frac{1}{\delta}, \end{cases} \quad (5.121)$$

then Q solution of (5.70) is the limit of Q^* when $y_1^* \rightarrow +\infty$ (up to a constant). Next, Q^* minimizes the energy functional

$$\begin{cases} P(Q^*) \leq P(\tilde{Q}), \\ P(\tilde{Q}) = \int_{\mathcal{Y}_c^*} \frac{1}{2} |\nabla \tilde{Q}|^2 d\mathbf{y} - L(\tilde{Q}), \end{cases} \quad (5.122)$$

where

$$L(\tilde{Q}) = \frac{1}{\delta} \int_{Y_{(n)}} \tilde{Q}(y_1^*, x_2) dx_2 - \frac{1}{\delta} \int_{Y_{(n+1)}} \tilde{Q}(y_1^*, x_2) dx_2, \quad (5.123)$$

for any test function \tilde{Q} with a gradient being square integrable (in fact \tilde{Q} in $H^1(\mathcal{Y}_c^*)$). In particular we have

$$P(Q^*) = -\frac{L(Q^*)}{2}. \quad (5.124)$$

since an integration by part shows that $0 = \int_{\mathcal{Y}_c^*} Q^* \Delta Q^* \, d\mathbf{y} = -2P(Q^*) - L(Q^*)$. We now choose a test function \tilde{Q} of the form

$$\tilde{Q}(\mathbf{y}) = \begin{cases} \operatorname{sgn}(x_2) \frac{\gamma + \eta - x_1}{\delta}, & x_1 > \gamma + \eta, \\ 0, & \text{otherwise.} \end{cases} \quad (5.125)$$

The energy $P(\tilde{Q})$ of such function using (5.122) is

$$P(\tilde{Q}) = (\gamma + \eta - y_1^*)/\delta \quad (5.126)$$

and it is now sufficient to plug (5.124) and (5.126) in the inequality (5.122) to get

$$L(Q^*) \geq 2(y_1^* - (\gamma + \eta))/\delta. \quad (5.127)$$

Finally, using (5.71), we have for $y_1^* \rightarrow +\infty$ that $L(Q^*) \sim \mathcal{D}^* + 2y_1^*/\delta$, whence $\mathcal{D}^* \geq -2(\eta + \gamma)/\delta$ and given (5.95), we deduce that

$$\mathcal{D} \geq 0. \quad (5.128)$$

5.5 Validation of the effective model in the transient regime

In this section, we inspect the validity of the effective model in the transient regime by comparison with a reference numerical solution. The details on the numerics is provided in the next chapter. For simplicity, we consider hard walls with zero thickness, *i.e.* $\xi = \gamma = 0$; next, the length of the slots is $\ell = 2h$, and their width is h/N (hence $\delta = 1/N$), with $N = 3, 5, 7$.

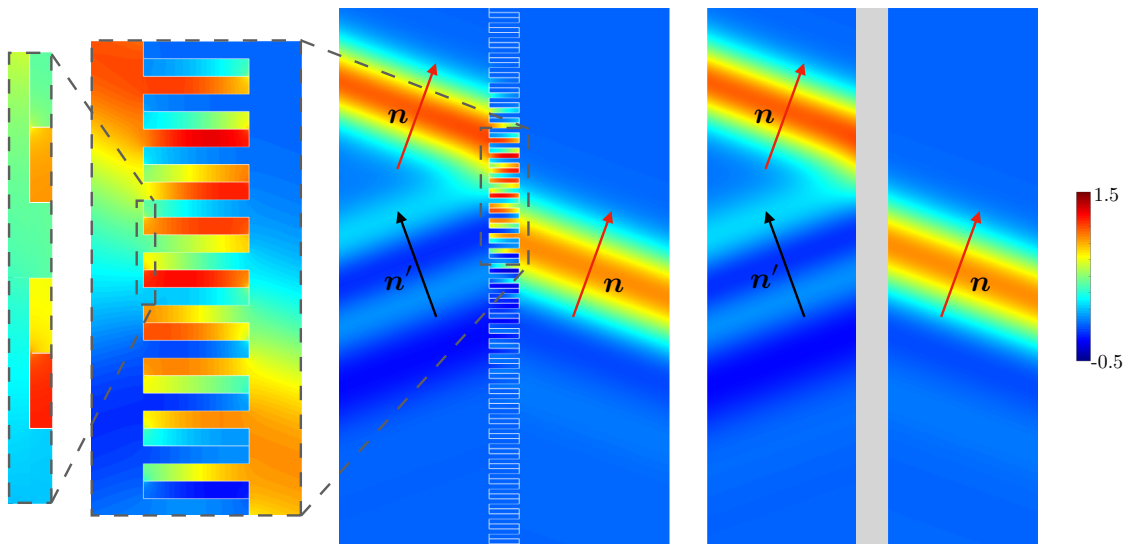


Figure 5.7: Pressure field in the coiled crystal for an incoming Gaussian pulse ($\theta = 70^\circ$ and $c\tau/h = 2.5$ in (5.129)), (left) from direct numerics; inset shows a magnification in the coiled structure, (right) from the effective model. The red arrow illustrates the vector \mathbf{n} and the black arrow the vector \mathbf{n}' .

We consider an incident pressure field in the form of a Gaussian pulse s at oblique incidence θ , namely

$$p^{\text{inc}}(\mathbf{x}, t) = s(\mathbf{x} \cdot \mathbf{n}/c - t), \quad \text{where} \quad s(t) = e^{-(t/\tau)^2}, \quad (5.129)$$

with τ the width of the Gaussian, $\mathbf{n} = (\cos \theta, \sin \theta)$ and $c = 1/\sqrt{\rho\chi}$ the speed of sound. The pressure field of the reference solution computed numerically at $t = 0$ is represented in figure 5.7 (left), for $\theta = 70^\circ$, $c\tau/h = 2.5$ and $N = 3$. The transmitted pulse is propagating with the same vector $\mathbf{n} = (\cos \theta, \sin \theta)$ as the incident pulse, and the reflected pulse is propagating with the vector $\mathbf{n}' = (\cos \theta, -\sin \theta)$. The corresponding pressure field in the homogenized model is obtained by solving the effective problem (5.2), (5.3), (5.5), (5.7) for a time harmonic dependency $e^{-i\omega t}$. The resulting reflected and transmitted fields are deduced from the scattering coefficients $r^h(\omega)$ and $t^h(\omega)$ by Fourier transform,

$$\begin{cases} p_r^h(\mathbf{x}, t) = 2\text{Re} \left\{ \int_0^\infty r^h(\omega) e^{-ikx_1} e^{ibx_2} \hat{s}(\omega) e^{-i\omega t} d\omega \right\}, \\ p_t^h(\mathbf{x}, t) = 2\text{Re} \left\{ \int_0^\infty t^h(\omega) e^{ik(x_1-\ell)} e^{ibx_2} \hat{s}(\omega) e^{-i\omega t} d\omega \right\}. \end{cases} \quad (5.130)$$

with $\hat{s}(\omega)$ the Fourier Transform of $s(t)$ (additional informations are provided in the supplementary material). The result is shown in figure 5.7(right) which is in good agreement with the reference solution.

To allow for quantitative comparisons, we report in figure 5.8 snapshots of the numerical solution (plain blue lines) and of the homogenized solution (dashed black lines) for $x/h \in (-60, 60)$ and $ct/h \in (-30, 100)$. For simplicity, that is to say to get a true one dimensional system, we have considered $\theta = 0$. The result is shown for $N = 3$, as in figure 5.7, and for $N = 5$ and 7. As expected, the time delay between the incident pulse and the first transmitted pulse is equal to $\Delta t \sim N\ell/c$ corresponding to the time-of-flight inside the coiled structure; likewise the time delay between two successive reflected pulses is equal to $2\Delta t$. In figure 5.8, it results that the non-dimensional time separation $2c\Delta t/h = 4N$, where $\ell/h = 2$, and non-dimensional spatial separation is $\Delta x/h = 4N$.

This feature is common to both of the winding arrangements shown in figure 5.1, that is to say that the behaviour of a Fabry-Pérot slab with a relative refraction index $\sim N$. In our metacrystal, however, the magnifications in the insets of the figures 5.8 and the single profile reported in 5.9, for $x/h \in (-400, 400)$ at time $ct/h = 350$, reveal additional scatterings at the turns associated with the shorter time-of-flight ℓ/c . These additional scatterings are attributable to the crystalline structure of the present arrangement and do not take place in the classical one as seen in the previous chapter. We note that in our model the main scattering at the extremities of the slab (the coiled crystal) is taken into account by the jump conditions (5.7), whereas the scattering at each turning region within the slab (the atoms of the crystal) is taken into account by the jump conditions (5.5). The combination of these two ingredients allows us to be faithfully reproduce the scattering properties of the metacrystal.

5.6 Conclusions

In this chapter, we have reported a space-coiled structure with properties that differs drastically from the one presented in the previous chapter 4. By rearranging the coiled slot, new dispersive effects can be obtained. A model that is able to accurately reproduces the scattering properties of a space-coiled metacrystal has been provided. The model accounts

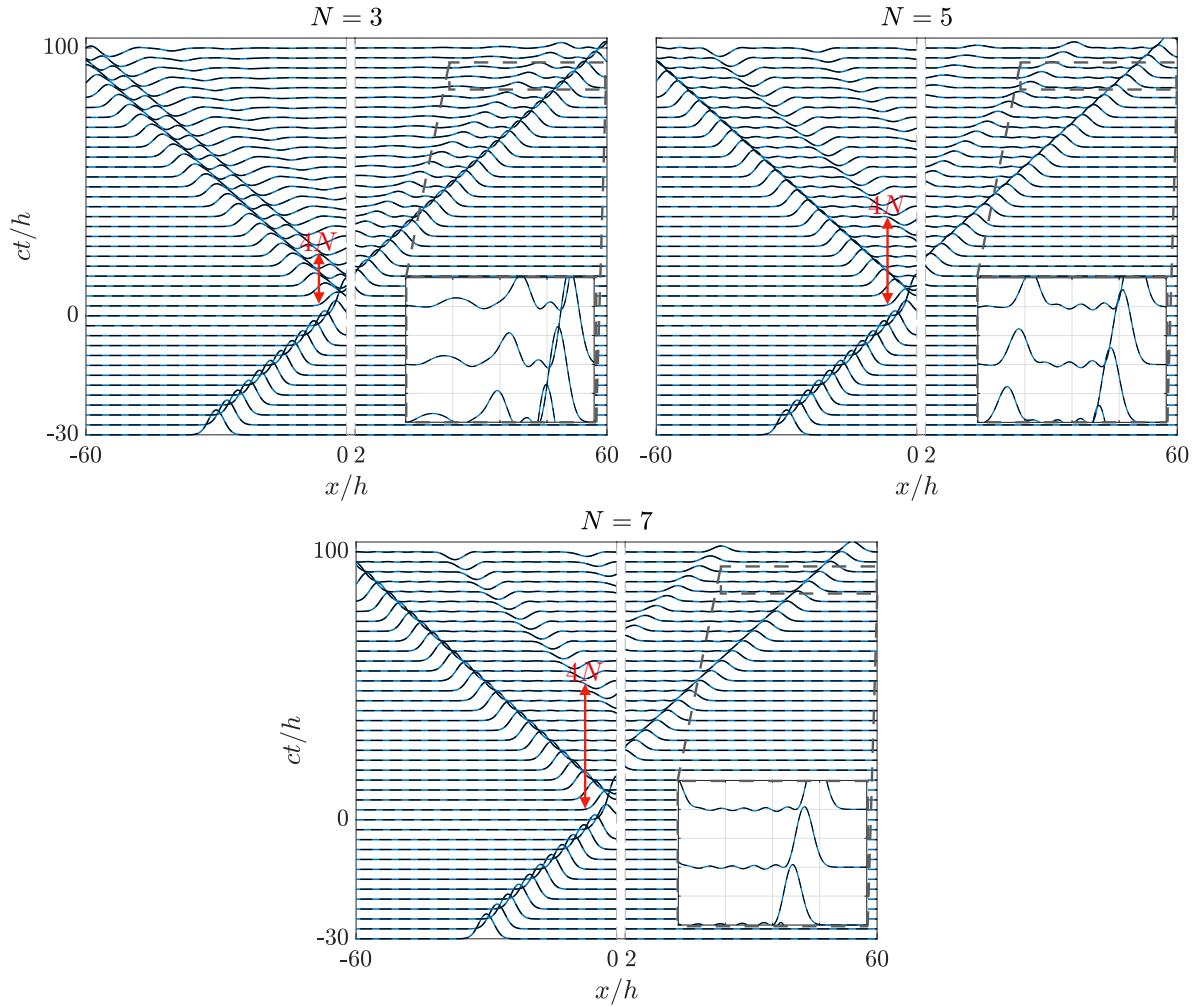


Figure 5.8: Snapshots of the pressure for the same structure as in figure 5.7 ($\theta = 0$) of the reference solution (plain blue lines) and of the homogenized solution (dashed black lines).

for the propagation inside the coiled up space by reducing the problem to one dimensional propagation with effective jump conditions at each turn which account for the presence of possible strong evanescent field. The treatment at the turns allows the model to take into account the crystalline structure and its dispersive behaviour inside the array. These effects have been illustrated in the transient regime, and validate compared to full wave numerics.

We discuss the perspectives the presented model. As the structure posses a crystallin structure, one can envision a model with slots in the coiled up space of different width. For instance, defect modes could be studied, with one slot of different width. Another possible extension is the one considering a multiple port system inside the coiled up space, for instance the junction of three slots with only one entry slot on one side of the array but two exit slots on the other side. This would need some additional treatment at each junction, but the method remains the same. One could then consider a symmetric unit cell, and obtain possibly more complex responses by some symmetry braking. Such system could exhibit trapped mode as presented in chapter 3.

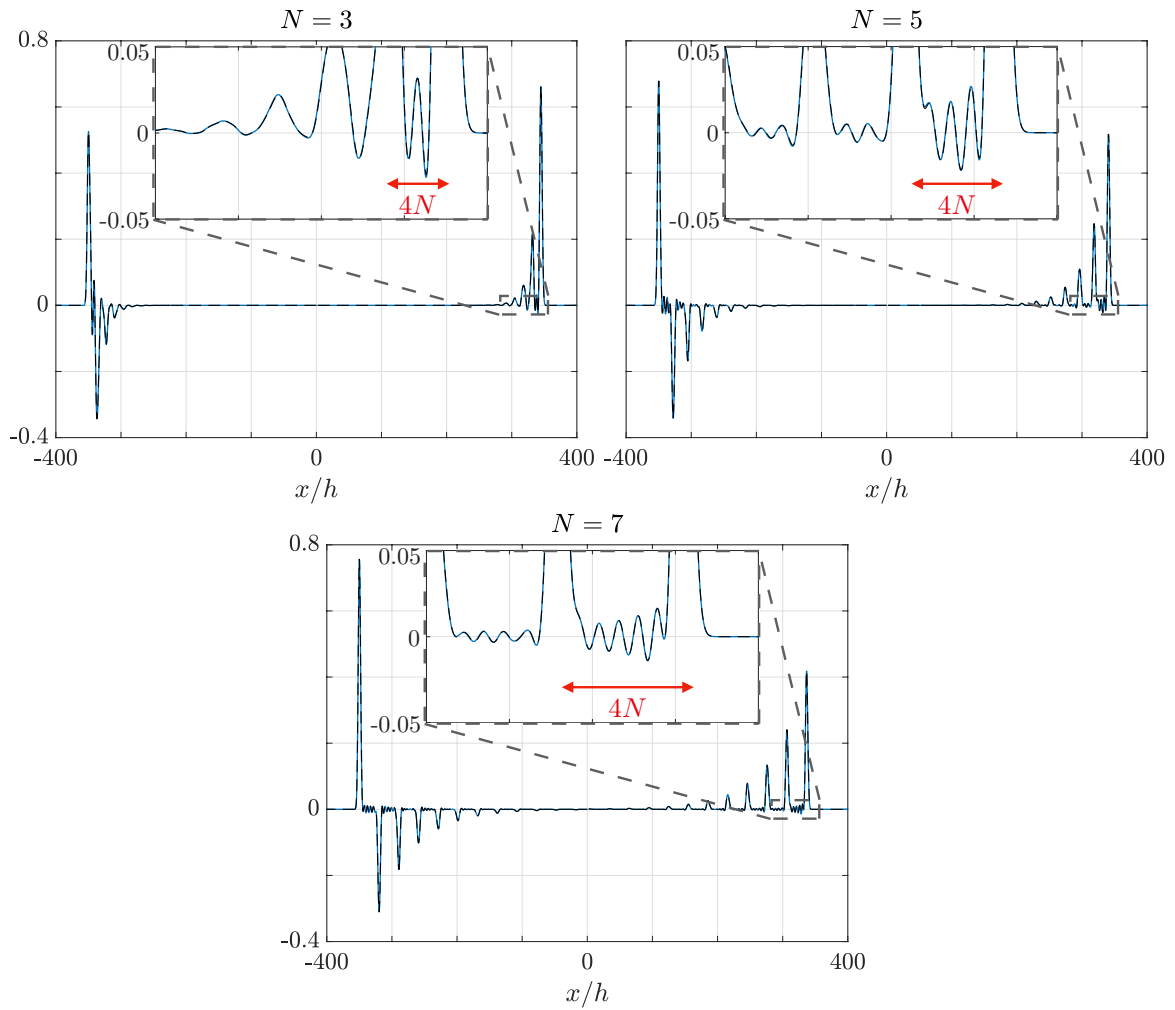


Figure 5.9: Pressure profile (as in (5.8)) for $ct/h = 350$. The multiply scattered pulses due to the crystalline structure are visible in the inset fo width $x/h \in (275, 355)$.

Chapter 6

Properties of the meta-crystal

Chapter summary: In this chapter, we present the solutions of both the numerical and effective model presented in the previous chapter. We solve the numerical problem in the harmonic regime, from which we obtain the time domain simulation. Similarly, we express the effective model in the harmonic regime. From this, we study the scattering problem of a plane wave. We analyse the band diagram of the embedded crystalline structure, and illustrate how it affects the scattering properties of the total structure.

Contents

6.1 Introduction	97
6.2 Validation of the model in the harmonic regime	97
6.2.1 Explicit solution of the effective model	97
6.2.2 Time domain formulation	100
6.3 Scattering properties of the effective model	100
6.4 Effect of the embedded crystal	102
6.5 Conclusion and perspectives	106
6.A Multimodal method	107

6.1 Introduction

In this chapter, we provide some numerical results to the structure presented in the previous chapter. Using a multimodal method, we provide the full wave numerical results from which the simulations in the transient regimes present in the previous chapter are obtained. We compare the effective model with direct numerics in the harmonic regime through a scattering problem of a plane wave. The effective model is rewritten thanks to a transfer matrix formulation, which only depends on the effective parameters or geometrical parameters.

6.2 Validation of the model in the harmonic regime

6.2.1 Explicit solution of the effective model

In the harmonic regime, the problem reduces to solve the Helmholtz equation for the pressure field \hat{P} . To simplify the notation, we drop the $\hat{\cdot}$. The jump conditions between $s = s_n^-$ and $s = s_n^+$ are

$$\begin{cases} \llbracket P \rrbracket_n = \rho h \mathcal{D} \delta \frac{\partial \langle P \rangle_n}{\partial s} - h(\delta + \xi) \frac{\partial \langle P \rangle_n}{\partial x_2}, \\ \llbracket \frac{\partial P}{\partial s} \rrbracket_n = -\chi \frac{h\eta}{\delta} (2\delta + \xi) k^2 \langle P \rangle_n - h(\delta + \xi) \frac{\partial^2 \langle P \rangle_n}{\partial s \partial x_2}, \end{cases} \quad (6.1)$$

and at the entry $s = s_0^+$ and the exit $s = s_N^-$ of the crystalline structure, the jump conditions reads

$$n \in \{0, N\}, \quad \begin{cases} \llbracket P \rrbracket_n = \rho h \mathcal{B} \frac{\partial \langle P \rangle_n}{\partial s}, \\ \llbracket \frac{\partial P}{\partial s} \rrbracket_n = h \mathcal{C} \frac{\partial^2 \langle P \rangle_n}{\partial x_2^2}. \end{cases} \quad (6.2)$$

For simplicity, we will consider the case of a sound hard material of zero width, meaning that $\xi = \gamma = 0$. We consider a structure of thickness 2ℓ that is centred along $x_1 = 0$. The incident plane wave p^{inc} has a wavenumber k and hits the slab at $x_1 = -\ell$ with an incidence θ ,

$$p^{\text{inc}}(\mathbf{x}) = e^{ik_0 x_1 + ib_0 x_2}, \quad (6.3)$$

with $k_0 = k \cos \theta$ and $b_0 = k \sin \theta$. We have the solution outside out the slab in the form of

$$p(\mathbf{x}) = e^{ib_0 x_2} \times \begin{cases} e^{ik_0(x_1+\ell)} + r e^{-ik_0 x_1}, & x_1 \in (-\infty, -\ell), \\ t e^{ik_0(x_1-\ell)}, & x_1 \in (\ell, \infty), \end{cases} \quad (6.4)$$

while the solution inside the slab is defined piecewise

$$p_n(s, x_2) = (\mathcal{S}_n \cos(ks) + \mathcal{A}_n \sin(ks)) e^{ib_0 x_2}, \quad (6.5)$$

We can obtain the explicit solution of the scattering coefficient in the form

$$\begin{pmatrix} t \\ 0 \end{pmatrix} = \mathbf{M}_{tot} \begin{pmatrix} 1 \\ r \end{pmatrix}, \quad \text{with } \mathbf{M}_{tot} = \mathbf{M}_{out}^{-1} \mathbf{M}^{N-1} \mathbf{M}_{in}, \quad (6.6)$$

where we have used a transfer matrix formulation. \mathbf{M}_{tot} represents the transfer matrix of the whole array, and is completely determined by the transfer matrices \mathbf{M}_{in} , \mathbf{M} and \mathbf{M}_{out} , corresponding respectively to the jump conditions at the entry, each junction and at the exit of the crystal. They are explicitly given by the effective parameters and the geometry, and reads

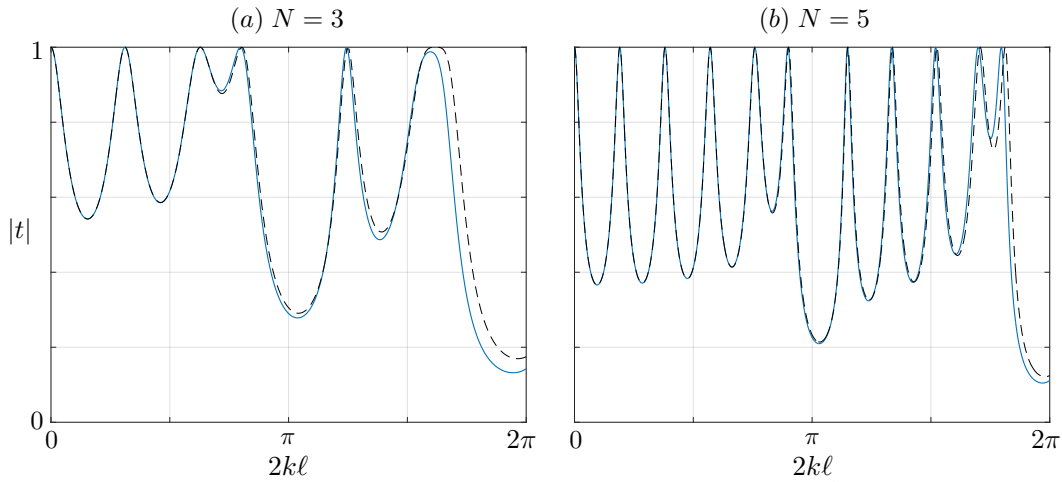


Figure 6.1: The transmission coefficient for two different configurations. Plain lines correspond to direct numerics and the dashed line to the effective model.

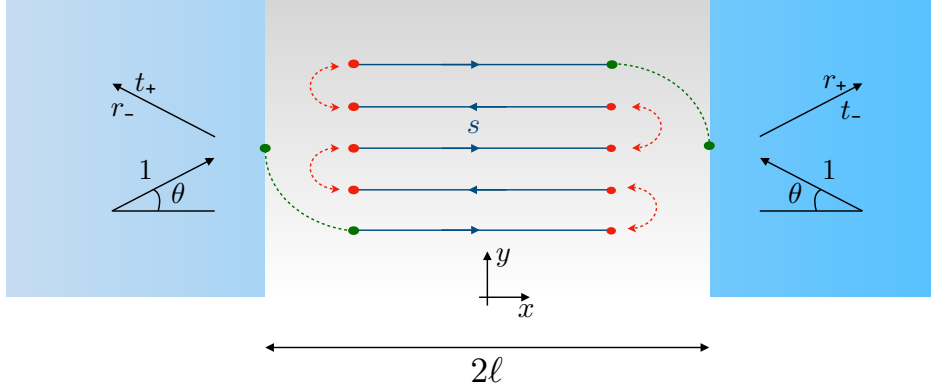


Figure 6.2: Symmetries of the array: Although the unit cell does not possess any symmetry along the x_1 or x_2 axis, it does possess a rotational symmetry. This implies that $r_+^h(k\ell, \theta) = r_-^h(k\ell, -\theta)$ and $t_+^h(k\ell, \theta) = t_-^h(k\ell, -\theta)$.

$$\mathbf{M}_{out} = \begin{pmatrix} Z_1^* \alpha^* & Z_2^* \alpha^* \\ Z_2 \alpha & Z_1 \alpha \end{pmatrix}, \quad \mathbf{M}_{in} = \begin{pmatrix} Z_1 \beta & Z_2 \beta \\ Z_2^* \beta^* & Z_1^* \beta^* \end{pmatrix}, \quad (6.7)$$

where

$$\begin{cases} Z_1 = 1 + \frac{k_0}{k\delta} + i \left(k_0 \rho h \mathcal{B} - \frac{b_0^2}{k\delta} \chi h \mathcal{C} \right), \\ Z_2 = 1 - \frac{k_0}{k\delta} - i \left(k_0 \rho h \mathcal{B} + \frac{b_0^2}{k\delta} \chi h \mathcal{C} \right), \end{cases} \quad (6.8)$$

and

$$\mathbf{M} = \frac{1}{z_3} \begin{pmatrix} z_1 \tau & z_2^* \tau^* \\ z_2 \tau & z_1^* \tau^* \end{pmatrix}. \quad (6.9)$$

where

$$\begin{cases} z_1 = 1 - Z_1 Z_2 - Z_3^2 + i(Z_1 + Z_2), \\ z_2 = i(Z_1 - Z_2), \\ z_3 = 1 + Z_1 Z_2 - Z_3^2 + 2iZ_3, \end{cases} \quad (6.10)$$

and

$$Z_1 = \chi k h (2\delta + \xi) \eta / 2, \quad Z_2 = \rho k h \mathcal{D} / 2, \quad Z_3 = b_0 h (\delta + \xi) / 2, \quad (6.11)$$

with $\alpha = e^{ik\eta h}$, $\beta = e^{ik(2\ell - \eta h)}$ and $\tau = e^{ik(2\ell - 2\eta h)}$. We report in figure 6.1 the transmission coefficient of the actual problem and the effective model for the cases $N = 3, 5$, with $\ell = h$, their corresponding width $\delta h = 1/N$ and $\eta = 0.05$. The two solutions are in excellent agreement.

6.2.2 Time domain formulation

As mentioned in the previous chapter 5, we consider an incident Gaussian pulse with a given angle θ

$$p^{\text{inc}}(\mathbf{x}, t) = s(\mathbf{x} \cdot \mathbf{n}/c - t), \quad \text{where} \quad s(t) = e^{-(t/\tau)^2}, \quad (6.12)$$

and we have its analytic Fourier transform $\hat{s}(\omega)$. We use a multimodal method to solve the actual problem in the harmonic regime. The derivation is presented in the appendix 6.A.

We obtain the scattering coefficient (r_n, t_n) , with n the number of modes. Knowing that $\hat{s}(-\omega) = \hat{s}^*(\omega)$, we have for the modal problem

$$\begin{cases} p_r(\mathbf{x}, t) = 2\text{Re} \left\{ \sum_{n=-\infty}^{+\infty} \int_0^\infty r_n(\omega) e^{-ik_n x_1} \psi_n(x_2) \hat{s}(\omega) e^{-i\omega t} d\omega \right\}, \\ p_t(\mathbf{x}, t) = 2\text{Re} \left\{ \sum_{n=-\infty}^{+\infty} \int_0^\infty t_n(\omega) e^{ik_n(x_1-\ell)} \psi_n(x_2) \hat{s}(\omega) e^{-i\omega t} d\omega \right\}, \end{cases} \quad (6.13)$$

with $k_n = \sqrt{k^2 - b_n^2}$, with $b_n = b_0 + 2n\pi/h$ for a given b_0 and for $n \in \mathbb{Z}$. The transverse function is given by

$$\psi_n(x_2) = n_n e^{ib_n x_2}, \quad (6.14)$$

where n_n is a normalisation factor. The same is done for each subdomain when performing the modal method. For the effective problem, we do not compute the field in the junctions, where we instead have effective jump conditions over an enlarged surface. We compute the reflected and transmitted field in the same way as for the modal problem.

$$\begin{cases} p_r^h(\mathbf{x}, t) = 2\text{Re} \left\{ \int_0^\infty r(\omega) e^{-ik_0 x_1} \psi_0(x_2) \hat{s}(\omega) e^{-i\omega t} d\omega \right\}, \\ p_t^h(\mathbf{x}, t) = 2\text{Re} \left\{ \int_0^\infty t(\omega) e^{ik_0(x_1-\ell)} \psi_0(x_2) \hat{s}(\omega) e^{-i\omega t} d\omega \right\}. \end{cases} \quad (6.15)$$

We can in a such manner easily retrieve the full time domain solution. Numerically, we truncate the integration at ω_F , for which we consider that the contribution of \hat{s} is insignificant. For a sufficient spectral precision, we consider the time step $\Delta t \leq 1/(f_{\max})$, where f_{\max} is the maximum frequency used to compute the harmonic solution.

6.3 Scattering properties of the effective model

In this section, we present some more general properties of the system. To simplify the notation, we set $\rho = \chi = 1$. We consider the scattering problem of the considered grating. We look for plane wave solutions of the form

$$\mathbf{p}(\mathbf{x}) = e^{ibx_2} \times \begin{cases} A_- e^{ik(x_1+\ell)} + B_- e^{-ik(x_1+\ell)}, & x_1 \in (-\infty, -\ell), \\ A_+ e^{ik(x_1-\ell)} + B_+ e^{-ik(x_1-\ell)}, & x_1 \in (\ell, \infty), \end{cases} \quad (6.16)$$

with the jump conditions (6.2) applied at $x_1 = \pm\ell$ outside the grating. A_\pm and B_\pm are the complex valued amplitudes of the left and right going wave components. We obtain through a transfer matrix formulation the scattering coefficients (r_-^h, t_-^h) , namely

$$\begin{pmatrix} A_+ \\ B_+ \end{pmatrix} = \mathbf{M}_{tot} \begin{pmatrix} A_- \\ B_- \end{pmatrix}, \text{ with } \mathbf{M}_{tot} = \mathbf{M}_{out}^{-1} \mathbf{M}^{N-1} \mathbf{M}_{in}. \quad (6.17)$$

The coefficients of the transfer matrix simplifies in the case of sound hard walls of vanishing thickness $\xi = \gamma = 0$. Namely,

$$\mathcal{Z}_1 = kh\eta, \quad \mathcal{Z}_2 = kh\mathcal{D}/2, \quad \mathcal{Z}_3 = b_0 h \delta / 2, \quad (6.18)$$

We take a moment to comment the obtained transfer matrix formulation of the problem. The transfer matrix method is often encountered for one dimensional problem, such as closed waveguides, or layered material, which although they depend on the angle of incidence, are not truly two dimensional problems. The presented structure differs from the ones mentioned above as the behaviour inside the grating/coiled media is two dimensional and does only interact with exterior at the opening at each end point of the crystalline structure. Although the problem is reduced to one dimension s inside the grating, it still depends on the variable x_2 . From a physical point of view, the dependence on x_2 is purely an artefact which appears in the derivation of the effective model in order to take into account the phase shift along x_2 inside the grating.

At normal incidence, the propagation is purely one dimensional and the matrix \mathbf{M} behaves as a typical transfer matrix of one dimensional problems, with the properties such as its diagonal and anti diagonal terms are respectively complex conjugated, and $\det \mathbf{M} = 1$. These properties translates out to the full total transfer matrix \mathbf{M}_{tot} . However, when considering an oblique incidence $\theta \neq 0$, the term z_3 admits an imaginary part in terms of b_0 . Several properties are revisited for $\mathbf{M}_{tot} = (m_{ij})$. $m_{12} = -m_{21}$, however no clear relation exist between m_{11} and m_{22} , and only $|\det \mathbf{M}_{tot}| = 1$ holds.

For an incident right going plane wave of incidence θ , $p^{\text{inc}}(\mathbf{x}) = e^{ik_0(x_1+\ell)+ib_0x_2}$, where $k_0 = k \cos \theta$ and $b_0 = k \sin \theta$, we obtain the scattering coefficients (r_-^h, t_-^h) by plugging in the form $(A_-, B_-)^\top = (1, r_-^h)^\top$ and $(A_+, B_+)^\top = (t_-^h, 0)^\top$. Similarly, for a left going wave $p^{\text{inc}}(\mathbf{x}) = e^{-ik_0(x_1-\ell)+ib_0x_2}$, we obtain (r_+^h, t_+^h) by plugging in the form $(A_-, B_-)^\top = (0, t_+^h)^\top$ and $(A_+, B_+)^\top = (r_+^h, 1)^\top$.

One easily obtain

$$r_-^h = r_+^h = r^h = -\frac{m_{21}}{m_{22}} = \frac{m_{12}}{m_{22}}, \quad (6.19)$$

and

$$t_-^h = m_{11} - \frac{m_{21}m_{12}}{m_{22}}, \quad t_+^h = \frac{1}{m_{22}}. \quad (6.20)$$

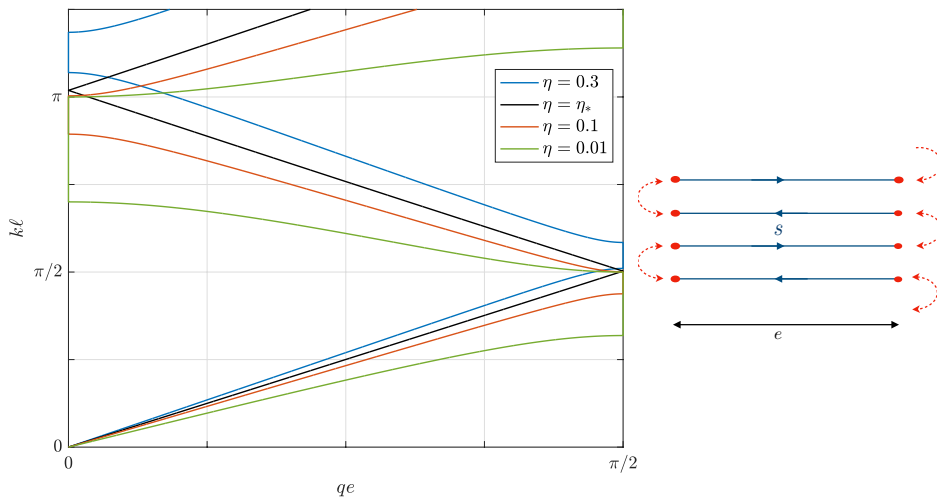


Figure 6.3: Band diagram of the embedded crystal at normal incidence with the corresponding geometry on the right.

The energy conservation $|r^h|^2 + |t_{\pm}^h|^2 = 1$ holds for all frequencies and for all angle of incidence θ . The above relations reflects some of the underlying symmetry properties of the geometry, see figure 6.2. The linear dependence of b cancel out in the formulation of r^h , consequently $r^h(k\ell, \theta) = r^h(k\ell, -\theta)$.

6.4 Effect of the embedded crystal

Using the transfer matrix formulation (6.17), we can identify the underlying mechanism of the complex structure. Indeed, the matrix given in (6.9) takes into account the effect the turns that acts as scatterer. To study its behaviour, we consider the infinite one dimensional crystal of periodicity $e = 2\ell - 2\eta$ and we look for solutions of Bloch waves. By considering the matrix \mathbf{M} at normal incidence, *i.e.* $k_0 = k$ and $b_0 = 0$, one obtains the analytical dispersion relation of the periodic crystal, namely

$$\cos(qe) = \frac{1 - (kh)^2 \frac{\mathcal{D}\eta}{2}}{1 + (kh)^2 \frac{\mathcal{D}\eta}{2}} \cos(k\ell) - \frac{kh(\frac{\mathcal{D}}{2} + \eta)}{1 + (kh)^2 \frac{\mathcal{D}\eta}{2}} \sin(k\ell), \quad (6.21)$$

where q is the effective Bloch wavenumber. The effective parameter \mathcal{D} depends on the geometry of the turn, and is thus a function of η . We report in figure 6.3 the band diagram for four different values of η . One can tune the dispersions relation so that coiled grating act as a homogeneous medium, obtained for a critical value $\eta = \eta_* = \mathcal{D}/2$. Numerically we obtain the value $\eta_* \approx 0.1868136$. For this value, the non-diagonal terms of transfer matrix in (6.9) vanishes resulting in a non-dispersive medium. The dispersion reads

$$\cos(qe) = \cos(k\ell + \phi), \quad \phi = \text{atan} \frac{kh\mathcal{D}}{1 - (kh)^2 \mathcal{D}^2/4}, \quad (6.22)$$

where ϕ is a nonlinear phase shift. As mentioned in the previous section, the physical study of \mathbf{M} only makes sense at normal incidence. For $\theta \neq 0$, the imaginary part of z_3 act as dissipation and no clear band gaps can be observed.

To study the effects that the dispersive material has on the properties of the grating, we plot in figure 6.4 the transmission coefficient for several values of η and $N = 3$, the simplest coiled material. The comparison between the full numerics and the model is shown, and we see that the model is extremely accurate in the low frequency regime. For the specific configuration $\eta = \eta_*$, the model exhibits perfect Fabry-Perot resonance, however with a non evident effective length ℓ_* . Otherwise, one can clearly observe the effects of the presence of band gaps inside the grating. As the band gaps open up on either side of the Dirac point, one can tune the transmission of the grating. Although the model loses in accuracy for larger frequencies, it still gives us good insight on the underlying mechanisms present in the problem.

A feature of a Fabry-Pérot slab is the presence of reflectionless excitation at half wavelength resonance $2k\ell_* = \pi$ when η_* . This is the case when the zeros of r^h , *i.e.* m_{12} lie on the real axis when k is extended to the complex plane. As band gaps open up in the medium, the closest zeros of r^h are pushed away on either of its side. Considering the case $\eta < \eta_*$, the reflectionless state is on the lower side of the band is pushed toward decreasing frequencies until it coalesces with another zero at an exceptional point of reflection less states at $\eta = \eta_{\text{EP}}$. The two transmission peaks becomes one quadratically flat transmission. As $\eta < \eta_{\text{EP}}$, the two zeros of r^h leave the real axis and become complex conjugate. This

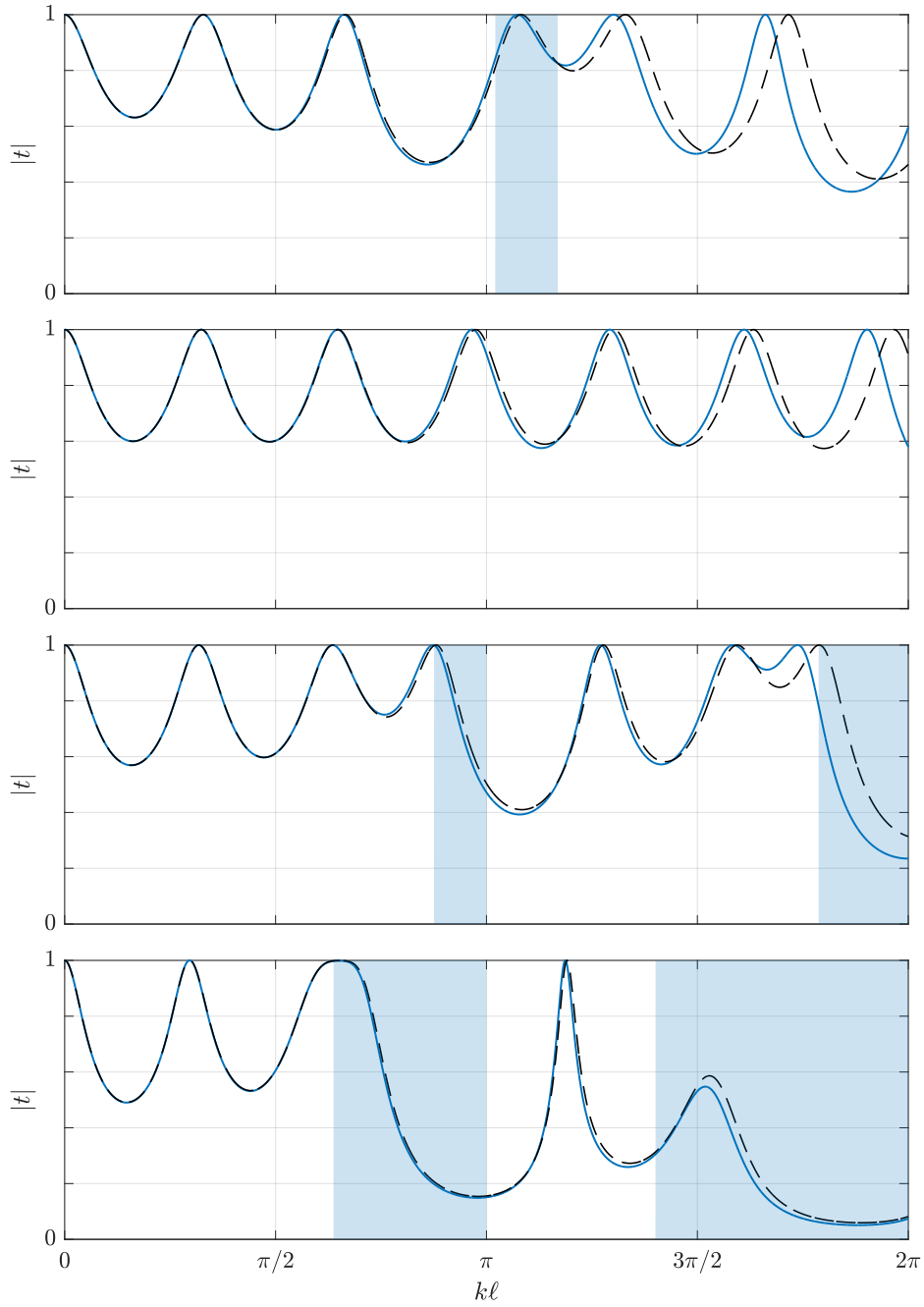


Figure 6.4: Transmission coefficient $|t|$ for four different values of η . From top, $\eta = 0.25, \eta_*, 0.1, 0.01$, where the three corresponds to the ones presented in 6.3, and the last corresponds to the extreme case of a small opening. The blue shaded areas corresponds to the band gaps of the embedded crystal.

is illustrated in figure 6.6. It is the coupling between the "opacity" of the medium and the Fabry-Pérot slab that give rise to this phenomenon. As illustrated in [143], this is an example of exceptional points in a lossless system. In another study [50], similar results are obtained experimentally. In this study, such points are observed in a Fabry-Pérot system in which

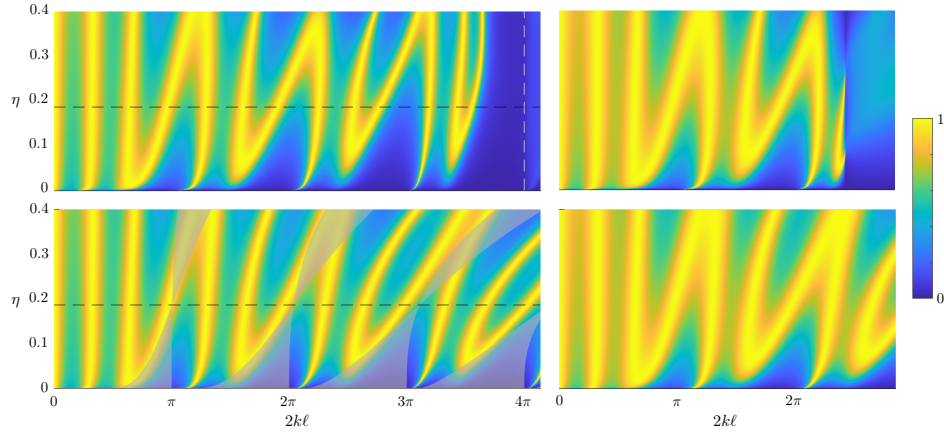


Figure 6.5: Transmission coefficient $|t|$ against the frequency $2k\ell$ and the opening of the turn η . Top, direct numerics and bottom effective model. Left, at normal incidence, and ,right, oblique incidence $\theta = 40^\circ$. The cut-off frequency is illustrated by a white dashed vertical line. The grey shaded area corresponds to the band gaps of the embedded crystal and the dashed black horizontal line illustrates the value η_*

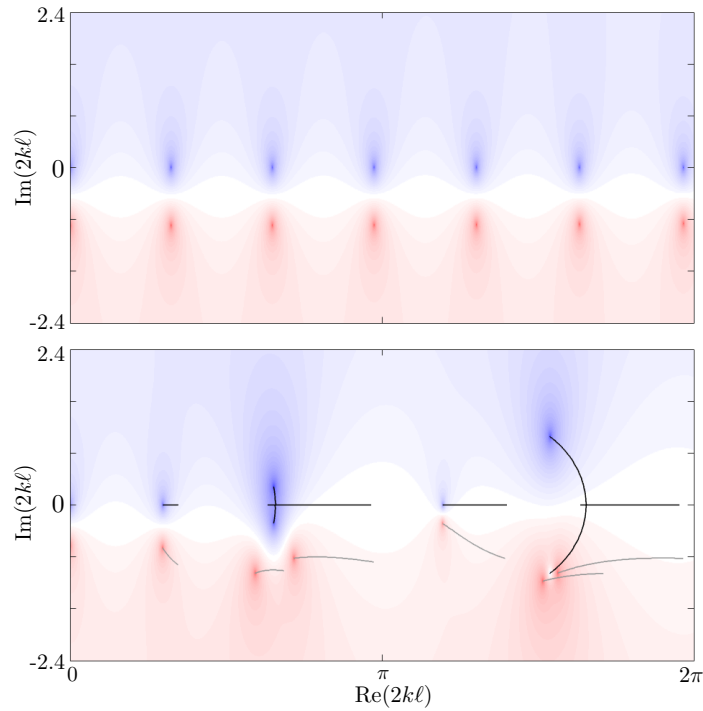


Figure 6.6: Reflection coefficient $\log|r|$ against the frequency $\text{Re}(2k\ell)$ and $\text{Im}(2k\ell)$ in the complex plane. Top corresponds to $\eta = \eta_*$, and zeros of reflection due to Fabry-Pérot resonance are visible in blue along the real axis. The corresponding pole in red and is located below the perfect transmission. Bottom corresponds to $\eta = 0.01$. The black and grey line corresponds to the path of the respectively zeros and poles. We observe two exceptional point at the coalescence of two zeros.

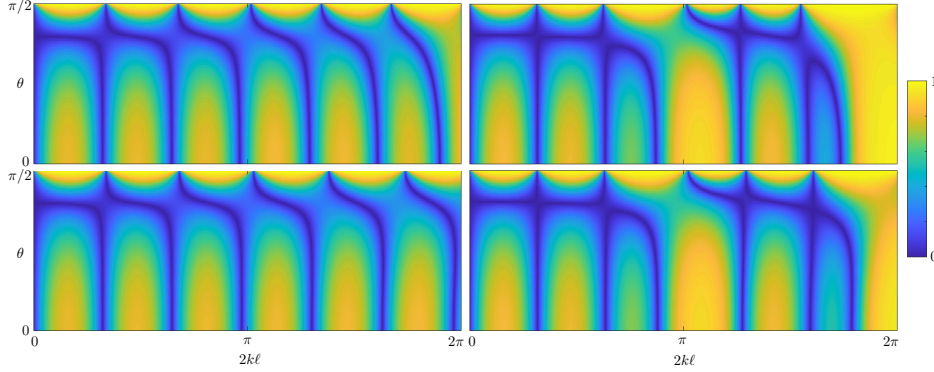


Figure 6.7: Reflection coefficient $|r|$ against the frequency $2k\ell$ and the angle of incidence θ . Top, direct numerics and bottom the effective model. Left, for $\eta = \eta_*$ and observe at low frequency the Brewster angle. Right, $\eta = 0.1$, the appearance of band gaps completely breaks the Brewster angle.

the scattering strength is tuned in a symmetrical manner. Such phenomena typically rely on some underlying symmetry.

We report the reflection coefficient in the complex plane in figure 6.6. We track the path of the zeros and poles as we vary the tuning parameter η . We observe exceptional points where two zeros coalesce on the real axis, and become complex conjugate. As they become complex, they follow the typical parabolic path. The path of the reflection less state when $\eta > \eta_*$ is less intuitive, as shown in the top in figure 6.4. As the reflectionless state is located inside the band gap of the medium, the physical interpretation is not evident.

The following results are summarised in the figure 6.5, where the amplitudes of the transmission coefficient t and t^h plotted against the frequency and the tuning parameter η for two different angle of incidence. We can observe that the predictions of the large model are accurate for surprisingly frequencies, as well as for fairly large η . The overall behaviour of the model completely fail at the cut off frequency, where a second propagating mode appears, as expected as the model is constructed for $kh \ll 1$.

The study of the problem at normal incidence gives us good insight in the band structure of the embedded media and the effect it has on the scattering properties of the grating. Similarly, we can observe what happens at oblique incidence. A Fabry-Pérot slab typically feature a Brewster angle $\cos \theta_B = \delta$, for which the structure admits perfect transmission for any frequency. As mentioned in [124] at the intersection between the perfect transmission of the Fabry-Pérot and Brewster angle, due to coupling of a strong evanescent field, the perfect transmission don't intersect. This is well captured by the model, as shown in figure 6.7. When band gaps appears, the Brewster angle disappears.

6.5 Conclusion and perspectives

In this chapter, we shown how the embedded crystal affects the scattering properties of the grating. The model derived in chapter 5 allows us to decouple the problem which leads to an analytical study of the one dimensional crystal and deeper insight. Some interesting perspective are straightforward, as we are interested in the future of the proposed systems in Figure 6.8. The first one consists of slots of different width. This means that the periodicity

is doubled, and as there is an odd number of slots, the last periodicity is cut in half. The second consist of a port like structure. The last one is similar to the second, but with the possibility of a phase shift as one branch is longer than the other.

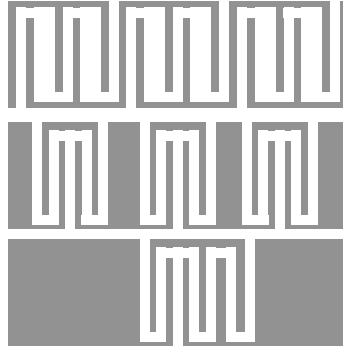


Figure 6.8: Possible metacrystal configurations

6.A Multimodal method

We present the method to solve the actual problem in the harmonic regime. This leads to solving the Helmholtz equation for which we use a multimodal method similar to Rigorous Coupled Wave analysis. It relies on partitioning the domain into different subdomains and projecting the waveform on adequate basis. We consider an incident plane wave of the form

$$p^{\text{inc}}(\mathbf{x}, \omega) = e^{ik_0 x_1 + ib_0 x_2}, \quad (6.23)$$

with $k_n = \sqrt{k^2 - b_n^2}$, with $b_n = b_0 + 2n\pi/h$ for a given b_0 and for $n \in \mathbb{Z}$. The solution of the scattering problem is expanded in the following way. To begin, we consider the domain outside the crystalline structure, and we write the solution as follows:

$$p(\mathbf{x}, \omega) = \begin{cases} p^{\text{inc}}(\mathbf{x}, \omega) + \sum_{n=-\infty}^{+\infty} r_n e^{-ik_n x_1} \psi_n(x_2), & x_1 \in (-\infty, -\ell), \\ \sum_{n=-\infty}^{+\infty} t_n e^{ik_n(x_1 - \ell)} \psi_n(x_2), & x_1 \in (\ell, \infty). \end{cases} \quad (6.24)$$

Next, we treat each slot in the region $x_1 \in (-\ell, \ell)$, where we define the interval $X_{(j)} = x_{(j)} + \delta h/2(-1, 1)$, with $x_{(j)} = (j-1)h(\delta + \xi) + \xi h/2$, for $j \in \{1, \dots, N\}$. In each horizontal slot of width δh , we write the fields as following

$$\begin{cases} p_{(1)}(x_1, x_2 \in X_{(1)}, \omega) = \sum_{n=0}^{\infty} \left(A_n^{(1)} e^{i\kappa_n(x_1 + \ell)} + B_n^{(1)} e^{-i\kappa_n(x_1 - \ell + e)} \right) \psi_n^{(1)}(x_2), \\ p_{(j)}(x_1, x_2 \in X_{(j)}, \omega) = \sum_{n=0}^{\infty} \left(A_n^{(j)} e^{i\kappa_n(x_1 + \ell - e)} + B_n^{(j)} e^{-i\kappa_n(x_1 - \ell + e)} \right) \psi_n^{(j)}(x_2), \\ p_{(N)}(x_1, x_2 \in X_{(N)}, \omega) = \sum_{n=0}^{\infty} \left(A_n^{(N)} e^{i\kappa_n(x_1 + \ell - e)} + B_n^{(N)} e^{-i\kappa_n(x_1 - \ell)} \right) \psi_n^{(N)}(x_2). \end{cases} \quad (6.25)$$

The junctions are treated in the same way, where we define the interval $X_{(j)}^c = x_{(j)}^c + (2\delta + \xi)h/2(-1, 1)$, with $x_{(j)}^c = j(\delta + \xi)h$, for $j \in \{1, \dots, N-1\}$. We write the fields in each junction

$$\begin{cases} p_{(j)}^c(x_1, x_2 \in X_{(j)}^c, \omega) = \sum_{n=0}^{\infty} C_n^{(j)} \cos(K_n(x_1 - \gamma h)) \varphi_n^{(j)}(x_2), & (j \text{ even}), \\ p_{(j)}^c(x_1, x_2 \in X_{(j)}^c, \omega) = \sum_{n=0}^{\infty} C_n^{(j)} \cos(K_n(x_1 - (\ell - \gamma h))) \varphi_n^{(j)}(x_2), & (j \text{ odd}). \end{cases} \quad (6.26)$$

The transverse functions

$$\begin{cases} \psi_n(x_2) = n_n e^{ib_n x_2}, \\ \psi_n^{(j)}(x_2) = n_n^{(j)} \cos(a_n(x_2 - x_{(j)})), \text{ with } a_n = n\pi/(\delta h), \\ \varphi_n^{(j)}(x_2) = n_n^c \cos(c_n(x_2 - x_{(j)}^c)), \text{ with } c_n = n\pi/((2\delta + \xi)h), \end{cases} \quad (6.27)$$

form orthonormal bases for the scalar products $(a, b)_Y = \int_Y a(x_2) b^*(x_2) dx_2$, with b^* the complex conjugate of b , for $Y = X, X_{(j)}, X_{(j)}^c$ respectively (with the proper normalisation

factors $n_n, n_n^{(j)}$ and n_n^c). For practical purposes, it is important that each order of the above expansion satisfies the Helmholtz equation. The wavenumbers κ_n and K_n are therefore defined as follows

$$\kappa_n = \sqrt{k^2 - a_n}, \quad K_n = \sqrt{k^2 - c_n}. \quad (6.28)$$

The solutions (6.24) and (6.25) are matched at $x_1 = \pm\ell$ by imposing continuity conditions for the pressure and the normal velocity field, for $i = 0, \dots$,

$$\begin{cases} \left(p_{|\ell}, \psi_i^{(1)} \right)_{X_{(1)}} = \left(p_{(1)|\ell}, \psi_i^{(1)} \right)_{X_{(1)}}, & \left(\partial_{x_1} p_{|\ell}, \psi_i^* \right)_X = \left(\partial_{x_1} p_{(1)|\ell}, \psi_i^* \right)_X, \\ \left(p_{|\ell}, \psi_i^{(N)} \right)_{X_{(N)}} = \left(p_{(N)|\ell}, \psi_i^{(N)} \right)_{X_{(N)}}, & \left(\partial_{x_1} p_{|\ell}, \psi_i^* \right)_X = \left(\partial_{x_1} p_{(N)|\ell}, \psi_i^* \right)_X. \end{cases} \quad (6.29)$$

When integrating over X , we have taken into account the Neumann boundary condition $\partial_{x_1} p_{|0,\ell} = 0$ for $x_2 \in X \setminus X_{(1)}$ and $x_2 \in X \setminus X_{(N)}$. By the same means, we match the solutions (6.25) and (6.26) in $x_1 = \pm(\ell - e)$ with $e = (\gamma + \eta)h$. For simplicity, we only consider the matching at $x_1 = -\ell + e$, and we have for $j = \{1, \dots, N - 1\}$ and for $i = 0, \dots$,

$$\begin{cases} \left(p_{|-\ell+e}^c, \psi_i^{(j)} \right)_{X_{(j)}} = \left(\hat{p}_{(j)|-\ell+e}, \psi_i^{(j)} \right)_{X_{(j)}}, \\ \left(p_{|-\ell+e}^c, \psi_i^{(j+1)} \right)_{X_{(j+1)}} = \left(p_{(j+1)|-\ell+e}, \psi_i^{(j+1)} \right)_{X_{(j+1)}}, \\ \left(\partial_{x_1} p_{|-\ell+e}^c, \varphi_i^{(j)} \right)_{X_{(j)}^c} = \left(\partial_{x_1} p_{(j)|-\ell+e}, \varphi_i^{(j)} \right)_{X_{(j)}} + \left(\partial_{x_1} p_{(j+1)|-\ell+e}, \varphi_i^{(j)} \right)_{X_{(j+1)}}, \end{cases} \quad (6.30)$$

where we have taken into account the Neumann boundary condition $\partial_{x_1} p_{|-\ell+e}^c = 0$ for $x_2 \in X^c \setminus X_{(j)} \cup X_{(j+1)}$. In practice, we truncate the series to M_p terms for p , M_d terms for $p_{(j)}$, and M_j terms for $p_{(j)}^c$. The modal matching problem thus reduces to $2 \times (2M_d N + M_j(N - 1) + M_p)$ equations for $(4M_d N + 2M_j(N - 1) + 2M_p)$ unknowns, and is solved by a simple matrix inversion, with a source term composed of the projections of p^{inc} onto $\psi_i^{(1)}$ and $\partial_{x_1} p^{\text{inc}}$ onto ψ_i^* (first line in (6.29)).

Chapter 7

General conclusions and perspectives

7.1 General conclusions

In this thesis, we have studied the properties and modelled several acoustical metamaterials. As mentioned in the introduction, the possibility of having local resonances in the context of acoustic waves in fluids is rather limited, and we have focused on the halfwavelength resonance due to slots in a sound hard grating. The microstructured grating can be replaced by an effective medium derived through different asymptotical homogenization methods. We have obtained closed form solutions of the approximated effective models, allowing for a physical study the problem.

The work has been divided into two main parts. The first part deals with scattering of an acoustical wave by a dual-period grating. In chapter 2, we have recalled classical homogenization results for layered media, and more specifically, we have applied it to a regular grating with sound hard part. We have shown that the dispersion relation of the SPP localized at the interfaces can be recovered by a homogenized model at dominant order.

The main contribution of this part is presented in chapter 3, where an effective model of a dual-period grating is derived. Such grating typically supports Fabry-Pérot resonances that interact with Fano resonances. When a dual period grating is considered, perfect trapped modes exist and do not interact with scattering continuum. By breaking the symmetry of the unit cell, by considering one slot wider than the other, the perfect trapped mode becomes a quasi-trapped mode, which leads to sharp asymmetric peaks in the transmission spectrum. The homogenization is done thanks to classical two-scale homogenization in the bulk combined with matched asymptotic techniques at the interface. The specificity of the bulk homogenization is the fact that two effective medium are derived in order to take into account the highly oscillatory fields from a slit to another. The two effective medium are matched to each other and the outside domain through non trivial jump conditions. The model has been validated by comparison with numerical results obtained with a multimodal method.

We have used the effective model to give some further insight into the physical phenomenon. By performing a local analysis around the Fabry-Pérot resonances explicit expressions of the two complex resonances poles are obtained, which provide a deeper understanding on their link with the perfect- and zero-transmissions. The limitation of the model has been addressed as well.

The second part of the thesis concerns the study of so-called space-coiled metamaterials. It concerns two types of winding arrangement which exhibits different scattering properties. In chapter 4, we deal with the classical space-coiled structure and it is the one that is most present in the existing literature. The major flaw of the existing effective models is the unclear

definition of the length of an uncoiled straight slot. We have revisited the problem with a two-scale homogenization approach. The model is derived at leading order, which yields an effective refractive index and impedance mismatch without any ambiguity. The space-coiled structure supports Fabry-Pérot resonances, and the intuition that it behaves as an equivalent straight slot holds.

In chapter 5, we present what we refer to as a meta-crystal. By considering a different coiling arrangement, one can benefit from two scales. As the straight part of coiled slot can be of the order of the wave length, Bragg scattering can be observed as the turns act as scatterer. This couples with the subwavelength nature of the grating. The homogenization leads to a reduced one dimensional propagation in the straight part with effective jump conditions at each turn. The reduced model is then coupled to the outside domain through additional jump conditions. The dispersive behaviour of the crystalline structure is accounted for and is illustrated in the transient regime. A detailed energy analysis is provided to assure the stability of the model in the time domain.

In chapter 6, we have presented some physical properties of the presented meta-crystal. The explicit solution of the effective model allow us to decouple the problem and study the dispersive behaviour of the embedded crystal. We illustrate how the opening of band gaps inside the array affects the scattering properties of the total structure.

7.2 Future perspectives

We conclude this chapter with an overview of some future interesting and possible extensions.

In the first part, we have only considered the case of acoustical waves in a two dimensional setting. Extending the acoustical setting to three dimensional propagation is straightforward. In this setting, one can be interested in different dual bi-periodic gratings. For instance, the honeycomb lattice is tempting as it has several symmetries. In general, extending this works to other types of waves is of high interest. In the case of elastodynamics, it can be interesting to study the interaction between shear waves and pressure waves in the presence of a dual-period.

In chapter 3, we mention the limitation of the model at the edge of the Brillouin zone. To overcome this, one can consider another asymptotic parameter, such as the width of slot small compared to the periodicity.

As mentioned in chapter 3, the study of double inclusions in a metasurface is also a possible extension. Notably, in the context of Minnaert resonance, a dual period setting has been considered in [6]. Inspired by the works in [126], we can consider the nonlinear bubble to bubble interaction in a dual-periodic setting.

In the second part, we have for the moment only considered the case of perfect periodicity. As space-coiled metamaterials has shown promising results in terms of wave-front manipulation, an extension toward quasi-periodicity is of high interest. Building on the works presented in [42, 138, 123], an effective model could be derived. Obtaining such a model could be interesting from a design and optimization point of view.

In chapter 6, we discuss the extension of the study of the meta-crystal. One can consider different periodicity of the embedded crystalline structure, as shown in figure 6.8. For the moment, we have only focused on the effect that the crystalline structure has on the scattering properties. A thorough study on the effect it has on the guided waves is an ongoing work.

Finally, we need to address the fact that all of the works presented in this thesis have been done in an ideal lossless setting. When accounting for losses due to viscothermal effects can become dominant leading to an absorbing medium. In this context, one can tune the parameters and obtain perfect absorption through critical coupling, see for instance [\[132\]](#).

Bibliography

- [1] Toufic Abboud and Habib Ammari. Diffraction at a curved grating: Tm and te cases, homogenization. *Journal of mathematical analysis and applications*, 202(3):995–1026, 1996.
- [2] Rasha Al Jahdali and Ying Wu. High transmission acoustic focusing by impedance-matched acoustic meta-surfaces. *Applied Physics Letters*, 108(3):031902, 2016.
- [3] Grégoire Allaire. Homogenization and two-scale convergence. *SIAM Journal on Mathematical Analysis*, 23(6):1482–1518, 1992.
- [4] Grégoire Allaire and Micol Amar. Boundary layer tails in periodic homogenization. *ESAIM: Control, Optimisation and Calculus of Variations*, 4:209–243, 1999.
- [5] Habib Ammari, Durga Prasad Challa, Anupam Pal Choudhury, and Mourad Sini. The equivalent media generated by bubbles of high contrasts: Volumetric metamaterials and metasurfaces. *Multiscale Modeling & Simulation*, 18(1):240–293, 2020.
- [6] Habib Ammari, Bryn Davies, Erik Orvehed Hiltunen, Hyundae Lee, and Sanghyeon Yu. Bound states in the continuum and fano resonances in subwavelength resonator arrays. *Journal of Mathematical Physics*, 62(10):101506, 2021.
- [7] Habib Ammari, Brian Fitzpatrick, David Gontier, Hyundae Lee, and Hai Zhang. Minnaert resonances for acoustic waves in bubbly media. In *Annales de l'Institut Henri Poincaré C, Analyse non linéaire*, volume 35, pages 1975–1998. Elsevier, 2018.
- [8] Habib Ammari and Kthim Imeri. A mathematical and numerical framework for gradient meta-surfaces built upon periodically repeating arrays of helmholtz resonators. *Wave Motion*, 97:102614, 2020.
- [9] Habib Ammari, Bowen Li, Hongjie Li, and Jun Zou. Fano resonances in all-dielectric electromagnetic metasurfaces. *arXiv preprint arXiv:2211.03224*, 2022.
- [10] Igor V Andrianov, Jan Awrejcewicz, and Alexander A Diskovsky. Homogenization of quasi-periodic structures. *TRANSACTIONS-AMERICAN SOCIETY OF MECHANICAL ENGINEERS JOURNAL OF VIBRATION AND ACOUSTICS*, 128(4):532, 2006.
- [11] Badreddine Assouar, Bin Liang, Ying Wu, Yong Li, Jian-Chun Cheng, and Yun Jing. Acoustic metasurfaces. *Nature Reviews Materials*, 3(12):460–472, 2018.
- [12] J.-L. Auriault and C. Boutin. Long wavelength inner-resonance cut-off frequencies in elastic composite materials. *International Journal of Solids and Structures*, 49(23):3269–3281, 2012.
- [13] JL Auriault and G Bonnet. Dynamique des composites élastiques périodiques. *Arch. Mech*, 37(4-5):269–284, 1985.

- [14] Nikolai Sergeevich Bakhvalov and Grigory Panasenko. *Homogenisation: averaging processes in periodic media: mathematical problems in the mechanics of composite materials*, volume 36. Springer Science & Business Media, 2012.
- [15] Abderrahmane Bendali and Keddour Lemrabet. The effect of a thin coating on the scattering of a time-harmonic wave for the helmholtz equation. *SIAM Journal on Applied Mathematics*, 56(6):1664–1693, 1996.
- [16] Alain Bensoussan, Jacques-Louis Lions, and George Papanicolaou. *Asymptotic analysis for periodic structures*, volume 374. American Mathematical Soc., 2011.
- [17] H. A. Bethe. Theory of diffraction by small holes. *Phys. Rev.*, 66:163–182, Oct 1944.
- [18] Anne-Sophie Bonnet-Ben Dhia and Felipe Starling. Guided waves by electromagnetic gratings and non-uniqueness examples for the diffraction problem. *Mathematical Methods in the Applied Sciences*, 17(5):305–338, 1994.
- [19] William Henry Bragg and William Lawrence Bragg. The reflection of x-rays by crystals. *Proceedings of the Royal Society of London. Series A, Containing Papers of a Mathematical and Physical Character*, 88(605):428–438, 1913.
- [20] Feiyan Cai, Fengming Liu, Zhaojian He, and Zhengyou Liu. High refractive-index sonic material based on periodic subwavelength structure. *Applied Physics Letters*, 91(20):203515, 2007.
- [21] Wenshan Cai, Uday K Chettiar, Alexander V Kildishev, and Vladimir M Shalaev. Optical cloaking with metamaterials. *Nature photonics*, 1(4):224–227, 2007.
- [22] Fioralba Cakoni, Bojan B Guzina, and Shari Moskow. On the homogenization of a scalar scattering problem for highly oscillating anisotropic media. *SIAM Journal on Mathematical Analysis*, 48(4):2532–2560, 2016.
- [23] M Callan, CM Linton, and DV Evans. Trapped modes in two-dimensional waveguides. *Journal of Fluid Mechanics*, 229:51–64, 1991.
- [24] Qing Cao and Philippe Lalanne. Negative role of surface plasmons in the transmission of metallic gratings with very narrow slits. *Physical Review Letters*, 88(5):057403, 2002.
- [25] Lucas Chesnel and Sergei A Nazarov. Exact zero transmission during the fano resonance phenomenon in non-symmetric waveguides. *Zeitschrift für angewandte Mathematik und Physik*, 71(3):1–13, 2020.
- [26] Lucas Chesnel and Vincent Pagneux. Simple examples of perfectly invisible and trapped modes in waveguides. *The Quarterly Journal of Mechanics and Applied Mathematics*, 71(3):297–315, 2018.
- [27] Lucas Chesnel and Vincent Pagneux. From zero transmission to trapped modes in waveguides. *Journal of Physics A: Mathematical and Theoretical*, 52(16):165304, 2019.
- [28] Doina Cioranescu and Patrizia Donato. *An Introduction to Homogenization*, volume 17. 01 1999.

-
- [29] Andrea Colombi, Daniel Colquitt, Philippe Roux, Sebastien Guenneau, and Richard V Craster. A seismic metamaterial: The resonant metawedge. *Scientific reports*, 6(1):27717, 2016.
- [30] Andrea Colombi, Philippe Roux, Sebastien Guenneau, Philippe Gueguen, and Richard V Craster. Forests as a natural seismic metamaterial: Rayleigh wave bandgaps induced by local resonances. *Scientific reports*, 6(1):1–7, 2016.
- [31] Rémi Cornaggia and Bojan B Guzina. Second-order homogenization of boundary and transmission conditions for one-dimensional waves in periodic media. *International Journal of Solids and Structures*, 188:88–102, 2020.
- [32] Richard V Craster and Sébastien Guenneau. *Acoustic metamaterials: Negative refraction, imaging, lensing and cloaking*, volume 166. Springer Science & Business Media, 2012.
- [33] Richard V Craster, Julius Kaplunov, and Aleksey V Pichugin. High-frequency homogenization for periodic media. *Proceedings of the Royal Society A: Mathematical, Physical and Engineering Sciences*, 466(2120):2341–2362, 2010.
- [34] David Crouse, Eric Jaquay, Abdur Maikal, and Alastair P Hibbins. Light circulation and weaving in periodically patterned structures. *Physical Review B*, 77(19):195437, 2008.
- [35] Gianni Dal Maso. *An introduction to Γ -convergence*, volume 8. Springer Science & Business Media, 2012.
- [36] EB Davies and L Parnowski. Trapped modes in acoustic waveguides. *The Quarterly Journal of Mechanics and Applied Mathematics*, 51(3):477–492, 1998.
- [37] Bérangère Delourme, Sonia Fliss, Patrick Joly, and Elizaveta Vasilevskaya. Trapped modes in thin and infinite ladder like domains. part 1: Existence results. *Asymptotic analysis*, 103(3):103–134, 2017.
- [38] Bérangère Delourme, Housseem Haddar, and Patrick Joly. Approximate models for wave propagation across thin periodic interfaces. *Journal de mathématiques pures et appliquées*, 98(1):28–71, 2012.
- [39] Bérangère Delourme, Housseem Haddar, and Patrick Joly. On the well-posedness, stability and accuracy of an asymptotic model for thin periodic interfaces in electromagnetic scattering problems. *Mathematical Models and Methods in Applied Sciences*, 23(13):2433–2464, 2013.
- [40] Bérangère Delourme, Eric Lunéville, Jean-Jacques Marigo, Agnès Maurel, Jean-François Mercier, and Kim Pham. Approximate models for wave propagation across thin periodic interfaces. *Proceedings of the Royal Society A*, 477:2020.0668, 2021.
- [41] AS Bonnet-Ben Dhia, Dora Drissi, and Nabil Gmati. Mathematical analysis of the acoustic diffraction by a muffler containing perforated ducts. *Mathematical Models and Methods in Applied Sciences*, 15(07):1059–1090, 2005.

- [42] Hao Dong, Yufeng Nie, Junzhi Cui, Yatao Wu, and Zihao Yang. Second-order two-scale analysis and numerical algorithm for the damped wave equations of composite materials with quasi-periodic structures. *Applied Mathematics and Computation*, 298:201–220, 2017.
- [43] Thomas W Ebbesen, Henri J Lezec, HF Ghaemi, Tineke Thio, and Peter A Wolff. Extraordinary optical transmission through sub-wavelength hole arrays. *nature*, 391(6668):667–669, 1998.
- [44] DV Evans. Trapped acoustic modes. *IMA journal of applied mathematics*, 49(1):45–60, 1992.
- [45] DV Evans and M Fernyhough. Edge waves along periodic coastlines. part 2. *Journal of Fluid Mechanics*, 297:307–325, 1995.
- [46] DV Evans, M Levitin, and D Vassiliev. Existence theorems for trapped modes. *Journal of Fluid Mechanics*, 261:21–31, 1994.
- [47] Ugo Fano. Effects of configuration interaction on intensities and phase shifts. *Physical Review*, 124(6):1866, 1961.
- [48] D Felbacq. Noncommuting limits in homogenization theory of electromagnetic crystals. *Journal of Mathematical Physics*, 43(1):52–55, 2002.
- [49] Didier Felbacq and Guy Bouchitté. Theory of mesoscopic magnetism in photonic crystals. *Physical review letters*, 94(18):183902, 2005.
- [50] Clément Ferise, Philipp Del Hougne, Simon Félix, Vincent Pagneux, and Matthieu Davy. Exceptional points of p t-symmetric reflectionless states in complex scattering systems. *Physical Review Letters*, 128(20):203904, 2022.
- [51] Vladimir Fokin, Muralidhar Ambati, Cheng Sun, and Xiang Zhang. Method for retrieving effective properties of locally resonant acoustic metamaterials. *Physical Review B*, 76(14):144302, 2007.
- [52] Enduo Gao, Zhimin Liu, Fengqi Zhou, and Zhenbin Zhang. Multiphase resonant properties in metallic dielectric gratings with three-slits. *Modern Physics Letters B*, 33(21):1950250, 2019.
- [53] FJ Garcia-Vidal, L Martin-Moreno, and JB Pendry. Surfaces with holes in them: new plasmonic metamaterials. *Journal of optics A: Pure and applied optics*, 7(2):S97, 2005.
- [54] David Gérard-Varet and Nader Masmoudi. Homogenization and boundary layers. *Acta Math.*, 209.1:133–178, 2012.
- [55] Reza Ghaffarivardavagh, Jacob Nikolajczyk, R Glynn Holt, Stephan Anderson, and Xin Zhang. Horn-like space-coiling metamaterials toward simultaneous phase and amplitude modulation. *Nature communications*, 9(1):1–8, 2018.
- [56] Zvi Hashin and Shmuel Shtrikman. A variational approach to the theory of the elastic behaviour of multiphase materials. *Journal of the Mechanics and Physics of Solids*, 11(2):127–140, 1963.

-
- [57] Alastair P Hibbins, Ian R Hooper, Matthew J Lockyear, and J Roy Sambles. Microwave transmission of a compound metal grating. *Physical Review Letters*, 96(25):257402, 2006.
- [58] Ian R Hooper, B Tremain, JA Dockrey, and Alastair P Hibbins. Massively sub-wavelength guiding of electromagnetic waves. *Scientific reports*, 4(1):1–5, 2014.
- [59] Chia Wei Hsu, Bo Zhen, A Douglas Stone, John D Joannopoulos, and Marin Soljavcić. Bound states in the continuum. *Nature Reviews Materials*, 1(9):1–13, 2016.
- [60] RA Hurd. The propagation of an electromagnetic wave along an infinite corrugated surface. *Canadian Journal of Physics*, 32(12):727–734, 1954.
- [61] Noe Jiménez, Weichun Huang, Vicent Romero-García, Vincent Pagneux, and J-P Groby. Ultra-thin metamaterial for perfect and quasi-omnidirectional sound absorption. *Applied Physics Letters*, 109(12):121902, 2016.
- [62] SGJ John, D Joannopoulos, Joshua N Winn, and Robert D Meade. Photonic crystals: molding the flow of light. *In Princeton University of Press: Princeton, NJ, USA*, 2008.
- [63] Patrick Joly and Adrien Semin. Construction and analysis of improved kirchoff conditions for acoustic wave propagation in a junction of thin slots. *ESAIM Proc.*, 25:44–67, 2008.
- [64] Nadège Kaina, Fabrice Lemoult, Mathias Fink, and Geoffroy Lerosey. Negative refractive index and acoustic superlens from multiple scattering in single negative metamaterials. *Nature*, 525(7567):77–81, 2015.
- [65] Luc Kelders, Jean F Allard, and Walter Lauriks. Ultrasonic surface waves above rectangular-groove gratings. *The Journal of the Acoustical Society of America*, 103(5):2730–2733, 1998.
- [66] Abdelkrim Khelif, Abdelkrim Choujaa, Sarah Benchabane, Bahram Djafari-Rouhani, and Vincent Laude. Guiding and bending of acoustic waves in highly confined phononic crystal waveguides. *Applied physics letters*, 84(22):4400–4402, 2004.
- [67] Charles Kittel. *Introduction to Solid State Physics*. New York: John Wiley & Sons, 8th edition, 2004.
- [68] Paul W Klipsch. A low frequency horn of small dimensions. *The Journal of the Acoustical Society of America*, 13(2):137–144, 1941.
- [69] Kirill Koshelev, Sergey Lepeshov, Mingkai Liu, Andrey Bogdanov, and Yuri Kivshar. Asymmetric metasurfaces with high-q resonances governed by bound states in the continuum. *Physical review letters*, 121(19):193903, 2018.
- [70] Sergey Kruk and Yuri Kivshar. Functional meta-optics and nanophotonics governed by mie resonances. *Acs Photonics*, 4(11):2638–2649, 2017.
- [71] Peter Kuchment. Graph models for waves in thin structures. *Waves in random media*, 12(4):R1, 2002.

- [72] Duc Trung Le and Jean-Jacques Marigo. Second order homogenization of quasi-periodic structures. *Vietnam Journal of Mechanics*, 40(4):325–348, 2018.
- [73] Hyuk Lee, Jun Kyu Lee, Hong Min Seung, and Yoon Young Kim. Mass-stiffness substructuring of an elastic metasurface for full transmission beam steering. *Journal of the Mechanics and Physics of Solids*, 112:577–593, 2018.
- [74] Fabrice Lemoult, Nadège Kaina, Mathias Fink, and Geoffroy Lerosey. Wave propagation control at the deep subwavelength scale in metamaterials. *Nature Physics*, 9(1):55–60, 2013.
- [75] Shiyu Li, Chaobiao Zhou, Tingting Liu, and Shuyuan Xiao. Symmetry-protected bound states in the continuum supported by all-dielectric metasurfaces. *Physical Review A*, 100(6):063803, 2019.
- [76] Yong Li, Bin Liang, Zhong-ming Gu, Xin-ye Zou, and Jian-chun Cheng. Reflected wavefront manipulation based on ultrathin planar acoustic metasurfaces. *Scientific reports*, 3(1):1–6, 2013.
- [77] Yong Li, Bin Liang, Zhong-ming Gu, Xin-ye Zou, and Jian-chun Cheng. Unidirectional acoustic transmission through a prism with near-zero refractive index. *Applied Physics Letters*, 103(5):053505, 2013.
- [78] Yong Li, Bin Liang, Xu Tao, Xue-feng Zhu, Xin-ye Zou, and Jian-chun Cheng. Acoustic focusing by coiling up space. *Applied Physics Letters*, 101(23):233508, 2012.
- [79] Yong Li, Bin Liang, Xin-ye Zou, and Jian-chun Cheng. Extraordinary acoustic transmission through ultrathin acoustic metamaterials by coiling up space. *Applied Physics Letters*, 103(6):063509, 2013.
- [80] Zixian Liang, Tianhua Feng, Shukin Lok, Fu Liu, Kung Bo Ng, Chi Hou Chan, Jinjin Wang, Seunghoon Han, Sangyoon Lee, and Jensen Li. Space-coiling metamaterials with double negativity and conical dispersion. *Scientific reports*, 3(1):1–6, 2013.
- [81] Zixian Liang and Jensen Li. Extreme acoustic metamaterial by coiling up space. *Physical Review Letters*, 108(11):114301, 2012.
- [82] Junshan Lin, Stephen P Shipman, and Hai Zhang. A mathematical theory for fano resonance in a periodic array of narrow slits. *SIAM Journal on Applied Mathematics*, 80(5):2045–2070, 2020.
- [83] Junshan Lin and Hai Zhang. Scattering by a periodic array of subwavelength slits ii: Surface bound states, total transmission, and field enhancement in homogenization regimes. *Multiscale Modeling & Simulation*, 16(2):954–990, 2018.
- [84] Junshan Lin and Hai Zhang. Fano resonance in metallic grating via strongly coupled subwavelength resonators. *European Journal of Applied Mathematics*, 32(2):370–394, 2021.
- [85] Christopher M Linton and Philip McIver. *Handbook of mathematical techniques for wave/structure interactions*. Chapman and Hall/CRC, 2001.

-
- [86] CM Linton and Maureen McIver. The existence of rayleigh–bloch surface waves. *Journal of Fluid Mechanics*, 470:85–90, 2002.
- [87] CM Linton and P McIver. Embedded trapped modes in water waves and acoustics. *Wave motion*, 45(1-2):16–29, 2007.
- [88] Zhengyou Liu, Xixiang Zhang, Yiwei Mao, YY Zhu, Zhiyu Yang, Che Ting Chan, and Ping Sheng. Locally resonant sonic materials. *science*, 289(5485):1734–1736, 2000.
- [89] Erwin G. Loewen and Evgeny Popov. *Diffraction Gratings and Applications*, volume 1st Edition. Boca Raton: Taylor & Francis, 1997.
- [90] Ming-Hui Lu, Xiao-Kang Liu, Liang Feng, Jian Li, Cheng-Ping Huang, Yan-Feng Chen, Yong-Yuan Zhu, Shi-Ning Zhu, and Nai-Ben Ming. Extraordinary acoustic transmission through a 1d grating with very narrow apertures. *Physical Review Letters*, 99(17):174301, 2007.
- [91] Guancong Ma and Ping Sheng. Acoustic metamaterials: From local resonances to broad horizons. *Science advances*, 2(2):e1501595, 2016.
- [92] YG Ma, XS Rao, GF Zhang, and CK Ong. Microwave transmission modes in compound metallic gratings. *Physical Review B*, 76(8):085413, 2007.
- [93] Stefan A Maier et al. *Plasmonics: fundamentals and applications*, volume 1. Springer, 2007.
- [94] Isroel M Mandel, Andrii B Golovin, and David T Crouse. Analytical description of the dispersion relation for phase resonances in compound transmission gratings. *Physical Review A*, 87(5):053833, 2013.
- [95] Jean-Jacques Marigo and Agnès Maurel. Homogenization models for thin rigid structured surfaces and films. *The Journal of the acoustical Society of America*, 140(1):260–273, 2016.
- [96] Jean-Jacques Marigo and Agnès Maurel. Second order homogenization of subwavelength stratified media including finite size effect. *SIAM Journal on Applied Mathematics*, 77(2):721–743, 2017.
- [97] Jean-Jacques Marigo, Agnes Maurel, Kim Pham, and Amine Sbitti. Effective dynamic properties of a row of elastic inclusions: the case of scalar shear waves. *Journal of elasticity*, 128(2):265–289, 2017.
- [98] Paul A Martin and Robert A Dalrymple. Scattering of long waves by cylindrical obstacles and gratings using matched asymptotic expansions. *Journal of Fluid Mechanics*, 188:465–490, 1988.
- [99] Agnès Maurel and Jean-Jacques Marigo. Sensitivity of a dielectric layered structure on a scale below the periodicity: A fully local homogenized model. *Physical Review B*, 98(2):024306, 2018.
- [100] Agnès Maurel, J-F Mercier, K Pham, J-J Marigo, and Abdelwaheb Ourir. Enhanced resonance of sparse arrays of helmholtz resonators—application to perfect absorption. *The Journal of the Acoustical Society of America*, 145(4):2552–2560, 2019.

- [101] Agnes Maurel, Jean-François Mercier, and Simon Félix. Modal method for the 2d wave propagation in heterogeneous anisotropic media. *JOSA A*, 32(5):979–990, 2015.
- [102] Francisco Medina, Francisco Mesa, and Diana C Skigin. Extraordinary transmission through arrays of slits: a circuit theory model. *IEEE Transactions on Microwave Theory and Techniques*, 58(1):105–115, 2009.
- [103] Francisco Medina, Francisco Mesa, and Diana C Skigin. Extraordinary transmission through arrays of slits: a circuit theory model. *IEEE transactions on microwave theory and techniques*, 58(1):105–115, 2009.
- [104] Shixu Meng and Bojan B Guzina. On the dynamic homogenization of periodic media: Willis’ approach versus two-scale paradigm. *Proceedings of the Royal Society A: Mathematical, Physical and Engineering Sciences*, 474(2213):20170638, 2018.
- [105] J-F Mercier, Maria-Luisa Cordero, Simon Félix, Abdelwaheb Ourir, and Agnes Maurel. Classical homogenization to analyse the dispersion relations of spoof plasmons with geometrical and compositional effects. *Proceedings of the Royal Society A: Mathematical, Physical and Engineering Sciences*, 471(2182):20150472, 2015.
- [106] Graeme W Milton, Marc Briane, and John R Willis. On cloaking for elasticity and physical equations with a transformation invariant form. *New Journal of Physics*, 8(10):248, oct 2006.
- [107] Graeme W Milton and John R Willis. On modifications of newton’s second law and linear continuum elastodynamics. *Proceedings of the Royal Society A: Mathematical, Physical and Engineering Sciences*, 463(2079):855–880, 2007.
- [108] Andrey E Miroshnichenko, Sergej Flach, and Yuri S Kivshar. Fano resonances in nanoscale structures. *Reviews of Modern Physics*, 82(3):2257, 2010.
- [109] MG Moharam and TK Gaylord. Rigorous coupled-wave analysis of planar-grating diffraction. *JOSA*, 71(7):811–818, 1981.
- [110] Miguel Molerón, Marc Serra-Garcia, and Chiara Daraio. Acoustic fresnel lenses with extraordinary transmission. *Applied Physics Letters*, 105(11):114109, 2014.
- [111] Miguel Molerón, Marc Serra-Garcia, and Chiara Daraio. Visco-thermal effects in acoustic metamaterials: from total transmission to total reflection and high absorption. *New Journal of Physics*, 18(3):033003, 2016.
- [112] Shari Moskow and Michael Vogelius. First order corrections to the homogenized eigenvalues of a periodic composite medium. the case of neumann boundary conditions. *Preprint, Rutgers University*, 1, 1997.
- [113] AB Movchan, Christopher G Poulton, Lindsay C Botten, NA Nicorovici, and Ross C McPhedran. Noncommuting limits in electromagnetic scattering: asymptotic analysis for an array of highly conducting inclusions. *SIAM Journal on Applied Mathematics*, 61(5):1706–1730, 2001.
- [114] Hussein Nassar, Q-C He, and Nicolas Auffray. Willis elastodynamic homogenization theory revisited for periodic media. *Journal of the Mechanics and Physics of Solids*, 77:158–178, 2015.

-
- [115] Miguel Navarro-Cía, Diana C Skigin, Miguel Beruete, and Mario Sorolla. Experimental demonstration of phase resonances in metallic compound gratings with subwavelength slits in the millimeter wave regime. *Applied Physics Letters*, 94(9):091107, 2009.
- [116] Gabriel Nguetseng. A general convergence result for a functional related to the theory of homogenization. *SIAM Journal on Mathematical Analysis*, 20(3):608–623, 1989.
- [117] NA Nicorovici, RC McPhedran, and LC Botten. Photonic band gaps: Noncommuting limits and the “acoustic band”. *Physical review letters*, 75(8):1507, 1995.
- [118] Andrew N Norris and Xiaoshi Su. Enhanced acoustic transmission through a slanted grating. *Comptes Rendus Mécanique*, 343(12):622–634, 2015.
- [119] Vincent Pagneux. Multimodal admittance method in waveguides and singularity behavior at high frequencies. *Journal of computational and applied mathematics*, 234(6):1834–1841, 2010.
- [120] Vincent Pagneux. Trapped modes and edge resonances in acoustics and elasticity. In *Dynamic Localization Phenomena in Elasticity, Acoustics and Electromagnetism*, pages 181–223. Springer, 2013.
- [121] J. B. Pendry. Negative refraction makes a perfect lens. *Phys. Rev. Lett.*, 85:3966–3969, Oct 2000.
- [122] JB Pendry, L Martin-Moreno, and FJ Garcia-Vidal. Mimicking surface plasmons with structured surfaces. *science*, 305(5685):847–848, 2004.
- [123] Kim Pham, Nicolas Lebbe, and Agnès Maurel. Diffraction grating with varying slit width: Quasi-periodic homogenization and its numerical implementation. *Journal of Computational Physics*, 473:111727, 2023.
- [124] Kim Pham, Agnès Maurel, J-F Mercier, Simon Félix, Maria Luisa Cordero, and Camila Horvath. Perfect brewster transmission through ultrathin perforated films. *Wave Motion*, 93:102485, 2020.
- [125] Kim Pham, Agnès Maurel, and Jean-Jacques Marigo. Two scale homogenization of a row of locally resonant inclusions - the case of anti-plane shear waves. *Journal of the Mechanics and Physics of Solids*, 106:80–94, 2017.
- [126] Kim Pham, Jean-François Mercier, Daniel Fuster, Jean-Jacques Marigo, and Agnes Maurel. Scattering of acoustic waves by a nonlinear resonant bubbly screen. *Journal of Fluid Mechanics*, 906, 2021.
- [127] JM Pitarke, VM Silkin, EV Chulkov, and PM Echenique. Theory of surface plasmons and surface-plasmon polaritons. *Reports on progress in physics*, 70(1):1, 2006.
- [128] Clair Poignard, Patrick Dular, Ronan Perrussel, Laurent Krahenbuhl, Laurent Nicolas, and Michelle Schatzman. Approximate conditions replacing thin layers. *IEEE transactions on magnetics*, 44(6):1154–1157, 2008.
- [129] Richard Porter. Plate arrays as a perfectly-transmitting negative-refraction metamaterial. *Wave Motion*, 100:102673, 2021.

- [130] Shuibao Qi, Yong Li, and Badreddine Assouar. Acoustic focusing and energy confinement based on multilateral metasurfaces. *Physical Review Applied*, 7(5):054006, 2017.
- [131] Lord Rayleigh. On the dynamical theory of gratings. *Proceedings of The Royal Society A: Mathematical, Physical and Engineering Sciences*, 79:399–416, 1907.
- [132] V Romero-García, Noe Jimenez, G Theocharis, V Achilleos, A Merkel, O Richoux, V Tournat, J-P Groby, and V Pagneux. Design of acoustic metamaterials made of helmholtz resonators for perfect absorption by using the complex frequency plane. *Comptes Rendus. Physique*, 21(7-8):713–749, 2020.
- [133] Vicente Romero-Garcia and Anne-Christine Hladky-Hennion. *Fundamentals and applications of acoustic metamaterials: from seismic to radio frequency*. John Wiley & Sons, 2019.
- [134] Imen Ben Salem, Reine-Marie Guillermic, Caitlin Sample, Valentin Leroy, Arnaud Saint-Jalmes, and Benjamin Dollet. Propagation of ultrasound in aqueous foams: bubble size dependence and resonance effects. *Soft Matter*, 9(4):1194–1202, 2013.
- [135] E. Sanchez-Palencia. *Non-Homogeneous Media and Vibration Theory*. Lecture Notes in Physics. Springer Berlin Heidelberg, 1980.
- [136] Logan Schwan, Olga Umnova, and Claude Boutin. Sound absorption and reflection from a resonant metasurface: Homogenisation model with experimental validation. *Wave Motion*, 72:154–172, 2017.
- [137] Adrien Semin. *Propagation d’ondes dans des jonctions de fentes minces*. PhD thesis, PhD thesis, Université Paris-Sud, 2010.
- [138] Danial P Shahraki and Bojan B Guzina. Homogenization of the wave equation with non-uniformly oscillating coefficients. *Mathematics and Mechanics of Solids*, 27(11):2341–2365, 2022.
- [139] S Shipman. Resonant scattering by open periodic waveguides. *Progress in Computational Physics (PiCP)*, 1:7–49, 2010.
- [140] Diana C Skigin. Transmission through subwavelength slit structures with a double period: a simple model for the prediction of resonances. *Journal of Optics A: Pure and Applied Optics*, 11(10):105102, 2009.
- [141] Diana C Skigin and Ricardo A Depine. Transmission resonances of metallic compound gratings with subwavelength slits. *Physical Review Letters*, 95(21):217402, 2005.
- [142] Diana C Skigin, Hung Loui, Zoya Popovic, and Edward F Kuester. Bandwidth control of forbidden transmission gaps in compound structures with subwavelength slits. *Physical Review E*, 76(1):016604, 2007.
- [143] A Douglas Stone, William R Sweeney, Chia Wei Hsu, Kabish Wisal, and Zeyu Wang. Reflectionless excitation of arbitrary photonic structures: A general theory. *Nanophotonics*, 10(1):343–360, 2021.

-
- [144] Andrew C Strikwerda, Kebin Fan, Hu Tao, Daniel V Pilon, Xin Zhang, and Richard D Averitt. Comparison of birefringent electric split-ring resonator and meanderline structures as quarter-wave plates at terahertz frequencies. *Optics Express*, 17(1):136–149, 2009.
- [145] Björn CP Sturmberg, Kokou B Dossou, Lindsay C Botten, Ross C McPhedran, and C Martijn De Sterke. Fano resonances of dielectric gratings: symmetries and broadband filtering. *Optics express*, 23(24):A1672–A1686, 2015.
- [146] EO Tuck. Matching problems involving flow through small holes. *Advances in applied mechanics*, 15:89–158, 1975.
- [147] R Ulrich and M Tacke. Submillimeter waveguiding on periodic metal structure. *Applied Physics Letters*, 22(5):251–253, 1973.
- [148] F Ursell. Trapping modes in the theory of surface waves. In *Proc. Camb. Phil. Soc.*, volume 47, pages 347–358, 1951.
- [149] John von Neumann and Eugene P Wigner. Über merkwürdige diskrete eigenwerte. *The Collected Works of Eugene Paul Wigner: Part A: The Scientific Papers*, pages 291–293, 1993.
- [150] GP Ward, AP Hibbins, JR Sambles, and JD Smith. Acoustic transmission through compound subwavelength slit arrays. *Physical Review B*, 94(2):024304, 2016.
- [151] John R Willis. Bounds and self-consistent estimates for the overall properties of anisotropic composites. *Journal of the Mechanics and Physics of Solids*, 25(3):185–202, 1977.
- [152] John R Willis. Variational principles for dynamic problems for inhomogeneous elastic media. *Wave Motion*, 3(1):1–11, 1981.
- [153] John R Willis. Effective constitutive relations for waves in composites and metamaterials. *Proceedings of the Royal Society A: Mathematical, Physical and Engineering Sciences*, 467(2131):1865–1879, 2011.
- [154] R.W. Wood. Xlii. on a remarkable case of uneven distribution of light in a diffraction grating spectrum. *The London, Edinburgh, and Dublin Philosophical Magazine and Journal of Science*, 4(21):396–402, 1902.
- [155] Dong Xiang, Ling-Ling Wang, Xiao-Fei Li, Liu Wang, Xiang Zhai, Zhong-He Liu, and Wei-Wei Zhao. Transmission resonances of compound metallic gratings with two subwavelength slits in each period. *Optics express*, 19(3):2187–2192, 2011.
- [156] Yangbo Xie, Bogdan-Ioan Popa, Lucian Zigoneanu, and Steven A Cummer. Measurement of a broadband negative index with space-coiling acoustic metamaterials. *Physical Review Letters*, 110(17):175501, 2013.
- [157] Hui Zhang, Li Fan, Jianmin Qu, and Shuyi Zhang. Sound transmission properties assisted by the phase resonances of composite acoustic gratings. *Journal of Applied Physics*, 119(8):084902, 2016.

- [158] Vasilii Vasil'evich Zhikov. On an extension of the method of two-scale convergence and its applications. *Sbornik: Mathematics*, 191(7):973, 2000.
- [159] Joar Zhou Hagström, Agnès Maurel, and Kim Pham. The interplay between fano and fabry–pérot resonances in dual-period metagratings. *Proceedings of the Royal Society A*, 477(2255):20210632, 2021.
- [160] Joar Zhou Hagström, Agnès Maurel, and Kim Pham. Modelling acoustic space-coiled metacrystals. *Submitted*, 2022.
- [161] Joar Zhou Hagström, Agnès Maurel, and Kim Pham. Revisiting effective acoustic propagation in labyrinthine metasurfaces. *Under revision*, 2022.

Titre : Méthodes asymptotiques pour des métamatériaux acoustiques résonants (en français)

Mots clés : Méthode asymptotique, métamatériaux, propagation des ondes, homogénéisation

Résumé : Dans cette thèse, on s'intéresse à la modélisation des métamatériaux acoustiques résonants. En utilisant des techniques d'homogénéisations asymptotiques, on dérive et analyse des modèles effectifs pour deux systèmes acoustiques résonants différents.

La première partie est consacrée à l'étude d'un réseau de période sub-longueur onde composé de fente. Dans le cas d'un réseau à double période, composé d'une cellule périodique avec deux fentes, on s'intéresse à la configuration où une certaine symétrie est brisée. Ce faisant, le champ évanescent le long de la structure peut se coupler avec le continuum qui se propage. Les résonances parfaites deviennent des quasi-résonances, ou des modes fuyants, ce qui entraîne un comportement frappant dans le spectre de transmission où l'on observe des pics asymétriques de type Fano. La dérivation du modèle effectif homogénéisé du réseau à période double est obtenue par une combinaison d'homogénéisation en volume

et des méthodes de raccordements asymptotiques. Le modèle obtenu permet d'obtenir des solutions explicites et analyser les mécanismes résonnants sous-jacents du système.

La deuxième partie porte sur les matériaux labyrinthiques ou 'space-coiled materials'. Ces matériaux reposent sur l'idée que l'onde acoustique est forcée de suivre la trajectoire de la fente enroulée. Deux types d'enroulement sont étudiés.

L'enroulement communément rencontré dans la littérature est revisité par l'homogénéisation et donne un résultat plus précis que des études précédentes. Le deuxième type d'enroulement est ce que nous appelons un méta-cristal. Cela peut être interprété comme un cristal phononique unidimensionnel imbriqué dans un réseau sub-longueur d'onde, et bénéficie maintenant de deux échelles de longueurs. La structure peut exhiber des bandes interdites dues à la diffusion de Bragg qui sont couplées aux résonances Fabry-Pérot.

Title : Asymptotic methods for resonant acoustical metamaterials (en anglais)

Keywords : Asymptotic method, metamaterials, wave propagation, homogenization

Abstract : In this thesis, we are interested in the modelling of resonant acoustic metamaterials. Using asymptotic homogenization techniques, we derive and analyse effective models for two different acoustical resonant systems.

The first part is devoted to the study of subwavelength grating composed of slits in a sound hard slab. We are interested in the case of a dual-period array, sometimes referred to as compound gratings. When dealing with a dual-period grating, composed of a periodic unit cell with two slits, we are interested in the configuration where some symmetry is broken. By doing so, the evanescent field along the structure can couple with the propagating continuum. The perfect resonances become a quasi-resonance, or leaky modes, and this leads to some striking behaviour in the transmission spectra, where asymmetric Fano like peaks are observed. The derivation of the homogenized effective model of a dual period metagrating is obtained through

a combination of bulk homogenization and matched asymptotic techniques. The obtained model allows for the derivation of closed form solutions and an analytical study of underlying resonant mechanisms.

The second part focuses on space-coiled materials or labyrinthine materials. These materials rely on the idea that the acoustic wave is forced to follow the path of the coiled slot. Two types of coiling arrangement are studied.

We revisit the most encountered coiled arrangement through homogenization and show that it gives a more precise result than previous studies. The second arrangement is what we refer to as a meta-crystal. It can be interpreted as a one dimensional phononic crystal embedded in a subwavelength grating, which now benefits from two length-scales. The structure benefits from band gaps due to Bragg scattering, that is coupled with the Fabry-Pérot resonances.